

**Electrochemical and Corrosion behavior of Ni-base
Amorphous Alloys and Coating for Nitric Acid
Application**

By

Chiranjit Poddar

CHEM02201404006

Indira Gandhi Centre for Atomic Research

Kalpakkam

*A thesis submitted to the
Board of Studies in Chemical Sciences
In partial fulfillment of requirements
for the Degree of*

DOCTOR OF PHILOSOPHY

of

HOMI BHABHA NATIONAL INSTITUTE



December, 2019

Homi Bhabha National Institute¹

Recommendations of the Viva Voce Committee

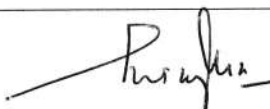
As members of the Viva Voce Committee, we certify that we have read the dissertation prepared by Chiranjit Poddar entitled "Electrochemical and Corrosion behavior of Ni-base Amorphous Alloys and Coatings for Nitric Acid Application" and recommend that it may be accepted as fulfilling the thesis requirement for the award of Degree of Doctor of Philosophy.

Chairman: Prof. S. Rangarajan,



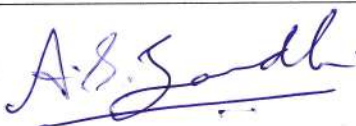
Date 19.12.2019

Guide / Convener: Prof. S. Ningshen



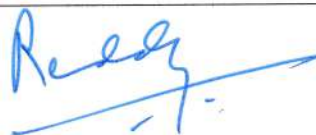
Date : 19/12/19

Examiner: Prof. Ashutosh S Gandhi



Date : 19/12/19

Member 1: Prof. B.P. Reddy



Date : 19/12/19

Member 2: Prof. John Philip



Date : 19/12/19

Member 3: Prof. K.I. Gnanasekar



Date : 19/12/19

Final approval and acceptance of this thesis is contingent upon the candidate's submission of the final copies of the thesis to HBNI.

I/We hereby certify that I/we have read this thesis prepared under my/our direction and recommend that it may be accepted as fulfilling the thesis requirement.

Date: 19/12/2019

Place: Kalpakam

Signature

Guide

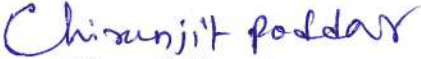

(S. NINGSHEN)

¹ This page is to be included only for final submission after successful completion of viva voce.

STATEMENT BY AUTHOR

This dissertation has been submitted in partial fulfilment of requirements for an advanced degree at Homi Bhabha National Institute (HBNI) and is deposited in the Library to be made available to borrowers under rules of the HBNI.

Brief quotations from this dissertation are allowable without special permission, provided that accurate acknowledgement of the source is made. Requests for permission for extended quotation from or reproduction of this manuscript in whole or in part may be granted by the Competent Authority of HBNI when in his or her judgment the proposed use of the material is in the interests of scholarship. In all other instances, however, permission must be obtained from the author.


Name & Signature

of the student

DECLARATION

I, hereby declare that the investigation presented in the thesis has been carried out by me. The work is original and has not been submitted earlier as a whole or in part for a degree / diploma at this or any other Institution / University.

Chiranjit Poddar

Name & Signature

of the student

List of Publications arising from the thesis

Refereed Journals:

Published

1. **Chiranjit Poddar**, J. Jayaraj, C. Mallika, U. Kamachi Mudali, Oxidation behavior of $\text{Ni}_{60}\text{Nb}_{30}\text{Ta}_{10}$ metallic glass below its glass transition temperature, **Journal of Alloys and Compound**, 728 (2017) 1146-1152.
2. **Chiranjit Poddar**, J. Jayaraj, S. Ningshen, Passive film characteristics and corrosion behavior of thermally oxidized $\text{Ni}_{60}\text{Nb}_{30}\text{Ta}_{10}$ metallic glass in nitric acid medium, **Journal of Alloys and Compound**, 783(2019) 680-686.
3. **Chiranjit Poddar**, J. Jayaraj, S. Ningshen, U. Kamachi Mudali, Effect of thermal oxidation on the oxide characteristic and corrosion behavior of $\text{Ni}_{60}\text{Nb}_{40}$ amorphous ribbon in nitric acid, **Applied Surface Science**, 479 (2019) 430-439.
4. **Chiranjit Poddar**, J. Jayaraj, S. Amirthapandian, S. Ningshen, Effect of the thermally grown amorphous oxide film on the corrosion properties of the $\text{Ni}_{50}\text{Zr}_{25}\text{Nb}_{25}$ metallic glass in nitric acid, **Intermetallics** 113 (2019) 106571.
5. **Chiranjit Poddar**, J. Jayaraj, S. Ningshen, Electrochemical and Passive film properties of $\text{Ni}_{60}\text{Nb}_{30}\text{Ta}_{10}$ metallic glass and partially crystalline alloy in nitric acid, **Journal of Alloys and Compound**, 813 (2020) 152172.

Communicated:

6. **Chiranjit Poddar**, Akash Singh, S. Amirthapandian, S. Ningshen, Corrosion behaviour of $\text{Ni}_{60}\text{Nb}_{30}\text{Ta}_{10}$ metallic glass coated 304 L SS in nitric acid medium, **Electrochemica Acta** (Under Revision 2019).

Conference/Symposium

1. **Best oral presentation Award**, **Chiranjit Poddar**, J. Jayaraj, S. Ningshen, Oxidation and Corrosion behavior of Ni-based amorphous alloy in the nitric acid environment, International Corrosion Prevention Symposium for Research Scholars, CORSYM-2018, 23-24 March, IIT Madras, Chennai. India
2. **Chiranjit Poddar**, J. Jayaraj, S. Ningshen, Oxidation and corrosion behaviour of $\text{Ni}_{50}\text{Zr}_{25}\text{Nb}_{25}$ metallic glasses in aggressive nitric acid, International Conference on Surface Engineering INCOSURF-2018 on 9 -11 August 2018, IISc Bangalore, India.

3. **Chiranjit Poddar**, J. Jayaraj, C. Mallika, U. Kamachi Mudali, Oxidation and corrosion behaviour of $\text{Ni}_{60}\text{Nb}_{30}\text{Ta}_{10}$ bulk metallic glass, "International Corrosion Prevention Symposium for Research Scholars:, CORSYM-2015", 31st July-1st August 2015 IIT Madras, India.
4. **Chiranjit Poddar**, J. Jayaraj, U. Kamachi Mudali, Electrochemical corrosion properties of $\text{Ni}_{60}\text{Nb}_{30}\text{Ta}_{10}$ metallic glass and its partially crystallized alloys, RSM-MSENM, May 7-9, 2018, IGCAR, India.
5. **Chiranjit Poddar**, National Workshop on High Entropy Alloys from March 28-29th, 2015 at IIT Madras, India.
6. **Chiranjit Poddar**, J. Jayaraj, A. Pandian, S. Ningshen, Corrosion behavior of thermally oxidized $\text{Ni}_{50}\text{Zr}_{25}\text{Nb}_{25}$ metallic glasses in aggressive nitric acid, International Conference on Surface Engineering ISMANAM-2019 on 8 -12 July 2018, The Raintree, Chennai, India.

Chiranjit Poddar

Name & Signature

of the student

DEDICATIONS

My Ph.D thesis is dedicated to my family for their immense love and faith on me

ACKNOWLEDGEMENTS

I would like to convey my gratitude to all who made this work possible. First and foremost, this work has been possible due to the excellent guidance of Dr. S. Ningshen. His guidance to the students is very polite and exceptional. During the frustrating times of my research work for the past five years, he encouraged me a lot. As a guide, he has gone beyond his responsibility and helped in many paths for doing fruitful research.

I would like to thank Dr. A. K. Bhaduri, Director, Indira Gandhi Centre for Atomic Research (IGCAR) and Dr. G. Amarendra, Director, Metallurgy and Materials Group, IGCAR for allowing me to pursue Ph.D research degree at Indira Gandhi Centre for Atomic Research.

I express my gratitude to Dr. U. Kamachi Mudali, and Dr. J. Jayaraj for their exceptional advice toward the initial research work plan and sincere appreciation to both for allowing me to enjoy and giving me the real meaning of doing research. Also, I would like to thank the Chairman of my thesis committee Dr. S. Rangarajan and other member Dr. John Philip, Dr. P. Reddy and Dr. K. I. Gnanasekar for their constructive comments and encouragement in various stages during my research works.

Special thanks to the staff and friend of Corrosion Science and Technology Division, especially Madhura B, Polson, Hareesh Rongali, Geetsubra Jena, Manu Sriharilal, Dr. Jagdeeshwar Rao, and Mr. E. Vetrivendan who were always ready to help me with their warm heart.

It goes without saying my many thanks to Mr. Avinash Kumar, K. Kaliraj and Yogesh Kumar and Mr. C. Thinaharan, because without their help, many things certainly would have

been tedious. They taught me to operate various equipment and our friendship has proved very fruitful over the past few years, to which I am deeply grateful.

My deepest thanks go to Praveen Kumar, Saytam Jawsbal, Sumit bahuguna, King Chubby. Murali Krishna, and Anil Kumar, with them I had the finest companionship, and they are always with me at my worst and my best since the beginning of this journey.

I would like to thank Dr. P. Parameshwaran and Dr. Akash Singh, PMD, MMG, for their help in metallic glassy coating developmental work.

I wish to extend my thanks to all my teachers and friends, though their names are not printed in these pages and but it is printed in my heart.

Table of contents

Abstracts	iv
List of Figures	vii
List of Tables	xiv
1 Introduction	1
1.1 Metallic glass	1
1.1.1 Definition of metallic glass	1
1.1.2 Formation of metallic glass	2
1.1.3 Models to predict glass forming compositions	3
1.1.4 Developments of metallic glasses	5
1.2 Corrosion	11
1.2.1 Nitric acid corrosion issue for the structure materials in nuclear reprocessing plant	11
1.2.2 Literature survey on the corrosion behaviour of metallic glass	15
1.3 Oxidation	19
1.3.1 Thermodynamics of Oxidation	20
1.3.2 Kinetics of Oxidation	21
1.3.3 Initial Stages of Oxidation and Scale Growth	23
1.3.4 Oxidation of Alloys	25
1.3.5 Methods for finding protective and un-protective growth (Pilling Bedworth ratio)	25
1.3.6 Literature survey for the Oxidation of metals, Amorphous or metallic glassy alloys	27
1.4 Other properties of metallic glassy alloys	30
1.5 Statement of problems and Objectives	32
1.5.1 Statement of problems	32
1.5.2 Objectives	34
2 Materials and Experimental Procedures	36
2.1 Sample preparation	36
2.1.1 Arc melting	36
2.1.2 Melt spinning	37
2.1.3 Magnetron sputtering	37
2.2 Structural characterization	39
2.2.1 X-ray Diffraction (XRD) and grazing incident X-ray Diffraction (GIXRD)	39
2.2.2 Transmission Electron Microscopy	39

2.3	Oxidation of the Metallic Glass.....	40
2.3.1	Thermal oxidation in a tubular furnace	40
2.3.2	Thermogravimetric analysis	40
2.4	Corrosion property evaluation.....	42
2.4.1	Specimen preparation for corrosion test.....	42
2.4.2	Electrolyte Medium	42
2.4.3	Potentiodynamic and potentiostatic polarization test.....	43
2.4.4	Electrochemical Impedance Spectroscopy measurements	44
2.4.5	Mott-Schottky analysis of the oxide film:.....	46
2.5	X-ray photoelectron spectroscopy.....	48
2.6	FESEM analyses of corrosion morphology.....	50
2.7	AFM analyses of surface topology.....	51
3	Effect of the structure (Amorphous & Crystalline) on corrosion resistance in nitric acid medium.....	53
3.1	Introduction:	53
3.2	Results and Discussion	54
3.2.1	XRD analysis of the as-spun and heat treated Ni ₆₀ Nb ₃₀ Ta ₁₀ alloy	54
3.2.2	HRTEM analysis of the as-spun and heat treated Ni ₆₀ Nb ₃₀ Ta ₁₀ alloy.....	55
3.2.3	XPS studies of Ni ₆₀ Nb ₃₀ Ta ₁₀ metallic glassy and partially-crystallized ribbon samples before immersion in nitric acid.....	56
3.2.4	Polarization behaviour of metallic glass and its crystallized alloy.....	58
3.2.5	Electrochemical Impedance Spectroscopy (EIS) analysis.	61
3.2.6	XPS studies of the metallic glass and partially crystallized ribbon after potentiostatic polarization test at 1.6 V for 30 min.....	63
3.2.7	Depth profiling studies of the potentiostatic polarized metallic glass and partially crystallized ribbon.	66
3.2.8	Surface morphology of the metallic glass and partially crystallized ribbon.	69
3.2.9	Semiconducting behaviour of the passive film formed on Ni ₆₀ Nb ₃₀ Ta ₁₀ glass and its crystallized alloy.....	74
3.3	Summary.....	76
4	Oxidation behavior of Ni-based metallic glassy alloys.....	78
4.1	Introduction:	78
4.2	Results and discussion:.....	80
4.2.1	Oxidation behaviour of as-spun and thermally oxidized Ni ₆₀ Nb ₄₀ ribbon.	80

4.2.2	Oxidation behaviour of as-spun and thermally oxidized Ni ₆₀ Nb ₃₀ Ta ₁₀ ribbon in air environments.	92
4.2.3	Oxidation behaviour of the Ni ₅₀ Nb ₂₅ Zr ₂₅ metallic glass	100
4.3	Summary:	110
5	Effects of the thermally grown oxide film on the corrosion properties of Ni-based MG in nitric acid environments	111
5.1	Introduction:	111
5.2	Results and Discussions	112
5.2.1	Electrochemical Corrosion behavior of as-spun and thermally oxidized Ni ₆₀ Nb ₄₀ ribbon in the concentrated medium.....	112
5.2.2	Electrochemical Corrosion behavior of as-spun and thermally oxidized Ni ₆₀ Nb ₃₀ Ta ₁₀ metallic glass ribbon in 1, 6, and 11.5 M nitric acid medium (effect of the nitric acid concentration).	119
5.2.3	Electrochemical corrosion behavior of as-spun and thermal oxidized Ni ₅₀ Nb ₂₅ Zr ₂₅ in 11.5 M nitric acid.	132
5.3	Summary.....	142
6	Corrosion behavior of Ni-based metallic glassy coating	144
6.1	Introduction	144
6.2	Results and discussion.....	145
6.2.1	Synthesis of Ni ₆₀ Nb ₃₀ Ta ₁₀ Thin Film Metallic glass (TFMG) coatings.	145
6.2.2	Surface and cross-sectional analyses of TFMG coating.....	146
6.2.3	XPS studies of the surface as well as depth passive film on the immersed metallic glass coated 304 L SS sample.	148
6.2.4	Comparison of the potentiodynamic polarization behaviour of TFMG coated and bare 304 L SS substrate in 1, 6 and 11.5 M nitric acid.	150
6.2.5	Electrochemical impedance analyses of TFMG coated and bare 304 L SS substrate in 1, 6 and 11.5 M nitric acid.....	153
6.2.6	Mott-Schottky behavior of TFMG coated and bare 304 L SS nitric acid.	154
6.2.7	Weight loss measurements in 11.5 M nitric acid environment under the boiling condition and surface analyses.	157
7	Conclusion and future work	162
7.1	Conclusion.....	162
7.2	Future work	163
	Reference	165

Abstracts

Bulk metallic glass (BMG) alloys possess a remarkable physical, chemical, oxidation, good mechanical properties, and soft magnetic properties, etc. In the last two decade, extensive studied has been investigated on the structure, physical and mechanical properties, glass formation ability (GFA), glass transition and crystallization process of metallic glasses. However, little has been reported about the development of high corrosion resistance of bulk metallic glasses for the aggressive nitric acid environment. Among the BMG materials, Ni-based metallic glass or amorphous alloys systems have attracted considerable attention in recent decades because of their commercial importance related to the functional applications for corrosion, and thermal oxidation. The Zr-, Ti-, Fe-, and Ni-based metallic glasses were exhibited excellent corrosion resistance corrosion resistance which attributed to the higher passivation ability in the corrosive environment. Excellent passivation ability of the metallic glasses was correlated with the structural and chemical homogeneity.

However, nitric acid is the main process medium used for reprocessing of the spent nuclear fuel. During different stages of the spent fuel dissolution, nitric acid is used in various concentrations (1 M–14 M). Therefore, the materials for reprocessing plant equipment should have excellent corrosion resistance in nitric acid media. The construction materials of type 304L stainless steel (SS) and nitric acid grades SS most commonly used for aqueous reprocessing plants and they were undergone a severe intergranular corrosion (IGC) attack in high concentrated nitric acid. BMG materials will be a potential candidate material for spent nuclear fuel reprocessing applications. Owing to its high corrosion resistance, the Ni-based metallic glasses are explored in the nitric acid for the service in spent nuclear fuel reprocessing plant.

However, the corrosion resistance of metallic glass and crystalline alloys in different enviro

-ments are related to structure and passive film properties. Similarly, metallic glassy alloys and its coating provides outstanding corrosion resistant due to their chemically homogeneous nature of its passive film. Thus, this study was systematically designed such that the corrosion behavior of three Ni-based metallic glasses alloy systems and its coatings (i.e., Ni₆₀Nb₄₀, Ni₆₀Nb₃₀Ta₁₀, and Ni₅₀Nb₂₅Zr₂₅) were investigated by considering the three different aspects such as environment, structure, and processing.

The corrosion resistance and passive film properties of Ni₆₀Nb₃₀Ta₁₀ metallic glass and partially crystallized ribbon were investigated in 11.5 M nitric acid environment. After the crystallization in a vacuum (10⁻⁶ mbar) at 650 °C, nano-crystalline Ni phase (primary precipitate) has formed in the Nb-Ta amorphous matrix. The electrochemical corrosion results confirmed the higher corrosion resistance of the alloy in the glassy state when compared to its crystalline counterpart.

Air-oxidation is proposed as one of the techniques to further improve the corrosion resistance of metallic glasses. In the present work, the corrosion resistance behavior of metallic glasses oxidation of Ni₆₀Nb₄₀, Ni₆₀Nb₃₀Ta₁₀, and Ni₅₀Nb₂₅Zr₂₅ metallic glass alloys were carried out in air environment below its glass transition temperature. The thermal oxidation of the Ni₆₀Nb₄₀, Ni₆₀Nb₃₀Ta₁₀ and Ni₅₀Nb₂₅Zr₂₅ metallic glass at lower temperature further increased corrosion resistance compared to the as-spun glassy structure in corrosive nitric acid environment. The effect of Ta and Zr-addition in Ni-Nb alloy subjected to air-oxidation was investigated at different temperature under isothermal condition. The comparison between oxidation kinetics, oxidation mechanism, surface morphology and structure of oxide film indicated better thermal stability of metallic glasses at 450 °C. However, low thermal stability of oxide film observed at higher oxidation temperature of 550 °C. The change in the thickness and surface composition with the oxidation temperature was investigated using XPS depth profiling techniques. Results of the potentiodynamic

polarization and EIS studies of the thermally grown oxide film at or below 450 °C on the Ni-based glassy alloys exhibited improved corrosion resistance when compared to as-prepared metallic glass in nitric acid environment. The change in the semiconducting properties with oxidation temperature in nitric acid medium was evaluated by Mott-Schottky method. The thermally grown oxides at low temperature oxidation were exhibited high corrosion resistance compared to the high oxidation temperature in nitric acid environment.

In recent decades, several attempts have been made to obtain corrosion resistant metallic glass coatings by different methods (electrodeposition, PLD, laser remelting, laser surface coating, kinetic sprayed, etc.). Among these, the magnetron sputtering technique is one of the promising and useful techniques that can be used to produce the metallic glass thin film on the different metallic substrates. Inter granular corrosion (IGC) is one of the unwanted problems with the conventional crystalline alloy like 304 L SS in concentrated nitric acid. In order to minimize the IGC of 304 L SS in 11.5 M nitric acid, the Ni₆₀Nb₃₀Ta₁₀ metallic glass coating was deposited on type 304 L SS using magnetron sputtering at RT and 200 °C. The magnetron sputtered glassy coating at 200 °C was exhibited significantly higher corrosion resistance compared to that of RT and bare 304 L SS in 1, 6, and 11.5 M nitric acid. The difference in corrosion resistance of glassy coating at RT, and 200 °C with bare 304 L SS was discussed with the context of the surface morphology, passivation ability, and also point defect density (vacancy defects). Moreover, in this study, the effect of nitric acid concentration was also emphasized on the corrosion behavior of the Ni-based glassy coating. The 200 °C glassy coating was exhibited thicker passive film while thin passive film was formed on RT coating. Both the film enriched with stable Nb₂O₅ and Ta₂O₅.

List of Figures

Fig. 1.1 Schematic TTT diagram for the onset crystallization.	2
Fig. 1.2 Images of the Vitreloy bulk metallic glass hardware, including golf clubs, electronic casings, optical hardware, ingots, 12 mm diameter rod, and large plate (under the samples). Hardware courtesy of Liquid metal Technologies.....	5
Figure 1.3 Picture of recently synthesized bulk metallic glass.....	7
Figure 1.4 Schematic time-temperature-transformation (TTT) diagrams comparing the crystallization kinetics of (a) rapidly quenched, (b) slower quenched (c) bulk glass forming alloys. The two curves with arrows show the cooling history during rapid quenching (RQ) at $\sim 10^6$ K/s and relatively slow quenching (SQ) at $\sim 10^2$ K/s.	8
Figure 1.5 Phase diagram of the Ni-Nb system	9
Figure 1.6 General flowchart of the PUREX process.....	11
Figure 1.7 General electrochemical behaviour of austenitic stainless steels in acidic media as a function of the potential.	12
Figure 1.8 The variations in the grain boundary attack of conventional and nitric acid grade special SS after boiling nitric acid test, (c) commercial type 304L SS, (b) Uranus 16 SS, and (a) Uranus 65 SS.....	14
Figure 1.9 Selective corrosion attacked leading to the formation of ‘corrosion tunnels’	14
Figure 1.10 Schematic representation of some aspects of the oxide scale formation.....	23
Figure 1.11 Relationship between tensile strength and Young’s modulus for various bulk amorphous and conventional alloys.....	31
Figure 1.12 A complex micro gear BMG processed by SPF.....	32
Figure 1.13 A coil shaped BMG processed by SPF.....	32
Figure 2.1 Schematic diagram of Arc-melting apparatus.	36
Figure 2.2 Schematic diagram of the melt spinning apparatus.....	37
Figure 2.3 Schematic diagram of Magnetron sputtering coating.....	38
Figure 2.4 the mean free paths of the photo-electron vs. electron kinetics energy for the different elements.....	50
Figure 3.1 (a) DSC traces of as-spun metallic glass, and (b) XRD pattern of as-spun $\text{Ni}_{60}\text{Nb}_{30}\text{Ta}_{10}$ metallic glass and crystallized ribbon at 650 °C after 1 hour.	55
Figure 3.2 SEM images with EDS for as-spun metallic glass	55

Figure 3.3 (a) TEM image and (b) electron diffraction pattern obtained from the metallic glass; (c) image and (d) electron diffraction pattern obtained from the crystallized counterpart.	56
Figure 3.4 (a-c) High-resolution XPS spectra measurement of the as-polished metallic glass: (a) Ni 2p spectra, (b) Nb 3d spectra, and (c) Ta 4f spectra.	57
Figure 3.5 Potentiodynamic polarization curves for the metallic glass and crystallized ribbon in 11.5 M HNO ₃ environment at room temperature.	59
Figure 3.6 Pourbaix diagram of (a) Ni, (b) Nb, and (c) Ta.	60
Figure 3.7 Electrochemical impedance spectra for the metallic glass and crystallized ribbon in 11.5 M HNO ₃ environment at room temperature in aerated condition: (a) Nyquist plots, (b) Bode modulus, and (c) Bode phase.	61
Figure 3.8 High-resolution XPS spectra obtained for the metallic glassy ribbon after 30 min polarization at 1.6 V in 11.5 M nitric acid; (a) Ni 2p, (b) Nb 3d, and (c) Ta 4f.	63
Figure 3.9 High-resolution XPS spectra obtained for the surface of the crystallized ribbon after 30 min polarization at 1.6 V in 11.5 M nitric acid; (a) Ni 2p, (b) Nb 3d, and (c) Ta 4f.	65
Figure 3.10 XPS depth profile representing the concentration (%) of oxide/metallic states of Ni 2p, Nb 3d, and Ta 4f spectra with depth of the passive film formed after 30 min after polarization at 1.6 V in 11.5 M nitric acid (sputtering time 0 min accounts for the as-received surface) ; (a) for metallic glass, and (b) for crystallized alloy.	67
Figure 3.11 XPS depth profile representing the concentration (%) of (oxide + metallic states) of Ni 2p, Nb 3d, and Ta 4f spectra with depth of the passive film formed after 30 min after polarization at 1.6 V in 11.5 M nitric acid; (a) metallic glass, and (b) crystallized alloy.	68
Figure 3.12 Potentiostatic polarization studies in 11.5 M nitric acid at 1.6 V (Ag/AgCl) indicated the change in current with respect to time plotted in; (a) normal scale of time, and (b) logarithmic time.	68
Figure 3.13 Surface morphology of the metallic glass and partially crystallized sample before and after immersion test for 7 days in 11.5 M nitric acid; (a-b) before immersion-(a) as-spun metallic glass, (b) partially crystallized sample. (c-d) after immersion (c) metallic glass, and (d) partially crystallized sample.	69

Figure 3.14 FESEM morphology of the surface after 30 min polarization at 1.6 V (Ag/AgCl) in 11.5 M nitric acid: (a-b) images of the passive film formed on the metallic glass.....	71
Figure 3.15 FESEM morphology of the surface after 30 min polarization at 1.6 V (Ag/AgCl) in 11.5 M nitric acid: (a-b) images of corroded surface on crystallized ribbon..	71
Figure 3.16 Schematics diagram of the passive films formed on metallic glass and partially crystallized alloy in 11.5 M nitric acid representing: (a) Passive film on surface of the glassy alloy enriched with stable Nb ₂ O ₅ and Ta ₂ O ₅ with small amount of NiO and Ni ₂ O ₃ , (b) The surface of the crystallized ribbon undergoes attacked and crystalline Ni-oxide dissolved completely from the surface. The agglomerated surface layer consisted of oxide and traces metallic fraction of Nb and Ta.....	72
Figure 3.17 Mott-Schottky plots of Ni ₆₀ Nb ₃₀ Ta ₁₀ glassy and crystallized alloy ribbon in 11.5 M HNO ₃ environment at room temperature.	74
Figure 4.1 (a) Isothermal thermogravimetric analysis (TGA) of the as-spun Ni ₆₀ Nb ₄₀ ribbon for 5 h under 20% O ₂ environment at 450 °C and 550 °C.	80
Figure 4.2 (a) XRD pattern of as-spun, 450, and 550 °C thermally oxidized Ni ₆₀ Nb ₄₀ ribbon sample for 5 h, (b) GIXRD traces of the 450 and 550 °C thermally oxidized ribbon for 5 h	82
Figure 4.3 Images (a-b) are FESEM morphologies of the surface of air-oxidized Ni ₆₀ Nb ₄₀ ribbons for 5 h; (a) at 450 °C and (b) at 550 °C.....	83
Figure 4.4 Images (a-b) are AFM surface topology of the surface of air-oxidized Ni ₆₀ Nb ₄₀ ribbons for 5 h; (a) at 450 °C and (b) at 550 °C.....	83
Figure 4.5 High-resolution XPS spectra of the surface, of the as-spun Ni-Nb amorphous alloy sample; (a) surface Ni 2p spectra (b) surface Nb 3d spectra.	85
Figure 4.6 High-resolution XPS spectra of the surface, of the 450 °C air-oxidized sample; (a) surface Ni 2p spectra (b) surface Nb 3d spectra. High-resolution XPS spectra of the surface of the 550 °C air-oxidized sample; (c) Surface Ni 2p spectra (d) absence of Nb 3d spectra at the surface.	85
Figure 4.7 Bar chart was depicting the surface atomic concentration of the species on as-spun Ni ₆₀ Nb ₄₀ amorphous ribbon and their variation at different oxidation temperature.	87
Figure 4.8 XPS depth profile represents the concentration (%) of oxide/metallic states of Ni 2p, and Nb 3d as a function of sputtering time; sputtering time 0 min accounts	

	for the as-received surface; (a) for 450 °C oxidized sample, and (b) for 550 °C oxidized sample.	88
Figure 4.9	An illustration of the elementary step for the film formation at 550 °C involves Step1 outward diffusion of the Ni through the anion vacancies. Step2 Ni diffusion created cationic at M/O interface vacancy and film growth. Step3 cation vacancy accumulation at near M/O interface and formation of tick film enriched with Ni-oxide.	91
Figure 4.10	(a) Isothermal thermogravimetric analysis (TGA) of the as-spun Ni ₆₀ Nb ₃₀ Ta ₁₀ metallic glassy (MG) ribbon at 450 and 550 °C for 5 h under O ₂ environment and (b) depicts the GIXRD and XRD patterns of as-spun and air-oxidised MG ribbon at 450 and 550 °C	93
Figure 4.11	SEM images of the air-oxidised Ni ₆₀ Nb ₃₀ Ta ₁₀ ribbons for 5 h; (a) smooth morphology at 450 °C and (b) speckled contrast at 550 °C.....	94
Figure 4.12	AFM images of the surface morphologies of air-oxidised Ni ₆₀ Nb ₃₀ Ta ₁₀ ribbons for 5 h; a and b are the images at 450 °C; (a) 2D and (b) 3D image; c and d are the images for oxidised sample at 550 °C revealing particle-like features; (c) 2D and (d) 3D image.....	95
Figure 4.13	(a-c) High-resolution XPS spectra of as-spun Ni ₆₀ Nb ₃₀ Ta ₁₀ ribbon (a) Ni 2p, (b) Nb 3d and, (c) Ta 4f. (d-e) High-resolution XPS spectra of thermally oxidized Ni ₆₀ Nb ₃₀ Ta ₁₀ ribbon sample at 450 °C (450MG), (d) Ni 2p, (e) Nb 3d and, (f) Ta 4f. (g-h) High-resolution XPS spectra of thermally oxidized Ni ₆₀ Nb ₃₀ Ta ₁₀ ribbon sample at 550 °C (550MG) are (g) Ni 2p, (h) Nb 3d and, (i) Ta 4f	96
Figure 4.14	Bar chart was depicting the surface atomic concentration of the species on as-spun Ni ₆₀ Nb ₄₀ amorphous ribbon and their variation at different oxidation temperature.	97
Figure 4.15	XPS depth profiles representing the concentration of oxide/metallic states of Ni 2p, Nb 3d and Ta 4f; (a) at 450 °C and (b) at 550 °C.	98
Figure 4.16	(a) Differential Scanning Calorimetry (DSC) traces of as-prepared Ni ₅₀ Zr ₂₅ Nb ₂₅ metallic glass and (b) Thermo-gravimetric analysis of this metallic glass at 200 °C and 400 °C for 5 h under 20% O ₂ environment.....	101
Figure 4.17	XRD and GIXRD pattern of the as-prepared and thermally oxidized metallic glass at (a) 200 °C and (b) 400 °C.	102

Figure 4.18 Cross-sectional FESEM with EDS results in the backscattered mode of thermally oxidized $\text{Ni}_{50}\text{Zr}_{25}\text{Nb}_{25}$ metallic shows film/substrate for (a) OMG200 sample, and (b) OMG400 sample.	103
Figure 4.19 (a) XRD pattern and (b) cross-sectional SEM image of oxidized $\text{Ni}_{50}\text{Zr}_{25}\text{Nb}_{25}$ metallic glass after thermal oxidation in oxygen environments at 530 °C for 5 h.	104
Figure 4.20 High-resolution XPS spectra obtained from the surface of the as-prepared $\text{Ni}_{50}\text{Zr}_{25}\text{Nb}_{25}$ MG sample; (a) Ni 2p spectra, (b) Nb 3d spectra, and (c) Zr 3d spectra.	105
Figure 4.21 (a-c) High-resolution XPS spectra of the surface of the thermally oxidized $\text{Ni}_{50}\text{Zr}_{25}\text{Nb}_{25}$ at 200 C (OMG200) sample; (a) Ni 2p spectra (b) Nb 3d spectra, and (c) Zr 3d spectra. The spectra recorded on the surface of OMG400 sample; (d) Ni 2p spectra (e) Nb 3d spectra, and (f) Zr 3d spectra.	106
Figure 4.22 Atomic concentration of the metallic and oxide species of as-prepared $\text{Ni}_{50}\text{Zr}_{25}\text{Nb}_{25}$ metallic glass and oxidized metallic glass ribbon (OMG).	107
Figure 4.23 XPS depth profiles representing the distribution of oxide and metallic species throughout the depth of the oxide film, the depth 0 nm accounts for the as-received surface; (a) oxidized sample at 200 °C, and (b) oxidized sample at 400 °C.	107
Figure 4.24 XPS depth profiles representing the distribution of species (oxide + metallic) throughout the depth of the oxide film; (a) oxidized sample at 200 °C, and (b) oxidized sample at 400 °C.	108
Figure 5.1 Electrochemical impedance spectra of air-oxidized and as-spun $\text{Ni}_{60}\text{Nb}_{40}$ amorphous ribbon in 11.5 M HNO_3 media.....	113
Figure 5.2 The equivalent circuits [$R_S(\text{CPE} R_P)$] used for fitting the experimental impedance data; R_S is the solution resistance, CPE is the constant phase element in parallel connection, and R_P is the polarization resistance.....	114
Figure 5.3 Potentiodynamic polarization curves for the as-spun and thermally oxidized $\text{Ni}_{60}\text{Nb}_{40}$ amorphous alloys in 11.5 M nitric acid medium at room temperature.	116
Figure 5.4 Mott-Schottky plots for thermally oxidized and as-spun $\text{Ni}_{60}\text{Nb}_{40}$ ribbon at room temperature in the aerated condition in 11.5 M HNO_3 environment.....	118

Figure 5.5 FESEM images of thermally oxidized ribbon after potentiodynamic polarization test at 2200 mV in 11.5 M HNO ₃ environment; (a) for as-spun ribbon, (b) for 450AR, and (b) for 550AR sample.....	120
Figure 5.6 (a-c) Impedance spectra obtained from as-spun Ni ₆₀ Nb ₃₀ Ta ₁₀ metallic glass ribbon sample (a) in 1 M, (b) 6 M, and (c) 11.5 M nitric acid.....	122
Figure 5.7 (a-c) Potentiodynamic polarization obtained from as-spun Ni ₆₀ Nb ₃₀ Ta ₁₀ metallic glass ribbon sample (a) in 1M, (b) 6 M, and (c) 11.5 M nitric acid medium. ..	124
Figure 5.8 Mott-Schottky plots obtained in 1, 6, and 11.5 M nitric acid environment; (a) as-spun Ni ₆₀ Nb ₃₀ Ta ₁₀ metallic glass ribbon, (b) thermally oxidized Ni ₆₀ Nb ₃₀ Ta ₁₀ ribbon sample at 450 °C (450 TO-MG), (c) thermally oxidized Ni ₆₀ Nb ₃₀ Ta ₁₀ ribbon sample at 550 °C (550 TO-MG).....	128
Figure 5.9 Impedance results of the as-prepared and thermally oxidized metallic glass (OMG) ribbon in 11.5 M nitric acid at room temperature; (a) Nyquist plots, (b) Bode modulus, and (c) Bode phase.....	133
Figure 5.10 The equivalent circuits with schematic of substrate/film/electrolyte interface of the passive film: (a) [R _s (CPE R _p)] circuits used for fitting of the experimental impedance data obtained from as-prepare ribbon, and (b) (R _s (CPE _{OMG1} R _f (CPE _{OMG2} R _{ct})) circuits used for fitting of the experimental impedance data obtained from OMG ribbon.....	135
Figure 5.11 Potentiodynamic polarization curves for the as-prepared and thermally oxidized Ni ₅₀ Zr ₂₅ Nb ₂₅ metallic glass (200-OMG and 400-OMG) in 11.5 M nitric acid medium at room temperature.....	136
Figure 5.12 The SEM images in different magnifications of the as-prepared MG sample surface ((a) 5µm and (b) 1µm)) after potentiostatic polarization test at 2.2 V (Ag/AgCl) in 11.5 M nitric acid environments.....	139
Figure 5.13 SEM and EDS images of the sample surface after potentiostatic polarization test at 2.2 V (Ag/AgCl) in 11.5 M nitric acid environments; (a-b) for 200MG, and (c-d) for 400MG sample.....	140
Figure 5.14 Schematic diagram representing the corrosion process in 11.5 M HNO ₃ environment (a) passive film on the as-prepared metallic glass undergoes a severe attack following the Ni ions dissolution. (b) The thermally oxidized film at 200 °C sample show minor attack and along with Ni ions dissolution (c) The	

thick Nb ₂ O ₅ and ZrO ₂ film at 400 °C with no sign of corrosion attack in 11.5 M nitric acid.	141
Figure 6.1 XRD of Ni ₆₀ Nb ₃₀ Ta ₁₀ amorphous alloy in the form of coating prepared Magnetron sputtering.....	146
Figure 6.2 Microstructure of the (a) bare 304 L SS, (b-c) Ni ₆₀ Nb ₃₀ Ta ₁₀ Metallic glass coating deposited at RT, and (c-d) Ni ₆₀ Nb ₃₀ Ta ₁₀ Metallic glass coating deposited at 200 °C.	146
Figure 6.3 200 °C -TFMG/304 L SS substrate cross-sectional images.	147
Figure 6.4 (a-c) High-resolution XPS spectra obtained on the surface of the passive film (a-c) of the 200 °C-coating after immersion test in boiling 11.5 M nitric acid for 24 h.; for surface peak (a) NiO, Ni ₂ O ₃ (Ni 2p), (b) Nb ₂ O ₅ (Nb 3d), and (c) Nb ₂ O ₅ (Ta 4f). Complete metallic peak after 10 min sputtering (a) Metallic Ni (Ni 2p), (b) Metallic Nb (Nb 3d), and (c) Metallic Ta (Ta 4f).	148
Figure 6.5 High-resolution XPS spectra obtained on the surface of the passive film for RT-coating after immersion test in boiling 11.5 M nitric acid for 24 h.; for surface peak (a) Ni 2p (b) Nb 3d, and (c) Ta 4f. After 5 min sputtering (a) Metallic Ni (Ni 2p), (b) Metallic Nb (Nb 3d), and (c) Metallic Ta (Ta 4f).	149
Figure 6.6 (a-c) Potentiodynamic polarization obtained from as-spun Ni ₆₀ Nb ₃₀ Ta ₁₀ metallic glass coated and bare 304 L SS (a) in 1M, (b) 6 M, and (c) 11.5 M nitric acid.	150
Figure 6.7 (a-c) Electrochemical impedance spectra (Nyquist plots) obtained on the room temperature (RT), 200 °C metallic glass coated and bare 304 L SS sample (a) in 1M, (b) 6 M, and (c) 11.5 M nitric acid.	153
Figure 6.8 Mott-Schottky plots of RT, 200 °C-Coating, and bare 304 L SS sample; (a) in 1 M, (b) in 6 M, and (c) in 11.5 M nitric acid.	155
Figure 6.9 Surface morphology of 200 °C-metallic glass coating sample after immersion test for 240 h in 11.5 M nitric acid solution under boiling condition.....	159
Figure 6.10 Surface morphology of severely attacked RT-metallic glass coating sample after immersion test for 240 h in 11.5 M nitric acid solution under boiling condition.	159
Figure 6.11 Surface morphology (Optical images) of severely Inter-granular attacked of bare 304 L SS sample after immersion test for 240 h in 11.5 M nitric acid solution under boiling condition.	160

List of Tables

Table 1.1 Deformation data of some bulk metallic glasses in the supercooled liquid region.	31
Table 3.1 The binding energy of de-convoluted high-resolution XPS spectra and concentration values obtained from the surface for as-spun metallic glass (MG) and as-crystallized ribbon	57
Table 3.2 The binding energy of deconvoluted high-resolution XPS spectra and concentration values obtained from the surface film on metallic glass and crystallized ribbon after polarized at 1.6 V for 30 min in 11.5 M nitric acid.....	65
Table 3.3 Mott-Schottky analyses and the defect densities of passive film form on glassy and crystallized alloy at the frequency of 1 kHz and 3 kHz in 11.5 M HNO ₃ environment at room temperature.	75
Table 4.1 Parabolic rate constants and R ² (fitting accuracy) for the oxidation of Ni ₆₀ Nb ₄₀ amorphous ribbon in 20 % dry oxygen (k _p : in g ² / cm ⁴ .s).....	82
Table 4.2 The binding energy of de-convoluted high-resolution XPS spectra including metallic and oxides of Ni, Nb, Ta and Zr recorded for the oxidized sample	86
Table 4.3 Physical properties of the alloying elements of Ni, Nb, Ta and Zr	92
Table 4.4 Parabolic rate constants and R ² (fitting accuracy) for the oxidation of Ni ₆₀ Nb ₃₀ Ta ₁₀ metallic glassy (MG) ribbon (k _p : in g ² / cm ⁴ .s).	93
Table 4.5 Rate constants and R ² (fitting accuracy) for the oxidation of Ni ₅₀ Zr ₂₅ Nb ₂₅ metallic glassy ribbon in dry oxygen (k ₁ in g cm ⁻² s ⁻¹ ; k _p in g ² cm ⁻⁴ s ⁻¹).	101
Table 5.1 Equivalent circuit parameters of EIS results including the root-mean-square deviation and densities of charge carrier values for as-spun and air-oxidized Ni ₆₀ Nb ₄₀ ribbons in 11.5 M HNO ₃ at room temperature in aerated condition.....	114
Table 5.2 Potentiodynamic polarization parameter for as-spun and thermally oxidized Ni ₆₀ Nb ₄₀ amorphous alloys in 11.5 M HNO ₃ environment at room temperature.	115
Table 5.3 EIS parameter of as-spun and thermally oxidized (450°C and 550 °C) MG sample.	121
Table 5.4 Potentiodynamic polarization parameters for as-spun, thermally oxidized at 450 °C (450 TO-MG), and thermally oxidized at 550 °C (550 TO-MG) of the Ni ₆₀ Nb ₃₀ Ta ₁₀ ribbon samples in 1, 6, and 11.5 M HNO ₃ environments at room temperature in aerated condition.	125

Table 5.5 Defect densities obtained from the Mott-Schottky analyses for as-spun and thermally oxidized at 550 °C (550-MG), of the Ni ₆₀ Nb ₃₀ Ta ₁₀ ribbon samples in 1, 6 and 11.5 M HNO ₃ environment at room temperature in aerated condition	129
Table 5.6 Electrochemical Impedance spectroscopy parameters obtained for as-prepared and oxidized metallic glass (OMG) sample in 11.5 M nitric acid.	135
Table 5.7 Potentiodynamic polarization parameters obtained of as-prepared and oxidized metallic glass ribbon sample in 11.5 M nitric acid.....	137
Table 6.1 Potentiodynamic polarization parameters of metallic glass coated and bare 304 L SS in 1, 6 and 11.5 M nitric acid.	151
Table 6.2 EIS parameters of metallic glass coated and bare type 304 L SS in 1, 6, and 11.5 M nitric acid.	154
Table 6.3 Defect density of the passive film on metallic glassy coating and bare 304 L SS in 1, 6, 11.5 M nitric acid.	156
Table 6.4 Weight loss verses immersion time for RT, and 200 °C coating along with 304 L SS in 11.5 M nitric acid.....	158

1 Introduction

The chapter deals with the exploration of the metallic glass towards engineering application in corrosive nitric acid environments for spent nuclear fuel application. The corrosion issues in structure materials made of component used for spent nuclear fuel reprocessing are briefly explained. Out of several problems, the chapter focuses on the selection of corrosion resistance metallic glass, and its coating based on the simulated reprocessing environmental conditions. The chapter also gives a brief introduction to the development of various Ni-based metallic glasses based on the Ni-Nb phase diagram. Apart from this, the chapter also introduces to the elevated temperature oxidation, current nitric acid corrosion problems, and mechanical properties of the metallic glasses and objectives of the present work.

1.1 Metallic glass

1.1.1 Definition of metallic glass

Metallic glasses are a random structure (non-crystalline) lacking rotational and translational symmetries i.e., lattice parameters of the atomic structure cannot be defined [1-5]. On the other hand, in most crystalline metallic materials, the atoms occupy well defined lattice sites, and are characterized by lattice parameter of well define inter-atomic distance, and well define 2θ values. The metallic materials with an amorphous structure are produced directly from the liquid state during cooling are called "glassy metals" or mostly commonly known as "metallic glasses" and these glassy alloys exhibit glass transition upon heating [1-3]. All the metallic glass exhibits amorphous structure but all the amorphous structure does not shows glass transition temperature. Thereby, all the amorphous alloys are not metallic glasses. However, there are several other ways in which amorphous structure can be produced in metals, including solid-state reaction, ion irradiation, and mechanical boll-

Chapter 1

milling alloying. Amorphous metals produced by these techniques are called metallic glasses only as when they exhibit the glass transition temperature.

1.1.2 Formation of metallic glass

In order to by-pass the crystallization, synthesizing glassy alloys requires rapid solidification [1-2]. Fig.1.1 is the TTT diagram showing schematically the time taken for a small amount of crystalline phase to form in an under-cooled liquid as a function of temperature. The critical cooling rate, R_c , to avoid crystallization is given by equation 1.a, for low under-cooling, i.e.

$$R_c = \frac{T_m - T_n}{t_o^*} \quad (1.a)$$

At temperature close to the melting point T_m , is the driving force for crystallization, so the crystal nucleation and growth rate takes place for a large onset time t_o .

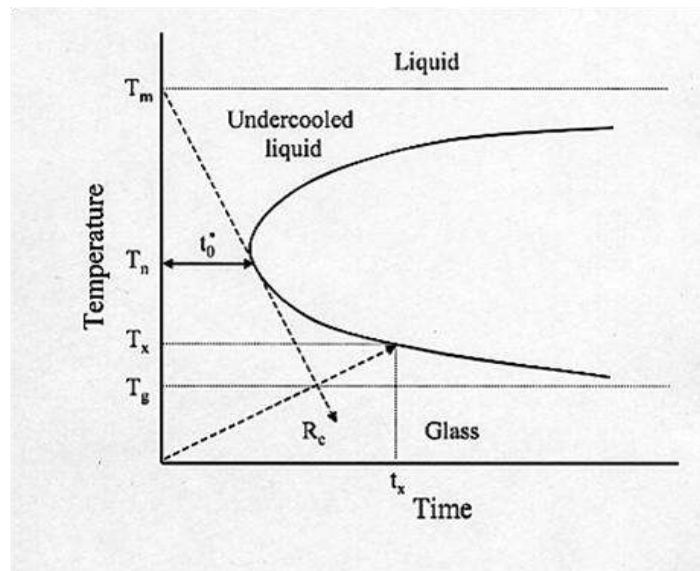


Fig. 1.1 Schematic TTT diagram for the onset crystallization [3].

As the temperature decreases, the crystallization onset time reaches a minimum value t_o^* at a temperature T_n , and then increases again as the thermal energy becomes insufficient for atomic rearrangement. Below the glass transition temperature T_g , the atomic motion is

completely suppressed and the amorphous structure is frozen into the solid, so that the crystallization onset time t_0 becomes larger.

1.1.3 Models to predict glass forming compositions

Several models to predict the glass forming alloy of metallic systems have already been proposed. A classical kinetic treatment incorporating the effects of both nucleation and crystal growth on the glass formation was firstly established by Johnson [4]. The results from this model concluded that the most favourable conditions for glass formation involve a large viscosity at the melting point of the crystalline phase and/or a rapidly rising viscosity with temperature below the melting point. Uhlmann determined the critical cooling rates of several oxide glass formers such as SiO_2 and GeO_2 , but also pure silver [5]. However, recently this model was used to determine the TTT curves and to calculate the critical cooling rates of well known bulk metallic glassy alloys such as $\text{Pd}_{40}\text{Cu}_{30}\text{Ni}_{10}\text{P}_{20}$ [6] and $\text{Zr}_{41.2}\text{Ti}_{13.8}\text{Cu}_{12.5}\text{Ni}_{10}\text{Be}_{22.5}$ (Vitreloy 1) [7]. It was found that the measured TTT diagram can be fitted exactly over the entire temperature range by the classical kinetic treatment applied to the bulk glass forming $\text{Pd}_{40}\text{Cu}_{30}\text{Ni}_{10}\text{P}_{20}$ alloy. In contrast, the same treatment fails to predict the experimentally determined TTT diagram for the Vitreloy 1 because of its significant high nose temperature [8].

From thermodynamic considerations, bulk glass formers naturally exhibit a low driving force for crystallization in the super-cooled liquid region. Since metallic glasses are metastable, their Gibbs free energies are larger than that of crystalline phases. The driving force for crystallization is approximated by the Gibbs free energy difference between the super-cooled liquid and crystalline states, ΔG . Models for the Gibbs free energy of metallic liquids have been developed [9]. For example, the $\text{Zr}_{62}\text{Ni}_{38}$ and $\text{Zr}_{41.2}\text{Ti}_{13.8}\text{Cu}_{12.5}\text{Ni}_{10}\text{Be}_{22.5}$ (Vitreloy 1) glassy alloys exhibit a critical cooling rate of about 1K/s and 10^4 K/s, respectively. A

Chapter 1

higher Gibbs free energy was obtained for the $Zr_{62}Ni_{38}$ glassy alloy when compared to the Vitreloy [10-11]. Thus, lower the Gibbs free energy difference between the liquid and the crystalline states, the better the glass forming ability of the Vitreloy according to the critical cooling rate.

A commonly followed thumb rule for the formation of bulk metallic glass proposed by Inoue (1998) has three sub-rules; a glass forming system should consist of (i) at least three elements, (ii) with large atomic size difference ($\Delta r \sim 12\%$) and (iii) negative enthalpy of mixing between these elements. If these empirical rules can help for the choice of elements, but they do not provide the composition forming of the amorphous structure, which is need to be determined by cumbersome trial and error experiment. A holistic explanation for glass formation in metals has been attempted by researcher [12]. Egami proposed a simple criterion for binary systems based on the topological instability applied to a local atomic structure that results in the absence of crystallization or melting and glass transition [13]. The model-based itself on the geometry of atomic packing and the advantage of this approach is that a single principle is able to explain the melting, amorphization and glass formation nature. However, it still falls short of a full first principles description of the structure of amorphous alloys. Recently, Miracle has proposed a structural model based on local order and generalized structures for clusters of solute atoms [14]. The clusters formed by solute atoms were found to have only three topologically distinct solutes: cluster forming solutes, cluster octahedral solutes and cluster-tetrahedral solutes. These solute clusters are visualized as spheres with radius ratios that enable efficient packing in the first coordination shell [15]. The insight offered by this model is that the mechanistic of glass formation is very similar to that of packing hard spheres of different sizes and that efficiently packed clusters can also be approximated as packing of clusters of different sizes. However, the predictive capabilities of this model have not been evaluated yet.

Chapter 1

Despite all efforts devoted by many researchers from all over the world, so far, no model can successfully enable the prediction of metallic glass as yet.

1.1.4 Developments of metallic glasses

In 1960, the first metallic glass of composition $\text{Au}_{75}\text{Si}_{25}$ was prepared by Duwez at Caltech, USA, [16]. They rapidly quenched the metallic liquids at very high rates of 10^5 – 10^6 K/s. In order to yield a frozen liquid configuration, the process of nucleation and growth of crystalline phase could be kinetically by-passed in alloy melts, that is, metallic glass. The nature of its formation, structure and property of metallic glasses have gain an attention because of their fundamental scientific importance and potential engineering applications [17].



Fig. 1.2 Images of the Vitreloy bulk metallic glass hardware, including golf clubs, electronic casings, optical hardware, ingots, 12 mm diameter rod, and large plate (under the samples). Hardware courtesy of Liquid metal Technologies [18].

Subsequently, the “bulk” (mm scale) metallic glass of the ternary Pd-Cu-Si alloy was prepared by Chen in 1974 [19]. To form millimeter-diameter rods of Pd-Cu-Si metallic glass sample they used suction-casting methods at a significantly lower cooling rate of 10^3 K/s [19]. In the 1980s, well-known Pd-Ni-P BMG was successfully prepared by Turnbull and

Chapter 1

co-workers by using boron oxide fluxing method in order to purify the melt and to eliminate heterogeneous nucleation [20]. Although the cost of Pd metal is high, the formation of Pd-based BMG is an achievement, but however, the interests were localized only in the academic field and its novelty faded after some years. Afterwards, larger centimetre sized BMGs were casted by researchers at Tohoku University, Japan and interest on the BMGs alloys persisted and continue today [15, 19, 20].

In the late 1980s, the Inoue group were developed rare-earth (RE-based) materials with Al. They found exceptional glass-forming ability with the compositions of La–Al–Ni and La–Al–Cu alloys [21]. The sheets of 5 mm thicknesses and cylindrical samples with same diameters (up to 5 mm) were successfully achieved as hole glassy by Cu molds casting of $\text{La}_{55}\text{Al}_{25}\text{Ni}_{20}$ (or later $\text{La}_{55}\text{Al}_{25}\text{Ni}_{10}\text{Cu}_{10}$ up to 9 mm). In 1991, the same group were developed the glassy Mg–Cu–Y and Mg–Ni–Y alloys with the considerably high glass-forming ability in $\text{Mg}_{65}\text{Cu}_{25}\text{Y}_{10}$ (Inoue et.al, 1991) [17]. At the same time, a family of Zr-based metallic glass of alloy system Zr–Al–Ni–Cu with high glass-forming ability and the critical casting thickness ranging up to 15 mm was developed by Inoue group [22]. The expansion of these alloys established that bulk metallic glass compositions not only involved a few laboratory curiosities but could be pretty motivated from the fundamentals and for engineering applications.

The importance of Inoue's work was quickly accepted by Johnson and others from Caltech, and they continued the work of Duwez, in order to search for new bulk metallic glass forming compositions. In 1993, Peker and Johnson synthesized the $\text{Zr}_{41.2}\text{Ti}_{13.8}\text{Cu}_{12.5}\text{Ni}_{10}\text{Be}_{22.5}$ bulk glass forming alloy with a critical casting thickness of centimeters, commonly known as Vitreloy 1, [23]. Fig.1.2 shows the various dimensions of the Vitreloy that are used in the formation hardware. In 1997, Inoue group re-visited the $\text{Pd}_{40}\text{Ni}_{40}\text{P}_{20}$ alloy and partially substitute Ni by Cu. As a consequence they came up an alloy

Chapter 1

with a critical casting thickness of 72 mm [17]. Interestingly, the metallic system of Pd–Cu–Ni–P family with the highest glass-forming ability is known to date.

Due to the limited Zr and Pd resources, development of new BMGs containing common metals as the major constituents is strongly desired for the extensive practical applications of BMGs. Lately, Kim's group in Korea has developed new engineering metal based glass forming systems such as Ni-, Cu-, Ti-, and Fe- based BMGs [24]. They developed a new Fe-B-Y-Nb glassy rod diameter up to 7 mm with soft magnetic properties (Kim et.al, 2005) [24]. Poon's group in the Virginia University, U.S.A, developed the first non-magnetic amorphous steel with a critical glassy diameter about 12 mm [25]. To date the glass forming ability of Mg, Ni, Ti (Park. et. al, 2005), Cu (Kim et.al, 2007), and Fe-based systems are about one centimetre in thickness [24, 26].

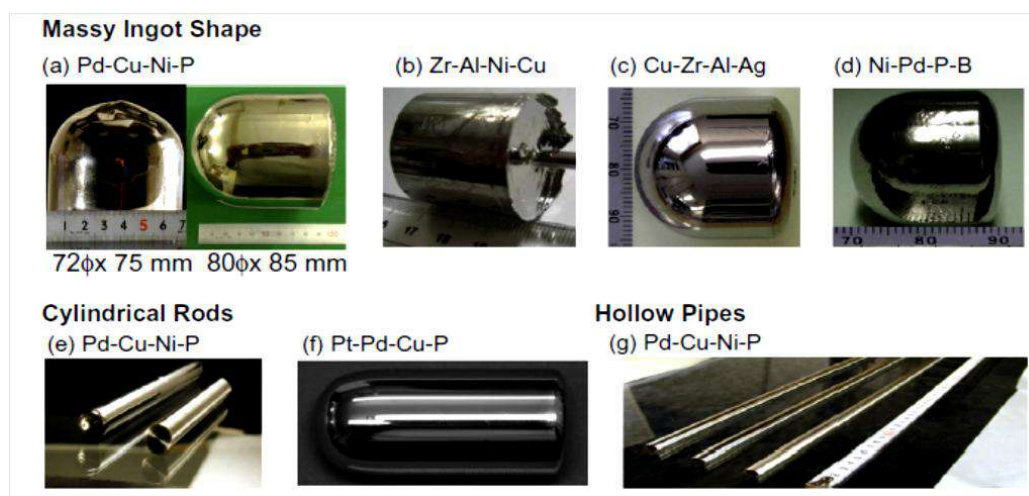


Figure 1.3 Picture of recently synthesized bulk metallic glass [29].

It is noticeable that the BMGs were developed in the series starting with the expensive metallic based Au-, Pd-, and Pt- followed by less expensive Zr-, Ti-, Ni- and Ln-based BMGs. Further work is still essential on Pd-, Pt-, and Zr- system and the much cheaper Cu- and Fe-based BMGs were recently developed that have attracted wide interests for

Chapter 1

engineering purposes [27-28]. The formation of the various Pd-, Pt-, Zr-, and Ni- metallic glass are reported, as shown in Fig. 1.3.

Fig.1.2 showed the development of various metallic glassy alloys towards industrial application. The schematic TTT diagram for crystallization of the under-cooled liquids is similar to Fig.1.1. The Au-Si glasses show nucleation kinetics in the under-cooled region (between the glass transition temperature and melting point) such that the time scale for crystallization also referred as the critical cooling rate R_c is in the hundreds of microseconds to millisecond range at the “nose” of the nucleation curve. For example, Chen’s Pd-Cu-Si glass has fallen in the

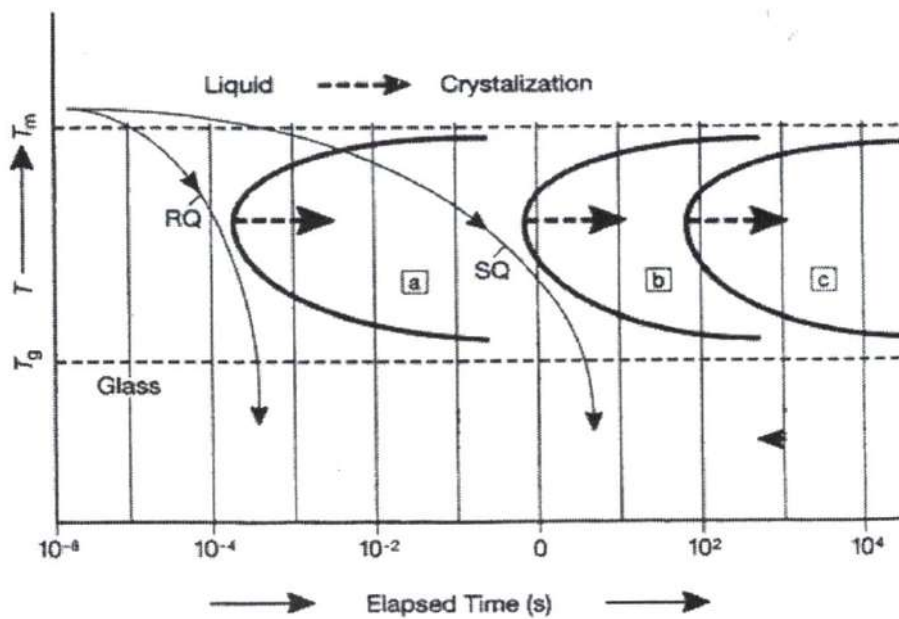


Figure 1.4 Schematic time-temperature-transformation (TTT) diagrams comparing the crystallization kinetics of (a) rapidly quenched, (b) slower quenched (c) bulk glass forming alloys. The two curves with arrows show the cooling history during rapid quenching (RQ) at $\sim 10^6$ K/s and relatively slow quenching (SQ) at $\sim 10^2$ K/s [3].

range where the crystallization occurs in time of tens milliseconds. The Pd-Ni-P glass studied by the Turnbull group exhibited a TTT diagram with a nose in the range of 1-10 seconds [30].

Chapter 1

The new glassy alloys developed by Inoue, Kim and Poon also exhibited a crystallization nose in the range of 1-10 seconds [31-32]. On the other hand, the alloy of the Vitreloy family and the Pd-Ni-Cu-P exhibit a nose in the TTT diagram at time scales of the order of 100 seconds [20]. The critical cooling rate can be correlated to the maximum glass forming ability of the alloy system, i.e., the larger the critical cooling rate R_c , the larger the critical diameter, D_c . The design of metallic glass thus consists in shifting the nose of the crystallization towards the right side of the TTT diagram as shown in Fig.1.4.

1.1.4.1 Synthesis of the Ni-based metallic glass based on Refractory Alloy Glasses

A few subsets of BMGs were known as Refractory Alloy Glasses (RAG). The high melting temperatures elements were used in RAGs to produce alloys with high glass transition temperatures, high thermal stabilities, and good yield strengths. The binary Ni-Nb system is a significant sub-system in several multi-component Ni-based alloys [33]. The Ni-Nb phase diagram is shown in Fig. 4 [33].

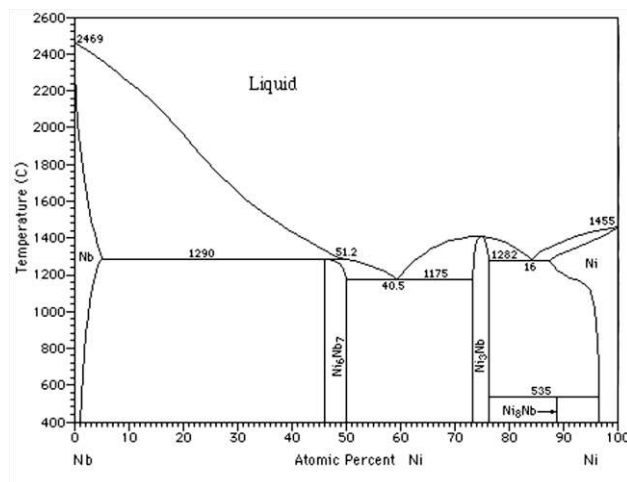


Figure 1.5 Phase diagram of the Ni-Nb system [33]

The equilibrium phases in Ni-Nb system are associated with the terminal fcc Ni-rich, bcc Nb-rich solid solutions and also the three intermetallic phases, namely Ni₈Nb, Ni₃Nb and Ni₆Nb₇. The Ni₈Nb belongs to the group of ordered phases, with a critical ordering

Chapter 1

temperature of 808 K [33]. The Ni_3Nb is a well-known orthorhombic phase and Ni_6Nb_7 is often called NiNb or μ -phase. The phase stability range of 50-57 at.% Nb is indicated by the experimental data. The binary Ni-Nb system in phase diagram (Fig. 1.5) is characterized by two eutectics, one at the $\text{Ni}_{84}\text{Nb}_{16}$ and other at the $\text{Ni}_{59.5}\text{Nb}_{40.5}$ composition. In the conditions of equilibrium solidification, the eutectic $\text{Ni}_{84}\text{Nb}_{16}$ melt solidifies into the Ni-rich fcc solid solution and Ni_3Nb phase. However, the eutectic $\text{Ni}_{59.5}\text{Nb}_{40.5}$ melt solidifies into the Ni_3Nb and Ni_6Nb_7 phases.

The binary Ni-Nb system exhibited amorphous structure within a large compositional range between 27.5-75 at.% Ni in the case of rapid quenching conditions. The near-eutectic composition of $\text{Ni}_{62}\text{Nb}_{38}$ found to be a best glass forming ability in the binary Ni-Nb system and reported with a critical casting thickness of 2 mm [34]. The crystallization of amorphous binary Ni-Nb alloys was extensively investigated as reported elsewhere [35]. The Ni-Nb based metallic glass showed desirable strength, and good glass forming ability, which further enlarged its application in other fields [34]. Amorphous samples up to nearly 2 mm thickness have been reported by quenching $\text{Ni}_{60}\text{Nb}_{40}$ melts. In order to further enhance the glass forming ability of the Ni-Nb alloy, elements such as Ta and Zr have been added in a multi-component alloy. The $\text{Ni}_{60}\text{Nb}_{30}\text{Ta}_{10}$ RAG family is a new class of the BMGs family [34] which a binary Ni-Nb system based on $\text{Ni}_{59.5}\text{Nb}_{40.5}$ eutectic composition. This $\text{Ni}_{60}\text{Nb}_{30}\text{Ta}_{10}$ system must exhibit a better glass forming ability (GFA) than that of Ni-Nb binary, since the ternary alloys system shows a marginally higher primary crystallization temperature compared to the binary system [34].

The refractory metals have high melting temperature (Nb: 2467 °C, Ta: 3014 °C, Zr: 1855 °C), and the amorphous alloys containing the refractory metals are expected to exhibit a higher thermal stability and a higher strength. The high thermal stability and glass forming ability of $\text{Ni}_{60}\text{Nb}_{40}\text{Ta}_{10}$ and $\text{Ni}_{60}\text{Nb}_{20}\text{Zr}_{20}$ metallic glass alloys are prepared by melt spinning

techniques. The $\text{Ni}_{60}\text{Nb}_{40}\text{Ta}_{10}$ and $\text{Ni}_{60}\text{Nb}_{20}\text{Zr}_{20}$ metallic glasses exhibit a high compressive failure strength of about 3346 MPa and 2678 MPa [34, 36]. Since the Nb and Zr elements are known for high corrosion resistance in nitric acid, we increase the Nb and Zr content in Ni-Nb-Zr system, and finally synthesize the metallic glass of composition $\text{Ni}_{50}\text{Nb}_{25}\text{Zr}_{25}$.

1.2 Corrosion

1.2.1 Nitric acid corrosion issue for the structure materials in nuclear reprocessing plant

The treatment of spent nuclear fuel is carried out using the PUREX chemical process (Plutonium and Uranium Refining by Extraction) [37]. In spent fuel reprocessing plants, various concentrations of nitric acid are used in the PUREX process for the separation of uranium and plutonium from fission products.

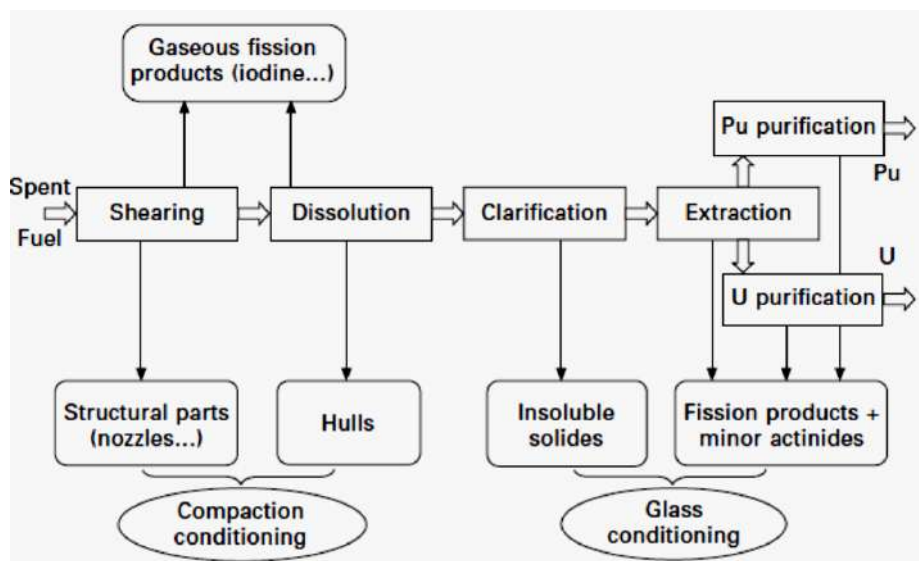


Figure 1.6 General flowchart of the PUREX process [37].

The well adopted procedure for reprocessing of spent nuclear fuel is aqueous route, and a typical flow sheet considered for a fast reactor fuel reprocessing plant by PUREX process is shown in Fig. 1. Chemical reprocessing plants engage various equipment/vessels as

fuel evaporators, dissolvers for various purposes and storage tanks for more active raffinate waste. Nitric acid is the main process medium for reprocessing of the spent nuclear fuel which received from both water reactors (for low plutonium content), and from fast breeder reactors, FBRs (for high plutonium content). The acid is used in various concentration from dilute (1–4 M) to concentrated (10–14 M), room temperature (solvent extraction) to intermediate (raffinate waste storage tanks) to boiling temperature (dissolver, evaporator). Structural materials type AISI 304L SS is most extensively used for fabrication of dissolver vessels, piping, tanks, and equipment at the reprocessing plants wherein the concentration of the acid is below 8 M and temperature of operation is below 353 K [38].

1.2.1.1 Corrosion behavior of austenitic stainless steels

Figure 1.2 shows the corrosion behaviour of an austenitic stainless steel under nitric acid media as a function of its potential [37]. The oxidation of the constitutive elements (mainly Fe, Cr and Ni) in the steel under the partial anodic process includes several domains. If the mediums are adequately reducing, the austenitic stainless steels are in an active domain, which is characterized by a uniform with a high-rate of dissolution. For a reasonably oxidizing medium of nitric acid solution, the austenitic stainless steels are in their passive state which is characterized by a uniform and low-rate of dissolution.

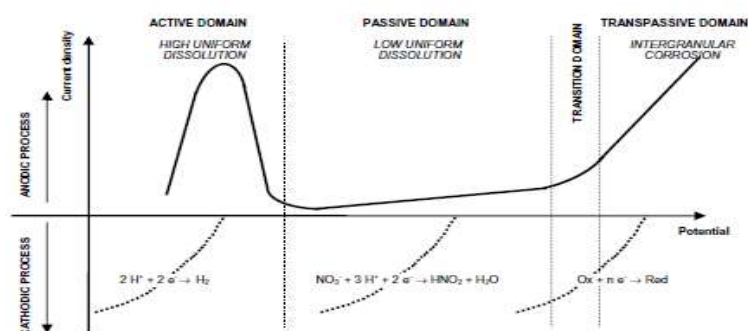


Figure 1.7 General electrochemical behaviour of austenitic stainless steels in acidic media as a function of the potential [37].

Chapter 1

For AISI 304L type steel, the passive layer, a few nm thick, is mainly composed of Cr_2O_3 . If the medium becomes excessively oxidizing, the passive film dissolution occurs, especially by oxidation of Cr(III) (as insoluble Cr_2O_3) to Cr(VI) (as soluble $\text{Cr}_2\text{O}_7^{2-}$), with a lesser chromium content of the film in this range of potential, compared to the passive domain (75 and 92 at% respectively, for 304L stainless steel) [37]. This results in fast and accelerating trans-passive corrosion. However, low corrosion attack is observed for the 4% Si added steel [37]. Except for 4% Si steel, these SS undergo a preferentially intergranular corrosion (IGC) attack, even if the steel has been optimized in silicon and phosphorus steel (for AISI 304L SS) in order to reduce the risk of this type of corrosion. Fortunately, only intergranular indentations are observed under the less severe conditions (transition domain). In the harshest oxidizing conditions, successive rows of material get lost resulting in grain losses [37-38].

However, the reprocessing research including development and plant activities is actively pursued at IGCAR, Kalpakkam, for reprocess the spent mixed nuclear (U, Pu) C fuel generated from fast breeder test reactor (FBTR) [39]. The corrosion assessments of the various structural materials from type 304 L SS to other nitric acid grade (NAG) stainless steel are evaluated in nitric acid ranging from 8-12 M concentration. The passive films formed at boundaries are known to be weaker. Such a film undergoes selective corrosion attack along grain boundaries. An IGC attack was observed in hot oxidizing nitric acid even without sensitization of SS. In Fig. 1.8(a)-(c), Kamachi Mudali and Ningshen et al. shows the variations in the grain boundary attack of traditional structural and nitric acid grade special stainless steel after the nitric acid test at boiling condition [40-41].

The alloy with low impurity elements is further decreases in the grain boundary corrosion attack. The corrosion resistance of AISI type 304L SS significantly affect in presence of the impurity elements like S, P and B in nitric acid [41]. The steel undergoes degradation further with the selective dissolution when manganese and sulphur form

Chapter 1

chemically soluble MnS inclusions in the steel. The major problems in using bars, with tapered machined parts of AISI type 304L SS is end grain attack or tunnel corrosion. The longitudinally aligned MnS inclusions are in the vertically cut, and such cut faces expose MnS inclusions for selective attack, resulting in corrosion tunnels (Fig. 1.9) which commonly shows a typical puff candy appearance due to severe corrosion [40].

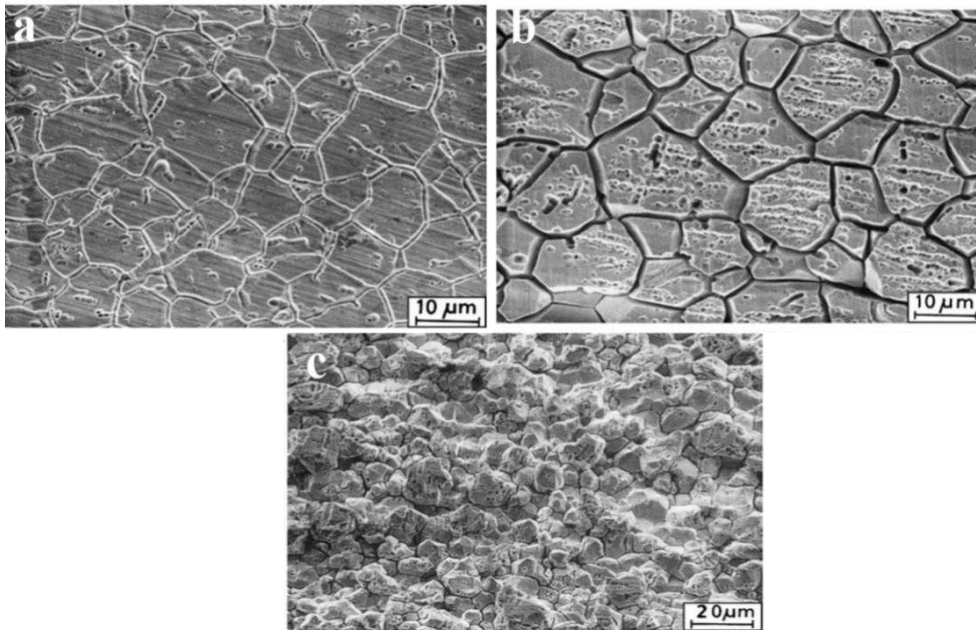


Figure 1.8 The variations in the grain boundary attack of conventional and nitric acid grade special SS after boiling nitric acid test, (c) commercial type 304L SS, (b) Uranus 16 SS, and (a) Uranus 65 SS [40].

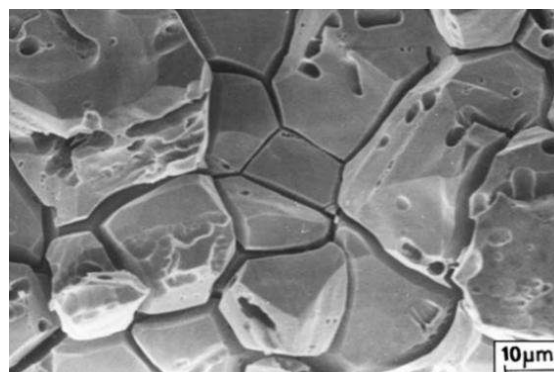


Figure 1.9 Selective corrosion attacked leading to the formation of 'corrosion tunnels' [40]

1.2.2 Literature survey on the corrosion behaviour of metallic glass

The amorphous structures are thermodynamically meta-stable, and also in higher energy state, which can be related to the surface properties such as corrosion and catalysis. However, high corrosion resistance is one of the essential requirements of the amorphous alloy compared to that of the crystalline alloy as they are free from defects to the crystalline state such as grain boundaries, stacking faults and dislocations [42]. In addition, amorphous alloys are free from heterogeneous phases, and segregations and precipitates which are usually formed by solid state diffusion during slow cooling or heat treatment. Thus, amorphous alloys are chemically homogeneous alloys in long range and with no potential sites for corrosion initiations like for localized attacks. However, it should be noted that, for the bulk glass alloy formation necessitate multi-components mostly including metal and metalloid (at least three elements) [43]. Such complicated composition especially metalloid was affected the corrosion resistance of the alloy [43].

The synthesis of high corrosion resistant metallic glass or amorphous alloy has always been of great interest, particularly require for its potential applications of such materials in different environments. Starting from the pioneering work of Naka and co-workers in 1974, the corrosion resistance of the $\text{Fe}_{75}\text{Cr}_5\text{P}_{13}\text{C}_7$ (atomic %) soft magnetic amorphous alloys has been demonstrated [44]. These alloys have the ability to passivate in 1N H_2SO_4 at room temperature with low chromium content of 5 at. %, while the conventional stainless steel requires more than 10 at% of Cr for the passivation. Thus, it was generally accepted that the amorphous structure is responsible for the high corrosion resistance in the Fe-base alloy. Later, it was shown that the addition of Mo or W to the system, i.e., Fe-Cr-(Mo,W)-P-C, increased the corrosion resistance by preventing the active dissolution of Cr, even in the concentrated HCl acid [45]. It should be noted that the conventional stainless steels undergo severe corrosion in the concentrated HCl acid. On the other hand, the importance of the

Chapter 1

concentration of Cr, and Mo, in the $\text{Fe}_{75-x-y}\text{Cr}_x\text{Mo}_y\text{C}_{15}\text{B}_{10}$ [43], Nb, and Ta in the $\text{Fe}_{45}\text{Cr}_{16}\text{Mo}_{14}(\text{Nb or Ta})_2\text{C}_{18}\text{B}_5$ [46] and P in Fe-Cr-Mo-C-B-P [47] alloy systems resulting in high resistance corrosion behavior in 1M HCl at room temperature are reported. The addition of varying Cr from 7.5 at% to 30 at%, indicated significantly increased in corrosion resistance [48]. Even small additions of Nb and Ta to the glassy alloy improve the corrosion resistance; however the addition of Ta appeared to be more effective than Nb in improving the corrosion resistance in HCl solution [46].

The corrosion behavior of several Zr-based bulk glass forming alloys were studied in different electrolytes such as 1N HCl, 1M H_2SO_4 , 0.1M Na_2SO_4 at room temperature [49]. Few of the studies were reported in nitric acid, 3.5 wt. % NaCl (marine environment), phosphate buffered solution at 37 °C (artificial body fluid) and in 0.1M Na_2SO_4 at 150-250 °C (hydrothermal environment) [50-51]. The Zr-Cu-Al-Ni glassy alloy exhibits higher corrosion resistance due to the formation of uniform protective Zr-oxides, in comparison to its crystalline counterpart in 0.1 M NaCl, at room temperature [52]. However, an accelerated degradation of the Zr-Cu-Al-Ni amorphous alloy samples under hot water conditions up to 250 °C was observed [53]. It was also further shown that the Zr-Ti-Nb-Cu-Al-Ni glassy alloy exhibits higher corrosion resistance in 1 N H_2SO_4 , and 1N HNO_3 , in comparison to its different microstructural states such as crystalline, nano-crystalline and quasi-crystalline of the same alloy [54]. The Zr-Cu-Pd-Al-Nb BMG exhibited excellent corrosion resistance in an artificial body fluid and shows good biocompatibility [55], thus demonstrating its promise for biomedical application. The Zr-Ti-Cu-Al-Ni glassy alloy also indicated high corrosion resistance with passivating ability in neutral chloride environment of 3.5 wt. % NaCl [56]. On the other hand, the Zr- based glassy alloy undergoes pitting corrosion in 1N HCl, and chloride containing acidic solution such as 1N H_2SO_4 + 0.2N NaCl [57]. The concept of

Chapter 1

micro-alloying of Ti, and Nb, to the Zr-based glassy alloys also significantly improves the corrosion resistance of the Zr-based glassy alloys [56].

On the other hand, though several RE- based glassy alloys such as La-, Y-, Ce-, Er-, Gd-, Dy-, Sc- and Sm- are currently available, the corrosion properties of these glassy alloys are limited. However, information is available on the corrosion properties of these alloys from the work on the corrosion properties of the La-Zr-Al-Ni-Cu two-phase glassy alloys [58]. It was shown that in 1 M H₂SO₄ at room temperature, the Zr-rich phase of the alloy do not corroded, while the La-rich glassy phase dissolved quickly in the solution. Thus, it is understood that the rare earth based glassy alloys are unstable in the highly corrosive environment.

The information on the Ni-based bulk glass forming alloys and their corrosion properties are reported in few literatures [3, 35, 55]. The corrosion resistance of the Ni-based metallic glassy alloys, and the binary Ni-Zr amorphous alloy showed poor corrosion resistance in 1M HCl, due to pitting corrosion [59]. However, several compositions of Ni-based amorphous alloys like Ni-Nb-Cr-Mo-P-B, Ni-Cr (Mo, Ta)-P-B, Ni-Nb-Ta-P-B, Ni-Cr-Ta-Mo-P-B and Ni(Co)-Nb-Ti-Zr were recently synthesized by different authors, and these alloys show an improved corrosion resistance by passivating in aggressive chloride solutions attributed to the formation of a protective oxide layer of the passivating alloying elements like Nb, Cr, Mo and Ta [60-61]. From these investigations, it can be understood that the formation of Zr-oxide in the Ni-Zr amorphous alloys are not sufficient enough for protection in the chloride containing environment [59]

1.2.2.1 Corrosion behavior of the metallic glass for nitric acid applications

The nitric acid is the main medium generally used for the aqueous reprocessing of spent nuclear fuels from both thermal and fast breeder reactors. The spent fuel discharged from

Chapter 1

thermal nuclear reactors and fast breeder test reactor (FBTR) at Kalpakkam is dissolved in 8 M and 11.5 M M HNO₃ under boiling conditions, respectively [39]. The materials used in reprocessing plants should possess high corrosion resistance in the nitric acid medium. Owing to their excellent corrosion resistance, the bulk metallic glass (BMG) with an amorphous structure are being explored and considered for service under highly oxidizing nitric acid environment. The reason for the excellent corrosion resistance of the metallic glass is often due to the compositional and structural homogeneity in the long range [62]. This quality of glass usually helped to the development of uniform and dense protective passive film [62]. However, only a few results on the corrosion behavior of the metallic glass in nitric acid environment are reported. Nevertheless, the corrosion rates for the Fe-metalloid based glassy alloys such as Fe₄₃Cr₁₆Mo₁₆C₁₅B₁₀ and Fe₄₃Cr₁₁Mo₁₆C₁₅B₁₀Ta₅ are high as 87.9 and 74.9 mm/y in 9 M HNO₃ at 124 °C (i.e. at boiling condition). The corrosion rates of the Ni metalloid based glassy alloys of Ni₆₅Cr₁₅P₁₆B₄ and Ni₆₅Cr₁₀P₁₆B₄Ta₅ composition were about 1.4 and 0.2 mm/y respectively, in 9 M HNO₃ at 124°C [63]. These results imply that, though the metalloid based metallic glasses exhibited high corrosion resistance in 12 M HCl solution at 25-30 °C [43], they are not suitable for service applications in boiling nitric acid as it undergoes severe corrosion in 9 M HNO₃ at 124 °C. Similarly, the low corrosion rate of 0.01 mm/y in 9 M HNO₃ is observed for the Ni-valve metal based metallic glassy alloys Ni₅₇Nb₁₉Zr₁₉Ta₅ and Ni₆₀Nb₁₅Zr₅Ti₁₅Ta₅ at 124 °C [62] indicates that the corrosion resistance of Ni-valve metal based metallic glass are better than that of the Ni-metalloid based metallic glass. However, X-ray photoelectron spectroscopic (XPS) results on Ni₆₀Nb₁₅Zr₅Ti₁₅Ta₅ exposed to boiling nitric acid indicated that the alloying elements Ni, Zr and Ti undergo preferential dissolution with negligible influence on the passivation [62-63]. Only Nb and Ta were contributed to the passivation of the alloy when exposed to boiling nitric acid. Therefore, the corrosion point of view, the Ti and Zr alloying with the Ni-valve metal based

Chapter 1

glass forming alloy is not beneficial for an applications in boiling nitric acid. In the present thesis work, Ti and Zr-free, Ni-valve metal based glass forming alloys namely $Ni_{60}Nb_{40}$ and $Ni_{60}Nb_{30}Ta_{10}$ $Ni_{50}Nb_{25}Zr_{25}$ metallic glass were investigated for the purpose of evaluating their performance in concentrated nitric acid.

The excellent corrosion resistance is expected for Ni-based metallic glassy alloys based in the presence of the noble elements. Based on the comparative corrosion studies of the amorphous alloys, apart from the glassy structure, the presence of the passivating elements (Nb, Ta, Zr, etc.,) is expected to enhance corrosion resistance. However, the concentration of the passivating or noble type elements also plays a important role in its corrosion resistance. Also, for the application point of view related to high corrosion resistance, Ni-based glassy alloy systems are better candidates when compared to the, Fe-, Cu-, and RE- based glassy alloys. If cost effectiveness is the issue, then the Ni- based is the most appropriate and suitable materials. Moreover, the sample size limitation of glassy alloy produced by melt-spinning and copper mold casting can be advantageously overcome by depositing thin and thick coatings of Ni-based MG on structural materials substrates of type 304L SS as protection on structures for nitric acid applications. Similarly, the electrochemical and passivation behavior of $Ni_{60}Nb_{30}Ta_{10}$ metallic glassy investigated in 1, 6 and 11.5 M HNO_3 at room temperature.

1.3 Oxidation

The elements or usually the metal loses one or more electrons is referred in terms to oxidation process. The oxidation is used to describe the chemical reaction between a metal and oxygen. The oxidation reaction of can be written as:



where M is a metal and O_2 is the oxygen

The following term describes generally the oxidation behaviour of a metal or an alloy:

- a. Thermodynamics,
- b. Kinetics of oxidation, and
- c. Morphology of the oxide scale.

1.3.1 Thermodynamics of Oxidation

The Gibbs free energy change (ΔG) is associated with metal-oxygen reaction, which is the main driving force of oxidation in the thermodynamic accept. When the Gibbs free energy change is negative, i.e. $\Delta G_r < 0$, the oxidation occurred spontaneously until the equilibrium state is attained, i.e. $\Delta G_r = 0$. For Eq. (4) the ΔG_r can be written as:

$$\Delta G_r = \Delta G^\circ + RT \ln K_r \quad (1.t)$$

where ΔG° , T and K_r are the difference in standard free energy, absolute temperature and the reaction constant, respectively. At equilibrium condition, the reaction constant of an oxidation is generally expressed by the Eq. (11) as:

$$K_{eq} = \frac{1}{P_{O_2eq}} \quad (1.u)$$

where K_{eq} is the equilibrium constant and P_{O_2eq} is the oxygen partial pressure at equilibrium with the oxide and that can be expressed as:

$$P_{O_2eq} = \exp\left(\frac{\Delta G^\circ}{RT}\right) \quad (1.v)$$

The values of ΔG° as a function of temperature are generally represented by the Ellingham/Richardson diagram from which the relative stabilities of different oxides could be assessed [64].

1.3.2 Kinetics of Oxidation

The thermodynamic reflection point concerning the more stable oxide products for results of oxidation, other than the final product may be significantly limited by the overall oxidation kinetics of the process. The oxidation rate depends on the following parameters, such as oxygen pressure, temperature, surface and microstructure. The following parameters are also indicators of the oxidation mechanisms which can take place at the sample surface and interface. The following equations are briefly described below which are often suggested for oxidation behaviour of many metal and alloys.

1.3.2.1 Linear equation

The linear oxidation law in the eq. (1.y), is describes the oxidation behaviour when the oxidation rate remains constant with time [65].

$$Y = k_l t \quad (1.y)$$

whereas, $Y = \Delta m/A$

where A , k_l , Δm , and t , are exposed sample area (cm^2), the linear rate constant ($\text{g cm}^{-2} \text{s}^{-1}$), mass gain data (in mg), and time (s) for isothermal condition, respectively. The rate constant values can be obtained from the linear least fitting of the experimental data. The linear oxidation behaviour is often an indication of surface reaction which is the rate determining factors.

1.3.2.2 Parabolic equation

The high-temperature oxidation behaviour, where the thermal diffusion is the rate determining the process, in many cases can be described with the parabolic equation.

$$Y^2 = k_p t + C \quad (1.x)$$

where, k_p , and C are the parabolic rate constant ($\text{g}^2 \text{cm}^{-4} \text{s}^{-1}$), and integration constant, respectively. The rate constant values are obtained from the linear and parabolic least square fitting of the experimental data.

The combinations of different equations are also observed depending on the system, e.g. para-linear behavior is characterized by the parabolic oxidation followed by linear oxidation. The parabolic oxidation behaviour was described by the Wagner that explained the oxidation is accompanied by the solid state diffusion [66].

1.3.2.3 Logarithmic equation

The logarithmic oxidation is protective oxidation kinetics where usually form a thin oxide film growth at low temperatures. In the case of logarithmic oxidation, the curves and reaction rate rise fast at the beginning of the oxidation (Onset) and then slows down rapidly towards saturation accompanying the fast forming oxide scale which is a protective film in nature. The logarithmic oxidation behavior usually described by simple logarithm and also an inverse logarithmic equations, Eq. (1.z) and Eq. (1.aa), respectively.

The simple logarithmic equation is represented by;

$$Y = k \log t + C \quad (1.z)$$

Inverse logarithmic equation

$$Y^{-1} = k \log t + D \quad (1.aa)$$

where Y can signify the mass gain or oxide thickness, and t stand for the isothermal time. The K_i and K are the inverse and direct logarithmic rate constants, respectively, whereas C and D are integration constants. The logarithmic rate law for the oxidation is first observed by the Caber and latter is known as Mott-Cabera model. Based on this model, the growth of the film is control by the electrostatic force between the metal cations and the oxygen anions.

Chapter 1

1.3.2.4 The activation energy for oxidation (E_a)

The temperature dependence of the oxidation rate generally expressed by well known Arrhenius equation, as shown in eq.(1.ab)

$$K = A \exp \left(\frac{E_a}{RT} \right) \quad (1.ab)$$

where K is the rate constant, the E_a is the activation energy (J/mol) and A is a pre-exponential. The oxidation rate constant (K) is determined by isothermal oxidation experiments by means of a $\log(K)$ vs. $(1/T)$ plot. The E_a is usually determined from the line slope $(-E_a/2.303R)$. If $\log(K)$ vs. $(1/T)$ shows a changing slope which may indicates a change in the oxidation mechanism, in the temperature interval.

1.3.3 Initial Stages of Oxidation and Scale Growth

The reaction between the bare metal surface and oxygen (or gas/metal interface) is a fast process, even at room temperature. The initial stages of oxidation at gas phases and metal solid phase are very complicated. When the oxygen gas comes in contact with the virgin metal surface and that resulting in the physical adsorption of oxygen molecules on the metal-

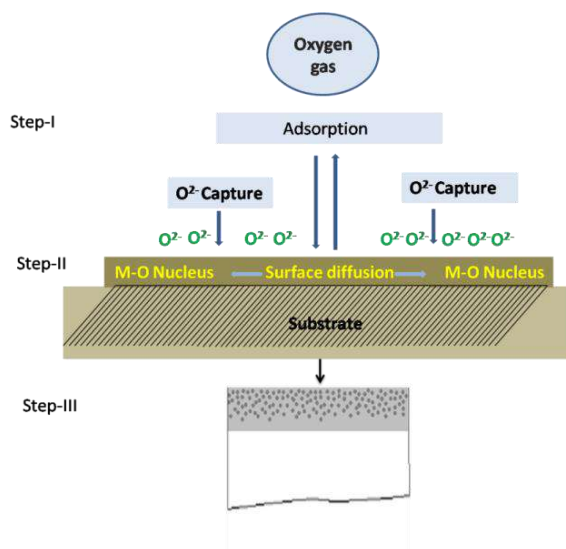


Figure 1.10 Schematic representation of some aspects of the oxide scale formation

Chapter 1

surface with adsorption energy of 20-25 kJ/mol, and this is considered to be a weak bond which is famously known Van der Waals forces. After dissociation of the physically adsorbed molecules, the process of chemi-sorption could leads to a stronger bond of the energy of around 600 kJ/mol.

The schematic diagram shown in Fig. 1.9 is to provide an understanding of the formation of the thin layer of adsorbed oxygen. Step - (II) is the formation of oxide nuclei and their lateral growth, which can result in continuous oxide layer (Step-III). The progression of nucleation can possible through either heterogeneous or homogeneous manner. Heterogeneous nucleation generally proceeds in the conditions of low temperature and low super-saturation, whereas under the opposite conditions homogeneous nucleation is more likely possible.

After a continuous thin oxide layer is formed, oxide layer growth, i.e. thickening, proceeds as shown in Fig. 1.9 (III). When the oxide layer becomes thicker and the term 'scale' is visible. The scale growth is connected to the following reactions:

- a. The oxygen reacts with electrons to form O_2^- att the gas-oxide interface
- b. The metal atoms (M) to form metal ions (M^{n+}) - and electrons (n^e) at the metal-oxide interface.
- c. The O^{2-} ions diffused towards the metal ions (Mn^+) from the gas-oxide interface and from the metal-oxide interface, the electrons (ne^-) moved outwards. The outward transport of the electron though the ions go together by the electron counter current or by the inward vacancy diffusion.

Finally, as the oxide scale thickens, due to the cell volume differences between the metal and the oxide, the formation of cracks and pores could lead to the severe oxidation.

The cracking is expected in the cases when the oxide scale grows inwards.

1.3.4 Oxidation of Alloys

The issue of alloys with higher oxidation resistance needs to be addressed when designing a new alloy. Hence, it would be an interest to predict the influence of alloying elements on oxidation behaviour. However, the following factors need to be considered when an alloy is being oxidized which includes [67]:

- a. The affinity of the metal atoms towards oxygen and to each other.
- b. Diffusion rates of metal or oxygen in the alloy and ions in oxides.
- c. Mutual solubility of oxidation products.
- d. Relative volumes of the different phases.

Firstly, it is important to decide which elements in the alloy are more expected to be oxidized by comparing ΔG° values. Knowing this for the binary alloys of A-B, whereas B is the less noble metal, which can be classified into three concentration ranges [67]

- a. Alloys composition at A-rich end of the system, which form only A oxides at the surface.
The maximum concentration of the less noble element B, for this type of oxidation to occur, depends on oxygen affinities of A and B, temperature and mutual solubility of oxides.
- b. Alloys composition rich with the B side of the system, forms only B oxides.
- c. In the case of intermediate compositions, whereas oxides of both A and B form either as separate layers or as mixtures. Even layers of double oxides such as CrNbO_4 in Nb-Cr alloys system formed.

1.3.5 Methods for finding protective and un-protective growth (Pilling Bedworth ratio)

The Pilling–Bedworth ratio (P–B ratio) of metals is the ratio of the volume of the metal oxide elementary cell to the volume of the corresponding metal elementary cell (from which

Chapter 1

the metal oxide is created). the P-B ratio can be referee if the metal is likely to passivate in dry air by creation of a protective oxide layer.

The P.B is expressed in equation below;

$$R_{PB} = \frac{V_{oxide}}{V_{metal}} \cdot \frac{M_{oxide} \cdot \rho_{oxide}}{n \cdot M_{Metal} \cdot \rho_{oxide}} \quad (1ac)$$

where,

- R_{PB} – Pilling–Bedworth ratio
- R_{PB} – atomic or molecular mass
- M – number of atoms of metal per molecule of the oxide
- ρ – density
- V – molar volume

N.B. Pilling and R.E. Bedworth indicated in 1923 that metals could classify into main two categories [68]: first those who form protective oxides, and those who cannot. They described the protective oxidation is ratio of the volume of oxide takes places in comparison to volume of the metal used to produce this oxide during the corrosion process in dry air. The oxide layer is predictive to be un-protective when the ratio is less than unity, and in this case film formed on the metal surface is cracked and/or porous. Conversely, the ratio more than 1 indicated that the oxidation trends to be protective and effective barrier can forms that further prevent the gas from further oxidizing the metal. The following connection can be shown basis of measurements;

- a. $R_{PB} < 1$: In this case, the oxide coating layer is too thin, more likely to be broken and offers no protective effect (for example magnesium).
- b. $R_{PB} > 2$: In this case, the oxide coating chips off and may offer no protective effect (example iron).

- c. $1 < R_{PB} < 2$: In this case, the oxide is passivating in nature, uniform and provides a protective effect in opposition to further oxidation at surface (examples aluminium, titanium, chromium-containing steels).

However, there are numerous example are exceptions to the above P-B ratio rules. Many of the exceptions are mainly due to the different oxide growth mechanism. The main underlying assumption of the P-B ratio is that oxygen needs to be diffused through oxide layer towards the fresh un-oxidized metal; in reality, it is often the metal ion that diffuses to the air-oxide interface.

1.3.6 Literature survey for the Oxidation of metals, Amorphous or metallic glassy alloys

1.3.6.1 Oxidation of metals (Ni, and Nb)

The high temperatures oxide form of Ni is NiO. The growth of NiO oxide scale is controlled by Ni^{2+} diffusion through the oxide scale and the oxidation reaction precede at oxide-gas interface [69]. The oxide formation of the Ni at grain boundary diffusion is NiO reported in elsewhere [69]. This type of growth is favourable if the stress concentration is lower in the oxide layer and a as a result lower the tendency for crack formation.

The oxidation behavior of Nb is a complex process, not only because it involves three different stable Nb oxides: NbO, NbO₂ and Nb₂O₅, but also because Nb₂O₅ can form in different polymorphic forms. In the initial stages of oxidation, the formation of different metastable phases of the form NbO_x, NbO_y, and NbyO is also possible [70]. The oxidation behavior of Nb is characterized by two main stages. In the first stage, oxygen dissolves in Nb and forms metastable NbO_x, NbO_y, NbyO phases. The acceleration of the oxidation rate in the second stage is associated with the nucleation and growth of Nb₂O₅, which is well known to form porous scales, and offer poor protection against oxidation [69].

1.3.6.2 Oxidation behaviour of the metallic glass

Bulk metallic glasses (BMGs) based on Cu, Ti, Zr, and Ni possess high glass-forming ability (GFA) and exhibit oxidation and corrosion resistance superior to those of conventional crystalline materials [71-73]. The reason for the excellent oxidation resistance of the metallic glasses in the air is often attributed to the structural and compositional homogeneity, resulting in the formation of uniform protective oxide films. Metallic glass alloys comprising the refractory elements like Zr, Cr, Nb, Ta, Ti, etc. interact with the environment through an adherent amorphous oxide film, which was either formed naturally or grown artificially [49, 74]. The oxide film formed act as an excellent protective barrier for further oxidation or corrosion in atmospheric air, acidic and basic environments [49].

It is a matter of fact, that thin oxide films find potential industrial applications in electrochemical devices [75]. Nickel-based bulk metallic glassy alloy has wide-ranging applications owing to its corrosion resistance as well as nano-scale tribological behavior [76] and used in electrochemical devices. Walz et al. [77] reported that the oxidation of $\text{Ni}_{91}\text{Zr}_9$ and $\text{Ni}_{64}\text{Zr}_{36}$ amorphous alloys in dry oxygen resulted in the formation of an oxide which was relatively rich in Zr, when the alloy was oxidized below its crystallization temperature at 300 °C or lower. When the temperature of oxidation was higher than 300 °C, the surface became predominantly of Ni-oxide.

The inverse oxidation behaviour of $\text{Ni}_{65}\text{Nb}_{35}$ metallic glass, investigated by Song et al. [77] revealed the segregation of Nb on the surface in the form of Nb-oxide at 100 °C. However, at 250 °C, Ni diffused towards the surface. Kai et al. [78] observed triplex scales on the air-oxidized $\text{Ni}_{53}\text{Nb}_{20}\text{Ti}_{10}\text{Zr}_8\text{Co}_6\text{Cu}_3$ glassy alloy at the temperature range of 400-550 °C. The outer layer consisting of exclusively NiO and Nb_2O_5 intermixed with Ni in the intermediate and inner layers. Lee et al. [34] reported that alloying of Ni-Nb with Ta enhanced the glass

Chapter 1

transition temperature and GFA. Thin amorphous Nb_2O_5 and Ta_2O_5 films act as protective barriers against severe corrosive environment [74].

On the other hand, researchers have explored thermal air oxidation below the glass transition temperature to improve the corrosion behavior of metallic glassy alloys in recent decades [49]. Nie et al. studied the corrosion behavior of the thermally oxidized film on $\text{Zr}_{64}\text{Cu}_{16}\text{Ni}_{10}\text{Al}_{10}$ and $\text{Zr}_{46}\text{Cu}_{37.6}\text{Ag}_{8.4}\text{Al}_{18}$ metallic glasses [49] and thermal oxidation at 320 °C resulted in the formation of 940 nm thick ZrO_2 and Cu-depletion on the outer surface of $\text{Zr}_{64}\text{Cu}_{16}\text{Ni}_{10}\text{Al}_{10}$ metallic glass, which exhibited superior passivity in 0.5 M NaCl and 0.05 M H_2SO_4 solutions. For $\text{Zr}_{46}\text{Cu}_{37.6}\text{Ag}_{8.4}\text{Al}_{18}$ metallic glass, the thermally grown ZrO_2 oxide films have a thickness of about 0.72 and 1.80 μm , at 168 and 336 °C, respectively, and such oxide film are known to hinders the electro-dissolution of Cu in 0.5 M H_2SO_4 + 0.01 M NaCl solution [44].

It was observed that the crystallization processes often accompany oxidation and that in some instances, intermetallic phases different from those found after crystallization in a vacuum environment can form [79]. In comparison to their microcrystalline counterparts, amorphous alloys often exhibit more intense oxidation. Furthermore, the microstructures observed in the oxidation penetration distance and the identified oxide phases may differ significantly from those observed on microcrystalline samples.

However, air-oxidation below the glass transition temperature showed for the development of amorphous oxide film with a thickness of a few tens of nanometer [79]. Amorphous oxide films are known to exhibit high dielectric constant and stability against the environments [49]. On the other hand, the thermal oxidation studies focus on the oxidation states, kinetics, phase transformation, structure, and mechanical properties. Far less attention has been paid to the corrosion behavior of thermally oxidized Ni-based metallic glass and its role in enhancing the passivity breakdown potential. However, before the actual application

as engineering materials, the fundamental chemical and environmental stability of such oxide layer need to be evaluated.

Comparative studies [49] suggested that the tailoring a desired stable amorphous oxide layer is possible at an elevated temperature which can withstand the trans-passivity breakdown. Thus, in this present thesis work, the thermal oxidation behavior of $\text{Ni}_{60}\text{Nb}_{40}$ and $\text{Ni}_{60}\text{Nb}_{30}\text{Ta}_{10}$ and $\text{Ni}_{50}\text{Zr}_{25}\text{Nb}_{25}$ metallic was carried out at various temperatures below the glass transition temperature for developing a highly protective oxide layers.

1.4 Other properties of metallic glassy alloys

At room temperature, the bulk glassy alloys exhibit higher fracture strength (σ_f), and lower Young's modulus (E) than those of crystalline alloys as shown in Fig.2.9 [68]. On the other hand, metallic glasses exhibit limited plasticity (~ 2%) in compression. It is known that dislocations are responsible for plastic deformation in crystalline metals, by lowering the activation energy for interplanar movement [80]. In amorphous structure, there are no atomic planes and thus, deformation can occur solely through the formation of shear bands [66].

This process requires far more activation energy and thus, amorphous metals have a strength which is 3 to 5 times higher than their crystalline counterparts. Bulk metallic glassy alloys exhibit thermal stability in the supercooled liquid region (SCLR), defined as the temperature region above the glass transition (T_g) and before the onset of crystallization (T_x).

Though, metallic glasses exhibit a limited ductility at a temperature lower than T_g ; they can be deformed with a super plastic behaviour in the SCLR ($\Delta T = T_x - T_g$).

A brief summary of deformation data from several different metallic glass systems in the SCLR is listed in Table 1.1. The viscous flow can be related to the applied stress (σ) with the equation.

$$\sigma = \eta(\dot{\epsilon})^m \quad (1.ad)$$

where η is the viscosity, $\dot{\epsilon}$ is the strain rate, m is the flow behaviour index.

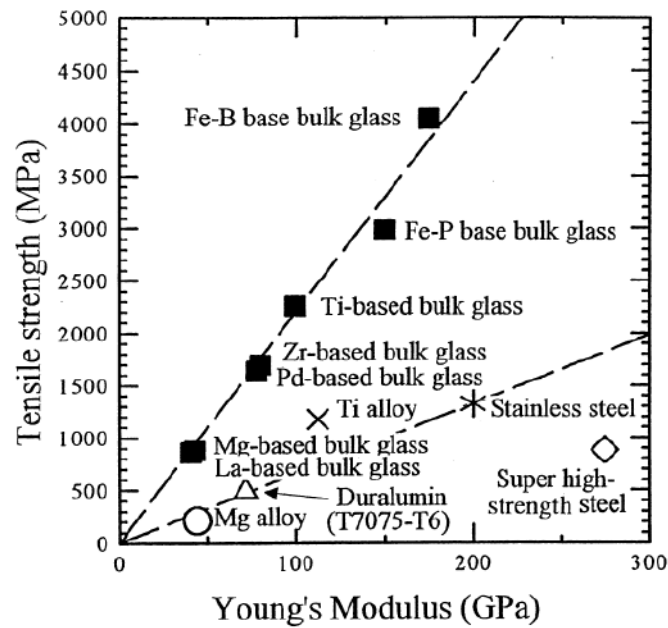


Figure 1.11 Relationship between tensile strength and Young's modulus for various bulk amorphous and conventional alloys [68].

Table 1.1 Deformation data of some bulk metallic glasses in the supercooled liquid region.

Alloy (in at. %)	T_g	T_x	m value	Ductility%	Ref.
$Pd_{40}Ni_{40}P_{20}$	578	651	0.4–1.0	1260	(Kawamura et.al, 1998)
$Zr_{52.5}Al_{10}Ti_5Cu_{17.9}Ni_{14.6}$	358	456	0.55	650	(Neih et.al, 1999)
$Zr_{55}Al_{10}Cu_{30}Ni_5$	670	768	0.5–0.9	800	(Chu et.al, 2003)
$Zr_{41.25}Ti_{13.75}Ni_{10}Cu_{12.5}Be_{22.5}$	614	698	0.4–1.0	1624	(Wang et.al, 2005)
$Ni_{60}Nb_{30}Ta_{10}$	665	675	--	--	(Lee et. al 2013)

As the temperature of the glass is raised to values defining SCLR, the viscosity of the glass can be as low as 10^6 poise and the m values suggesting a near Newtonian flow. At these low values of viscosity, shaping and forming operations of the metallic glassy alloys can be done with forces of the order of 1 atmosphere, similar to blowing of oxide glasses. Thus, the

Chapter 1

superplastic properties of metallic glasses can be used advantageously to process near-shape products at relatively low temperature ($2/3$ of the melting temperature, i.e. $T_g/T_m \sim 0.6$) by metal processing techniques like die-forging and stamping. The processing ability of three-dimensional parts of the BMG by super plastic forming (SPF) method is shown in Fig.11 for a complex micro gear and Fig. 1.12 a coil shape spring.

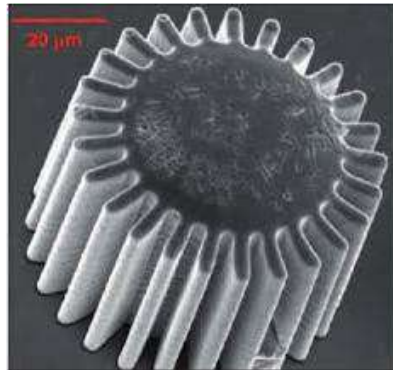


Figure 1.12 A complex micro gear BMG processed by SPF [Schroers et.al, 2006].

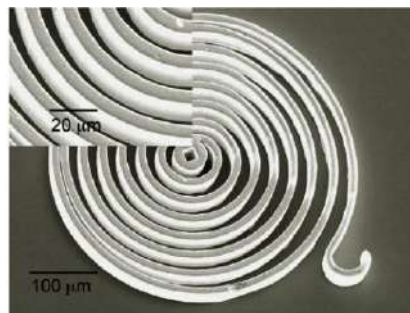


Figure 1.13 A coil shaped BMG processed by SPF [Schroers et.al, 2006].

1.5 Statement of problems and Objectives

1.5.1 Statement of problems

The inter-granular corrosion under the highly oxidizing nitric acid condition is a major issue for the structural components such as stainless steel (SS) of type 304L, and nitric acid grade alloys used in spent nuclear fuel reprocessing plants [49]. The conventional structural

Chapter 1

alloy such as type 304 L stainless steel (SS) cannot be used in boiling concentrated nitric acid (>9 M HNO₃), as it undergoes severe end grain and inter-granular corrosion attack [49].

Unlike conventional crystalline alloys with grain boundary defects, the metallic glass alloys are known to exhibit superior passivity owing to its homogeneous nature in the composition and amorphous structure in a long-range scale [62]. The passivation behavior on the Ni-based metallic glass in concentrated nitric acid has not received adequate attention which could be expected in order to take advantage of these properties.

Similarly, the other major problem of the structural alloys (Inconel 690, and 693 alloys) is the trans-passivity breakdown in nitric acid medium. The Ni-based with high refractory elements such as Nb, Ta and Zr are expected to enhance the resistance to the trans-passive breakdown which can be used for the concentrated nitric acid application. Surface properties particularly the oxidation under air environments at elevated temperature that enhances corrosion resistance has not been properly investigated and require further investigations to provide understanding of these properties.

Most of the metallic glasses are micro-alloying with the metalloid such as B, and C to enhance glass forming ability and other mechanical properties, unfortunately, metalloid B and C did not take part in passivation. Hence, metalloid is not beneficial for concentrated nitric acid corrosion. The Ni-based metallic glasses without metalloid have been designed for improving corrosion resistance in concentrated nitric acid corrosion. Furthermore, the effects of elements such as Ta and Zr were qualitatively evaluated to provide understanding to the mechanism responsible for the enhancement of the corrosion properties.

Some studies suggest a better corrosion resistance of metallic glasses however the differences in the corrosion behavior of metallic glass to its crystalline counterpart are not clearly reported in terms of protective nature of the passive film and its growth mechanism.

Chapter 1

The corrosion behavior of thermally oxidized Ni-based metallic glass, and its comparison with it's the as-spun alloys are attempted. However, novel thick amorphous oxide produced from the control air-oxidation need proper understanding in terms of corrosion resistance.

Furthermore, the corrosion properties of the glassy alloys in form of only thin ribbon or rod have been extensively studied. However, far less information about the corrosion properties of glassy alloy prepared by other processing techniques, such as Magnetron sputtering.

Moreover, research studies have not been attempted to find on the application of metallic glasses alloys as candidate materials for thermo-well application in nitric acid medium for reprocessing applications.

1.5.2 Objectives

This work was undertaken to address the following objectives.

- a. To provide understanding to the passive film growth mechanism of Ni-Nb-Ta metallic glass and it's partially crystallized alloy in 11.5 M nitric acid medium at room temperature.
- b. To provide a basic understanding to electrochemical corrosion, passivation and semiconductive behavior of Ni-Nb amorphous alloy in concentrated nitric acid and also effects of Ta and Zr to Ni-Nb system on corrosion and semi-conductive nature.
- c. To develop thick amorphous oxide film through the control temperature oxidation below its glass temperature for enhancing the corrosion resistance and stability against trans-passive breakdown. Based on the achieved properties, to introduce a novel application to Ni- metallic glasses as thermo-well for dissolver tank application by improving its corrosion properties.

Chapter 1

- d. Thick Ni-Nb-Ta glassy coating on 304 L SS by DC magnetron sputtering to minimize the inter-granular corrosion in concentrated nitric acid.

2 Materials and Experimental Procedures

The chapter describes briefly the various experimental techniques used for the synthesis and characterization, and corrosion investigation. The following experimental techniques and electrolytic medium have been used to investigate the metallic glasses in the present study such as surface modification, surface morphological analyse, surface analytical and electrochemical techniques (EIS, and Potentiodynamic Polarization, and Mott-Schottky).

2.1 Sample preparation

2.1.1 Arc melting

Arc melting required alloy composition granules of the mixture by weighing metal and a total quantity of 10 g was prepared. Fig. 2.1 showed a schematic diagram of a suction casting apparatus. The elements were placed on the water-cooled copper plate and the entire chamber was evacuated by alloying backfilled ultra high purity Ar gas three times.

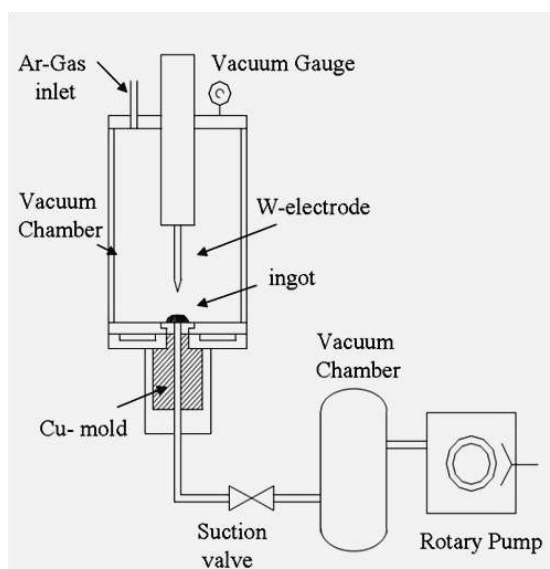


Figure 2.1 Schematic diagram of Arc-melting apparatus [3].

The ingots were re-melted at least four times to ensure the homogeneity. Typical mass losses of the melted ingots samples are less than 1% of the initial mass.

2.1.2 Melt spinning

The arc-melted ingots were crushed into several small pieces, re-melted and rapidly quenched onto a water-cooled rotating copper wheel at the speed of 3200 Hz to obtain ribbons of the alloy. A schematic diagram of the melt-spinning apparatus is shown in Fig.2.2. Molten mass of alloy samples was placed in fused silica or boron nitride (BN) tube with a small nozzle. The chamber was evacuated by subjecting a back-filled with ultra-high purity Ar gas. The samples were inductively remelted in fused silica or BN tube, followed by ejection with a 35 kPa pressure through a nozzle onto a rotating water-cooled copper wheel with a surface velocity of 40 m/s. The prepared ribbon samples exhibit a thickness of about 40 to 50 μm and a width of about 10 mm.

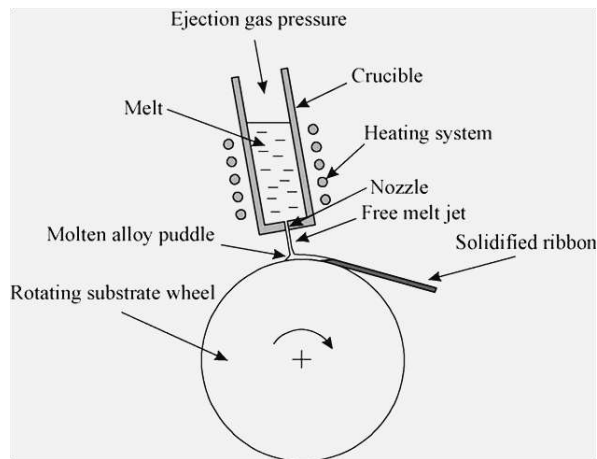


Figure 2.2 Schematic diagram of the melt spinning apparatus.

2.1.3 Magnetron sputtering

Magnetron sputtering is the physical process wherein atoms or molecules of material are ejected from a target by the bombardment of high-energy particles (Ar^+). Magnetron sputtering is a high-rate vacuum coating technique for depositing alloys onto a wide range of materials with thicknesses ranging from nm to 5 μm . It has several advantages over other vacuum coating techniques like electron beam evaporation and plasma spray coating and development of a number of commercial applications such as corrosion application. Fig. 2.3

showed the schematics diagram of the instrument apparatus and deposition process. The cathodic sputtering is the process where bombardment is by positive ions derived from an electrical discharge in a gas. Material is ejected from the target alloy, which can be coated directly onto substrates.

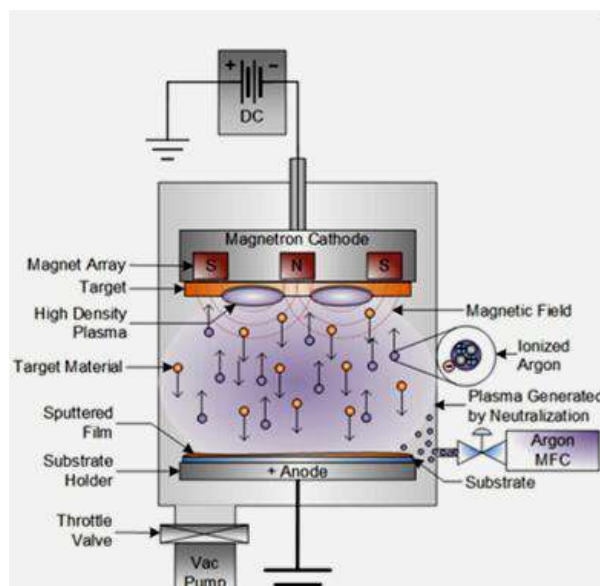


Figure 2.3 Schematic diagram of Magnetron sputtering coating.

In the simplest of applications, the magnetron was used to deposit metallic materials by DC sputtering. In the Rf mode, the target directly conducts electricity and is subject to IR losses and can be operated up to currents of 70 W cm' averaged over the target. The medium deposition rates on moving substrates of 3 micrometers per 15 minute making this y suitable to form the smooth and adherent coating.

In this work, the power 50 kW was used due to the large target size. In corrosion processes sputtering have become an attractive method for developing high corrosion resistance coating on low corrosion alloy in order to protect the surface of the substrate from the severe corrosive medium. The film develops must have good adhesion, uniformity and 'step coverage of the substrate. The atoms and compounds impacts on the substrate surface and rapidly ($\sim 10^6$ °K/s) cools which can results in forming an amorphous coating. The

magnetron sputtering can be used either in vacuum or in a protective environment using chambers back filled with Ar gas at low pressure or in the air.

2.2 Structural characterization

2.2.1 X-ray Diffraction (XRD) and grazing incident X-ray Diffraction (GIXRD)

Characterization of the metallic glass alloys was performed by X-ray diffraction (XRD), using a diffractometer (INEL 2000) with Co K α radiation source ($\lambda=1.7205$ Å). XRD patterns were collected over a range of diffraction angle, 2θ , 20-80° using a step size of 0.002° from the coated or ribbon metallic glass samples. The X-ray diffraction experiments are used to confirm the amorphous state of the specimens and to identify the structural phase, which might be present in the oxidized sample.

The grazing incidence X-ray diffraction (GIXRD) measurements were carried out in the range of 20-80° at a very low angle of about 0.1 to 0.5 Ω to evaluate the amorphous state of the of the metallic glass coating and also to identify the structural phases present in the oxidized sample.

2.2.2 Transmission Electron Microscopy

High-resolution transmission electron microscopy (HRTEM) of 2 Å resolution provides the detailed structure about the amorphous and crystalline state of the alloys including random orientation of metallic glass and precipitation of phase in annealed MG sample. The ribbon samples were prepared using a combination of electrolytic jet thinning and ion milling. Samples were first thinned with a solution of HClO₄ (30%) and ethanol (70%), using a jet thinner (Struers, Tenupol-3). Then, the edge of the hole was further thinned, using an ion miller (Gatan, Model 600). The angle between the ion beam and the surface of the sample was set at approximately from 6 to 10 degrees. In contrast, the preparation of the coating sample for HRTEM examination is much easier than the MG ribbon sample. The coating

sample is prepared by scratching followed by loaded on Cu-grid, and then placing in a sample holder for phase examination.

In the present experiments, a TEM (JEOL, 2010F) operated at 200 kV was used to study the structure of the sample. The structure of a single particle/phase was identified by electron diffraction pattern (EDP) and the chemical composition of grain was determined using an energy dispersive spectrometer (EDS).

2.3 Oxidation of the Metallic Glass

2.3.1 Thermal oxidation in a tubular furnace

An open tube furnace with an electric heating device was used for conducting the oxidation experiment of metallic glass in an air environment. The apparatus used for the tubular furnace, where the design consists of a cylindrical cavity surrounded by heating coils that are embedded in a thermally insulating matrix.

Temperature is controlled via feedback from a thermocouple in the temperature ranges from 200 to 600 °C under isothermal condition. The digital temperature controllers are programmable with segments for ramping, soaking, sintering, etc.

2.3.2 Thermogravimetric analysis

Thermal gravimetric analysis or thermo-gravimetric analysis (TGA) is a method of thermal analysis in which changes in physical and chemical properties of materials (here is metallic glass) are measured as a function of time (with constant temperature or isothermal mode). The changes in the mass of a sample due to various thermal events such as absorption, and oxidation properties are studied while the sample is subjected to a different time for constant temperature. Therefore, TGA can be used in the analysis of the formation of protective films or coatings on alloy sample, etc.

2.3.2.1 Different types of TGA available

- A. Isothermal or Static TGA
- B. Quasi-static TGA: In this technique, the sample is heated to a constant weight at each of a series of increasing temperature.
- C. Dynamic TGA: In this type of analysis, the sample is subjected to the condition of a continuous increase in temperature at a constant heating rate, i.e., usually linear with time.

The instrument used for TGA analysis is a programmed precision balance for a rise in temperature (called as Thermobalance, thermobalance consists of an electronic microbalance (important component), a furnace, a temperature programmer and a recorder.

2.3.2.2 Applications of TGA

- a. Thermal stability of the related materials can be compared at elevated temperatures under the required atmosphere. TGA curve helps to explicate passive and decomposition mechanisms.
- b. Kinetic studies: A variety of methods can be used to analyze the kinetic features of weight gain and weight loss through controlling chemistry.
- c. The recorded curves in TGA can be fitted with particular equations in order to obtain the nature or mechanism of oxidation and rate constants.
- d. The activation energy of the oxidation reaction can be calculated by pursuing the TGA experiments at various temperatures.
- e. Corrosion studies: TGA provides a means of studying oxidation or reactions kinetic with other reactive gases or vapors.

In this work, the TGA is used to provide the oxidation kinetics behaviours of the growth of the film on the metallic glass.

2.4 Corrosion property evaluation

2.4.1 Specimen preparation for corrosion test

The 40-50 μm various nickel base metallic glassy ribbons were cut into dimensions of 15 mm width and 30 mm length. Before the corrosion test, the surface was ultrasonically cleaned in ethanol or acetone, washed in distilled water, and dried in air for 1 h for reproducibility of the results. The MG ribbon samples were not polished, and the corrosion studies were carried out on the air side of the ribbon. The 0.5 cm^2 area of the ribbon specimens were exposed in the test solution while the rest of the area mask with green adhesive poly-amide and Teflon tape which are inert to the corrosive solution.

2.4.1.1 Preparation of the coating sample for corrosion test:

- a. Type 304L SS was cut into a specimen of dimensions 10 mm x 10 mm x 5 mm. The specimens were mechanically polished up to 1200 grit finish using SiC emery sheet and further polished up to 1 μm diamond finish.
- b. After deposition of the Ni-based metallic glassy coating on 304L SS, the uncoated side of the sample were mounted with epoxy resin, and a brass rod was attached. For coated specimen, the brass rod was used to provide the electrical conductivity using silver paste between the ribbon specimen and the Cu- tape for conductivity.
- c. The coated side of Ni-based metallic glass of dimension 1 cm^2 area is exposed for evaluating the corrosion behaviour using electrochemical techniques such as potentiodynamic polarization, electrochemical impedance spectroscopy and Mott-Schottky analysis.

2.4.2 Electrolyte Medium

The nitric acid is used as a primary medium for all the corrosion studies. The solutions were prepared using Analytical Grade (AR) nitric acid. Different concentrations of 1, 6, and

11.5 M nitric acid was used to study the electrochemical behaviour of the glassy alloys. The corrosion behaviour of Ni-based metallic glass was carried out in fluorinated nitric acid (11.5 M HNO₃ + 0.05 M NaF) in order to evaluate the effect of the fluoride effect on the surface of alloys specimens.

2.4.3 Potentiodynamic and potentiostatic polarization test

Potentiodynamic polarization is one of the most widely used corrosion testing methods. These techniques provided information on such as corrosion rate, corrosion mechanisms, and susceptibility of materials to the desire environments [81]. The major advantage of this technique is the rapid determination of corrosion rates as compared to weight loss measurements. The well known Tafel extrapolating method in the semi-logarithmic plot of the linear segment of cathodic and anodic regions of the potentiodynamic curves was used to determine the corrosion current density. A polarization curve gives information about material behavior in electrolytes like active, passive or active-passive state material [82]. The open circuit potential (OCP) of the working electrode was monitored until it achieves a steady state in the tested environment for all the glassy sample. In general, the time taken for the stable OCP was about 15 to 30 min. The potentiodynamic and potentiostatic tests were conducted in a three-electrode cell, using a potentiostat (Autolab, The Netherland). The glassy or crystalline alloys were treated as a working electrode; Ag/AgCl glass electrode used as a reference and platinum sheet as auxiliary electrodes.

In the potentiodynamic test, a potential range was applied to the working electrode at a scanning rate of 0.166 mV/s. The initial potential range starts from 200 mV lower with respect to the open circuit potential (OCP) and until the transpassive or dissolution potential range. As a variation of the potential was applied, the change in current was measured by the potentiostatic method. The semi-logarithmic plot of the potentiodynamic curves, i.e., log (I) vs. E, provide information on the corrosion potential (E_{corr}), corrosion current (I_{corr}),

passivation current density (I_{pass}), and pitting potential (E_{pit}), which were used as the measure of corrosion properties. Though, E_{corr} and OCP have similar meaning always a small difference in their values could be noticed due to the electrode kinetics and differences in the methods of measurements.

Potentiostatic tests were performed after the potentiodynamic test. The desired potential, at a potential corresponding to the passive, active or transpassive region of the potentiodynamic curves, was applied to the working electrode for a predetermined time. Thus, in a potentiostatic test, the change in current is measured over the time for the applied constant potential. The area under the potentiostatic curves gives the total charge density (Q) transferred, which gives the direct information about the corrosion reaction taking place. Moreover, the slope of the double-logarithmic plot of potentiostatic curves i.e., $\log(I)$ vs. $\log(t)$, gives the information about the rate determining mechanism.

2.4.4 Electrochemical Impedance Spectroscopy measurements

Electrochemical impedance spectroscopy (EIS) is powerful technique used for the characterization of corrosion properties of the metallic glass and alloy/electrolytes interfaces in different environments. Impedance is the opposition to the flow of current, which is given by the ratio of the applied voltage to the resulting current. It is the combination of resistance and reactance in an electrochemical system. The locus of impedance as a function of angular frequency is called the impedance spectrum. This technique involves the determination of cell impedance, in response to a small AC signal at any constant DC potential over frequencies ranging from a micro to mega-hertz. EIS is widely used to analyze the complex properties in a material such as dielectric properties, mass transport, defect density, passive film stability, coating degradation, microstructural and compositional effects on the conductance of solids, and impedance of biological membranes [82]. The wide spread application of this technique is due to the use of very small amplitude signal without disturbing the desired properties of

Chapter 2

materials to be measured. The most common approach is based on the equivalent circuit concept, exemplified in the model of equivalent or Randles circuit elements [82-83]. In the Nyquist plot, the impedance is represented by the opposite of the imaginary part as a function of the real part. Therefore, the Nyquist plot is termed as the complex plane impedance plot. In the Bode plot, the modulus of the impedance and the phase angle are both plotted as a function of the log of frequency. For a simple resistor-capacitor ($R-C$) circuit, the Nyquist plot is characterized by a semicircle. Nyquist plot allows an easy prediction of the properties of the electrode-electrolyte interface; however, it does not provide the information regarding the frequency dependence of impedance. Bode plot provides the necessary information for clear interpretation of the results. The interpretation of the impedance data from either Nyquist or Bode plot is carried out by means of an electrical equivalent circuit consisting of circuit elements and representing the physical phenomenon occurring in the electrochemical cell. In general, the circuit consists of the following basic elements [74]. The capacitance is given by the equation [84-85]

$$Z_{CPE} = Y_0 (j\omega)^{-n} \quad (2.a)$$

where, Y_0 is a constant ($\Omega^{-1}S^n$), ω is the angular frequency, n is the power index of CPE, and j is the imaginary number equal to $(-1)^{1/2}$. In order to account for non-ideal behavior of capacitance, real capacitance is replaced by constant phase element (CPE) whose impedance is given by Eq 2.b. The transfer of Y_0 to the capacitance calculated from the equation is given below [83,85].

$$C = Y_0 (\omega_m'')^{n-1} \quad (2.b)$$

where, C is the capacitance of thin passive film and ω_m is the frequency at which the imaginary impedance (Z'') has a maximum value. The n are frequency-independent fit parameters, and $\omega = 2\pi f$, where f is the frequency in Hz. n is defined as $n = 1 - 2\alpha/180$,

where α is the depression angle (in degree). When $n = 1$, CPE describes an ideal capacitor [83-85].

The equivalent circuits are used to provide understanding to the nature of the working electrode, and the physicochemical process is occurring at the electrode-electrolyte interface. Depending upon the shape of the EIS spectrum, a circuit model and initial circuit parameters are assumed and input is provided by the operator. The program then fits the best frequency response of the given EIS spectrum to obtain the fitting parameters. The quality of the fitting is judged by how well the fitting curve overlaps the original spectrum. By fitting the EIS data it is possible to obtain a set of parameters which can be correlated with the electrochemical properties of the substrate. Before EIS experiments, the open circuit potential (OCP) was monitored for 30 min for each sample in 11.5 M nitric acid until the stabilization of the system. EIS measurement was performed at room temperature using PGSTAT302N electrochemical workstation (Autolab, Netherland). The EIS experiments were performed on the various Ni-based metallic glasses ribbon at their corresponding open circuit potential (OCP) in a nitric acid environment. A three-electrode cell comprising two platinum electrodes as a counter electrode was used for the electrochemical experiments in the present thesis. The impedance data were recorded at the OCP and frequency range was adjusted from 100 KHz to 0.01 Hz with an applied ac perturbation of 10 mV. The impedance data were analyzed by a commercial software package "NOVA". Constant phase element has been used in the present investigation to obtain a better fit for the experimental data, which would represent the capacitance of the passive oxide layer.

2.4.5 Mott-Schottky analysis of the oxide film:

The electronic structure of the passive film was evaluated by the Mott-Schottky analysis. In this test, the electrode capacitance was measured as a function of the applied potential under the passive region for a single frequency or multiple frequencies. This

analysis is important in situ technique for passive films analysis of glassy alloys [85]. The capacitance of the passive film, C_f is considered to be a combination of three capacitances in series [85].

$$\frac{1}{C_f} = \frac{1}{C_M} + \frac{1}{C_{sc}} + \frac{1}{C_{dl}} \quad (2. c)$$

where, C_M is the metal/film interface capacitance, C_{sc} is the space charge capacitance, and C_{dl} is the Helmholtz double layer capacitance. The value of C_{dl} is a few tens of $\mu\text{F}/\text{cm}^2$ in nitric acid, and typical C_{sc} is found in nano-meter range. The C_{sc} is much lower than the C_{dl} and therefore C_{dl} can be neglected for analyses of the Mott-Schottky experiments. The C_{sc} in passive films is minimal when compared with the C_M and C_{dl} because of the relatively thick space charge layer. The contributions of C_M and C_{dl} can be therefore neglected, and C_f is taken as the value of C_{sc} . This assumption is acceptable when the frequency is reasonably high enough as 1000 Hz-3000 Hz [85]. Consequently, the data points in the plots of $(\frac{1}{C_{sc}^2})$ versus E can describe the semiconducting behavior of the passive region. The C_{sc} of an n-type and p-type semiconductor is given by the following equations [85]. The semiconducting properties such as flat band potential, type of semiconductivity, donor, and acceptor densities are obtained from the Mott-Schottky analyses [85]. The charge distribution in the film is determined by space charge capacitance $(\frac{1}{C_{sc}^2})$ versus applied potential E (Ag/AgCl), as shown in equation 2.d and 2.e [76].

$$\frac{1}{C_{sc}^2} = \frac{2}{\varepsilon\varepsilon_0 e N_d} \left(E_{fb} - E - \frac{k_B T}{e} \right) \quad (2. d)$$

$$\frac{1}{C_{sc}^2} = -\frac{2}{\varepsilon\varepsilon_0 e N_a} \left(E_{fb} - E - \frac{k_B T}{e} \right) \quad (2. e)$$

where, ε_0 is the vacuum permittivity, ε is the dielectric constant of the metal oxide, N_d is the donor density for an n-type semiconducting oxide film, N_a is the acceptor density for a p-type

semiconducting passive film, e is the charge of an electron, E_{fb} is the flat band potential, E is the applied potential, T is the temperature in Kelvin, and k_B is the Boltzmann constant.

Mott-Schottky plots with positive and negative slope indicating the formation of the n-type and p-type semiconductivity, respectively [85]. The donor density (N_d) and acceptor density (N_a) of an n-type and p-type semiconductor are obtained by the given equations 6 and 7, respectively [85].

$$N_d = \frac{2}{\varepsilon\varepsilon_0 e C^{-2}} \left(E_{fb} - E - \frac{k_B T}{e} \right) \quad (2. f)$$

$$N_a = -\frac{2}{\varepsilon\varepsilon_0 e C^{-2}} \left(E_{fb} - E - \frac{k_B T}{e} \right) \quad (2. g)$$

The corrosion phenomenon is closely related to its point defect structure associated with oxygen vacancies in n-type semiconducting properties and cation vacancies in p-type semiconducting properties of the oxide/passive film in acidic environments [85]. The detailed study about the defect structure, semiconducting properties, and electrochemical behaviour are essential for the application of metallic glassy alloys for nitric acid application.

Based on the Point Defect Model (PDM), the donor density and acceptor density are oxygen and cation vacancy defect in an oxide film [86]. The combination of the Mott-Schottky and points defect model provides essential information about the defect structure of the passive film. Generally, the defect densities (N_d and N_a) have a significant influence on the stability of the passive films.

2.5 X-ray photoelectron spectroscopy

X-ray Photoelectron Spectroscopy (XPS) is a widely used surface analysis technique that provides different oxidation and chemical states of elements. These include identification of oxidation state metal oxide films, surface analysis of semi-conducting, conducting,

Chapter 2

insulating materials, and elemental depth profiling along with the depth of the oxide film. In XPS, the photoelectrons is emitted from the test sample specimen's surface, when the specimens is irradiated with low-energy (~1.5 keV) X-rays. The energy analyzer measures the kinetic energy of the emitted photoelectron. The measure binding energies are the characteristic of the elemental identity, chemical state. As the primary sources of X-ray, Al-K α (1486.6 eV) and Mg-K α (1253.6 eV) are used in XPS techniques.

$$EB = hv - EK - W \quad (2.h)$$

The kinetic energy of the electrons is related to photon energy (hv) of the primary X-ray source. The relation between binding energy ' E_B ', kinetic energy E_K , photon energy and work function W of spectrometer parameters is given by equation 2.h.

In the present thesis work, the X-ray photoelectron spectroscopy (XPS, SPECS Surface Nano Analysis, GmbH, Germany) was carried out to study the passive film compositions form on the surface of the Ni-based metallic glassy specimens or coating before and after corrosion tests. The width zone of the sample analyses is 4 mm. The monochromatic Al α source of photon energy (1486.71 eV), pass energy (10 eV), resolution (FWHM 0.62 eV of Ag), and take-off angle (53°) were used for XPS characterization. The high-resolution XPS data were processed and analyzed using SpecsLab2 and Casa2318PR1 XPS software, respectively. The binding energy of C1s (284.8 eV) was used as a reference for charging correction. The background of each spectrum was corrected using Shirley approximation algorithm and the high-resolution Ni 2p, Nb 3d and Ta 4f spectra were de-convoluted using the Gaussian-Lorentz functions. The area under de-convoluted peaks corresponded to the concentrations of the species and was corrected for the sensitivity factor of the respective photoelectron lines.

Moreover, the mean free paths of the photo-electron vs. electron kinetics energy for the different elements are discussed [86]. In present work, most of the glassy alloys studied in the

thesis are made of Ni, Nb, Ta, and Zr. Since the metallic glass studied for this thesis are only Ni-based (i.e., balance with Ni (60% content)) and the mean free path of the photo-electron is around 7 Å on Ni metal [86]. The 100% photo electron is coming from 3 times of mean free path of the electron. By considering the mean free roughly of 1 nm based on the universal curve of photo-electron vs. electron kinetics energy (Fig. 2.6), and therefore, the 100% photo electron is coming from 3 nm depth of the oxide film. However, the kinetic energy of the Nb- and Ta-oxide is roughly around 1459 and 1258 (eV). Therefore, the photo-electron is from maximum 3.5 to 4 nm depth of the oxide film of the Nb- and Ta-oxide, respectively.

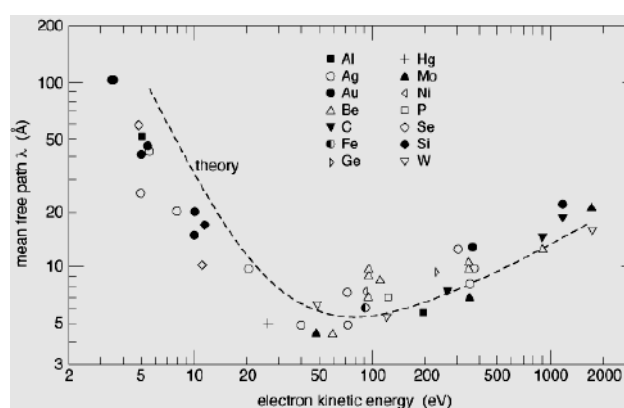


Figure 2.4 the mean free paths of the photo-electron vs. electron kinetics energy for the different elements.

2.6 FESEM analyses of corrosion morphology

The field emission scanning electron microscope (FESEM, Carl Zeiss Crossbeam 340, Germany) was used to analyse the morphologies of materials. The SEM generates the images by scanning the object with a focused beam of electrons. The electron beam was initially emitted from tungsten filament or lanthanum hexaboride (LaB6) cathode. The beam was accelerated to the energy around 0.2 to 40 keV and focused by condenser lenses into a spot size of 0.4-5 nm in diameter. The following physical phenomenon like, an absorption, reflection, backscattering, and secondary electrons are results of electron beam when it interacts with matter.

In the present thesis work, before and after the corrosion tests such as potentiodynamic, potentiostatic or immersion tests, the glassy specimens were examined by field emission scanning electron microscope with an energy dispersive x-ray spectrometer (EDS) for composition analysis. FESEM measurements were carried out using SESI (Secondary Electrons and Secondary Ions) and Inlens duo (for backscattered mode) detector at primary beam energy of 2 kV.

2.7 AFM analyses of surface topology

Atomic force microscopy (AFM) provides a nano-scale surface feature in 3-dimensional profile, by maintaining a surface and probe at a very short distance of about 0.2-10 nm and forces between a sharp probe (tip diameter <10 nm). The probe commonly known as AFM tip is attached with flexible cantilever, which gradually touches the surface. While tip approaches to the surface, the small force between the probe and the surface was recorded. The several length, shape, and materials cantilever tip is available which allow for required resonant frequencies and spring constants. In this work, Si₃N₄ tip was used, (ND-MDT, Russia). The AFM analysis was carried out on the oxidized metallic glasses in contact mode.

The feedback loop and piezoelectric scanners controlled the motion of the tip while the probe scans the surface. The “beam bounce” method was used to determine the deflection of the probe. A semiconductor diode laser is reflected from the cantilever onto a position sensitive to a photodiode detector. This detector measures the bending of cantilever during the tip, which is scanned across the surface. The map of the surface topography generates from the several number deflections of the cantilever.

The dominant interactions between the tips with the surface are Vander Waals interactions while probe approaches the surface at short distances. In contrast, capillary, magnetic, electrostatic interactions are considerable when the probe is away from the sample surface.

Chapter 2

The following three primary modes of imaging operation modes are involved in the AFM techniques [87].

- (1) Contact mode (probe-surface distance < 0.5 nm)
- (2) Tapping mode (0.5-2 nm probe- probe-surface distance)
- (3) Non-contact AFM (0.1-10 nm probe-surface distance)

All the oxidized and corroded surface topography in this work were carried out in contact mode. During scanning the surface in contact mode, the probe predominately experiences repulsive Vander Waals forces in resulted tip deflection. The attractive Van der Waals forces are dominant (non-contact mode) as the tip moves away from the surface. In contact mode of operation, the cantilever bends when the spring constant of the cantilever is less than the surface. The feedback a loop helps to remains the force constant between the probe and the sample by maintaining a constant deflection of the cantilever in consequence surface topography image. One of the advantages of the contact mode operation is the fast scanning, good for rough samples, and even we can measure the volume or shape corrosion pits.

3 Effect of the structure (Amorphous & Crystalline) on corrosion resistance in nitric acid medium

This chapter deals with the passive film growth behavior of $\text{Ni}_{60}\text{Nb}_{30}\text{Ta}_{10}$ metallic glass and its partially crystallized ribbon in concentrated (11.5 M) nitric acid environment. XRD results confirmed the formation of nano-crystalline α -Ni in the amorphous matrix during crystallization at 650 °C under vacuum for 1 h. The EIS, potentiodynamic polarization, and Mott-Schottky results were indicated higher corrosion resistance of the metallic glass compared to the partially crystallized ribbon. Similarly, XPS measurement reveals the enrichment of Nb_2O_5 , Ta_2O_5 , and NiO on the passive film of the glassy structure, while α -Ni depleted on the corroded passive film of partially crystallized alloy and that affected the corrosion resistance.

3.1 Introduction:

The corrosion resistance of metallic glass and crystalline alloys in different environments is related to the passive film properties. The corrosion resistance and stability of passive film of metallic alloys are very sensitive to the chemical composition, and as well as the materials structural i.e (amorphous and conventional grain structure) [88-89]. The passive film acts as a barrier which plays an essential role in corrosion resistance of the alloys. Understanding the growth of passive film on the metallic glass and crystalline structure is essential for assessing the passive film stability in corrosive nitric acid environments. Since the passive film determine the corrosion performance [88], thus it is essential to understand how the alloying elements affect the passivation behaviours in metallic glass and crystalline alloys. The passivity and corrosion resistance of the amorphous matrix and nano-crystalline intermetallics of Zr-based metallic glasses system was well reported [91]. However, the passivation and corrosion behaviour of the Ni-based metallic glass and crystalline alloy has not been investigated in details for the nitric acid application.

Therefore, this chapter dealt with the comparison of the passive film stability of metallic glass and crystalline structure of the $\text{Ni}_{60}\text{Nb}_{30}\text{Ta}_{10}$ alloy in nitric acid (11.5 M) and nature of the semiconducting properties are evaluated. Further, stability of passive film on the metallic glasses and crystalline alloys also correlated with the defect structure of the passive film.

3.2 Results and Discussion

3.2.1 XRD analysis of the as-spun and heat treated $\text{Ni}_{60}\text{Nb}_{30}\text{Ta}_{10}$ alloy

The $\text{Ni}_{60}\text{Nb}_{30}\text{Ta}_{10}$ metallic glassy (MG) ribbon sample of 40 μm average thickness was obtained by the melt spinning technique as reported elsewhere [34]. The glass transition temperature (T_g), and onset crystallization temperature (T_x) of the metallic glass measured from differential scanning calorimetry (DSC) are 665 and 689 °C, respectively [34] (Fig 3.1a). The composition of the metallic glass was confirmed by the point EDS, as shown in Fig. 3.2. The heat treatment of $\text{Ni}_{60}\text{Nb}_{30}\text{Ta}_{10}$ MG ribbon was carried out at 650 °C, for 1 hr under high vacuum (10^{-6} mbar). The 20 °C/min heating rate was employed to obtain the crystallization temperature. All the experiments and characterization were performed on the air side of the metallic glass ribbon. The XRD of the $\text{Ni}_{60}\text{Nb}_{30}\text{Ta}_{10}$ metallic glass in Fig.3.1b exhibited broad halo peak, which is attributed to the amorphous structure of metallic glass. After heat treatment at 650 °C (Fig.3.1b), the crystalline peaks are superimposed on the amorphous structure corresponding to FCC-Ni (α -Ni) (#00-001-1266). Apart from the α -Ni crystalline peak, no other crystalline metal or intermetallics of alloying elements were detected within the resolution limit of the XRD technique. XRD result of the partial crystallized sample at 650 °C for 1 h shows the crystalline α -Ni is the primary precipitate in Nb-Ta amorphous matrix. The atomic size of Nb (146 pm) and Ta (187 pm) are significantly higher than Ni (125 pm) [92]. The smaller size of Ni tends to diffuse more easily in the amorphous matrix during the annealing process and could have locally crystallized. Zhang et al. [36] reported that the FCC Ni was the primary crystallization product in the Nb and Zr

amorphous matrix when $\text{Ni}_{62}\text{Nb}_{33}\text{Zr}_5$ metallic glass annealed at a near crystallization temperature of 607°C . The nano-crystalline $\alpha\text{-Ni}$ in the Nb-Ta amorphous matrix is a composite structure.

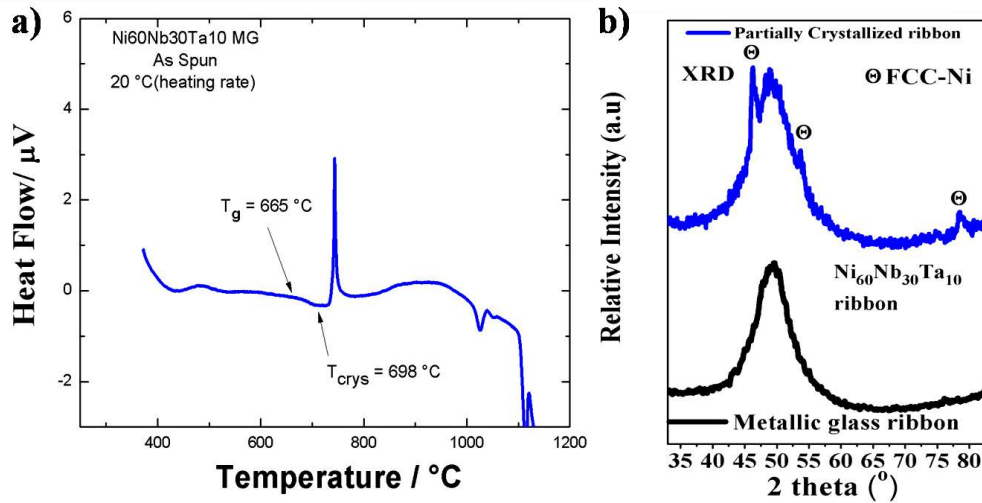


Figure 3.1 (a) DSC traces of as-spun metallic glass, and (b) XRD pattern of as-spun $\text{Ni}_{60}\text{Nb}_{30}\text{Ta}_{10}$ metallic glass and crystallized ribbon at 650°C after 1 hour.

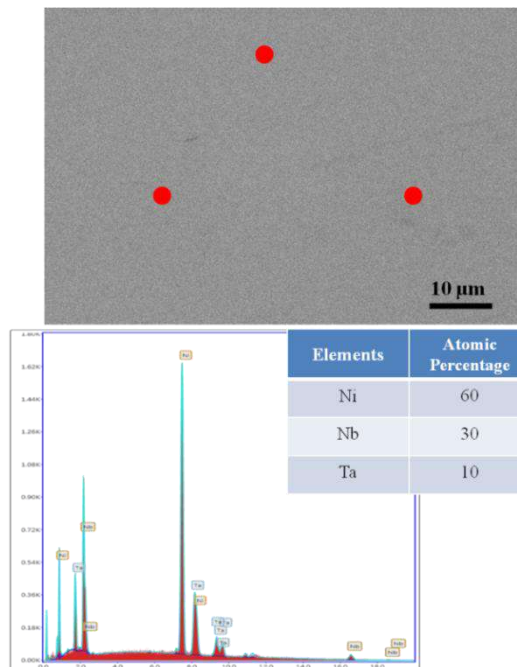


Figure 3.2 SEM images with EDS for as-spun metallic glass

3.2.2 HRTEM analysis of the as-spun and heat treated $\text{Ni}_{60}\text{Nb}_{30}\text{Ta}_{10}$ alloy

The bright field image and SAED pattern of the as-quench metallic glass presents a broad diffuse halo diffraction ring, which is attributed to an amorphous structure, shown in Fig. 3.3 (b). The TEM image (Fig. 3.3(c)) showed the appearance of the crystalline phase when the glass sample was heated at 670 °C for 1 h. The primary crystalline precipitate was the FCC Ni phase with (1 1 1), (2 0 0), (2 2 0) and (3 1 1) planes, as shown in SAED pattern (Fig. 3.2(d) (#00-001-1266)).

3.2.3 XPS studies of Ni₆₀Nb₃₀Ta₁₀ metallic glassy and partially-crystallized ribbon samples before immersion in nitric acid.

The X-ray photoelectron spectroscopy was carried out to study the passive film formed on the surface of the metallic glass and crystallized sample.

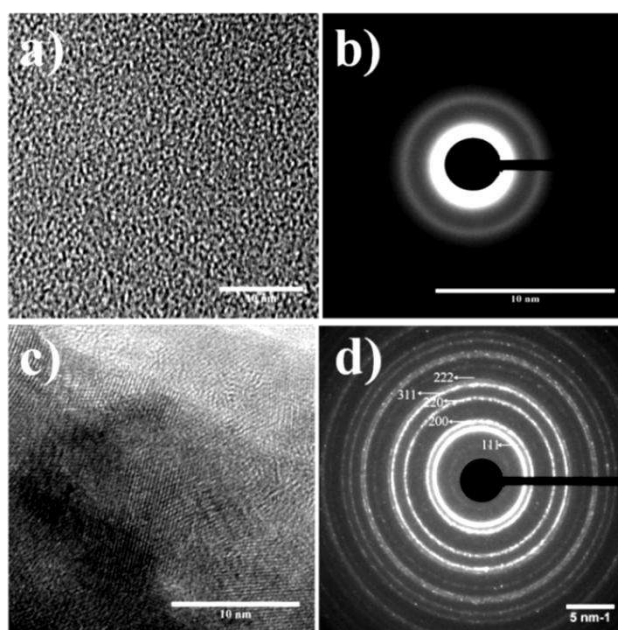


Figure 3.3 (a) TEM image and (b) electron diffraction pattern obtained from the metallic glass; (c) image and (d) electron diffraction pattern obtained from the crystallized counterpart.

High-resolution Ni 2p, Nb 3d, and Ta 4f spectra of the MG surface are shown in Fig.3.4. For the reproducibility of the data, XPS data was recorded on three different places of the sample and consistency in the XPS peaks observed. The Ni 2p spectra (Fig. 3.4(a)) are

Chapter 3

de-convoluted with the 4 sets of the doublet ($2p_{3/2}$ and $2p_{1/2}$) at their corresponding binding energy (Table 3.1). One doublet consisted of intense metallic Ni^0 peak and low-intensity stable oxide (NiO and Ni_2O_3) with satellite peak. Similar observations of the Ni-oxide satellite peak is also reported [93]. The photoelectron peak of Nb 3d and Ta 4f spectra's were de-convoluted using two sets of doublets, one set for metal peak (Nb^0 and Ta^0) and another set for most stable oxide (Nb_2O_5 and Ta_2O_5). High-resolution Nb 3d (Fig. 3.4(b)), and Ta 4f (Fig. 3.4(c)) spectra on the as-prepared (as-spun) metallic glass were exhibited intense metallic peak with low intensity oxide peak. The Nb_2O_5 and Ta_2O_5 oxides are stable penta valence (Nb^{5+} and Ta^{5+}) of Nb and Ta [74].

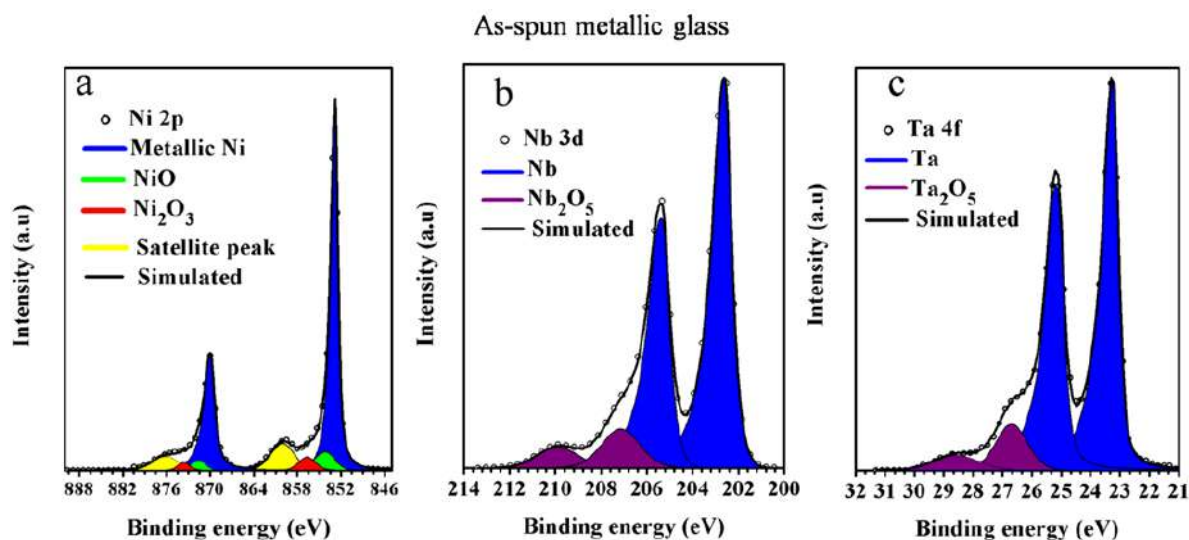


Figure 3.4 (a-c) High-resolution XPS spectra measurement of the as-polished metallic glass: (a) Ni 2p spectra, (b) Nb 3d spectra, and (c) Ta 4f spectra.

Table 3.1 The binding energy of de-convoluted high-resolution XPS spectra and concentration values obtained from the surface for as-spun metallic glass (MG) and as-crystallized ribbon. [85, 94]

Element Spectral line	Oxidation state	Binding energy (eV)	Atomic Concentration (%)
		Metallic glass	Metallic glass
Ni $2p_{3/2}; 2p_{1/2}$	Ni^{3+} (Ni_2O_3)	856.5:873.9	3
	Ni^{2+} (NiO)	854.2:871.6	5

Chapter 3

	Ni ^o	852.7:869.9	39
Nb	Nb ⁵⁺ (Nb ₂ O ₅)	207.1:209.9	8
3d _{5/2} :3d _{3/2}	Nb ^o	202.6:205.3	29
Ta	Ta ⁵⁺ (Ta ₂ O ₅)	26.8:28.8	3
4f _{7/2} :4f _{5/2}	Ta ^o	23.3:25.2	13

The binding energy and atomic concentration (in %) of the metallic and oxide species of Ni, Nb, and Ta are shown in Table 3.1 [85]. The concentration of the species was calculated from the area under de-convoluted peaks, and it was corrected further for the sensitivity factor of the respective photoelectron peaks. As reported, the “error limit” in concentration of the species in XPS quantitative analyses falls within 3-10 % [94]. The concentration (Table 3.1) of the photoelectron peaks showed that the as-prepared metallic glass was comprised a significantly higher fraction of metallic state compared to the oxide state on native film. The XPS analyses on as-spun sample confirmed the very thin native film with underlying the metallic state. The presence of the native oxide film on the Ni-Nb-Ta metallic glass was due to the negative Gibbs free energy for the formation of those oxides (Ni-, Nb- and Ta-oxide) [95-96].

3.2.4 Polarization behaviour of metallic glass and its crystallized alloy

The open circuit potential (OCP) was monitored for 30 min in 11.5 M nitric acid until it stabilized. The potentiodynamic polarization results of the metallic glass and partially crystalline test for both the samples in 11.5 M HNO₃, are shown in Fig. 3.5. The scan rate of 0.166 mV/s is used for the potentiodynamic polarization of the as-spun metallic glass and partially crystallized Ni₆₀Nb₃₀Ta₁₀ alloy. The differences in E_{corr} values for the metallic glass (0.910 V) and crystallized sample (0.780 V) indicated the natures of the passive films are different. The shift of E_{corr} to nobler potential is attributed to the high passivation ability of the metallic glass. No active-passive transition could be observed revealing the spontaneous passivation ability of both the samples.

Chapter 3

The j_{pass} values for the glassy and crystallized sample are 5 and 260 nA/cm², respectively. Significantly lower j_{pass} for the metallic glass is an indicative of the better corrosion resistance. Scully et al. reported that the high corrosion resistance of the glassy structure is attributed to the amorphous nature of the passive film [97]. Generally, the passive film with amorphous structure exhibited high dielectric properties and corrosion resistance [97].

The amorphous passive film was minimizing the fast ions diffusion pathway which further protects the underlying substrate. In contrast, higher j_{pass} of partially crystalline sample is evidenced for lower corrosion resistance in aggressive 11.5 M nitric acid. A low corrosion resistance is attributed to defective passive film on the crystalline counterparts which usually allows high permeability of the electro-active species. Recent research [97] reported that the role of the inter-granular site and ions vacancy defects resulting in the breakdown of the passive film on the crystalline counterparts.

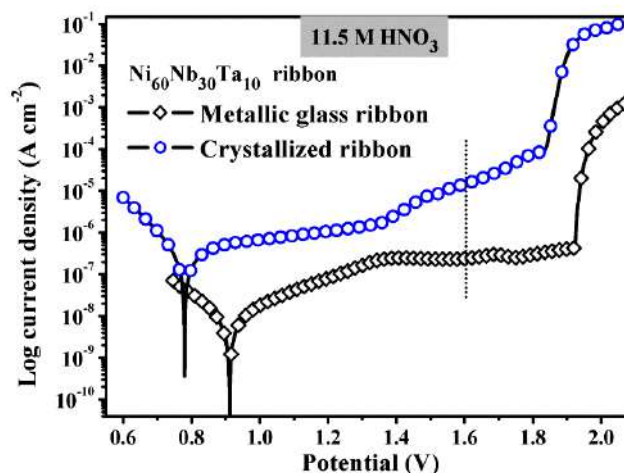


Figure 3.5 Potentiodynamic polarization curves for the metallic glass and crystallized ribbon in 11.5 M HNO₃ environment at room temperature.

The trans-passive potential (E_{trans}) for metallic glass ribbon is 1.92 V (Ag/AgCl) (Fig. 3.4). However, two regions appeared for the partially crystallized sample, a primary E_{trans} at 1.36 V and secondary E_{trans} at 1.82 V. A wider passive region exhibited on the glassy sample

Moreover, the Pourbaix diagram of Ni, Nb, and Ta to compare the passivity breakdown and α -Ni dissolution in 11.5 M nitric acid from partially crystalline sample is included [90]. In Fig. 3.6(a), the dissolution of crystalline Nickel-oxide initiate near 1.4 V when the pH ranges within 3.5 to -2. However, there is no breakdown for Nb₂O₅ and Ta₂O₅ within the same voltage and pH range. Hence, the breakdown and dissolution of the α -Ni are evident based on the Pourbaix diagram.

3.2.5 Electrochemical Impedance Spectroscopy (EIS) analysis.

Electrochemical impedance spectroscopy (EIS) was performed at their corresponding OCP to examine the passivation behavior of as-spun Ni₆₀Nb₃₀Ta₁₀ metallic glass and its partially crystalline alloy in 11.5 M nitric acid. In Fig. 3.7(a), Nyquist plot shows the diameter of the capacitive loop for as-spun MG ribbon increased compared to the crystallized alloy. Thus, indicating that the film resistance is higher on a glassy structure compared to the crystallized state.

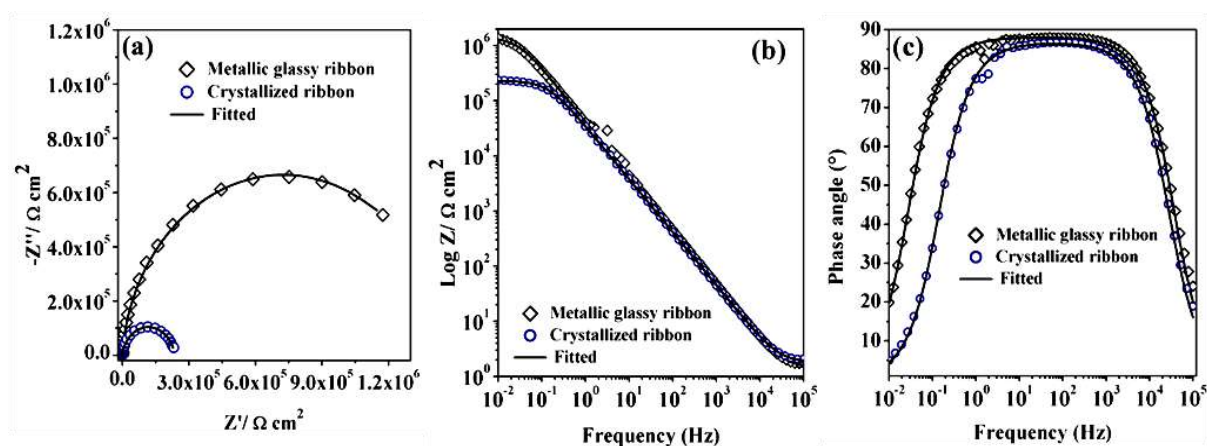


Figure 3.7 Electrochemical impedance spectra for the metallic glass and crystallized ribbon in 11.5 M HNO₃ environment at room temperature in aerated condition: (a) Nyquist plots, (b) Bode modulus, and (c) Bode phase.

The as-spun metallic glass and crystallized samples show a similar pattern of Bode plots (Fig. 3.7(b)) in the lower and middle-frequency ranges. Both the samples present a linear slope at

Chapter 3

about -1, which is a typical response of the capacitive behavior of passive film [88]. The phase angle in the Bode phase plots (Fig. 3.7 (c)) drops to near 0 at the high-frequency region, which is a response of the solution resistance. In the mid-frequency range, the phase angles remain near to 88° in the glassy state, and 83° in the crystallized state, which indicates a characteristic nature of passive film on the surface [88]. The experimental data of the Nyquist, impedance modulus ($\log Z$), and phase angle (φ) plots matched well with the simulated fitted line using the equivalent circuit model [$R_S(R_P|CPE)$]. The validity of the experimental data was further verified by the application of the Kramers-Kronig transformation. The R_S is solution resistance, R_P is polarization resistance, and CPE is the constant phase element. The low χ^2 values for metallic glass and crystallized sample were in the range of 0.004 and 0.003, respectively, indicating the best fit of the experimental data using a proposed circuit. The n of the metallic glass and crystalline sample are 0.96 and 0.93, respectively suggesting that the capacitance values are near to the pure capacitance.

The low solution resistance (R_S is roughly $1.8 \Omega \text{ cm}^2$) for both the sample is negligible when compared to polarization resistance (R_P). The R_P for the metallic glass and the crystallized sample are 3×10^6 and $1.8 \times 10^5 \Omega \text{ cm}^2$, respectively. In comparison to the crystallized sample, the appearance of one order R_P for metallic glass revealed the low charge transfer at the solution/ film interface. The elements in the amorphous structure of the passive film are densely packed compared to that of the crystalline film [73]. Therefore, the diffusion of corrosive electrolytes or ions in the amorphous passive layer is more difficult compared to the crystalline passive film. The stability of the passive film with amorphous structure affects the corrosion resistance of Ni-based metallic glass in concentrate nitric acid. Above studies corroborated that the passive film on the metallic glassy surface significantly improved corrosion resistance compared to crystalline alloy. In contrast, the low polarization resistance for crystalline sample could be attributed to heterogeneity or more defective site present in

the passive film. Electrolytes can diffused through the defective sites and consequently increased ionic conductivity, which makes passive film less-protective. Recent work reported [98] that the non-protective nature of the crystalline passive film is mainly due to presence of nano inter-granular defective sites in the film through which the corrosive electrolytes easily diffused. In presents studies, CPE representing the capacitance owing to the chemically homogeneous passive film with the mono-energetic surface state. The conversion of CPE into the capacitance is described in Eq. 2a and 2b (Chapter 2). Moreover, a low value of capacitance for metallic glass ($3 \mu\text{F}/\text{cm}^2$) compared to the crystallized ribbon ($6.2 \mu\text{F}/\text{cm}^2$), implies a decrease in the reactive area due to better passivation ability in the glassy state. The relatively higher capacitance on the crystalline counterparts is attributed to the inhomogeneous nature of the passive film [88]. These results are consistent with the polarization experiments.

3.2.6 XPS studies of the metallic glass and partially crystallized ribbon after potentiostatic polarization test at 1.6 V for 30 min.

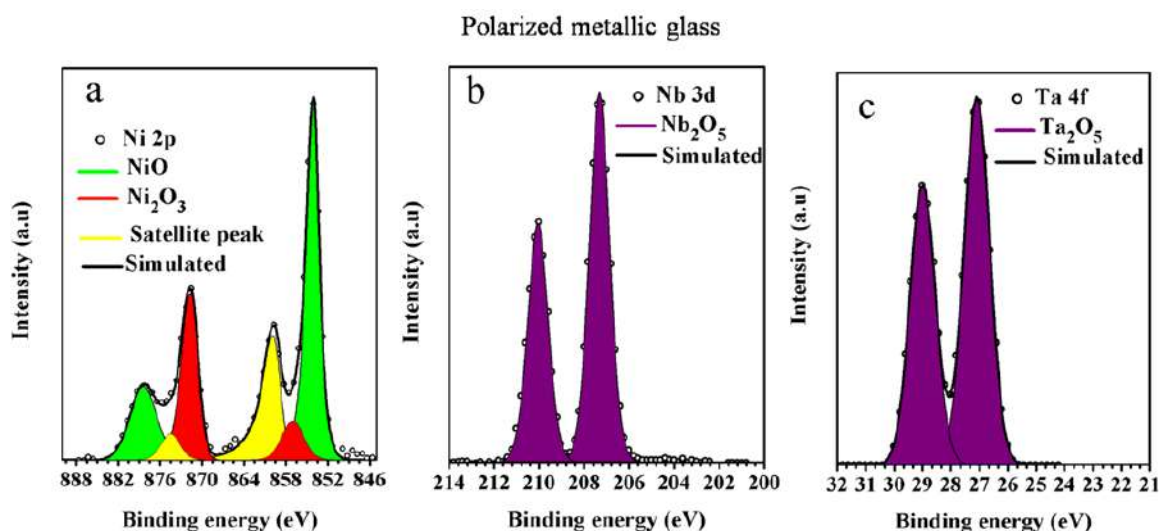
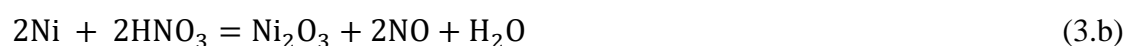


Figure 3.8 High-resolution XPS spectra obtained for the metallic glassy ribbon after 30 min polarization at 1.6 V in 11.5 M nitric acid; (a) Ni 2p, (b) Nb 3d, and (c) Ta 4f.

Chapter 3

The XPS results of the polarized Ni₆₀Nb₃₀Ta₁₀ metallic glassy and crystallized ribbons in 11.5 M nitric acid medium are presented in Fig. 3.8 (a-c) and Fig. 3.9 (a-c), respectively. Table 3.2 showed the binding energy and concentration of stable oxide species after polarization. The passive film on the glassy alloy composed predominately stable Nb₂O₅ (68%) and Ta₂O₅ (26%) with a minor fraction of NiO (4.5%) and Ni₂O₃ (1.5%), as shown in Fig. 3.7 (a-c) and Table 3.2. The XPS results (Fig. 3.7 (b-c)) show the concentration of Nb₂O₅ and Ta₂O₅ increases abruptly on the passivated metallic glass sample. The increment of the Nb₂O₅ and Ta₂O₅ could be attributed due to the dissolution of the Ni ions. The Ni ions dissolve from the surface with the accumulation of the nobler Nb⁵⁺ and Ta⁵⁺, resulting in the enrichment of the Nb₂O₅ and Ta₂O₅ on the surface oxide.

In other accept, such concentration increment can be attributed to the much lower Gibbs free energy formation (ΔG°_f) of Nb₂O₅ (-1758 kJ/mol) and Ta₂O₅ (-1859 kJ/mol) compared to NiO (-230 kJ/mol) and Ni₂O₃ (-189 kJ/mol) in nitric acid solution [95]. Therefore, the metallic state underlying the native film on as-spun glassy alloy (Fig. 3.3b and 3.3c) was preferentially passivated to stable Nb₂O₅ and Ta₂O₅. It was also revealed that the thickness of the passive film increases after polarization. The balance chemical equation has been proposed for the formation of the NiO (Eqs-3.a), Ni₂O₃ (Eqs-3.b), Nb₂O₅ (Eq.-3.c) and Ta₂O₅ (Eq.-3.d), when the metal (Ni, Nb and Ta) reaction with nitric acid solution.



Since all constituent elements randomly spread in the glassy substrate, the high oxygen affinity elements (Nb and Ta) preferentially involved in the passivation reaction, and form a homogeneous passive film. The lower oxygen affinity of Ni accumulated underneath of the

Chapter 3

surface passive film. Qin et al. [63] reported that the enrichment of Ni concentration found underneath of the surface passive film when $\text{Ni}_{57}\text{Nb}_{19}\text{Zr}_{19}\text{Ta}_5$ metallic glass was characterized after the immersion test in boiling 6 M nitric acid.

On the other hand, after polarization at 1.6 V (Ag/AgCl) for 30 min, the spectra on partially crystallized alloy composed of Nb_2O_5 and Ta_2O_5 with significant amount of metallic state of Nb and Ta, as shown in Fig.3.9 (b-c). The surface layer consisted of oxide, with underlying metallic Nb and Ta. This result suggested that the film on partially crystallized sample was relatively thinner than metallic glass alloy and therefore underlying metallic state appeared in the XPS spectra. The Ni 2p spectra is completely absent on the crystallized counterpart (Fig. 3.9(a)).

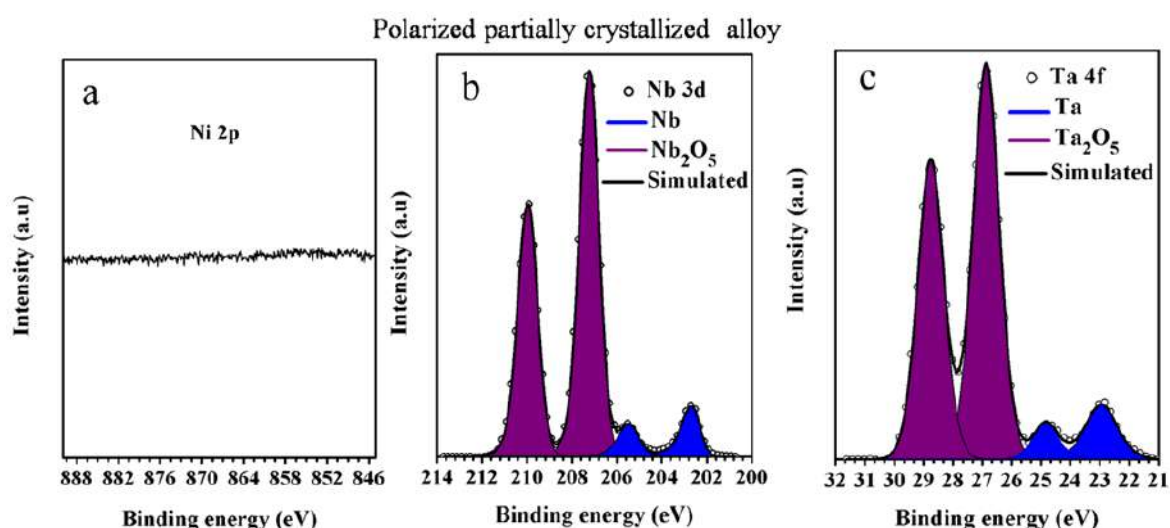


Figure 3.9 High-resolution XPS spectra obtained for the surface of the crystallized ribbon after 30 min polarization at 1.6 V in 11.5 M nitric acid; (a) Ni 2p, (b) Nb 3d, and (c) Ta 4f.

Table 3.2 The binding energy of deconvoluted high-resolution XPS spectra and concentration values obtained from the surface film on metallic glass and crystallized ribbon after polarized at 1.6 V for 30 min in 11.5 M nitric acid.

Element/ Spectral line	Oxidation state	Binding energy(eV)		Atomic concentration (%)	
		Film on Metallic Glass	Film on Crystallized sample	Metallic Glass	Crystallized

Chapter 3

Ni 2p _{3/2} :2p _{1/2}	Ni ³⁺ (Ni ₂ O ₃)	856.9:874.	-	4.5	-
	Ni ²⁺ (NiO)	1854.2:871.8	-	1.5	-
	Ni ⁰	-	-	-	-
Nb 3d _{5/2} :3d _{3/2}	Nb ⁵⁺ (Nb ₂ O ₅)	207.3:210	207.2:209.9	68	60
	Nb ⁰	-	202.7:205.5	-	8
Ta 4f _{7/2} :4f _{5/2}	Ta ⁵⁺ (Ta ₂ O ₅)	26.9:28.9	26.8:28.7	26	26
	Ta ⁰	-	22.9:24.9	-	6

3.2.7 Depth profiling studies of the potentiostatic polarized metallic glass and partially crystallized ribbon.

In Fig. 3.10, the distribution of metallic and oxide states in the passive film on metallic glass alloy and partially crystalline alloy after polarization at 1.6 V (Ag/AgCl) for 30 min are presented as a function of the depth of the film. The sputtering rate for XPS depth profile was calibrated on the silver. The nature of the matrix is different between silver and the samples that are analyzed. Therefore, the sputtering rate is marginally different between the calibration on silver and the samples. As-received passivated glassy alloy (0 min sputtering) comprised predominately of Nb₂O₅ and Ta₂O₅ with a minor fraction of Ni-oxide (Fig. 3.10(a)). The oxide species of Nb and Ta decreased gradually with increasing film depth. However, the metallic species (Ni⁰, Nb⁰ and Ta⁰) was identified at a certain depth of the passive film (Fig. 3.10(a) and (b)) and then increased with the depth of the passive film. For the crystallized sample (Fig. 3.10b), the oxide state of Nb and Ta decreased gradually up to 3 nm sputtering depth and afterwards decreased rapidly along with the depth of the oxide film. The Ni-content is absent from 0 to 3 nm sputtering depth of the film on crystallized counterparts (Fig. 3.10b) which is due to the preferential dissolution of the crystallized α -Ni. After 3 nm sputtering, the metallic Ni has increases with the depth of the film.

In order to understand the dissolution of the α -Ni on the partially crystallized sample, the (oxide + metallic) contribution of each element with respect to the depth of the passive film is

shown in Fig. 3.11. The XPS depth profile (Fig. 3.11b) reveals the absence of the Ni-content in the certain depth of the polarized partially alloys, whereas the Nb and Ta-content is enriched. This studies further confirmed that the selective dissolution of α -Ni in the Nb-Ta amorphous matrix. The thicker film on glassy structure was revealing the feasible growth of the amorphous passive film. This could be due to the enhance bond flexibility at amorphous oxide/amorphous substrate interface [99].

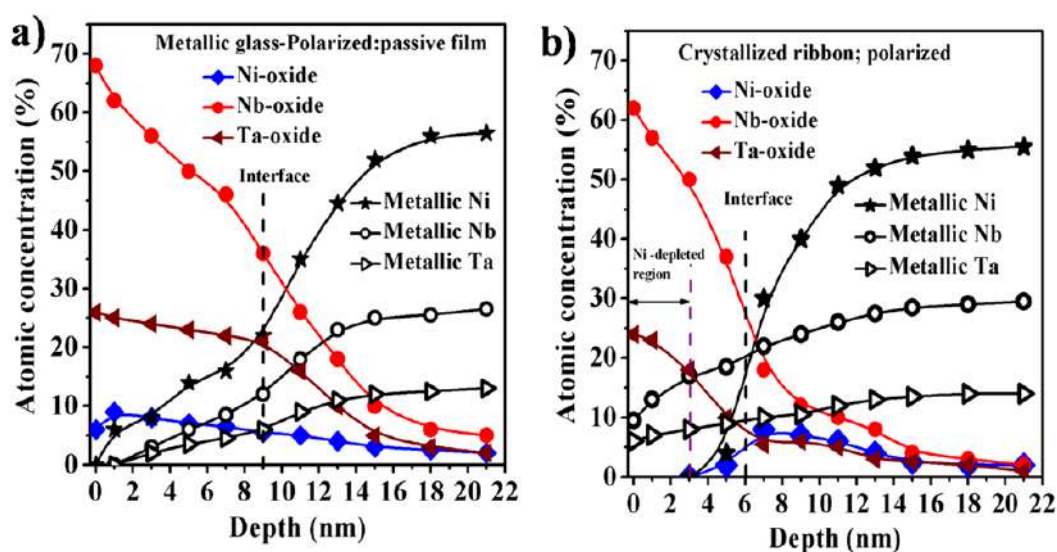


Figure 3.10 XPS depth profile representing the concentration (%) of oxide/metallic states of Ni 2p, Nb 3d, and Ta 4f spectra with depth of the passive film formed after 30 min after polarization at 1.6 V in 11.5 M nitric acid (sputtering time 0 min accounts for the as-received surface) ; (a) for metallic glass, and (b) for crystallized alloy.

The enhance bond flexibility decreased the interfacial energy and also destabilized defects at the film/substrate interface because both film and substrate are structurally amorphous phase [100]. Since an amorphous passive film are densely packed, the growth of the relatively thick passive film occurred by the transport of Nb^{5+} and Ta^{5+} from the glassy matrix towards oxide phase rather than the transport of the oxygen anion (O^{2-}) from the film/solution interface [100]. Easy transports of the Nb^{5+} and Ta^{5+} cations rather than the oxygen anion (O^{2-}) is due to the smaller cationic radius than oxygen anion [92].

Chapter 3

Consequently, the growth rate of the amorphous passive film is effectively reliant on how the cations surmount the oxide/metal interfacial energy barrier [100]. By comparing glassy alloys with its partially crystallized sample, large passive width of metallic glassy sample is due to the relatively thick passive film formed, as evidenced from the XPS depth profiling (Fig. 3.9(a)). A thicker and stable passive film with amorphous structure is known to delay the early stage of trans-passive breakdown [49].

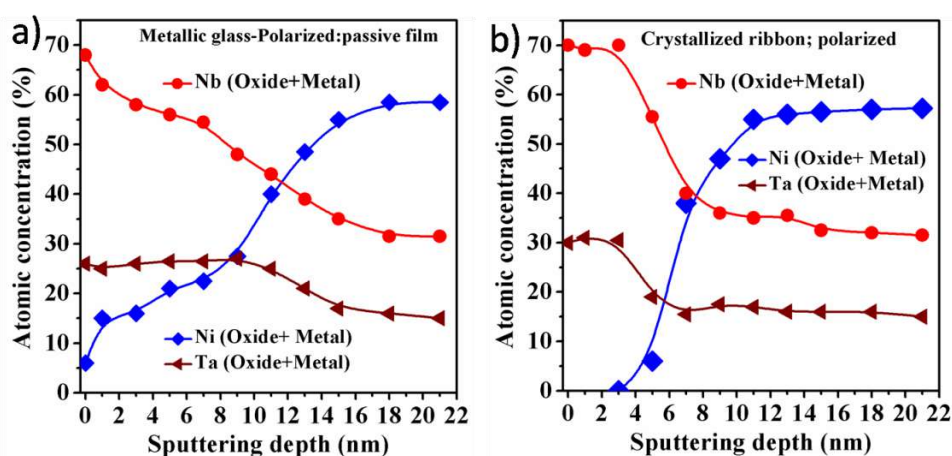


Figure 3.11 XPS depth profile representing the concentration (%) of (oxide + metallic states) of Ni 2p, Nb 3d, and Ta 4f spectra with depth of the passive film formed after 30 min after polarization at 1.6 V in 11.5 M nitric acid; (a) metallic glass, and (b) crystallized alloy.

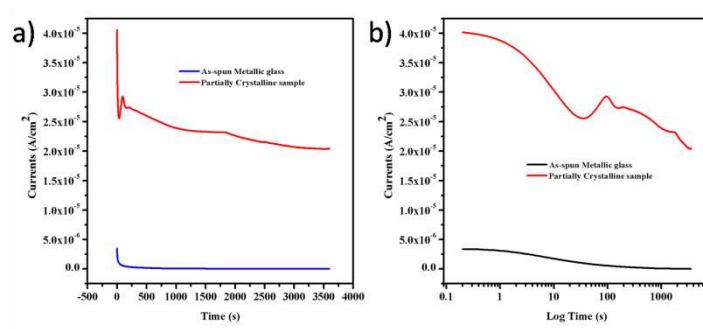


Figure 3.12 Potentiostatic polarization studies in 11.5 M nitric acid at 1.6 V (Ag/AgCl) indicated the change in current with respect to time plotted in; (a) normal scale of time, and (b) logarithmic time.

In addition, to further confirm the easy growth of the passive film on glassy and crystalline structure, the chrono-amperometry results are presented. Fig. 3.12 showed the change of the current on as-spun metallic glass and partially crystallized ribbon with respect to time at 1.6 V/Ag/AgCl. The log time curve (Fig.3.12) shows a significant difference between the as-spun MG and partially crystallized alloys. The current increases for the partially crystallized within the range of 20 s to 300 s may be to the selective dissolution of the α -Ni in 11.5 M nitric acid. However, blue curves showed the good passivation ability of the metallic glass.

3.2.8 Surface morphology of the metallic glass and partially crystallized ribbon.

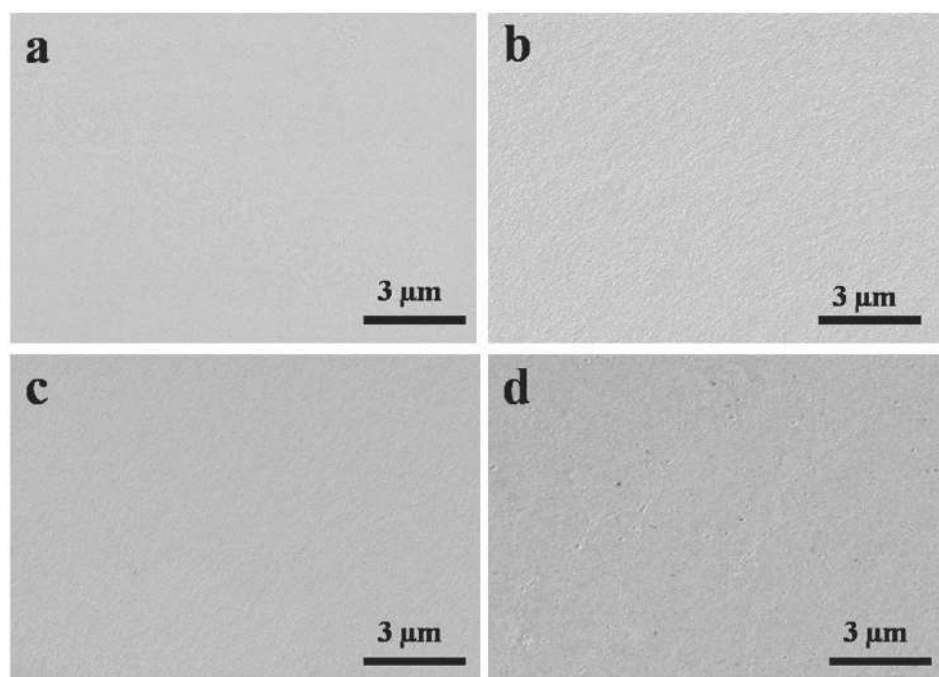


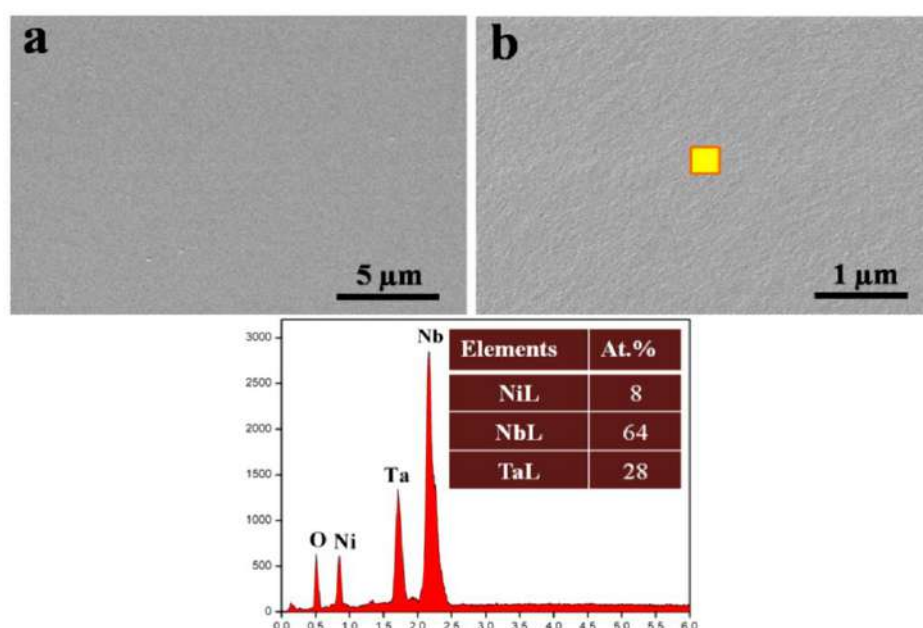
Figure 3.13 Surface morphology of the metallic glass and partially crystallized sample before and after immersion test for 7 days in 11.5 M nitric acid; (a-b) before immersion-(a) as-spun metallic glass, (b) partially crystallized sample. (c-d) after immersion (c) metallic glass, and (d) partially crystallized sample.

To provide a clear understanding of the depletion of the α -Ni on the crystalline counterparts, the survey scan for successive sputtering time, is shown in Fig.3.11. The Ni 2p

Chapter 3

spectra are not observed at 0, 1 and 3 min sputtering. However, after 5 min sputtering, less fraction Ni content was observed. After 11 min sputtering, high concentration of the Ni-content was observed, as shown in Fig.3.11.

The SEM analyses on the as-spun and partially crystallized ribbon before and after immersion in the 11.5 M nitric acid for 7 days are presented in Fig.3.13. Insignificant changes in the morphology is observed on the surface of the as-spun metallic glass (MG) and partially crystallized sample before immersion (Fig. 3.13a-b). Due to the very smaller sizes, such crystalline grain is visible in the SEM morphology. Smooth surface was observed on the as-spun ribbon after immersion test in 11.5 M nitric acid, indicating the stable passive film formation on the metallic glass sample. However, the surface of the partially crystalline sample is marginally rougher compared to the as-spun metallic glass, indicating the passive film is inferior in nature. The less stable nature of the passive film formed on partially crystalline sample could be due the presence of the structural heterogeneity (α -Ni in amorphous matrix). The α -Ni could dissolved from the matrix, resulting in the rough surface. After polarization at 1.6 V (Ag/AgCl) for 30 min in 11.5 M nitric acid, the surface of the glassy sample was characterized by FESEM techniques, as shown in Fig. 3.14.



Chapter 3

Figure 3.14 FESEM morphology of the surface after 30 min polarization at 1.6 V (Ag/AgCl) in 11.5 M nitric acid: (a-b) images of the passive film formed on the metallic glass.

The smooth morphology (Fig. 3.14(a-b)) indicated that the formation of the uniform passive film on the metallic glass ribbon. The concentrations of the Ni, Nb, and Ta obtained by EDS point analysis are consistent with the XPS studies (Table 3.2). However, the non-uniformity attack observed on the partially crystallized sample (Fig. 3.15(a-b)) which could significantly affect the corrosion resistance and passive film property.

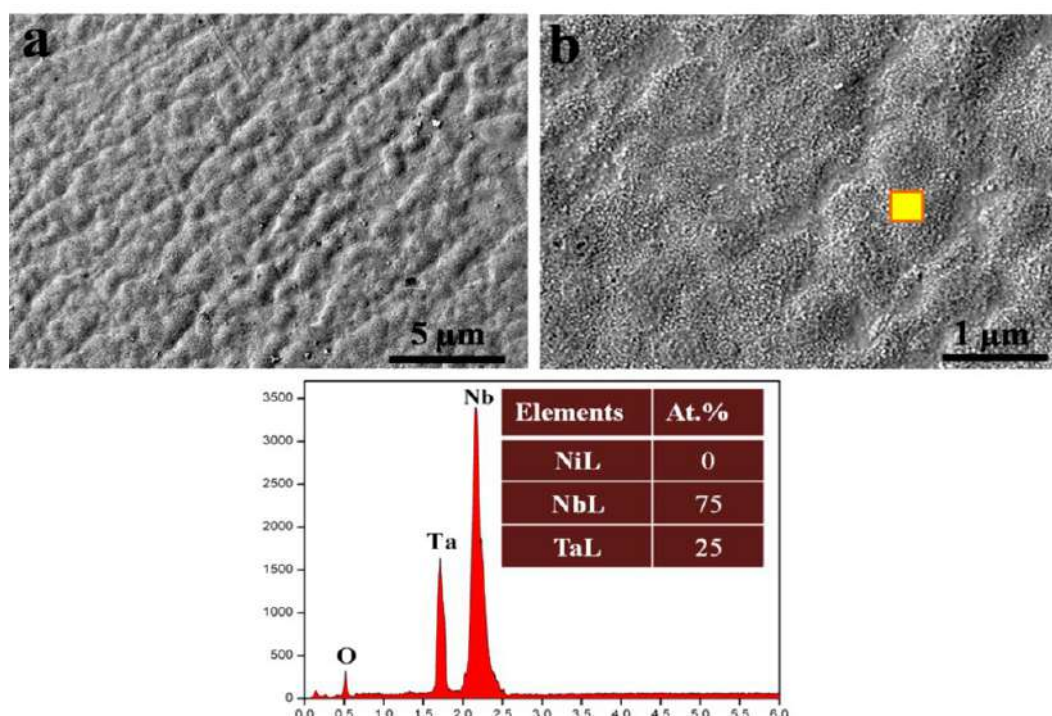


Figure 3.15 FESEM morphology of the surface after 30 min polarization at 1.6 V (Ag/AgCl) in 11.5 M nitric acid: (a-b) images of corroded surface on crystallized ribbon.

The schematic diagram to provide a better understanding of the film formed on the glassy and partially crystallized alloy sample is shown in Fig. 3.16. The corrosion properties are the surface phenomenon, and thus, the degradation of the materials initiates from the surface. The metallic glass forms homogeneous and protective passive film even in severe nitric acid environment (Fig. 3.16a). In contrast, the surface heterogeneity is the preferential

Chapter 3

site for the corrosion attack and presence of the small crystalline heterogeneity (like α -Ni) in the amorphous matrix could initiate the degradation process in 11.5 M nitric acid (Fig. 3.15b). At the initial stage of the polarization, surface try to polarized, whereas the crystalline Ni are dissolving to the solution in forms of ions Ni^{2+} and Ni^{3+} . The dissolution of the Ni ions breaks the passivity and forms the gap in the passive film through which the corrosive nitrate ions diffuse in the film. The Nb and Ta pentaoxide are aggregated to form the island like morphology, as shown as in SEM Fig. 3.15b. Therefore, once the degradation of the crystalline phase (or heterogeneity, α -Ni) in the amorphous phase is initiated, the passive film areee not protective. The absence of α -Ni and its oxide up to 3 nm depth (XPS depth profile- Fig. 3.10(b), suggested that reactive Ni-cation diffused from the metal/oxide interface to the film/solution interface.

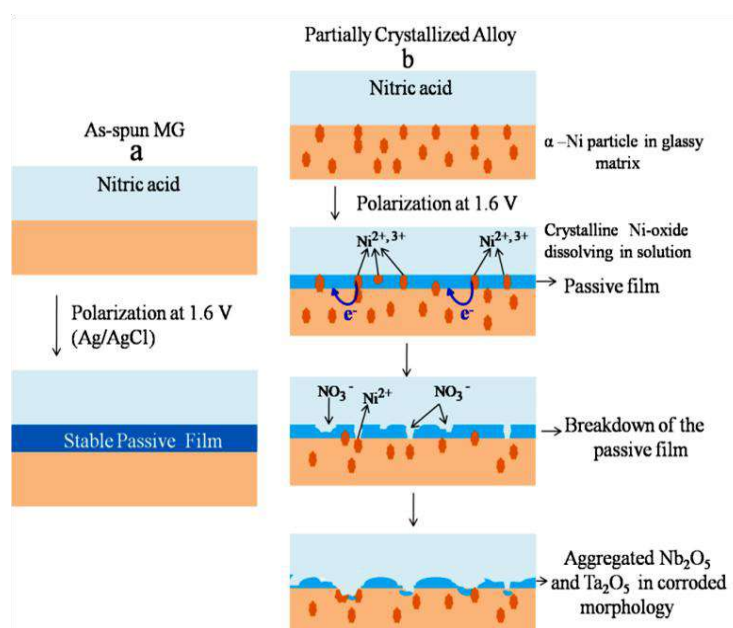
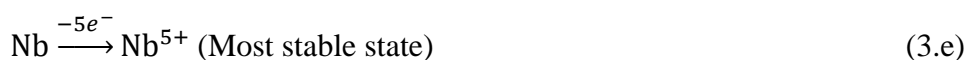


Figure 3.16 Schematics diagram of the passive films formed on metallic glass and partially crystallized alloy in 11.5 M nitric acid representing: (a) Passive film on surface of the glassy alloy enriched with stable Nb_2O_5 and Ta_2O_5 with small amount of NiO and Ni_2O_3 , (b) The surface of the crystallized ribbon undergoes attacked and crystalline Ni-oxide dissolved

Chapter 3

completely from the surface. The agglomerated surface layer consisted of oxide and traces metallic fraction of Nb and Ta.

Generally, the passive films on crystalline counterparts are associated with grain boundaries, ion vacancies, and interfacial defect which provide an easy pathway for inward diffusion of corrosive electrolytes and dissolve less noble metal. As crystalline α -Ni and its oxide dissolved in the nitric acid solution, subsequently the enrichments of the Nb-oxide and Ta-oxide were favoured. Moreover, due to the lower mobility of the Nb and Ta cations as compare to Ni-cation, the dissolution of Nb and Ta oxide are much slower compared to Ni-oxide. Comparing the earlier results (table 1) and after polarization (table 3.2) test, the marginal change in the binding energy of the crystallized sample can be an indication of slow dissolution of the Nb and Ta oxide. To understand the passivation, and corrosion mechanism of the glassy alloy and its crystallized counterparts in nitric acid solutions, the electron transfer process can be represented in Eqs. 3.e and 3.f, as given below.



Initially, the surfaces of the alloys are covers with predominantly metallic state and small amounts of oxide state. When the metal are exposed in an oxidizing nitric acid environment, the metallic state of Nb changed through the electron transfer process to the most stable oxidation state Nb^{5+} (i.e., Nb_2O_5). Similar steps are also followed for Ta oxidation to the most stable oxidation state of Ta^{5+} (Ta_2O_5). Mixtures of Nb_2O_5 and Ta_2O_5 with the metallic state (Nb° and Ta°) were identified on the crystallized sample by the XPS analyses (Fig. 3.9 (b-c)). Since the higher passivation ability (low j_{pass} value-Fig. 3.5) of the glassy structure, only the most stable penta-oxide state of Nb_2O_5 and Ta_2O_5 oxides were identified in XPS results (Fig. 3.8(b-c)).

The reaction schemes for anodic dissolution of the α -Ni and its oxide have been presented in various models [61]. The defective film on partially crystallized alloys promote easy trans-passive dissolution in nitric acid medium. Similarly, the dissolution of Ni involved mass and electron transfers by adsorbed the surface active anions A^- ($A^- = NO_3^-$ - Eq. 3.g) at the reactive interface [61].



The electrochemical reactions shown in an eq. (3.h) and (3.i) involves the absorbed intermediate species $Ni-A_{acid}$, whereas K_1 and K_2 are rate constants.

3.2.9 Semiconducting behaviour of the passive film formed on $Ni_{60}Nb_{30}Ta_{10}$ glass and its crystallized alloy.

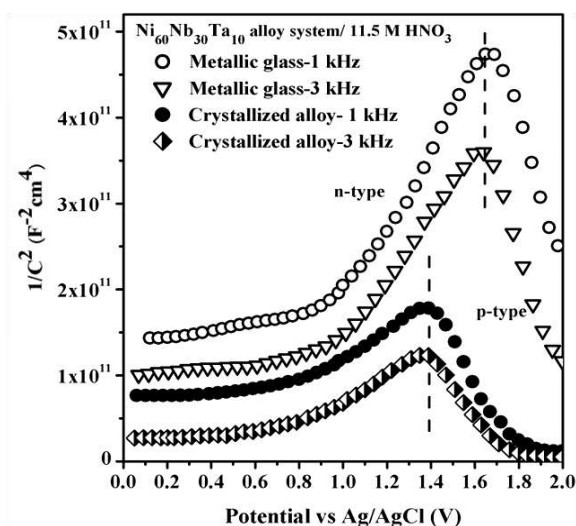


Figure 3.17 Mott-Schottky plots of $Ni_{60}Nb_{30}Ta_{10}$ glassy and crystallized alloy ribbon in 11.5 M HNO_3 environment at room temperature.

The Mott-Schottky plots of the metallic glass and partially crystallized sample in 11.5 M nitric acid environment is shown in Fig. 3.17. For each experiment, the space charge capacitance was measured against the applied potential at the frequency of 1 kHz and 3 kHz.

Chapter 3

This analysis provides information about the electronic structure of passive film such as type of semiconductivity, defect structure, flat band potential, etc. The higher flat band potential of as-spun metallic glassy ribbon at both frequencies indicates a higher passivation ability of the glassy structure than that of crystallized structure.

Table 3.3 Mott-Schottky analyses and the defect densities of passive film form on glassy and crystallized alloy at the frequency of 1 kHz and 3 kHz in 11.5 M HNO₃ environment at room temperature.

Alloy condition	Flat band potential		Defect density			
			Donor density (cm ⁻³)		Acceptor density (cm ⁻³)	
	1 kHz	3 kHz	1 kHz	3 kHz	1 kHz	3 kHz
As-spun metallic glass	3.7	3.6	6.2x 10 ¹⁸	8.1x 10 ¹⁸	6.8x 10 ¹⁸	8.7x 10 ¹⁸
Partially Crystallized alloy	2.2	2.15	2.4x 10 ¹⁹	5.5x 10 ¹⁹	3x 10 ¹⁹	6x 10 ¹⁹

The positive and negative slope in Mott-Schottky plots revealed that the formation of the n and p-type semiconducting film, respectively. At the both frequency, the as-spun metallic glass showed as n-type semiconductivity up to 1.68 V (Ag/AgCl) and then changed into p-type semiconductivity in nitric acid medium. However, the crystalline sample exhibited first n-type semiconductivity up to 1.38 V (Ag/AgCl) and thereafter changed into p-type semiconductivity. The formation of n-type semiconductor is attributed to the passive film enriched with Nb₂O₅ and Ta₂O₅, while, p-type semi-conductivity may be attributed to underlying Ni-oxide [101]. Bondarenko et al. [102] reported that the transition from n- to p-type was related to the various oxidation states at the metal/film and the film/electrolyte interface. In general, the oxide film on the metals (e.g., Nb, Ta, Zr, Ti, Cr, etc.) exhibited n-type semiconductor, while Ni, Fe oxides formed p-type semiconducting [85]. On the other hand, both the metallic glass and crystalline alloy exhibited relatively higher slope of space charge capacitance (1/C²) at 1 kHz compared to 3 kHz (Fig. 3.17). The reason for a higher slope of the passive film is attributed to the higher impedance at the lower frequency. The

donor density (N_d) (for the n-type semiconducting film) and acceptor density (N_a) (for the p-type semiconducting film) were estimated considering the dielectric constant of 60 for mixed Nb_2O_5 and Ta_2O_5 oxide, as presented in Table 3. Franco et al. [103] reported the high dielectric value of 60 for the mixed oxide of Nb_2O_5 and Ta_2O_5 . The majority of the defect density in n- and the p-type semiconducting film is oxygen and metal cation vacancies, respectively [85]. At both frequencies, the defect densities (N_d and N_a) of the semiconducting film on the metallic glass are significantly lower than that of the crystallized sample which further indicates the stability of the amorphous passive film. The thicker passive film with very low defect density prevents the diffusion of electrolyte to the film and dissolution of cations into the solution, therefore improving the corrosion resistance. In contrast, significantly higher defect N_d and N_a observed for partially crystallized alloy compared to the glassy alloy revealed that the less protective nature of the passive film. The change of the Mott-Schottky slope to p-type at 1.38 V (Ag/AgCl) for the crystalline alloy is corroborated with the primary breakdown appearing at the similar potential in potentiodynamic curve (Fig. 3.5). The change of the n-type to p-type slope at higher anodic potential is associated with the breakdown of the film followed by the generation of more cation vacancies [85]. The dissolution of the nano-crystalline Ni-oxide has increased cation vacancies, which is reflected in a negative slope with high acceptor densities in Mott-Schottky plots (Fig. 3.15). Sikora et al. [101] reported that Ni^{2+} , $3+$ ions are incapable of the annihilation of cation vacancies, resulting in the more defective passive film on crystallized counterparts. The defective natures of passive film form on the crystalline structure are reported by using TEM [104].

3.3 Summary

The major conclusions which can be drawn from the present study are as follows:

- a. At 650 °C, after the crystallization in a vacuum (10^{-6} mbar), nano-crystalline α -Ni phase is formed in the Nb-Ta amorphous matrix. The XPS results of as-spun metallic glass

Chapter 3

showed the presence of a very thin layer composed of Ni, Nb and Ta oxides at the surface with the underlying metallic state. After crystallization, the oxide fractions relatively increased on the surface compared to that of metallic glass.

- b. Electrochemical impedance spectroscopy and potentiodynamic anodic polarization studied confirmed metallic glassy ribbon exhibited higher corrosion resistance compared to its crystalline alloy. The formation of crystalline α -Ni phase in the amorphous matrix decreased corrosion resistance.
- c. The XPS results indicated that the surface of a passive layer on the glassy alloy comprised predominately of Nb_2O_5 and Ta_2O_5 with a small fraction of NiO and Ni_2O_3 . For crystallized ribbon, the crystalline Ni-oxide dissolved resulting to corroded surface with both oxide and trace of metallic Nb and Ta.
- d. The Mott-Schottky analysis revealed that the passive film on metallic glass and crystallized ribbon exhibited first n-type and then changed into p-type semiconducting properties in a nitric acid medium. The passive film on metallic glass is less defective (lower N_d and N_a), while a highly defective passive film (higher N_d and N_a) observed on the crystallized sample.

4 Oxidation behavior of Ni-based metallic glassy alloys

This chapter deals with the investigation on the oxidation behaviour of Ni-based metallic glassy alloys of both amorphous alloys ribbon ($\text{Ni}_{60}\text{Nb}_{40}$ and $\text{Ni}_{60}\text{Nb}_{30}\text{Ta}_{10}$) at 450 and 550 °C in air environments using different experimental techniques, including XPS, AFM and FESEM, etc. The surface oxide layers formed at 450 °C and 550 °C were characterized using XPS. The film formed on the $\text{Ni}_{60}\text{Nb}_{40}$ amorphous alloy at 450 °C comprises predominantly of Nb_2O_5 oxide, while $\text{Ni}_{60}\text{Nb}_{30}\text{Ta}_{10}$ metallic glass are enriched with Nb_2O_5 and Ta_2O_5 . In contrast, the oxide layer formed, both 550 °C oxidized sample is composed of only NiO and Ni_2O_3 where other oxides are depleted. The thermodynamic and kinetic roles in the oxidation and also the diffusion of Ni during the oxidation-induced crystallization of the glass at 550 °C in air medium; the film thickness and its correlations to the oxidations behaviors of the $\text{Ni}_{60}\text{Nb}_{40}$, and $\text{Ni}_{60}\text{Nb}_{30}\text{Ta}_{10}$ metallic glasses are also described. The oxidation properties including oxidation kinetics, surface morphology, and oxide film thickness for $\text{Ni}_{50}\text{Nb}_{25}\text{Zr}_{25}$ metallic glass at 200 and 400 °C oxidation temperature are elaborated in details in this chapter.

4.1 Introduction:

The binary eutectic alloys based metallic glass of $\text{Ni}_{60}\text{Nb}_{40}$, is two eutectic elements combined an early late transition metal being formed by fast cooling. The addition of the refractory elements such as Ta, and Zr relatively decreased cooling rate and enhanced glass forming ability. These systems show that there is a pronounced difference in electro negativity between the Ni, Nb, (or Ta and Zr) species. In an oxidizing (air) environment this results in the preferential oxidation of one of the species, partitioning and early crystallization even slightly below the glass transition temperature. In general, based on the thermodynamic facts below the glass transition; kinetics must slow down to improve resistance against

Chapter 4

oxidation and crystallization. Moreover, the good multi-component glass forming systems are highly dense random-packed, and viscous in nature. In such system, the sluggish kinetics is the most important factor that impedes the nucleation and growth of crystals [105]. In addition, sluggish kinetics is one the main factor that not only controls the thermal stability in the subject of resistance to crystallization, but it also controls the resistance to the rapid oxidation.

However, recently, air-oxidation below the glass transition temperature has been adopted for the development of amorphous oxide film with a thickness of a few tens of nanometer [49]. Nie et al. studied [49] the effect of the thermally grown amorphous film on the corrosion behavior of the Zr-based metallic glass in saline environment. Oxidation of $Zr_{64}Cu_{16}Ni_{10}Al_{10}$ metallic glass at 320 °C results in a thick amorphous oxide film. This oxide film exhibited high passivation ability in 0.5 M NaCl environment [49]. Apart from the corrosion application, the amorphous oxide film can be used for several other applications such as semiconductor, catalyst, DRAM, MEMS and nano-scale tri-biological, etc [76, 106].

However, the $Ni_{60}Nb_{40}$ system has been selected as an example to investigate the effect of the addition of atoms with large size mismatch (e.g., Ta and Zr) on the air-oxidation. These metallic glasses of Ni-Nb-Ta, and Ni-Nb-Zr systems were found to exhibits higher glass transition, primary crystallization temperature and also exhibits larger super cooled liquid region [34]. These properties are common to the Ni-Nb based glassy system and have a great potential for practical importance, making it a technology relevant refractory alloy glass material. In this chapter, the thermodynamic and kinetic roles played in the inverse oxidation and also the diffusion Ni during the oxidation-induced crystallization of the glass at elevated temperature in air is examined.

4.2 Results and discussion:

4.2.1 Oxidation behaviour of as-spun and thermally oxidized Ni₆₀Nb₄₀ ribbon.

4.2.1.1 Oxidation kinetics and phase analyses of Ni₆₀Nb₄₀ amorphous alloy.

A 50 μm thick Ni₆₀Nb₄₀ amorphous ribbon sample was prepared by melt spinning as described in method and materials section, in the previous chapter. Differential scanning calorimetry (PerkinElmer, Germany) measurement was carried out at the heating rate of 20 $^{\circ}\text{C}/\text{min}$ to confirm the crystallization onset temperature (T_x) at 668 $^{\circ}\text{C}$. The oxidation studies of as-spun Ni₆₀Nb₄₀ ribbon were carried out at 450 and 550 $^{\circ}\text{C}$ (below T_x) for 5 h in a tubular furnace under air environment. The heating rate (20 $^{\circ}\text{C}/\text{min}$) was maintained till the attainment of the oxidation temperatures. The isothermal thermo-gravimetric analysis (TGA) was carried out to understand the oxidation kinetics of Ni₆₀Nb₄₀ ribbon at 450, and 550 $^{\circ}\text{C}$ in oxygen-argon gas (20% O₂) environment with a flow rate of 20 ml/min for 5 h.

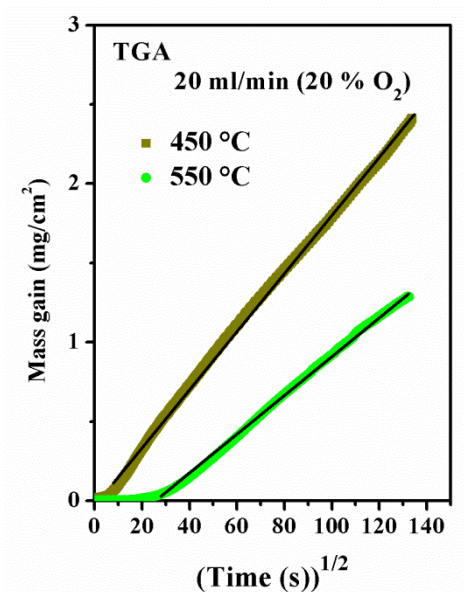


Figure 4.1 (a) Isothermal thermogravimetric analysis (TGA) of the as-spun Ni₆₀Nb₄₀ ribbon for 5 h under 20% O₂ environment at 450 $^{\circ}\text{C}$ and 550 $^{\circ}\text{C}$.

The parabolic oxidation equation is given as below,

Chapter 4

$$(\Delta m/A)^2 = kt \quad (4. a)$$

where Δm , k , A , and t are mass gain data (in mg), sample exposed area (cm^2), rate constant ($\text{g}^2/\text{cm}^4/\text{s}$), and exposed time (s) in isothermal condition, respectively. Better techniques to cross-check the parabolic nature of the oxidation curve is to convert oxidation time to square root of the time as shown mathematically below.

$$(\Delta m/A) = (kt)^{1/2} \quad (4. b)$$

$$(\Delta m/A) = k_p t^{1/2} \quad (4. c)$$

whereas k_p is parabolic rate constant, and the square root of the x-axis the plots give linear slope.

After converting the X-axis (Exposed time) to the square root of (Exposed time)^{1/2}, the parabolic region of the experimental data for both oxidation temperature, changes to single the linear line except onset region. The mass gain of Ni₆₀Nb₄₀ amorphous ribbon at 450 and 550 °C for 5 h (18000 s), is shown in Fig. 4.1. This indicated that the oxidation of Ni₆₀Nb₄₀ metallic glass at 450 °C and 550 °C predominately followed the single parabolic rate laws. However, the onset oxidation (initial oxidation) at 450 °C and 550 °C is not parabolic in nature and that could be attributed due to the dissolution of the oxygen in the glass metal matrix. The k_p values given in Table 4.1 were obtained from the best linear fitting (shown as a solid line in Fig. 4.1) of the obtained experimental data.

The oxidation of Ni₆₀Nb₄₀ amorphous alloy at 450 °C, the parabolic oxidation stage is observed from 21.2 s^{1/2} to 134.16 s^{1/2}. The rate constant at 550 °C was marginally higher than the 450 °C oxidation (Table 4.1). However oxidation of Ni₆₀Nb₄₀ amorphous alloy at 550 °C, the parabolic oxidation stage is observed from 9 s^{1/2} to 21.2 s^{1/2} to 134.16 s^{1/2}. The k_p values for both stages (Table 4.1) suggested that the mass gain at 550 °C was higher than 450 °C. The multiple-stage parabolic-rate law kinetics was reported for the oxidation of the other Ni-based

Chapter 4

metallic glassy alloys [74]. The two stage parabolic rate law, however the 1st stage is attributed to the

Table 4.1 Parabolic rate constants and R^2 (fitting accuracy) for the oxidation of $Ni_{60}Nb_{40}$ amorphous ribbon in 20 % dry oxygen (k_p : in $g^2/cm^4.s$).

Oxidation stage	$Ni_{60}Nb_{40}$ AR	
	450 °C	550 °C
Parabolic stage	k_p	2×10^{-10}
	R^2	0.99

interfacial metal and gas reaction which developed the initial oxide film on the surface. After forming the initial oxide layer on the surface, the rate law changed the slope, which indicated the oxidation is controlled by the solid-state diffusion.

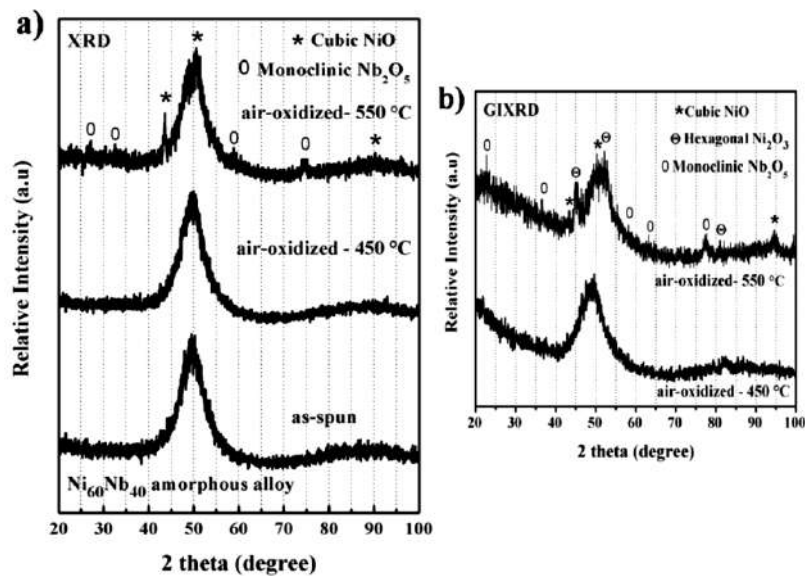


Figure 4.2 (a) XRD pattern of as-spun, 450, and 550 °C thermally oxidized $Ni_{60}Nb_{40}$ ribbon sample for 5 h, (b) GIXRD traces of the 450 and 550 °C thermally oxidized ribbon for 5 h .

The GIXRD and XRD techniques were used to characterize the phase of the surface oxide film and its underlying substrate. In the Fig.4.2, the thermally oxidized $Ni_{60}Nb_{40}$ amorphous ribbon at 450 °C exhibit only a broad halo peak, indicating the sample retained its

amorphous structure as similar to that of as-spun ribbon. On the other hand, the GIXRD and XRD patterns of thermally oxidized ribbon at 550 °C exhibited few Bragg peaks on the amorphous hump which are corresponding to the cubic NiO (JCPDS No #01-089-7130), Ni₂O₃ (JCPDS No #00-014-0481) and Nb₂O₅ (JCPDS No #00-037-1436).

4.2.1.2 Surface morphology of thermally oxidized metallic glass

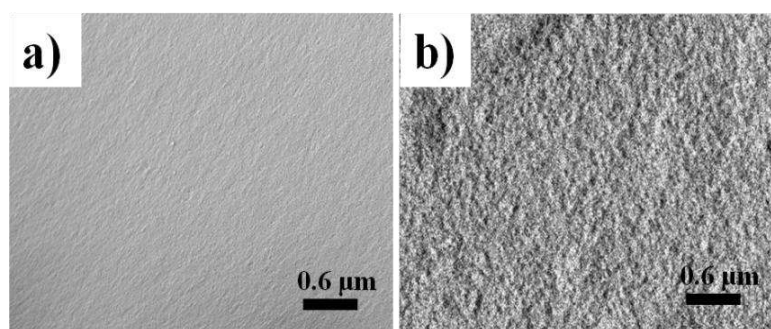


Figure 4.3 Images (a-b) are FESEM morphologies of the surface of air-oxidized Ni₆₀Nb₄₀ ribbons for 5 h; (a) at 450 °C and (b) at 550 °C.

After oxidation at 450 and 550 °C, the morphology of both Ni₆₀Nb₄₀ were characterized by SEM, as shown in Fig.4.3. Relatively smooth morphology observed for the oxidation at 450 °C, suggests that the protective growth of the oxide film. In contrast, speckled contrast observed for the air-oxidized sample at 550 °C and that indicated the formation of a relatively thick oxide layer when compared to 450 °C oxidation.

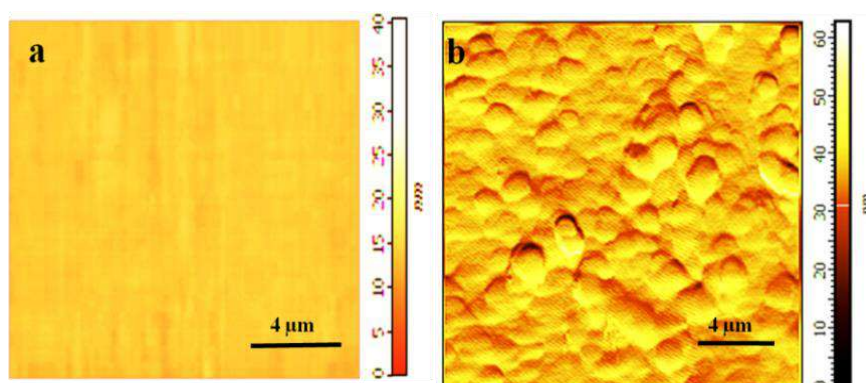


Figure 4.4 Images (a-b) are AFM surface topology of the surface of air-oxidized Ni₆₀Nb₄₀ ribbons for 5 h; (a) at 450 °C and (b) at 550 °C.

The results of the AFM analysis carried out in contact mode are shown in Figs. 4.4 (a-b). The oxide film topography was characterized by atomic force microscopy (AFM) to understand the change of the surface and roughness during the oxidation, as shown in Fig. 4.4. The oxidation at 450 °C, the sample showed a smooth topology with rms roughness within 1 nm. However, the oxidation at 550 °C, various dimples-like features shape appeared on the surface of the oxidized Ni₆₀Nb₄₀ ribbon with the rms roughness of about ~4.5 nm as shown (Fig. 4.4(b)). The appearance of the dimple shape feature for the oxidation at 550 °C could be attributed to the agglomeration of oxide particles. Moreover, the rough surface on the Ni₆₀Nb₄₀ amorphous alloy at 550 °C is due to the un-protective growth and agglomeration of oxide particles. The speckled contrast appeared in FESEM (Fig. 4.3 (b) which could be correlated to the dimple like feature.

4.2.1.3 XPS analyses before and after thermally oxidized Ni₆₀Nb₄₀ amorphous alloy at 450 °C and 550 °C.

The X-ray photoelectron spectroscopy a technique was used to characterise the oxide and metallic species. The high-resolution Ni 2p and Nb 3d photoelectron spectra were recorded on the surface of the as-spun Ni₆₀Nb₄₀ amorphous ribbon, as shown in Fig.4.5. The high-intensity photoelectron peaks were de-convoluted at respective binding energies.

The Ni 2p (Fig. 4.5(a)) spectra is de-convoluted with 4 set of doublets at their corresponding binding energy, whereas first sets of doublets correspond to the metallic Ni. The 2 sets of doublets correspond to the NiO and Ni₂O₃, and other one accounts for satellite peak. However, photoelectron a line of Nb 3d spectra is de-convoluted with four sets of doublets, whereas the first one corresponds to the metallic Nb, and other three sets of doublets is corresponds to the NbO, Nb₂O₄, and Nb₂O₅ (Fig. 4.5(b)). Both the spectres exhibit high-intensity metallic peaks with small amounts of their sub-oxide and the stable oxide. The appearance of the small amounts of the oxide on the as-spun surface could be due to the

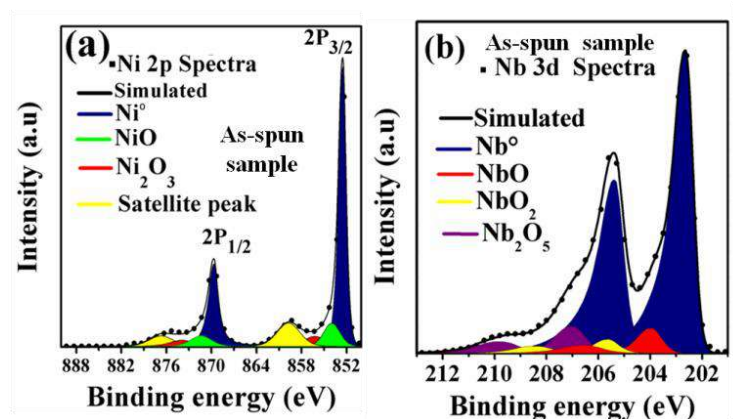


Figure 4.5 High-resolution XPS spectra of the surface, of the as-spun Ni-Nb amorphous alloy sample; (a) surface Ni 2p spectra (b) surface Nb 3d spectra.

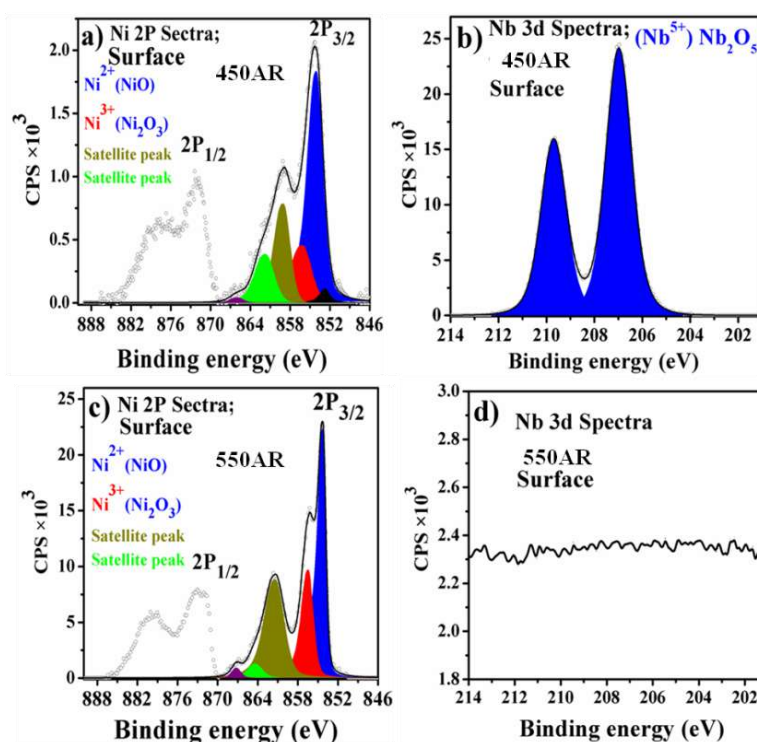


Figure 4.6 High-resolution XPS spectra of the surface, of the 450 °C air-oxidized sample; (a) surface Ni 2p spectra (b) surface Nb 3d spectra. High-resolution XPS spectra of the surface of the 550 °C air-oxidized sample; (c) Surface Ni 2p spectra (d) absence of Nb 3d spectra at the surface.

formation of the air-form native layer during handling the sample. The binding energy of the all the elements in metallic and cationic species are given in the Table 4.2.

Chapter 4

To understand the variation of chemical composition upon thermal oxidation at the different oxidation temperature, the XPS techniques was employed on the sample surface after oxidation at 450 °C and 550 °C, as shown in Fig. 4.6.

Table 4.2 The binding energy of de-convoluted high-resolution XPS spectra including metallic and oxides of Ni, Nb, Ta and Zr recorded for the oxidized sample [74, 107].

Element Spectral line	Oxidation state	Binding energy (in eV)
Ni 2p _{3/2} :2p _{1/2}	Ni ³⁺ (Ni ₂ O ₃)	856.3:874
	Ni ²⁺ (NiO)	854:871.4
	Ni ⁰	852.5:869.7
Nb 3d _{5/2} :3d _{3/2}	Nb ⁵⁺ (Nb ₂ O ₅)	207.1:209.9
	Nb ⁴⁺ (NbO ₂)	205.7:208.5
	Nb ²⁺ (NbO)	203.8:206.5
	Nb ⁰	202.6:205.3
Ta 4f _{7/2} :4f _{5/2}	Ta ⁵⁺ (Ta ₂ O ₅)	27:29
	Ta ⁴⁺ (TaO ₂)	26.2:28.1
	Ta ²⁺ (TaO)	24.4:26.7
	Ta ⁰	23.3:25.2
Zr 3d _{5/2} :3d _{3/2}	Zr ⁴⁺ (ZrO ₂)	182.8:185.3
	Zr ⁰	179.2:181.5

The XPS spectra of Ni 2p and Nb 3d observed on the top surface of the thermally oxidized sample at 450 °C (450AR), and 550 °C (550AR), is shown in Fig. 4.6(a-b), and Fig. 4.6(c-d), respectively. The Ni 2p spectra comprise of NiO, and Ni₂O₃ on the surface of 450 °C oxidized sample. However, sets of doublet peaks at their binding energy values corresponded to Nb₂O₅ [74]. As shown in Fig. 4.6 (c-d), only NiO and Ni₂O₃ were present on the top surface of the sample oxidized at 550 °C, whereas Nb₂O₅ was completely absent. Such inverse oxidation at 450 °C and 550 °C on the sample surface is attributed to the preferential oxidation and diffusion the constitute elements and discussed detailed in the oxidation mechanism section.

For quantitative analyses (Fig. 4.7), the concentrations of elements in the different chemical state were calculated from the area under the deconvoluted peak of individual

species and corrected for sensitivity factor [74]. The surface of the as-spun $\text{Ni}_{60}\text{Nb}_{40}$ amorphous ribbon constitute to 39% Ni content and 61% Nb-content. Further, the Nb_2O_5 are increases to 95% with 5% NiO and Ni_2O_3 on the surface of oxidized $\text{Ni}_{60}\text{Nb}_{40}$ sample at 450 °C (450AR). On the other hand, the surface of oxidized $\text{Ni}_{60}\text{Nb}_{40}$ sample at 550 °C (550AR) consisted of only 68% NiO and 32% Ni_2O_3 .

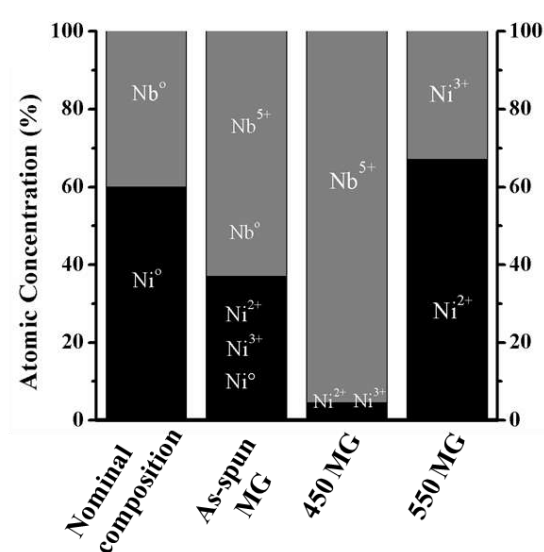


Figure 4.7 Bar chart was depicting the surface atomic concentration of the species on as-spun $\text{Ni}_{60}\text{Nb}_{40}$ amorphous ribbon and their variation at different oxidation temperature.

4.2.1.4 Distribution of the cationic species along with sputtering times or depth of the film.

The O 1s peaks, originating from oxygen as metal-oxide bond, appeared throughout the concentration depth profile of the film formed on the oxidised sample. Apart from the surface, the C 1s spectrum was not visible in core level XPS depth profile. In Fig.4.8 (a-b), the distribution of oxides and metallic states of the Ni and Nb species are plotted as a function of the sputtering time (depth of the oxide film). The surface of oxide film on the 450 °C oxidized sample (Fig. 4.8(a)) comprised predominantly of Nb_2O_5 .

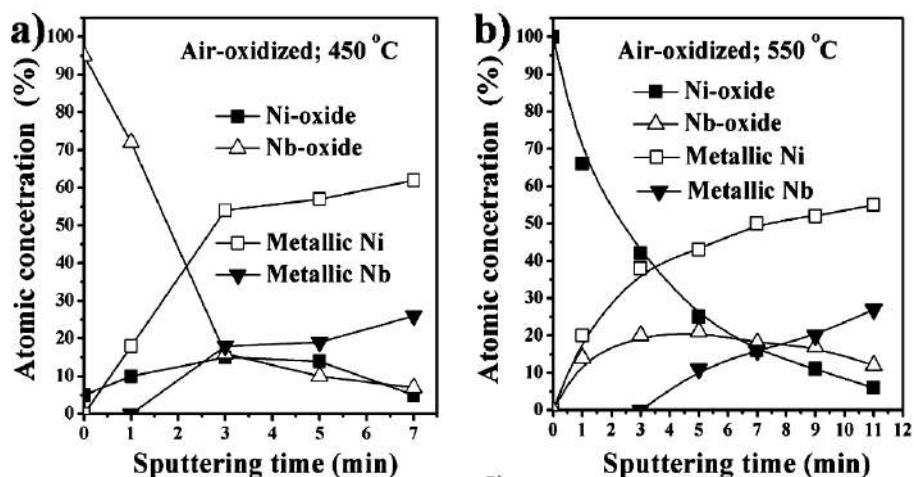


Figure 4.8 XPS depth profile represents the concentration (%) of oxide/metallic states of Ni 2p, and Nb 3d as a function of sputtering time; sputtering time 0 min accounts for the as-received surface; (a) for 450 °C oxidized sample, and (b) for 550 °C oxidized sample.

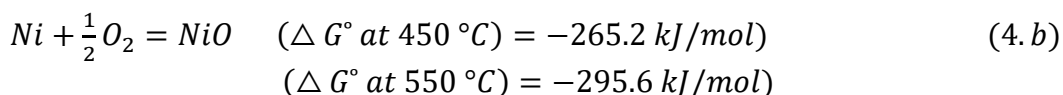
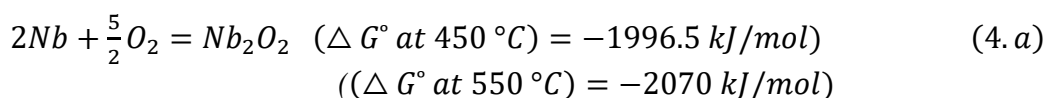
However, the decrements of the Nb-oxide occur rapidly up to first 3 min sputtering time and afterwards, a gradual decrease is observed in the latter sputtering. In contrast, the surface of 550 °C oxidized sample (Fig.4.8 (b)) comprises only of Ni-oxide (100 %) and decrease gradually with the sputtering time. However, for both the thermally oxidized film, the increment of the metallic Ni⁰ and Nb⁰ concentration against the sputtering time is similar. As the depth of the oxide film increases, the oxide state decreases and metallic states increase for both the oxidized sample. The similar metallic proportion of Ni, Nb and Ta are found at 7 min sputtering time for 450 °C oxidized sample and at 11 min for 550 °C oxidized sample. Thus, the results suggested the formation of thin oxide film on the 450 °C oxidized sample while a relatively thicker oxide film on 550 °C sample.

The reason for relatively thicker oxide film formed on 550 °C oxidized sample is due to the inwards diffusion of oxygen and outward diffusion of the Ni-cations (Ni²⁺ and Ni³⁺ ions). The thickness of the oxide film increases at the second parabolic stage, whereas the inwards diffusion of the oxygen and the outward diffusion of Ni happened. The increases in the

thickness of the oxide film formed at 550 °C is further evident by the higher parabolic rate constant compared to the 450 °C oxidation.

4.2.1.5 Thermodynamics of air-oxidation

The reaction of Ni, and Nb with oxygen results in the formation of the stable oxides NiO, Ni₂O₃, and Nb₂O₅ as shown in the Equations (4.a) - (4.c). At 450 °C, the standard Gibbs free energies of formation (ΔG°_f) of Nb₂O₅ (−1996.5 kJ/mol) are in absolute value much higher than that of NiO (−265.2 kJ/mol) and Ni₂O₃ (−241.3) kJ/mol [95]. Therefore, Nb were preferentially oxidised to Nb₂O₅, respectively, when compared to the oxidation of Ni. The Gibbs free energies formation for the oxides under consideration at 550 °C shows marginally higher negative values than that at 450 °C [95]. Since the diffusion of Ni from the bulk to the surface is higher at 550 °C than that at 450 °C, thereby, the content of Ni-oxides was higher as per the given equations.



4.2.1.6 Inverse oxidation mechanism (Elementary process in oxidation) of Ni₆₀Nb₄₀ amorphous alloys.

Oxidation mechanism at 450 °C:

Based on the XPS results of the oxide film on the 450 °C oxidized metallic glass sample which is enriched with Nb₂O₅ along with small fraction of NiO and Ni₂O₃. Enrichment of Nb₂O₅ and oxides on the sample surface was due to the preferential oxidation of Nb. Table 3.4 illustrates the parameters of the ionic radius, ionization potential, and electro-negativity of constituent elements of the metallic glass. It can be seen that the Nb exhibit lower ionization potential, and electro-negativity comparing to Ni, which implies a higher reactivity of Nb to

Chapter 4

the oxygen. Since the Nb comprises a higher reactivity towards oxygen compared to the Ni, a preferential bonding of Nb^{5+} with oxygen anions (O^{2-}) are more favourable. In addition, the Gibbs free energy formation for and Nb_2O_5 is much higher than NiO, and Ni_2O_3 at 450 °C [95]. Above enthalpy values suggested that the formation of Nb_2O_5 is energetically favoured. Significantly low electro-negativity of the Nb (compare to the Ni) promotes the selective oxidation Nb to forming a continuous amorphous Nb_2O_5 oxide film on the surface [96]. Considering the high affinity Nb to oxygen, their migration towards the surface during the oxidation process is expected [108-110]. As the selective oxidation proceeds forward, the concentration of Ni underneath the oxide film gets higher, resulting in Ni-enriched layer at or near oxide/metal interface. The results of XPS depth profiling on 450MG sample shows good agreements with the above discussion that shows a less reactive Ni cation depleted at near interface of the oxide film/Metal.

Oxidation mechanism at 550 °C:

The elementary process of the film formation at 550 °C involved several steps, as shown in Fig. 4.9. The preferential oxidations of Nb take place in the early stage of oxidation. Oxidation at 550 °C, leads to defect generation associated with crystalline phases which could be due to the oxygen vacancies (V_a) that are introduced into the oxide layer [67]. The oxygen vacancy arises due to the non-stoichiometric structure of the oxide. Thus, the outwards diffusion of the un-oxidized Ni-cations (Ni^{2+} and Ni^{3+}) proceed through oxide ion vacancies (V_a) present in Nb_2O_5 oxide. The diffusion of the Ni through the V_a created cationic vacancies at the metal/film interface, as shown in Fig. 4.9. The more Ni diffuses from the metal/interface; more cation vacancies accumulates near the interface resulting to a thick film formation enriched with the Ni-oxide layer as shown in step 3. The vacancies migrated towards oxide/metal interface and thus, the defective interface would be expected.

Atkinson [67] reported that the metal diffusion leads to the creation of such a cation vacancy at the metal/film interface at elevated temperature.

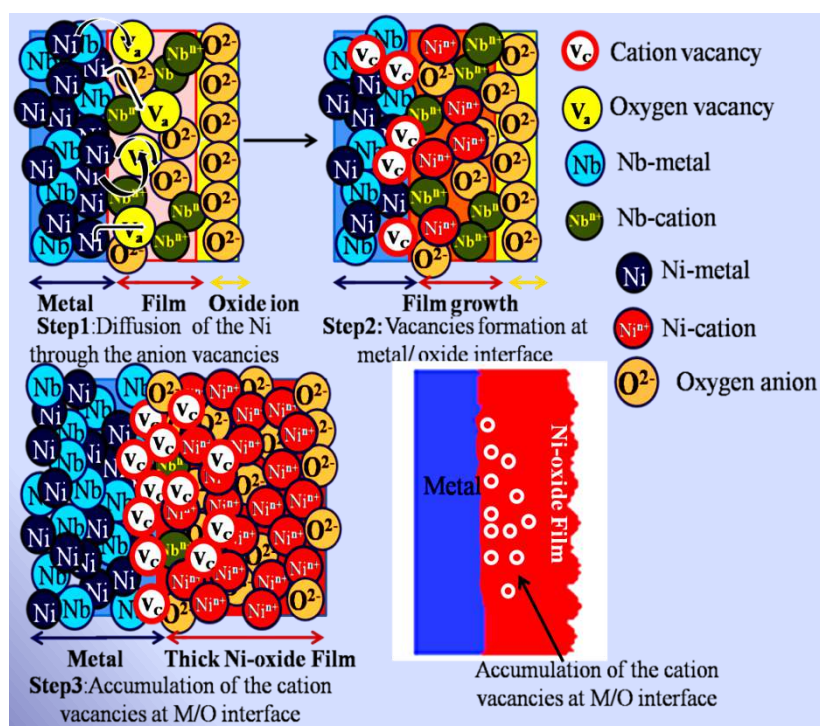


Figure 4.9 An illustration of the elementary step for the film formation at 550 °C involves **Step1** outward diffusion of the Ni through the anion vacancies. **Step2** Ni diffusion created cationic at M/O interface vacancy and film growth. **Step3** cation vacancy accumulation at near M/O interface and formation of thick film enriched with Ni-oxide.

XPS analysis has shown that the surface formed at 550 °C shows initially with only Ni-oxide, and the presence of Nb-oxide is observed after 1 min sputtering (Fig. 4.8(b)).

Based on the TGA results, the mechanism involved in the second stage kinetics is the preferential outward diffusion of the Ni^{2+} and Ni^{3+} . The driving force for Ni diffusion is the defect associated with the oxide layer. On the other hand, Nb^{2+} and Nb^{4+} oxides are observed at the inner layer of oxide film suggesting that the migration of these species are much slower than Nb^{5+} . The cationic size Nb^{2+} (86 pm) > Nb^{4+} (82 pm) > Nb^{5+} (78 pm) may be attributed to the sluggish diffusion of the metal species (Nb^{2+} and Nb^{4+}) [92]. Due to its

Chapter 4

higher thermal stability over Ni_2O_3 , the outer surface containing predominately NiO (Ni^{2+}). Similarly, the rate-determining step involved the diffusion of nickel ions for the oxidation of $\text{Ni}_{36}\text{Zr}_{64}$ metallic glass alloy [96]. Oxidation-induced Ni-cation diffusion has also reported in air-oxidation at high temperatures [77].

Table 4.3 Physical properties of the alloying elements of Ni, Nb, Ta and Zr [92]

Elements	Physical properties				Electro-negativity
	Stable cation	Cationic radius (pm)	Ionization potential (eV)		
			1 st	2 nd	
Ni	Ni^{2+}	86	7.635	18.167	191
Nb	Nb^{5+}	78	6.52	11.3	133
Ta	Ta^{5+}	78	6.52	11.3	133
Zr	Zr^{4+}	83	6.63	13.33	123

4.2.2 Oxidation behaviour of as-spun and thermally oxidized $\text{Ni}_{60}\text{Nb}_{30}\text{Ta}_{10}$ ribbon in air environments.

4.2.2.1 Oxidation kinetics and phase analyses of $\text{Ni}_{60}\text{Nb}_{30}\text{Ta}_{10}$ metallic glass.

The oxidation behaviour of $\text{Ni}_{60}\text{Nb}_{30}\text{Ta}_{10}$ metallic glass was carried out at the same condition at 450 °C and 550 °C in air. Similar to $\text{Ni}_{60}\text{Nb}_{40}$ amorphous alloy, the mass gain versus square root of (exposed time)^{1/2} of $\text{Ni}_{60}\text{Nb}_{30}\text{Ta}_{10}$ metallic glass (MG) data at 450 exhibits two-stage parabolic rate laws (Fig. 4.10 (a)), while at 550 °C, it followed single parabolic stage rate law. However, the onset oxidation (initial oxidation) at 450 °C is not parabolic in nature to the dissolution of the oxygen in the glass metal matrix. However, at 550 °C, single stage parabolic kinetics consisting of an growth stage from 5 s^{1/2} to 134.16 s^{1/2}. In comparison with $\text{Ni}_{60}\text{Nb}_{40}$ amorphous ribbon, the slightly higher rate constant (Table 4.4) was noticed for $\text{Ni}_{60}\text{Nb}_{30}\text{Ta}_{10}$ metallic glass at 450 and 550 °C in air-environment. At 450 °C, an first parabolic growth oxidation stage (12 s^{1/2} to 73.6 s^{1/2}), followed by the second steady-state oxidation (73.7 s^{1/2} to 134.16 s^{1/2}) was observed.

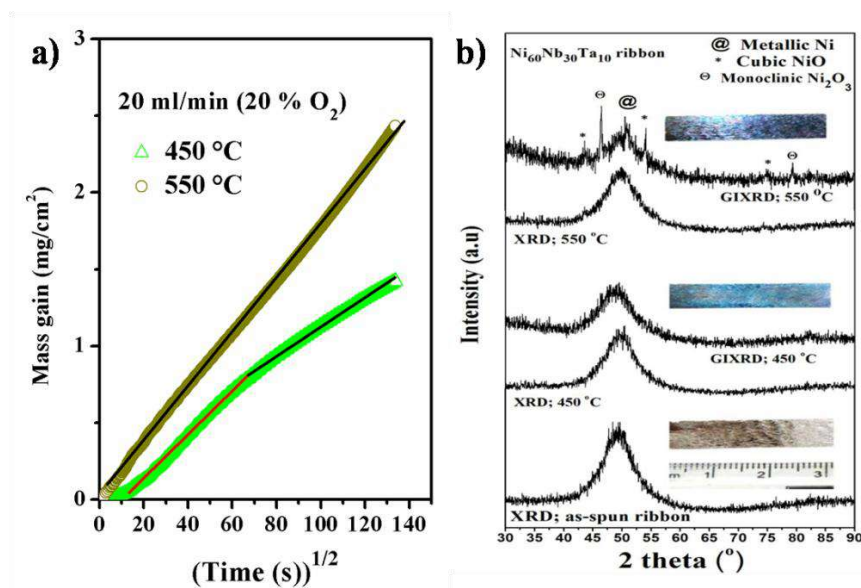


Figure 4.10 (a) Isothermal thermogravimetric analysis (TGA) of the as-spun Ni₆₀Nb₃₀Ta₁₀ metallic glassy (MG) ribbon at 450 and 550 °C for 5 h under O₂ environment and (b) depicts the GIXRD and XRD patterns of as-spun and air-oxidised MG ribbon at 450 and 550 °C.

In Fig. 4.10(b), the GIXRD and XRD broad peak of the as-spun and air-oxidised Ni₆₀Nb₃₀Ta₁₀ ribbons at 450 °C revealed the amorphous nature of the sample. On the other hand, the GIXRD pattern at 550 °C indicated few crystalline peaks that were superimposed on the amorphous halo peaks. However, at 550 °C, crystallization occurred on the surface and the bulk remained amorphous.

Table 4.4 Parabolic rate constants and R² (fitting accuracy) for the oxidation of Ni₆₀Nb₃₀Ta₁₀ metallic glassy (MG) ribbon (k_p in g²/cm⁴.s).

Oxidation stage	Ni ₆₀ Nb ₃₀ Ta ₁₀ MG	
	450 °C	550 °C
Initial stage	k _p	1.2 × 10 ⁻¹⁰
	R ²	0.98
Second stage	k _p	6.1 × 10 ⁻¹¹
	R ²	0.99

The crystalline peak positions at 550 °C corresponded to cubic NiO, (JCPDS No #01-089-7130), and monoclinic Ni₂O₃ (JCPDS No #00-014-0481). This study shows that the micro-alloying of Ni-Nb with the Ta enhance the thermal stability of the glassy substrate.

4.2.2.2 Surface morphology of thermally oxidized metallic glass:

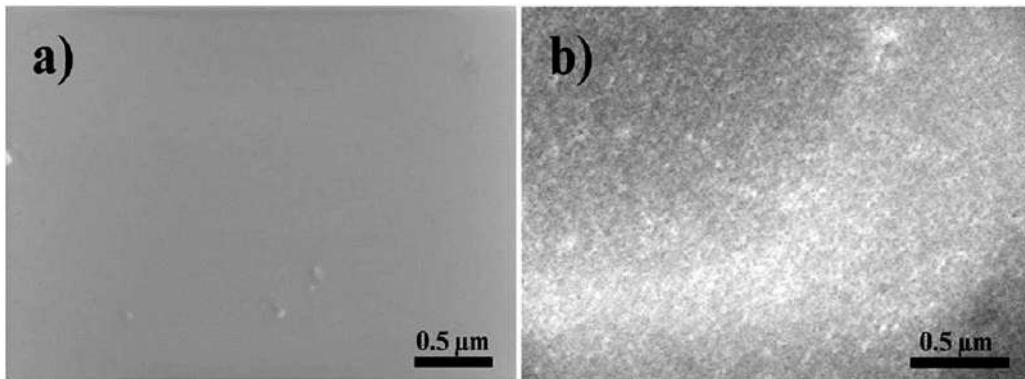


Figure 4.11 SEM images of the air-oxidised Ni₆₀Nb₃₀Ta₁₀ ribbons for 5 h; (a) smooth morphology at 450 °C and (b) speckled contrast at 550 °C.

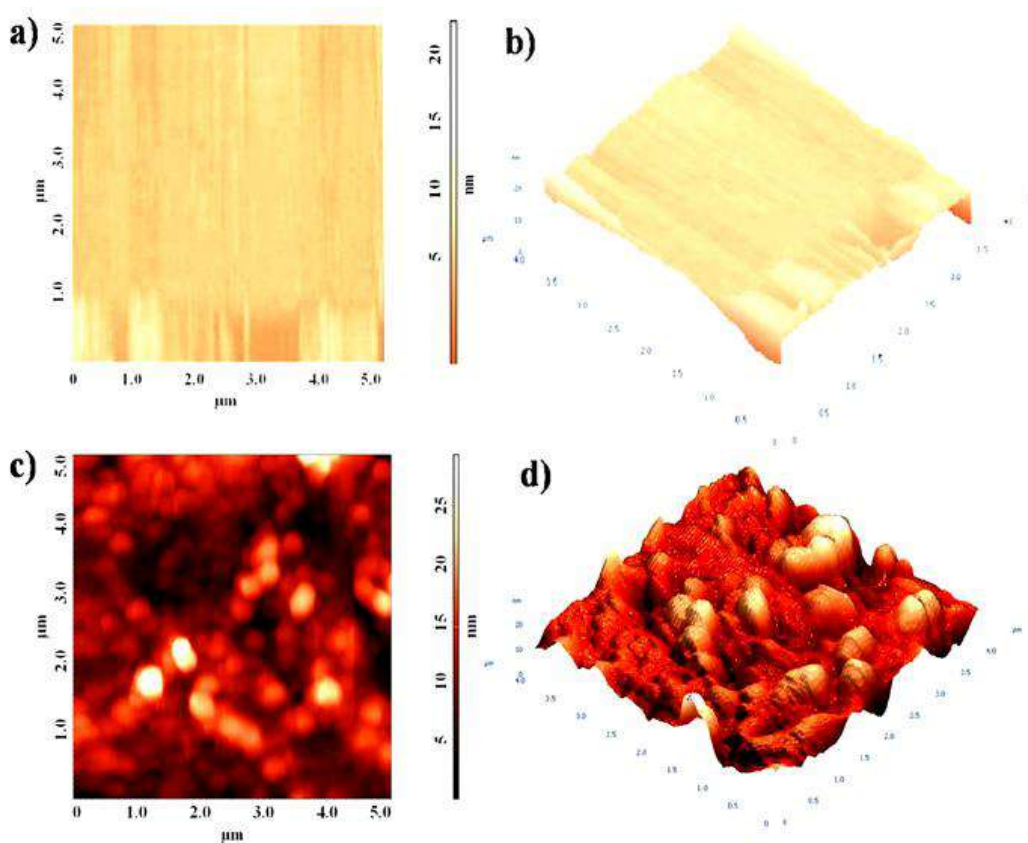


Figure 4.12 AFM images of the surface morphologies of air-oxidised $\text{Ni}_{60}\text{Nb}_{30}\text{Ta}_{10}$ ribbons for 5 h; a and b are the images at 450 °C; (a) 2D and (b) 3D image; c and d are the images for oxidised sample at 550 °C revealing particle-like features; (c) 2D and (d) 3D image.

Fig. 4.11(a) and 4.11(b) are the SEM images of air-oxidized $\text{Ni}_{60}\text{Nb}_{30}\text{Ta}_{10}$ ribbon samples at 450 and 550 °C respectively. Similar to the $\text{Ni}_{60}\text{Nb}_{40}$ amorphous alloy, the oxidized sample 450 °C exhibits a smooth surface while the speckled contrast observed for the sample air-oxidized at 550 °C. The smooth topology was also observed for the ribbon sample oxidized at 450 °C (Figs. 4.12a and 4.12b). The AFM image of the air-oxidized samples at 550 °C in Fig. 4.12c-d showed rms roughness value of about ~ 4.5 nm with some fine particles size in the range of 20-25 nm. The main reason for the rough surface is agglomeration of oxide particle particles at this high temperature oxidation(Fig. 4.12d). Similar rough surface is also observed on the $\text{Ni}_{64}\text{Zr}_{36}$ (or $\text{Ni}_{36}\text{Zr}_{64}$) metallic glass alloys at high oxidation temperature due to the Ni-oxide particle (agglomerated Ni-oxide) on the surface during elevated temperature oxidation [77, 96].

4.2.2.3 XPS analyses before and after thermally oxidized $\text{Ni}_{60}\text{Nb}_{30}\text{Ta}_{10}$ amorphous alloy at 450 °C and 550 °C.

As shown in Fig.4.13 (a-f), the high-resolution Nb 3d, Ni 2p, and Ta 4f photoelectron spectra are recorded on the surface. The binding energy corresponding to the oxide and metallic states of Ni, Nb, and Ta are given in Table 4.2.

The Fig.4.13 (a-f) of the as-spun and 450 °C oxidized sample showed the presence of Ni 2p, Nb 3d and Ta 4f. In contrast, the 550 °C oxidized sample exhibits only Ni 2p peak whereas Nb 3d and Ta 4f were absent. Similar to the $\text{Ni}_{60}\text{Nb}_{40}$ amorphous alloy, the surface of the as-spun $\text{Ni}_{60}\text{Nb}_{30}\text{Ta}_{10}$ metallic contributed both metallic and multiple oxidation states (Fig.4.13 (a-c)) which comes from air-form native layer at room temperature. In contrast, no

trace of the metal is observed after the thermal oxidation, revealing that the metallic state is converted completely to its corresponding oxide state during oxidation in air environments.

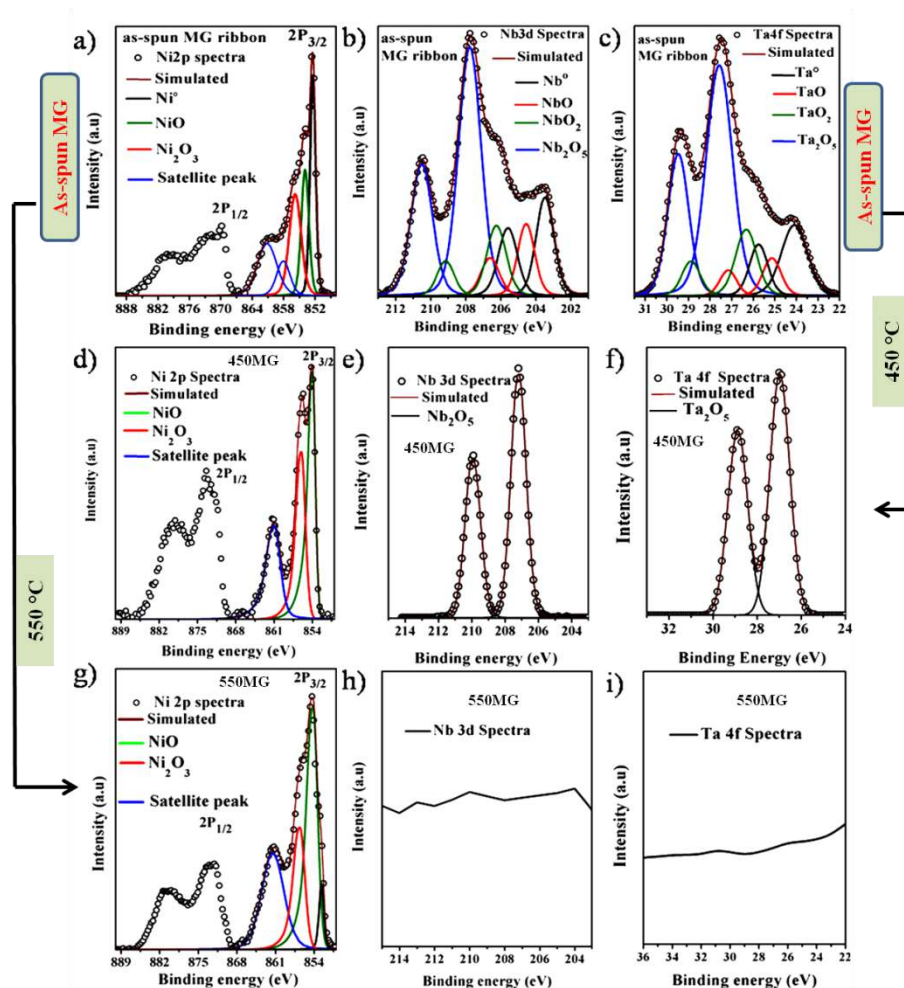


Figure 4.13 (a-c) High-resolution XPS spectra of as-spun $\text{Ni}_{60}\text{Nb}_{30}\text{Ta}_{10}$ ribbon (a) Ni 2p, (b) Nb 3d and, (c) Ta 4f. (d-e) High-resolution XPS spectra of thermally oxidized $\text{Ni}_{60}\text{Nb}_{30}\text{Ta}_{10}$ ribbon sample at 450 °C (450MG), (d) Ni 2p, (e) Nb 3d and, (f) Ta 4f. (g-h) High-resolution XPS spectra of thermally oxidized $\text{Ni}_{60}\text{Nb}_{30}\text{Ta}_{10}$ ribbon sample at 550 °C (550MG) are (g) Ni 2p, (h) Nb 3d and, (i) Ta 4f .

However, the surface of the oxidized sample at 450 °C (450 MG) was comprised predominantly of Nb_2O_5 and Ta_2O_5 oxides with traces of metallic Ni. On the other hand, the surface of the oxidized sample at 550 °C (550MG) consisted of NiO and Ni_2O_3 . It is evident

from XPS spectra that the different film compositions are different for the as-spun, as-spun, 450MG, and 550MG $\text{Ni}_{60}\text{Nb}_{30}\text{Ta}_{10}$ glassy alloys attributed due to the different thickness of the oxide layer formed.

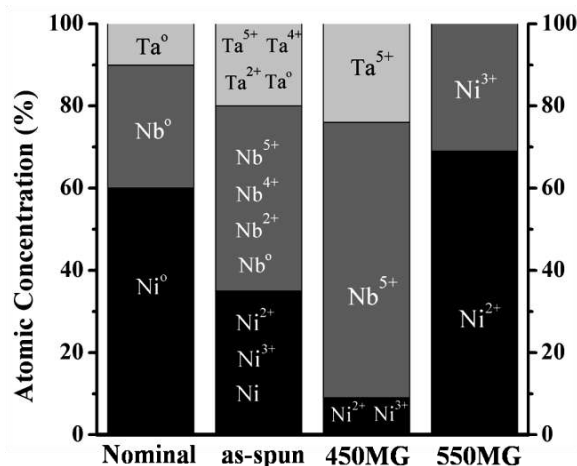


Figure 4.14 Bar chart was depicting the surface atomic concentration of the species on as-spun $\text{Ni}_{60}\text{Nb}_{40}$ amorphous ribbon and their variation at different oxidation temperature.

In quantitative analyses (Fig.4.14), the surface of the as-spun $\text{Ni}_{60}\text{Nb}_{30}\text{Ta}_{10}$ MG sample comprised 42% Ni-content, 40% Nb-content and 18% Ta-content for as-spun metallic glass sample. The oxidized $\text{Ni}_{60}\text{Nb}_{30}\text{Ta}_{10}$ sample at 450 °C (450MG) comprised predominantly of Nb_2O_5 (65%) and Ta_2O_5 (26%) oxides with traces of Ni-oxide (9%). This revealed that the Nb and Ta were preferentially oxidized when compared to the Ni on the surface. On the other hand, the surface oxidized at 550 °C (550MG) consisted of only NiO and Ni_2O_3 , Nb_2O_5 (65%) and Ta_2O_5 (26%) utterly deplete on the outer surface. The quantification showed different chemical composition on surface of the sample for 450 °C and 550 °C oxidation.

4.2.2.4 Distribution of the cationic species along with sputtering times for oxidized

$\text{Ni}_{60}\text{Nb}_{30}\text{Ta}_{10}$ metallic glass

The surface (0 min sputtered) of the oxide film at 450 °C are enriched with Nb_2O_5 and Ta_2O_5 , as shown in Figs. 4.15 (a). At 550 °C (Figs. 4.15 (b)), the sample surface was covered

with only Ni-oxide (100%). For the sample oxidised at 450 °C, the concentration of Nb₂O₅ and Ta₂O₅ oxide decreased rapidly up to 3 min. sputtering, after which gradual decrease was observed with respect to sputtering time as shown in Fig. 4.15 (a). The contribution of the metallic state of Ni increased rapidly and reached 55% after 7 min. sputtering, whereas the metallic state of Nb and Ta were 22 and 6% respectively, as shown in Fig. 4.15 (a).

On the other hand, an oxidized at 550 °C (Fig. 4.15(b)), the contribution of the oxide states of Ni (NiO and Ni₂O₃) decreases along with increasing metallic Ni with respect to depth profile. The Nb₂O₅ and Ta₂O₅ were detected at 1 and 3 min. sputtering respectively at 550 °C, while the metallic state of Nb and Ta were detected at 3 and 5 min. sputtering. After 7 min. sputtering, a comparatively higher concentration of the metallic state of Ni, Nb, and Ta were observed at 450 °C than that at 550 °C. The concentration of NiO (Ni²⁺) and Ni₂O₃ (Ni³⁺) species are shown in Fig. 4.14. Relatively higher metallic proportion are found at 7 min sputtering time for 450 °C oxidized sample compared to at 11 min for 550 °C oxidized sample.

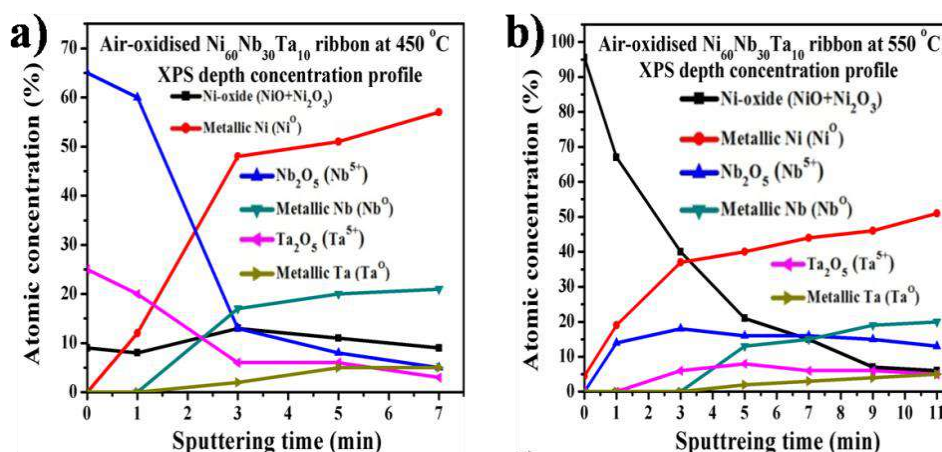
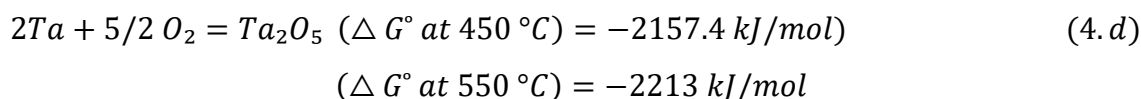


Figure 4.15 XPS depth profiles representing the concentration of oxide/metallic states of Ni 2p, Nb 3d and Ta 4f; (a) at 450 °C and (b) at 550 °C.

The sputtering depth profile analyses indicated that the air-oxidation at a higher temperature (550 °C) resulted in the formation of a relatively thicker oxide layer when compared to the

oxide layer formed at 450 °C. This could be due to the more negative Gibbs free energy of formation of Ta₂O₅ (4.d) when compared to the Nb₂O₅ (eq. 4.b). Hence, the XPS depth profile studies confirmed that the addition of the Ta in Ni-Nb alloy is beneficial for developing relatively thicker amorphous oxide film.



4.2.2.5 Inverse oxidation mechanism of Ni₆₀Nb₃₀Ta₁₀ metallic glass

Oxidation mechanism of Ni₆₀Nb₃₀Ta₁₀ alloy at 450 °C

The Nb and Ta have a similar affinity with low electro-negativity, and it is lower than that for Ni [96]. The similar affinity of Nb and Ta towards oxygen resulted in the outward migration of Nb and Ta ions. The Nb and Ta were then preferentially oxidized, and a smooth, thin amorphous oxide layer (Fig. 3a) containing predominantly of Nb₂O₅ and Ta₂O₅ was formed on the surface. The outward migration of Nb and Ta resulted in the preferential oxidation of Nb and Ta ions. Since the Nb and Ta have higher affinity towards the oxygen, the enrichment of the Nb- and Ta-oxide on the film is expected.

Oxidation mechanism at 550 °C

An inverse oxidation mechanism was observed at the higher oxidation temperature of 550 °C which is similar to the oxidation behavior of Ni₆₀Nb₄₀ amorphous alloy at 550 °C. Due to the effect of elevated temperature at 550 °C, the sample surface at the initial period could undergo rapid and preferential oxidation of Nb and Ta resulting in a surface predominately consisting of oxide layer composed of Nb₂O₅ and Ta₂O₅. These oxide layer formed at elevated temperature could be defective in nature, which could facilitate the diffusion of Ni cation through the vacancies present in Nb₂O₅ and Ta₂O₅ to form NiO and Ni₂O₃ on the surface layer. Oxygen-induced diffusion has been reported at higher temperatures subjected to air-oxidation [96]. Easy migration of Ni-cations (Ni²⁺ and Ni³⁺) was possible through the

oxide ion vacancies present in Nb_2O_5 and Ta_2O_5 lattices. Since ionic radii of the Ni-cations are smaller than the oxygen vacancies, the outward diffusion of Ni ions are more predominant than the oxygen anions. During prolonged oxidation, as the weight gain increased, an increase in the thickness of the oxide layer occurs. The parabolic rate constant, k_p (Table 4.4) determined from isothermal TGA at 550 °C increased twice when compared to that at 450 °C, revealing the higher oxidation rate. The higher oxidation rate is due to the higher mass gain which is come from the outward diffusion of the Ni-cations [96].

4.2.3 Oxidation behaviour of the $\text{Ni}_{50}\text{Nb}_{25}\text{Zr}_{25}$ metallic glass

The film formed at 450 °C for both on the $\text{Ni}_{60}\text{Nb}_{40}$ and $\text{Ni}_{60}\text{Nb}_{30}\text{Ta}_{10}$ metallic glass sample is amorphous structure while film at 550 °C is nano-crystalline nature. It is well know that the amorphous oxide film exhibits a high dielectric constant and higher corrosion resistance. However, the crystalline film formed at 550 °C is more defective and less protected in nature. The electrochemical analyses (potentiodynamic polarization in Fig. 5.3 and 5.7 and EIS in Fig. 5.2 and 5.6) results of air-oxidized $\text{Ni}_{60}\text{Nb}_{40}$ and $\text{Ni}_{60}\text{Nb}_{30}\text{Ta}_{10}$ samples at 450 °C exhibited higher corrosion resistance compared to the 550 °C air-oxidized sample. Reason for choosing a low temperature for the oxidation is for generating a mmmore protective amorphous oxide film. Since the Nb and Zr have better oxidation and corrosion resistance, its metallic glass should exhibit protective oxide film [49]. We carried out the oxidation behavior of Nb and Zr micro-alloying metallic glass of composition $\text{Ni}_{50}\text{Nb}_{25}\text{Zr}_{25}$ below its glass transition temperature ($T_g \approx 625$ °C). The advantages of the above composition of the alloys system is the improved glass forming ability (GFA) which enable to the easily glass formation enhanced [36]. However, very different oxidation behaviour $\text{Ni}_{50}\text{Nb}_{25}\text{Zr}_{25}$ metallic glass was observed at 200 and 400 °C (which are below $T_g \approx 665$ °C Fig. 4.16a) in the air environments. The oxidation behaviour is discussed detailed in below.

4.2.3.1 Oxidation kinetics and phase analyses of Ni₅₀Nb₂₅Zr₂₅ metallic glass

The oxidation kinetics of Ni₅₀Zr₂₅Nb₂₅ MG metallic glass at 200 and 400 °C followed two-stage rate law, as fitted and shown in Fig. 4.16b. The kinetics consists initially the transient oxidation stage (onset; from 0 to 12 s^{1/2}) and follows steady-state oxidation, fitted parabolically (from 12 s^{1/2} to 134 s^{1/2}). The rate constants are estimated by the parabolic fitting of the individual slope of the experimental data and presented in table 4.5.

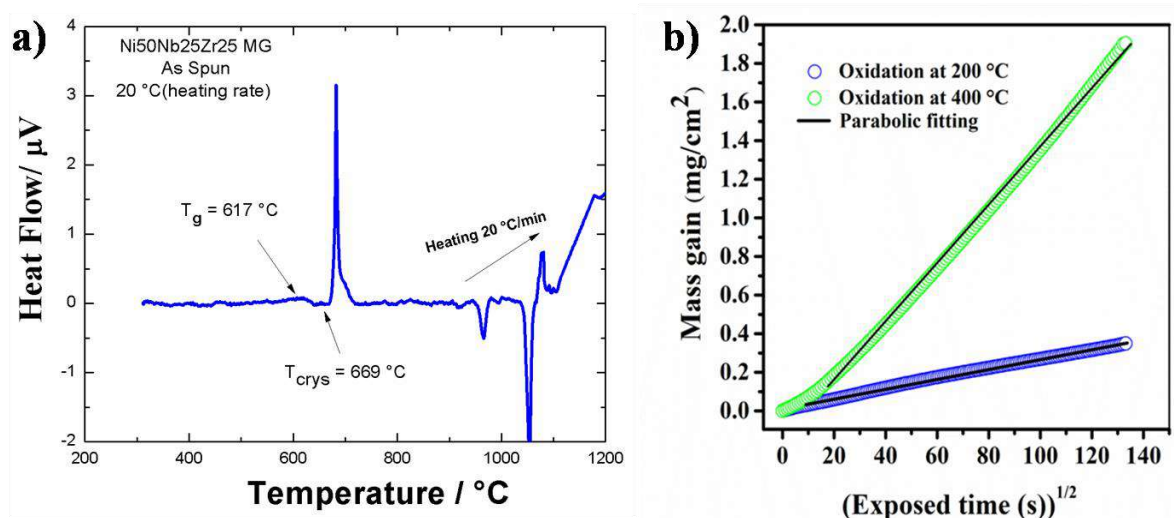


Figure 4.16 (a) Differential Scanning Calorimetry (DSC) traces of as-prepared Ni₅₀Zr₂₅Nb₂₅ metallic glass and (b) Thermo-gravimetric analysis of this metallic glass at 200 °C and 400 °C for 5 h under 20% O₂ environment.

Table 4.5 Rate constants and R² (fitting accuracy) for the oxidation of Ni₅₀Zr₂₅Nb₂₅ metallic glassy ribbon in dry oxygen (k_p in $\text{g}^2 \text{cm}^{-4} \text{s}^{-1}$).

Oxidation stage	Rate constant	Temperature
		Parabolic
200 °C	k_p	4.75×10^{-12}
	R ²	0.99
400 °C	k_p	5×10^{-11}
	R ²	0.99

The parabolic rate constant for oxidation at 400 °C is higher compared to the oxidation at 200 °C. The initial regime (onset) suggests that the rate-determining step is the gas/metal (Ni, Zr, and Nb with O²⁻) interfacial reaction is taken place, while after 12 s^{1/2} (Once the virgin metallic surface is cover with the metal oxide), the solid state diffusion of ions is the rate-limiting step for the parabolic growth regime.

Fig. 4.17 shows XRD and GIXRD patterns of oxidized Ni₅₀Zr₂₅Nb₂₅ metallic glass at 200 °C and 400 °C MG exhibited a broad peak, which indicates the amorphous structure of the surface oxide film and underlying glassy substrate. However, the oxide film on the Ni₅₀Zr₂₅Nb₂₅ metallic glass partially crystallized into the multiple oxides when the sample is oxidized at 530 °C in an air environment (Fig. 4.20). These studies show that the oxide film on the Ni₅₀Zr₂₅Nb₂₅ metallic glass undergoes nano-crystallization at 0.84T_g in air.

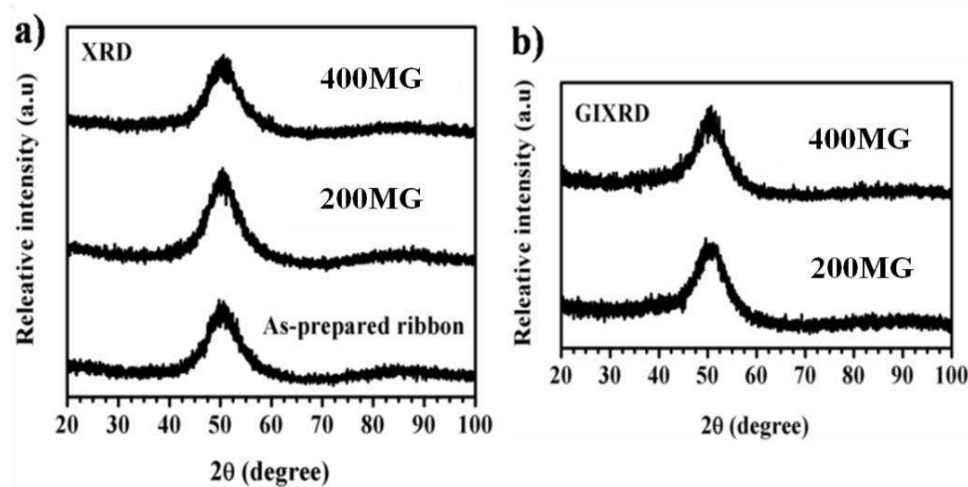


Figure 4.17 XRD and GIXRD pattern of the as-prepared and thermally oxidized metallic glass at (a) 200 °C and (b) 400 °C.

4.2.3.2 Cross-sectional analyses of thermally oxidized metallic glass Ni₅₀Nb₂₅Zr₂₅ metallic glass.

In Fig.4.18, the SEM investigations (in the backscattering mode) were performed on the film/substrate cross-section to determine the thickness of an oxide film formed on the

oxidized MG ribbon samples. Both the oxide film exhibits a darker contrast, which is due to the presence of the oxide ion (O^{2-}) in the film. However, the slightly brighter substrate is attributed to the absence of the oxygen in the metal matrix.

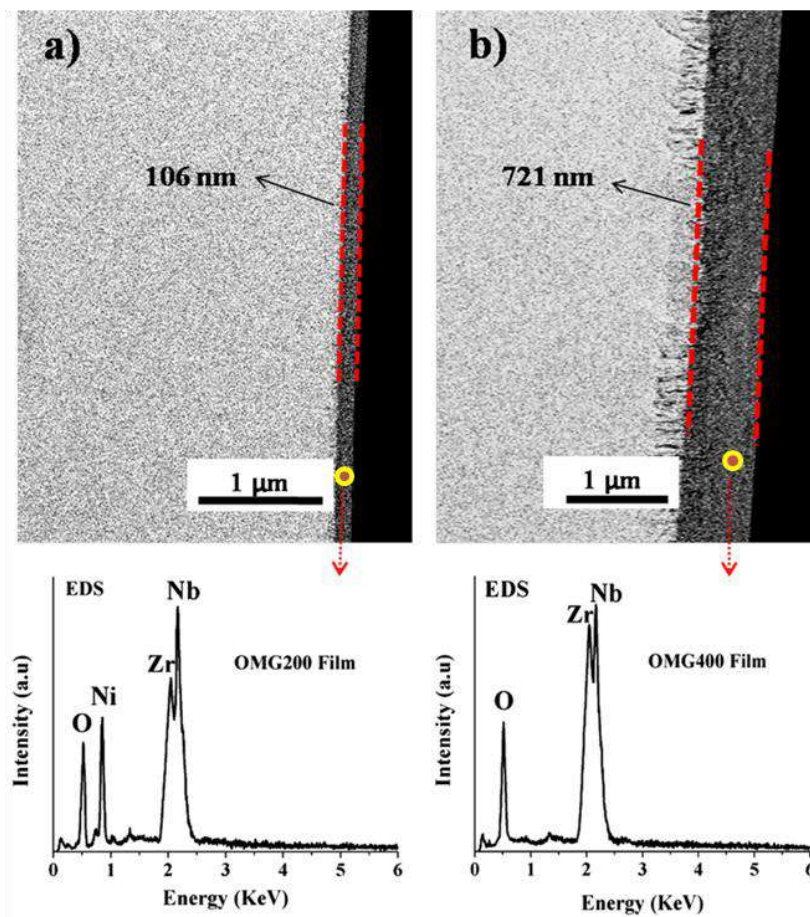


Figure 4.18 Cross-sectional FESEM with EDS results in the backscattered mode of thermally oxidized $Ni_{50}Zr_{25}Nb_{25}$ metallic shows film/substrate for (a) OMG200 sample, and (b) OMG400 sample.

The thin oxide film (106 nm) formed on the 200 oxidized sample and EDS analyses exhibits Ni, Nb, Zr and O peaks. In contrast, 400 oxidized sample exhibits significantly thicker oxide film of about 721 nm which is enriched with Nb, Zr and O. The SEM investigations revealed that the thickness of the oxide film increases with increasing oxidation temperature. It is also observed that the oxide film on the oxidized sample at 200

and 400 °C exhibited dense structure and very small pores are observed on the 400 °C oxide film.

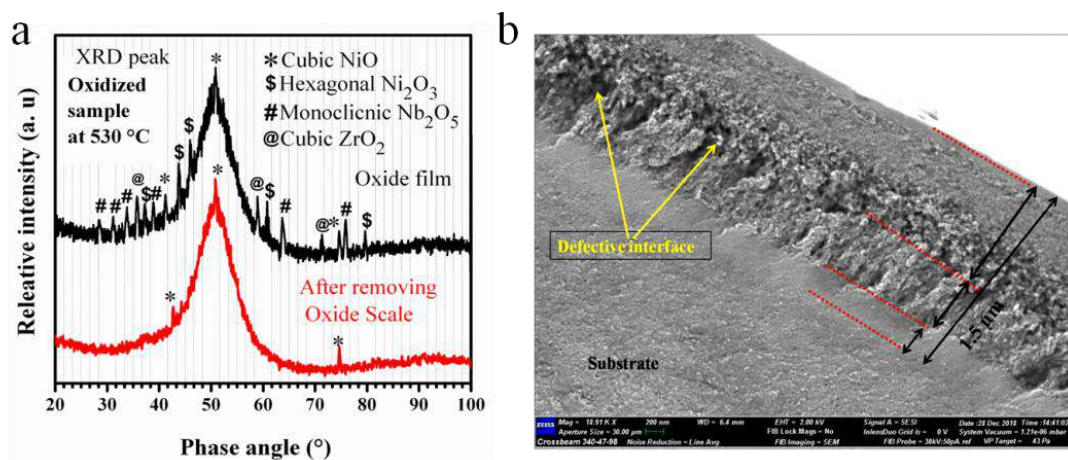


Figure 4.19 (a) XRD pattern and (b) cross-sectional SEM image of oxidized Ni₅₀Zr₂₅Nb₂₅ metallic glass after thermal oxidation in oxygen environments at 530 °C for 5 h.

Oxidation at 530 °C, the crystalline oxide (cross-sectional image, Fig.4.19) formed a highly defective multiple oxide layers near the film/substrate interfacial region. The voids are observed near the interfacial region, which significantly affects the protective growth of the oxide film. Since Nb₂O₅ and ZrO₂ both are n-type oxides [111], its crystalline oxide could contain a large number of the oxygen ion vacancies. Moreover, oxygen ions can easily transport through the defective crystalline oxide. Thereby, once the amorphous oxide is crystallized, it cannot effectively protect the substrate from further oxidation. A transformation from the amorphous-to-crystalline phase increases the permeability of the oxygen and elemental diffusion through the oxide film. In this case, the oxidation rate is largely influenced by the diffusion rate of constituent elements in the matrix. During the harsh oxidation condition, the oxygen ions diffused inwards and metal cation diffused outward. The outwards diffusion results in metal cation and generates the vacancy defect near the interface. As results of the elemental outwards diffusion, large numbers of the vacancies are accumulated into the voids at the film/substrate interfacial regions.

Moreover, the formation of crystallite at the interface is suppressed as long as the system retains the low film/substrate interfacial energy [72]. Once the oxide phase is crystallized, the severe oxidation processes occur by inward diffusion of the oxygen ions through grain boundary, and thus, the protective film is formed [72]. The crystalline oxide formed at 530 °C contained multiple oxide layers and highly defective film/substrate interfacial region. Thus, by the formations of the protective amorphous oxide layer, the inward oxygen diffusion is suppressed, which subsequently further suppressed the nucleation of crystalline oxide [72].

4.2.3.3 XPS studies of the oxidized surface of Ni₅₀Zr₂₅Nb₂₅ MG sample

The high-resolution Ni 2p, Nb 3d, and Zr 3d XPS peaks are recorded to provide understanding on the nature of the chemical composition of the oxide film form at the surface of as-prepared MG (Fig. 4.20(a-c)),

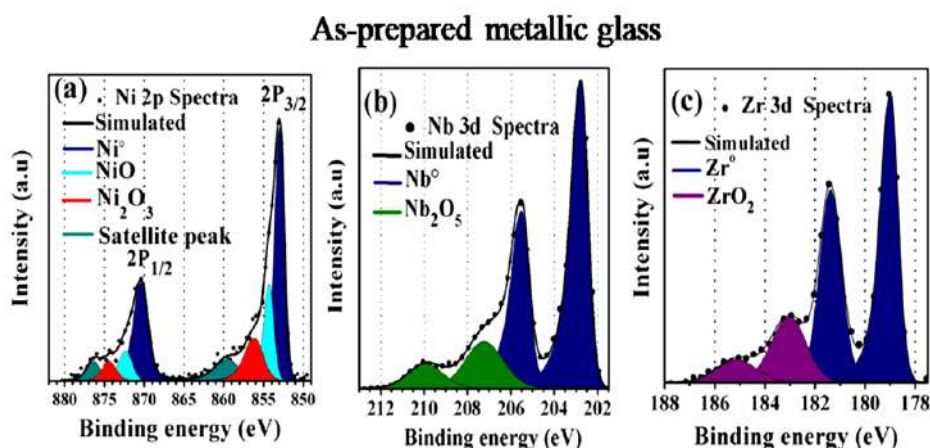


Figure 4.20 High-resolution XPS spectra obtained from the surface of the as-prepared Ni₅₀Zr₂₅Nb₂₅ MG sample; (a) Ni 2p spectra, (b) Nb 3d spectra, and (c) Zr 3d spectra.

Oxidized sample at 200 °C (Fig. 4.21(a-c)), and oxidized sample at 400 °C (Fig. 4.21(d-f)), respectively. As-prepared (as-spun) MG surface comprised both oxide and metallic state of Ni, Nb and Zr. The binding energy of the metallic and corresponding oxide

states are given in Table 4.2. However, no trace of the metallic peak was observed on the surface of the thermally oxidized sample. The oxide film on the 200 °C sample (Fig. 5d-f) composed of multiple chemical states such as NiO, Ni₂O₃, Nb₂O₅, and ZrO₂ at the surface. However, the oxide film on 400 °C sample comprised of Nb₂O₅ and ZrO₂, whereas the Ni-oxide (NiO and Ni₂O₃) are completely absent on the surface (Fig. 4.21(d)).

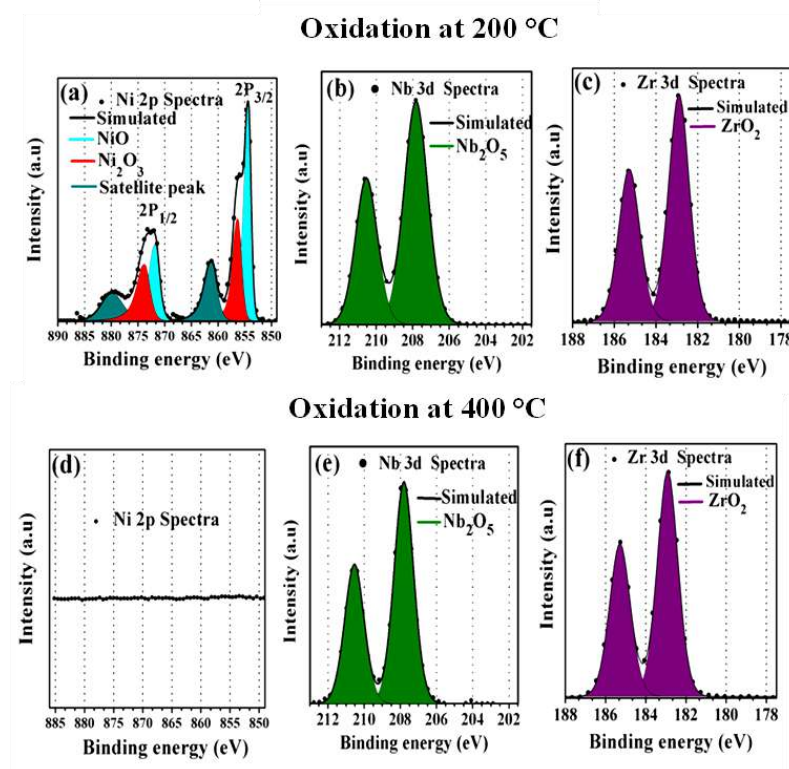


Figure 4.21 (a-c) High-resolution XPS spectra of the surface of the thermally oxidized Ni₅₀Zr₂₅Nb₂₅ at 200 C (OMG200) sample; (a) Ni 2p spectra (b) Nb 3d spectra, and (c) Zr 3d spectra. The spectra recorded on the surface of OMG400 sample; (d) Ni 2p spectra (e) Nb 3d spectra, and (f) Zr 3d spectra.

The composition of the different oxide states and variation upon thermal oxidation are shown in the bar chart in Fig. 4.22. Fig. 4.23 showed the distribution of the elements in the metallic and oxide state as a function of the depth of an oxide film on the oxidized metallic glassy

Chapter 4

samples. The outer surface (0 nm) of oxide film on 200 °C sample comprises of 40 *at.%* Nb(V), 38 *at.%* Zr(IV) and 22 *at.%* Ni-cation ((Ni(II)-15 *at.%* and Ni(III)-7 *at.%*). The oxide states (M^{OX}) decreases gradually with the depth of the oxide film

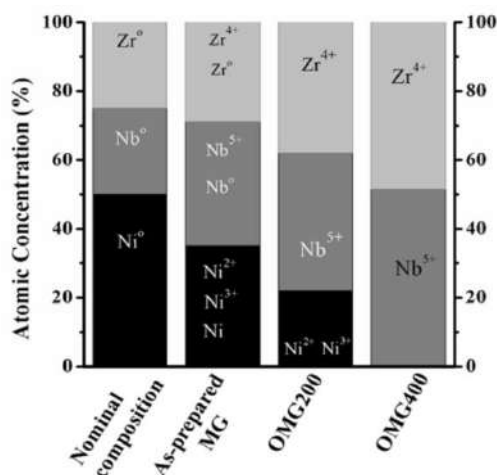


Figure 4.22 Atomic concentration of the metallic and oxide species of as-prepared $\text{Ni}_{50}\text{Zr}_{25}\text{Nb}_{25}$ metallic glass and oxidized metallic glass ribbon (OMG).

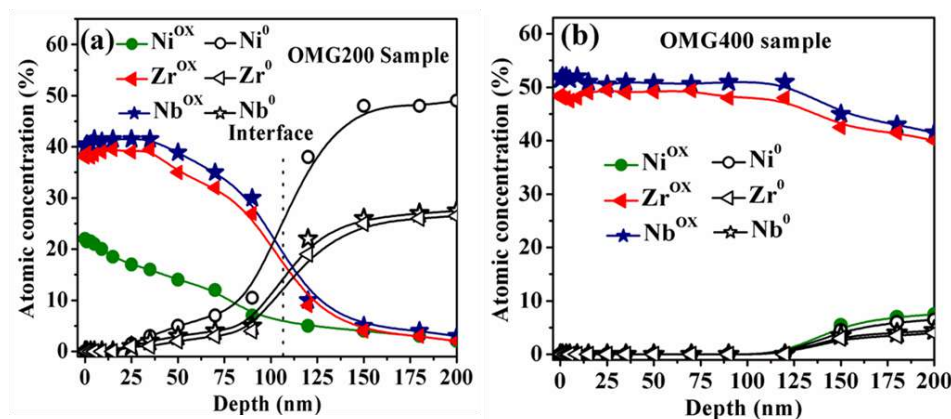


Figure 4.23 XPS depth profiles representing the distribution of oxide and metallic species throughout the depth of the oxide film, the depth 0 nm accounts for the as-received surface; (a) oxidized sample at 200 °C, and (b) oxidized sample at 400 °C.

The metallic states (M^0) are not identifiable in depth of the oxide film within 0-25 nm by Ar^+ ions sputtering, and afterwards, it started to increase gradually followed by quick rises

near the film/substrate interface. In Fig. 4.23(b), the surface of the oxide layer on OMG400 sample is composed only of 51.5 *at.%* Nb (V) and 48.5 *at.%* Zr(IV) cation fraction, whereas Ni^{OX} (Ni(II) and Ni (III)) were absent at a depth within 0-125 nm. It is also interesting to note that the similar concentration of Nb^{OX} and Zr^{OX} are maintaining to depth range of 0-125 nm oxide film. Beyond, the concentration of Nb (V) oxide Zr(IV) decreased steadily with the depth of an oxide film. No traces of the elements in the metallic state were identifiable up to 125 nm depths, and thereafter, the metallic fraction increases slowly with the depth of the oxide film as shown in 4.23(b).

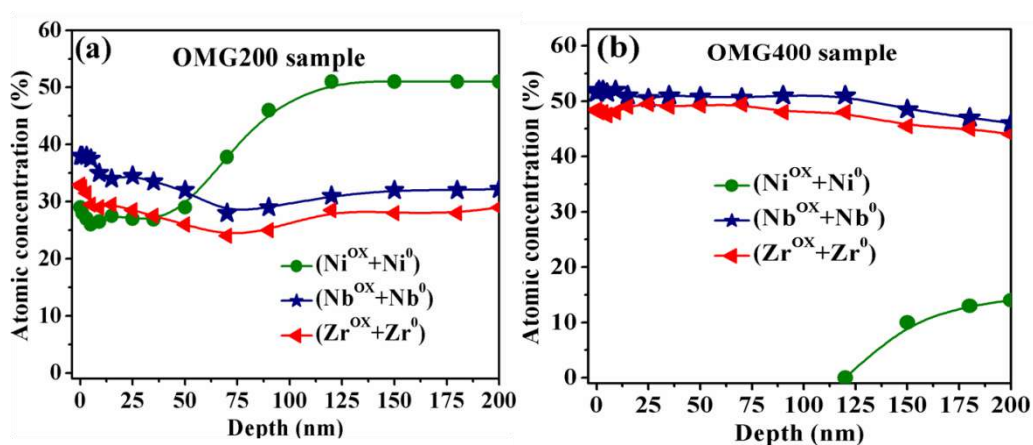


Figure 4.24 XPS depth profiles representing the distribution of species (oxide + metallic) throughout the depth of the oxide film; (a) oxidized sample at 200 °C, and (b) oxidized sample at 400 °C.

In addition, the concentration of the oxide and metallic state recalculated from the Fig. 4.23 are presented in the concentration (oxide + metallic) Vs depth of the oxide in Fig. 4.24; to show the outward diffusion of the Nb and Zr towards surface; and the enrichment of the Ni near metal/oxide interface. The XPS depth profile results in Fig. 4.24b shows the absence of the Ni-content in the up to certain depth of the oxide film formed on oxidized metallic glass (OMG400) sample, whereas film was enriched with the Nb and Zr-content. This result further confirmed that the enrichments of the Ni-content occur underneath of the oxide film.

4.2.3.4 Oxidation mechanism of the Ni₅₀Zr₂₅Nb₂₅ MG sample

The Gibbs free energy formation for ZrO₂ (-1094 kJ/mol at 200 °C and -1185 kJ/mol at 400 °C) and Nb₂O₅ (-1753 kJ/mol at 200 °C and -1924 kJ/mol at 400 °C) are much higher than NiO (-253 kJ/mol at 200 °C and -268 kJ/mol at 400 °C) and Ni₂O₃ (-203 kJ/mol at 200 °C and -235 kJ/mol at 400 °C) [95]. Based on the Gibbs free energy, the formation tendency of the ZrO₂ and Nb₂O₅ are more favourable than NiO and Ni₂O₃ at the initial stage of the oxidation. Above enthalpy values suggested that the formation of ZrO₂ and Nb₂O₅ are energetically favoured at the initial stages of the oxidation.

The amorphous oxide film on OMG400 specimen (Fig. 3c-d) is densely packed and exhibits relatively flat film/substrate interface. Generally, the amorphous oxide film contains a lesser number oxygen vacancies and thus the growth of the film could occur by the outwards diffusion of Zr⁴⁺ and Nb⁵⁺ cations rather than the inward diffusion of the oxygen ions. Diffusion of the oxygen ions in the amorphous film is slow due to the higher sizes of the O²⁻ (201 pm) compared to the Zr⁴⁺ and Nb⁵⁺ cations [72]. Consequently, the growth rate of film is limited by the energy barrier at the oxide/substrate interface [72]. Once the cations overcome the oxide/substrate interfacial energy barrier, movement is easy and contribute to the growth of the amorphous film. The diffusion rate of cations becomes faster information of a continuous amorphous ZrO₂, and Nb₂O₅ film without transforming a crystalline phase which is evidenced from the GIXRD result (Fig. 4.18). As the selective oxidation proceeds forward, the concentration of Ni underneath of the oxide film is higher, resulting in Ni-enriched layer at or near oxide/metal interface. Considering the chemistry of the alloying elements Zr-Nb, the growth of a thick amorphous oxide film at 400 °C would be expected. The diffusion of the Zr⁴⁺ in amorphous Zr-Ni alloy and Nb⁵⁺ in amorphous Ni-Nb alloy

towards the surface are further facilitated by a relatively smaller cationic radius of Zr^{4+} (≈ 83 pm) and Nb^{5+} (≈ 78 pm) compared to the Ni cation ($Ni^{2+} \approx 86$ pm) (Table 4.3) [92].

4.3 Summary:

- a) The oxidation kinetics of the both amorphous alloys ribbon ($Ni_{60}Nb_{40}$ and $Ni_{60}Nb_{30}Ta_{10}$) followed two stage parabolic rate laws at 450 and 550 °C in air environments. The parabolic rate constants increase with increasing the oxidation temperature. For $Ni_{60}Nb_{40}$ & $Ni_{60}Nb_{30}Ta_{10}$ amorphous glass, the surface oxide layer and underlying substrate are thermodynamically stable and retained amorphous structure at 450 °C in air environments. In contrast, oxidation at 550 °C, surface oxide film on both alloys is undergone partially crystallized. The micro-alloying Ta with Ni-Nb enhances thermodynamic stability of the glassy structure.
- b) The XPS analyses showed that the oxidation of $Ni_{60}Nb_{40}$ amorphous alloy at 450 °C comprises predominantly Nb_2O_5 oxide on the surface, while $Ni_{60}Nb_{30}Ta_{10}$ metallic glass enriched with Nb_2O_5 and Ta_2O_5 . In contrast, oxidation at 550 °C, both sample surfaces are composed with only NiO and Ni_2O_3 and other oxide depleted at surface.
- c) Distinct oxidation behavior observed for $Ni_{50}Nb_{25}Zr_{25}$ MG in air environments. Oxidation of $Ni_{50}Nb_{25}Zr_{25}$ MG at 200 °C and 400 °C follows two stage rate laws, initial, linear rate law following parabolic rate laws. Oxidation at 200 °C, a thin amorphous oxide film (106 nm) enriched with NiO, Ni_2O_3 , Nb_2O_5 and ZrO_2 on the surface. Oxidation at 400 °C, 721 nm thick amorphous oxide film enriched with only Nb_2O_5 and ZrO_2 on the surface whereas Ni-depleted completely.

5 Effects of the thermally grown oxide film on the corrosion properties of Ni-based MG in nitric acid environments

This chapter introduces the effect of the thermally grown oxide film on the corrosion resistance behavior of $\text{Ni}_{60}\text{Nb}_{40}$, $\text{Ni}_{60}\text{Nb}_{30}\text{Ta}_{10}$, and $\text{Ni}_{50}\text{Nb}_{25}\text{Zr}_{25}$ metallic glass in the nitric acid medium using different electrochemical techniques, such as EIS, Potentiodynamic Polarization, Potentiostatic Polarization, and Mott-Schottky etc. The oxide film on the 450 °C $\text{Ni}_{60}\text{Nb}_{40}$ oxidized sample exhibits a highly protective barrier in the nitric acid solution when compared to the oxide film at 550 °C and as-spun amorphous alloy. Similarly, for oxidized $\text{Ni}_{60}\text{Nb}_{30}\text{Ta}_{10}$ sample at 450 °C exhibits higher corrosion resistance in the nitric acid medium compared to that of as-spun and 550 °C oxidized sample. The Mott-Schottky analyses of the thermally oxidized film on both $\text{Ni}_{60}\text{Nb}_{40}$ and $\text{Ni}_{60}\text{Nb}_{30}\text{Ta}_{10}$ MG at 450 °C exhibits insulating behaviour, while the 550 °C oxidized MG exhibits p-type semiconducting behavior. Tailoring the semiconducting nature of the film based on the different surface composition by thermal oxidation are highlighted.

5.1 Introduction:

Recently, several Ni-based metallic glassy such as Ni-Nb-Zr-Ta and Ni-Nb-Zr-Ti-Ta metallic glassy alloys were explored for service in the nitric acid application of reprocessing plant of the spent nuclear fuel [62]. However, the nature of the passive film formed and its properties of $\text{Ni}_{60}\text{Nb}_{40}$ and $\text{Ni}_{60}\text{Nb}_{30}\text{Ta}_{10}$ metallic glass in 11.5 M nitric acid need more elaborate investigations. The main drawback is the passive film thickness of $\text{Ni}_{60}\text{Nb}_{40}$ (≈ 3 nm) and $\text{Ni}_{60}\text{Nb}_{30}\text{Ta}_{10}$ (≈ 1.5 nm) metallic glass alloy which are extremely thin and suffers passivity breakdown at the lower anodic potential in the concentrated nitric acid environment [88].

Recent research [49] reported that the thermally oxidized metallic glasses alloys exhibit higher corrosion resistance compared to the as-prepared metallic glass. The materials with

wider passive range and low current density provide higher durability in severe environments, and that motivated for developing a highly protective amorphous oxide film. Nie et al. studied the effect of the thermally grown amorphous film on the corrosion behavior of the Zr-based metallic glass in saline environments. Although the passive region width increased after thermal oxidation, only a marginal reduction of the corrosion current density was reported [49]. However, before the actual application as engineering materials, the fundamental chemical and environmental stability nature of such oxide layer needs to be properly evaluated. Owing to the high corrosion resistance of the Ni-based metallic glass, it can be used for thermo-well (thinnest part used in the dissolver tank) application in nitric acid medium. A fundamental contribution in the understanding of corrosion behavior of the metallic glass has been made for application of nitric acid [98]. However, comparable studies of the trace elements effect have not being reported on the Ni-based metallic glass in nitric acid environments. Therefore, the effects of the minor alloying elements such as Ta, Zr with Ni₆₀Nb₄₀ metallic glass on the corrosion behavior in 11.5 M nitric acid are evaluated.

5.2 Results and Discussions

5.2.1 Electrochemical Corrosion behavior of as-spun and thermally oxidized Ni₆₀Nb₄₀ ribbon in the concentrated medium.

The systematic electrochemical studies including anodic polarization and electrochemical impedance spectroscopy (EIS) and Mott-Schottky experiments, were performed in 11.5 M HNO₃ environment.

5.2.1.1 Electrochemical impedance spectroscopy analyses

The electrochemical impedance spectroscopy (EIS) measurements were carried out at their corresponding OCP to compare the corrosion stability of the as-spun, and thermally oxidized at 450 °C ribbons (450AR) and at 550 °C (550AR) in 11.5 M HNO₃ (Fig. 5.1 (a-b))

medium at room temperature. All the Nyquist and Bode modulus plots exhibited single time constant irrespective of the thermally grown oxide film on $\text{Ni}_{60}\text{Nb}_{40}$ alloy substrate.

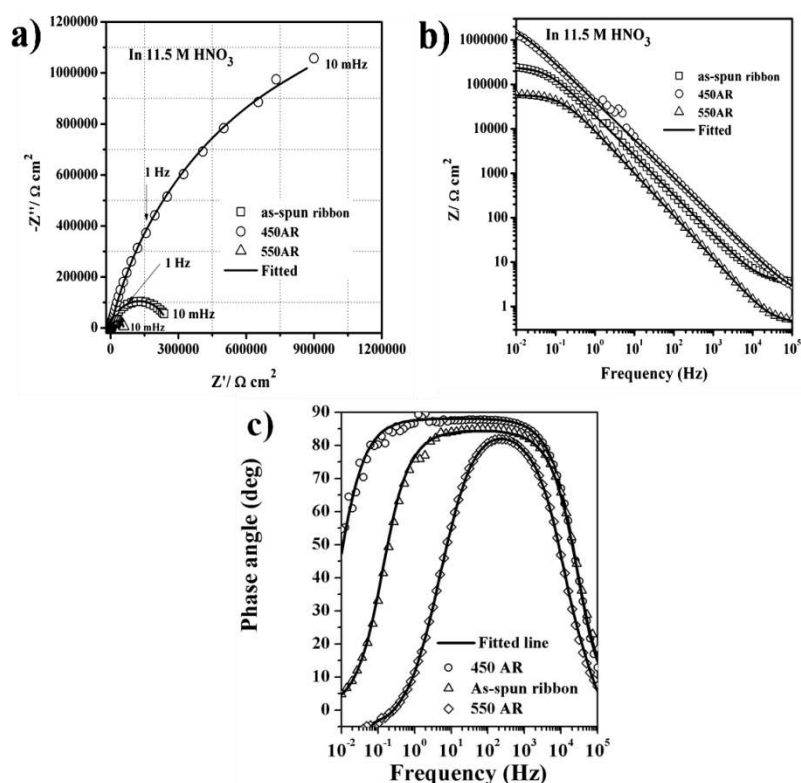


Figure 5.1 Electrochemical impedance spectra of air-oxidized and as-spun $\text{Ni}_{60}\text{Nb}_{40}$ amorphous ribbon in 11.5 M HNO_3 media

However, the impedance spectra of the impedance vs. frequency (in a log-log plot) exhibited a linear slope of about -1 at the mid-frequency range, indicating typically pure capacitive behaviour [88]. Bode phase angle exhibits the single semicircle and consistency with the Nyquist and Bode modulus results. In the mid frequency range, the 450 AR (air-oxidized ribbon), as-spun and 550 AR samples attained 88° , 84° , and 80° phase angle. This indicating that the air-oxidized sample at 450°C (450 AR) shows higher capacitive behaviour compared to the as-spun and 550 AR. The difference capacitive behaviour of the air-oxidized and as-spun samples is due the difference in the composition and thickness of the oxidized film. For all the conditions studied, the power index values are in the range of 0.90 - 0.97 which suggested that the deviation from pure capacitance behavior is relatively small [88].

Chapter 5

The observation of single semi-circle arc indicated that the thermally oxide film improved adhesion with underlying substrates [112].

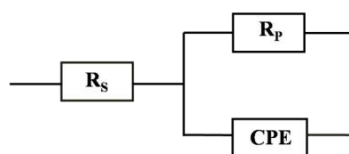


Figure 5.2 The equivalent circuits [$R_s(CPE||R_p)$] used for fitting the experimental impedance data; R_s is the solution resistance, CPE is the constant phase element in parallel connection, and R_p is the polarization resistance.

Table 5.1 Equivalent circuit parameters of EIS results including the root-mean-square deviation and densities of charge carrier values for as-spun and air-oxidized $Ni_{60}Nb_{40}$ ribbons in 11.5 M HNO_3 at room temperature in aerated condition.

Alloy condition	Electrochemical impedance parameters					Defect density	
	R_s $\Omega \text{ cm}^2$	R_p $k\Omega$ cm^2	C $\mu\text{F}/\text{cm}^2$	n -	χ^2 -	N_d cm^{-3}	N_a cm^{-3}
As-spun	0.7 ± 0.02	275 ± 2	15.6 ± 2	0.91 ± 0.02	0.05 ± 0.003	2×10^{19}	2.1×10^{19}
450 AR	3 ± 0.03	2635 ± 6	6.5 ± 1	0.90 ± 0.1	0.08 ± 0.003	4.1×10^{18}	-
550 AR	3.5 ± 0.04	59 ± 2	24.6 ± 3	0.93 ± 0.05	0.07 ± 0.004	-	3.6×10^{19}

The smaller R_s is attributed to the high conductivity of the 11.5 M nitric acid. The polarization resistance (R_p) of the as-spun and thermally oxidized sample in 11.5 M nitric acid follows the order (Table 5.1): 450AR sample > as-spun ribbon > 550AR sample. However, the capacitance of the film follows the order: 450AR sample < as-spun ribbon < 550AR sample. The corrosion resistance of the alloy is directly correlated to the polarization resistance (R_p) [88]. The higher R_p value of 450AR ribbon in 11.5 M HNO_3 indicated higher corrosion resistance. The reason for high corrosion resistance of 450AR sample is attributed to the thermally oxidized amorphous film enriched with Nb_2O_5 which act a compact barrier for the penetration of corrosive species in the nitric acid medium. In contrast, a low R_p value of the 550AR sample in the nitric acid medium is attributed to the film enriched with

crystalline Ni-oxide. The easier penetration of electrolytes through the defective crystalline oxide film decreased the polarization resistance. However, marginally higher R_p of the as-spun $Ni_{60}Nb_{40}$ ribbon sample in 11.5 M nitric acid is due to the passivation ability of Nb [88]. The 450AR sample exhibited relatively lower capacitance which is attributed to the less defective and homogeneous nature of the thermally grown oxide film compared to the 550AR and as-spun sample.

5.2.1.2 Potentiodynamic polarization behavior of as-spun and thermally oxidized

$Ni_{60}Nb_{40}$ ribbon in the nitric acid environment

The potentiodynamic polarization tests of the as-spun and thermally oxidized ribbon (450AR and 550AR) samples in 11.5 M HNO_3 environment at the scan rate of 0.166 mV/s are presented in Fig.5.3. Electrochemical parameters such as corrosion potential E_{corr} , corrosion current density I_{corr} , passive current density I_{pass} , and transpassive potential E_{trans} are estimated and shown in Table 5.2.

Table 5.2 Potentiodynamic polarization parameter for as-spun and thermally oxidized $Ni_{60}Nb_{40}$ amorphous alloys in 11.5 M HNO_3 environment at room temperature.

Alloy condition	Potentiodynamic polarization parameters		
	E_{corr} vs. (Ag/AgCl)	I_{pass}	E_{trans} vs. (Ag/AgCl)
	mV	$\mu A/cm^2$	mV
As-spun	829±2	0.03±0.002	1855±8
450 AR	898±2	0.002±0.001	2165±10
550 AR	688±3	0.2±0.008	1985±10

All the potentiodynamic polarization experiments were performed three times for checking the reproducibility of the results. The standard errors are less than ± 1 % mV for the potentials (E_{corr} and E_{pass}) and in the range between 0.01 to 2 for the currents densities (I_{corr} and I_{pass}). The potentiodynamic polarization curve above E_{corr} for all samples studied indicated the high passivation ability with no active-passive transition as shown in Fig.5.3.

Chapter 5

The corrosion and passivation current densities (I_{pass}) in 11.5 M nitric acid decreases in the following order: 450AR < as-spun ribbon < 550AR sample. The low I_{pass} value for the 450AR sample is attributed to the stable thermally grown amorphous Nb_2O_5 film. In comparison to the as-spun ribbon, the wider passive range is observed for the thermally oxidized ribbon. In contrast, the higher I_{corr} and I_{pass} for the 550AR sample, revealing that the film was inferior due to the relatively lower passivation ability of crystalline cubic NiO, and Ni_2O_3 in 11.5 M HNO_3 was evident from potentiodynamic polarization (Fig.5.3).

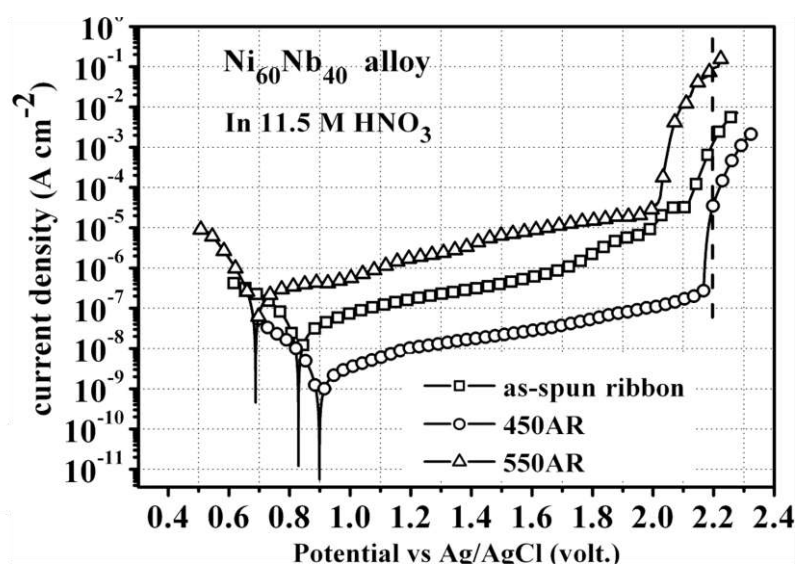


Figure 5.3 Potentiodynamic polarization curves for the as-spun and thermally oxidized $\text{Ni}_{60}\text{Nb}_{40}$ amorphous alloys in 11.5 M nitric acid medium at room temperature.

For the 450AR sample, the relatively nobler E_{corr} value is attributed to the surface enriched with stable oxide state of Nb^{5+} (Nb_2O_5) species. The E_{corr} value for the as-spun sample in nitric acid was slightly less noble than 450AR sample indicated that the surface composed of oxide and metallic state of Ni and Nb as shown in Fig. 4.3 [88]. The low E_{corr} value of oxide film on the 550AR sample was attributed to the surface enriched with less noble Ni^{2+} , and Ni^{3+} species evident from XPS analyses (Fig. 4.4). The distinct behaviors of the trans-passive potential (E_{trans}) of the samples is attributed to compositional variation in the thermally grown film and its dissolution behavior. The increase in the current just after E_{trans}

in the nitric acid medium could be due to oxygen evolution reaction leading to the breakdown of the oxide/passive film.

5.2.1.3 Mott-Schottky analysis of as-spun and thermally oxidized Ni₆₀Nb₄₀ ribbon samples

The Mott-Schottky analysis was performed at 1000 Hz to evaluate the electronic structure of the passive and/or oxide film on the as-spun, 450AR, and 550AR samples in 11.5 M HNO₃ (*Fig. 5.4*) solutions. The 450AR sample with a positive slope appeared in the range of 0.65 to 1.75 V (Ag/AgCl) indicating n-type semiconducting film. The n-type semiconducting properties of the oxide film on 450AR sample is due to the surface enriched with Nb₂O₅ evidenced from the XPS (*Fig. 4.4b*). On the other hand, the oxide film on 550AR sample exhibited p-type semiconductivity within the potential range of 0.65 to 1.75 V (Ag/AgCl) in nitric acid. The p-type semiconductivity within the potential range on 550AR sample is attributed to the surface film enriched with crystalline NiO and Ni₂O₃ [101]. The as-spun ribbon in 11.5 M nitric acid showed first n-type semiconductivity and changed to the p-type at 1.5 V (Ag/AgCl). The observation of n- and p-type semiconductivity could be due to the in-situ formation of the passive film on the as-spun ribbon in the nitric acid medium.

The dielectric constant of 45 (Nb₂O₅) was used to calculate the N_d for 450AR sample, while for the 550AR sample, the dielectric constant 12 (NiO) used to determine N_a, is shown in Table 5.1. The orders of the N_d values are as follows: 450AR < as-spun ribbon. The donor densities decreased by 4.9 times for 450AR sample compared to the as-spun ribbon in the nitric acid medium. Therefore, the thermally oxidized film on the 450AR sample is less defective, and more protective in nature compared to the film formed on the as-spun ribbon.

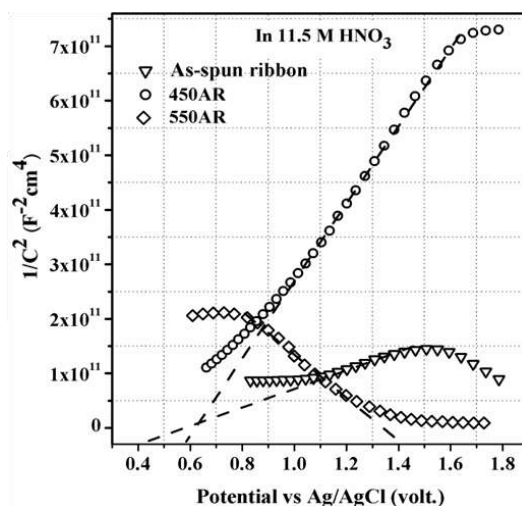


Figure 5.4 Mott-Schottky plots for thermally oxidized and as-spun $\text{Ni}_{60}\text{Nb}_{40}$ ribbon at room temperature in the aerated condition in 11.5 M HNO_3 environment.

For 450AR sample, the less defective oxide film restricts the diffusion of anions from the electrolyte and migration of cations from the oxide layer, thus improving the corrosion resistance. In contrast, an oxide film with remarkably higher defect density on the 550AR sample revealed easy diffusion of the corrosive electrolytes through the defective site. These results indicated that the N_d and N_a have a significant influence on the stability of the films on oxidized ribbon samples in the nitric acid environment.

5.2.1.4 Surface studies of as-spun and thermally oxidized $\text{Ni}_{60}\text{Nb}_{40}$ ribbon samples after polarization in 11.5 M nitric acid

The as-spun, 450AR and 550AR samples were removed at a trans-passive region of 2200 mV (Ag/AgCl) and characterized by the field emission scanning electron microscopy, as shown in Fig.5.5. The magnified micrographs showed the irregular attack features appeared on the surface of the as-spun ribbon in 11.5 M nitric acid, indicating a significant dissolution of the passive film at this potential (Fig.5.5 (a)). However, the surface of the 450AR oxidized sample in Fig.5.5 (b) showed a smooth morphology without any significant attack which is attributed to the protective nature of the Nb_2O_5 film. EDS showed the

marginal Nb-content increased which is similar to the composition before the corrosion test. This suggested that the oxide film formed on the 450AR sample remains almost the same even after the corrosion test. However, slight decreases of the Ni-concentration on the surface after the corrosion test could be indicative of dissolution of the Ni. On the other hand, micrographs (Fig.5.5 (c)) showed the surface was severely attacked, and half droplet-shaped features appeared on 550AR sample in 11.5 M nitric acid. The appearance of half droplet feature is attributed to the accumulation of the oxygen (during oxygen evolution reaction) in the form of the droplet that grows gradually resulting to swelling generating pressure that leads to the final collapse of the film (Fig.5.5 (c)).

The average concentration obtained from the EDS point analyses of half droplets (1, 2 and 3) comprises of Ni (43%) and Nb (57%). It is evident that the enriched Ni-oxide dissolved from the oxide film of 550 AR sample into the nitric acid solution at 2.2 V (Ag/AgCl). As the Ni-oxide dissolved from the surface oxide film, the Nb migrates towards the surface and aggregated in the form of droplets. The Nb has high corrosion resistance than that of Ni in nitric acid. The rapid Ni-dissolution from the surface of the 550AR sample can be correlated with the sudden increased of the current density at 2.2 V (Ag/AgCl) that appeared in the polarization experiments (Fig.5.3 (c)). The reason for the severe attack is due to highly defective crystalline Ni-oxide film on the 550AR sample. Finally, the peeling off the film made un-protective of the inner matrix is evident from the Fig. 5.5 (c).

5.2.2 Electrochemical Corrosion behavior of as-spun and thermally oxidized Ni₆₀Nb₃₀ Ta₁₀ metallic glass ribbon in 1, 6, and 11.5 M nitric acid medium (effect of the nitric acid concentration).

The previous studies showed the superior corrosion resistance of 450 °C thermally oxidized Ni₆₀Nb₄₀ alloy due to the formation of Nb₂O₅ enriched film. Jayaraj et. al [88] reported that the addition of the Ta increased the corrosion resistance of Ni-metallic glass in nitric acid

medium. Previous Chapter (4), discusses the formation of the Nb₂O₅-Ta₂O₅ stable film on the Ni₆₀Nb₃₀Ta₁₀, at 450 °C.

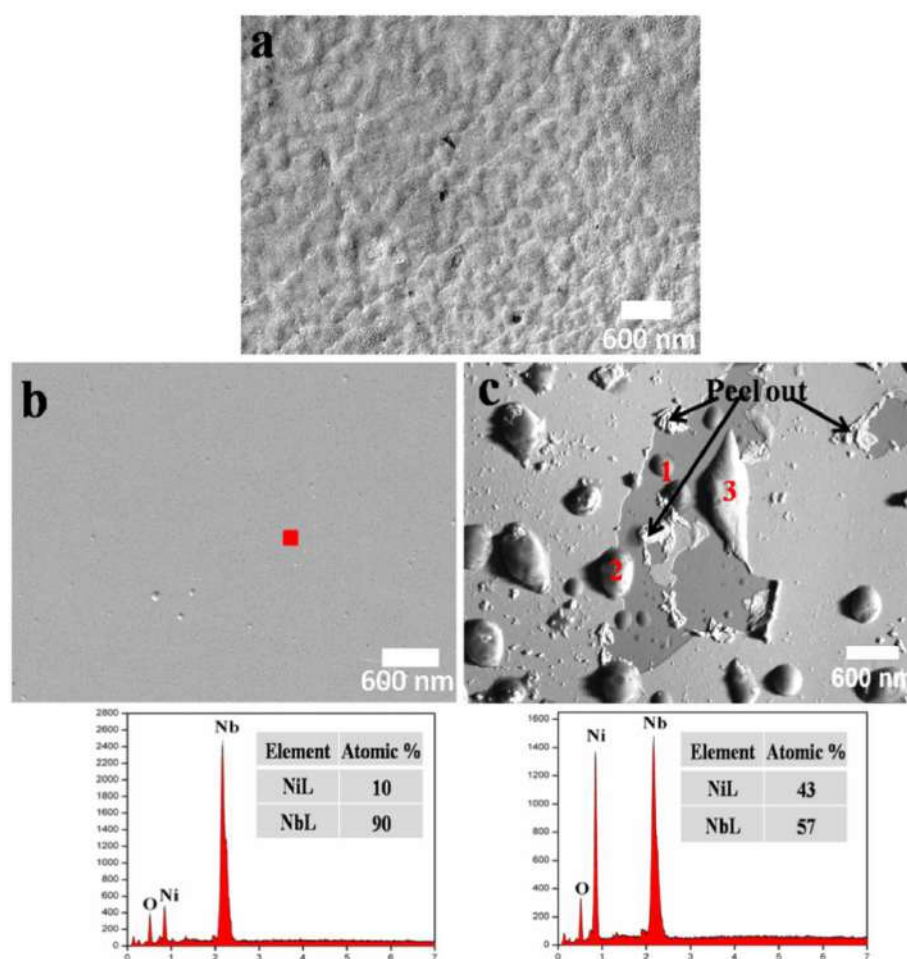


Figure 5.5 FESEM images of thermally oxidized ribbon after potentiodynamic polarization test at 2200 mV in 11.5 M HNO₃ environment; (a) for as-spun ribbon, (b) for 450AR, and (b) for 550AR sample.

Hence, it is essential to investigate the effects of the performance of the oxide film of thermally oxidized Ni₆₀Nb₃₀Ta₁₀ at 450 °C (hereinafter 450MG) and 550 °C (hereinafter 550MG) and its corrosion behavior in comparison with un-oxidized (As-spun MG) counterparts. Furthermore, to understand the effect of the nitric acid concentration on the impedance, polarization, and defect density, the studies on the as-spun and thermally oxidized sample immersed in the various 1, 6 and 11.5 M HNO₃ acid solutions are investigated.

5.2.2.1 Electrochemical impedance behavior of as-spun and thermally oxidized

Ni₆₀Nb₃₀Ta₁₀ metallic glassy alloy

EIS measurement was performed to examine the passivation behavior of as-spun Ni₆₀Nb₃₀Ta₁₀ metallic glass as well as the thermally oxidized counterparts in 1, 6 in 11.5 M nitric acid. In Fig. 5.6, Nyquist plots shows that the diameter of the capacitive loop of the 450MG ribbon is increased compared to capacitive loop in the as-spun MG and 550MG sample. Thus, indicating higher film resistance enriched with Nb₂O₅-Ta₂O₅ on 450MG sample. In Fig.5.6, 550MG sample exhibits a lower capacitive loop compared to the as-spun metallic glass, indicating a decrease in corrosion resistance of crystalline with NiO and Ni₂O₃.

The smaller values of solution resistance for both the sample are negligible when compared to polarization resistance (R_p), as given in table 5.3. The variation of the polarization resistance as per the nitric acid concentration followed the order as; 1 M > 6 M > 11.5 M. With the increasing in the nitric acid concentration from 1 M, 6 M to 11.5 M, the values of the polarization resistance of as-spun, 450MG and 550MG decreased, which indicates the higher oxidizing nature of the concentrated nitric acid.

The order of the polarization resistance is as followed in all three nitric acid; 450MG > as-spun MG > 550MG. The R_p for the 450MG sample are significantly higher than

Table 5.3 EIS parameter of as-spun and thermally oxidized (450°C and 550 °C) MG sample.

Alloy/ Condition	Impedance parameter								
	R_s (Ω cm ²)			R_p ($M\Omega$ cm ²)			C (μ F/cm ²)		
	1M	6M	11.5M	1M	6M	11.5M	1M	6M	11.5M
As-spun	3.6	2.7	2	16	9.5	7.5	0.81	1.1	3.8
450 TO-MG	3.7	2.8	2.1	20	13	3.3	0.68	0.91	2.2
550TO-MG	3.3	2.3	1.9	11	3.2	1.5	1	3.58	5.2

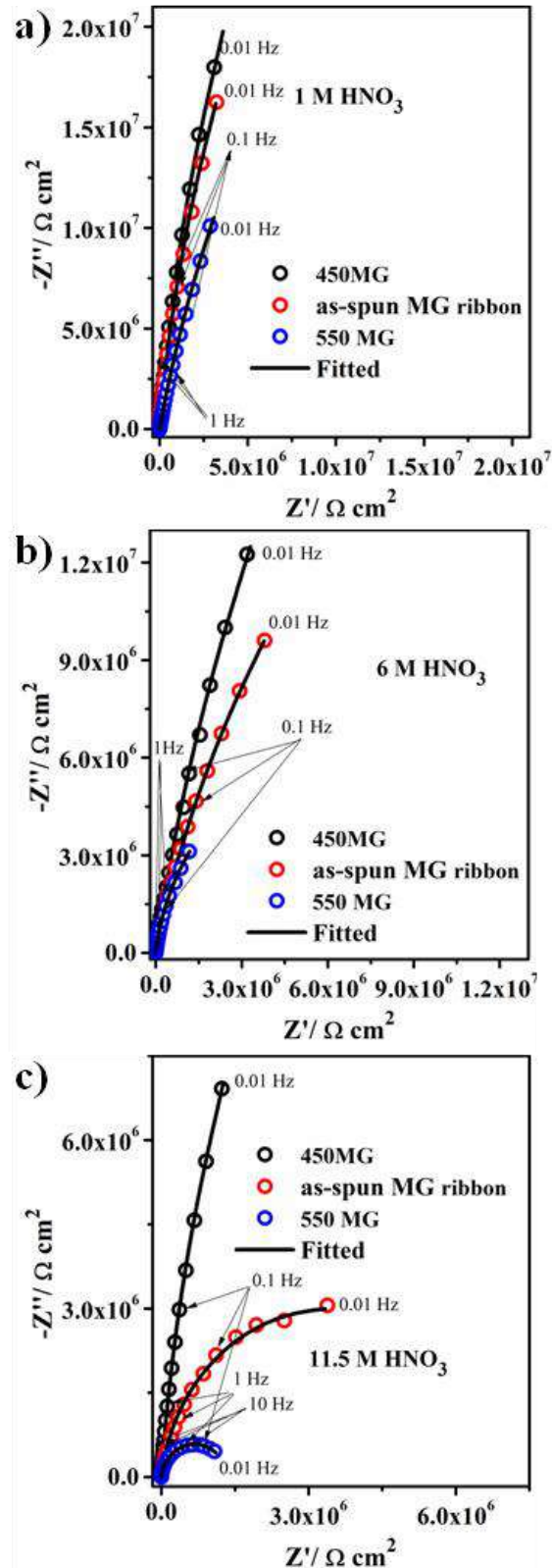


Figure 5.6 (a-c) Impedance spectra obtained from as-spun $\text{Ni}_{60}\text{Nb}_{30}\text{Ta}_{10}$ metallic glass ribbon sample (a) in 1 M, (b) 6 M, and (c) 11.5 M nitric acid.

that of as-spun and 550MG sample. The observation of higher polarization resistance (R_p) for

Chapter 5

450MG sample reveals the low charge transfer at the solution/ film interface. Since all the elements are densely packed in the amorphous $\text{Nb}_2\text{O}_5\text{-Ta}_2\text{O}_5$ oxide of thermally oxidized film than in the defective film enriched with NiO, Ni_2O_3 of 550MG sample, the diffusion of corrosive electrolytes or ions in the amorphous oxide layer is more difficult compared to the defective film of 550MG sample. The stability of the thermally oxidized film with the amorphous structure of 450MG sample has a significant effect on the corrosion resistance in concentrate nitric acid. Above results confirmed that amorphous $\text{Nb}_2\text{O}_5\text{-Ta}_2\text{O}_5$ oxide film on 450MG sample surface shows significantly improved corrosion resistance compared to its un-oxidized sample.

In contrast, the low polarization resistance for 550MG sample could be attributed to heterogeneity or more defective site present in the crystalline NiO, Ni_2O_3 oxide film [85]. Electrolytes could diffuse through the defective sites and consequently increased ionic conductivity, which makes film less-protective. Moreover, a low value of capacitance for 450MG sample in all three nitric acid solutions studied when compared to the as-spun and 550MG ribbon implies a decrease in the reactive area due to better passivation ability of an amorphous $\text{Nb}_2\text{O}_5\text{-Ta}_2\text{O}_5$ oxide film [88].

The relatively higher capacitance of the NiO, Ni_2O_3 enriched oxide layer is due to the thermally oxidized film at 550 °C is more defective in nature. On the other hand, in comparison to 450 °C oxidation, the $\text{Ni}_{60}\text{Nb}_{40}$ amorphous ribbon sample (450AR sample), the thermally oxidized $\text{Ni}_{60}\text{Nb}_{30}\text{Ta}_{10}$ metallic glass at 450 °C (450MG) exhibits higher polarization resistance. The increases R_p of 450MG is due to the formation of compact amorphous $\text{Nb}_2\text{O}_5\text{-Ta}_2\text{O}_5$ oxide film, while the absence of Ta_2O_5 in the 450AR film results in the relative decreases in the polarization resistance. Similarly, for as-spun $\text{Ni}_{60}\text{Nb}_{30}\text{Ta}_{10}$ metallic glass, relatively higher R_p resistance is observed when compared to that of $\text{Ni}_{60}\text{Nb}_{40}$ amorphous ribbon. This is due to the passive film formed in nitric acid which is incorporated

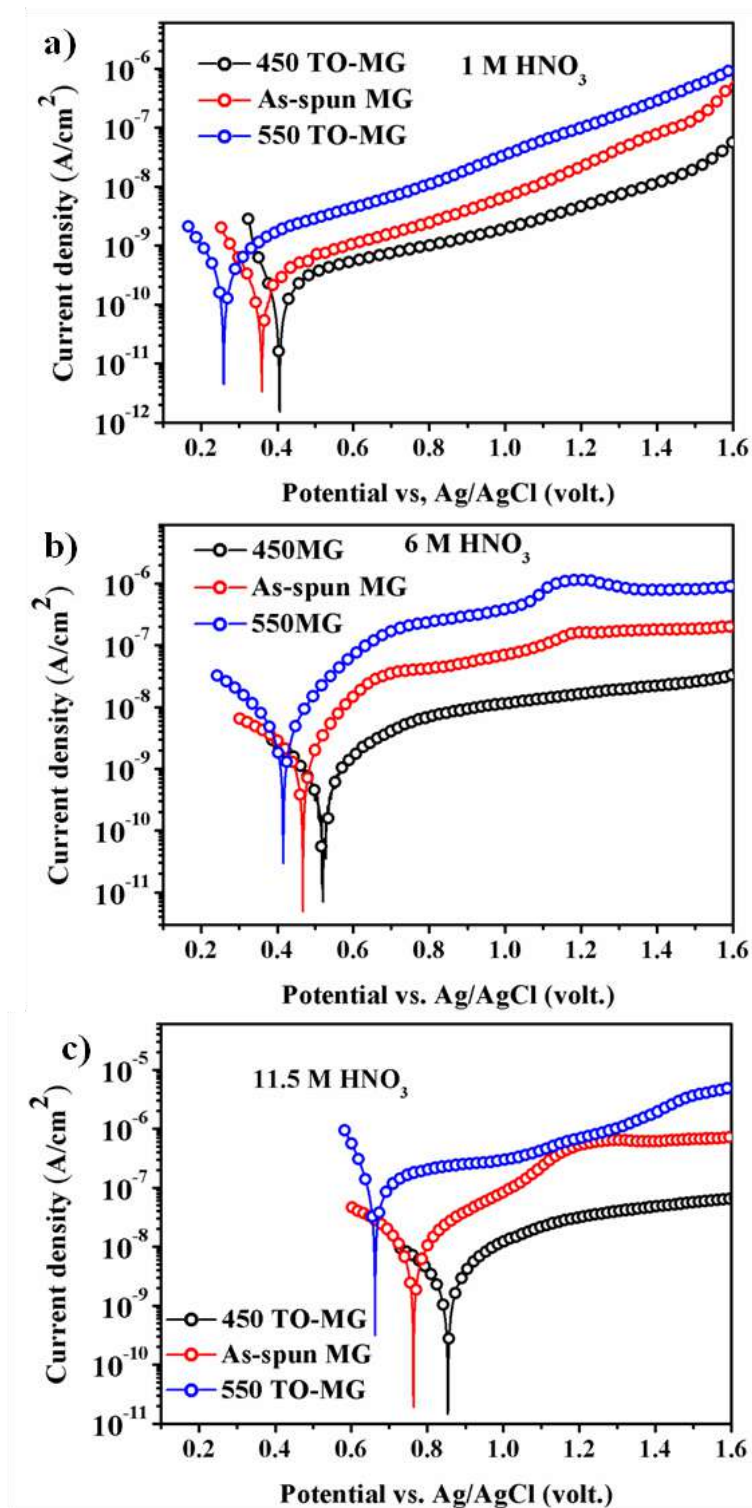


Figure 5.7 (a-c) Potentiodynamic polarization obtained from as-spun Ni₆₀Nb₃₀Ta₁₀ metallic glass ribbon sample (a) in 1M, (b) 6 M, and (c) 11.5 M nitric acid medium.

With both Nb- and Ta-oxide (Fig. 3.8), while passive film contributed only Nb-oxide on Ni₆₀Nb₄₀ amorphous ribbon.

5.2.2.2 Potentiodynamic polarization behavior of as-spun and thermally oxidized $\text{Ni}_{60}\text{Nb}_{30}\text{Ta}_{10}$ glassy alloy.

The potentiodynamic polarization tests on the as-spun, 450MG, and 550 MG samples were carried out in 1M (Fig.5.7 (a)), 6 M (Fig.5.7 (b)), and 11.5M (Fig.5.7 (c)) nitric acid at the scan rate of 0.166 mV/s. As previously discussed, the corrosion potential E_{corr} , and corrosion current density, I_{corr} , were measured by Tafel extrapolation method [113] and tabulated in Table 5.4. For all sample studied, the trans-passive region did not appear up to 1.6 V. The E_{corr} value on the as-spun MG in nitric acid was slightly higher than 550 MG sample, indicating that the passivation nature of Nb and Ta in nitric acid medium, as discussed in Chapter 3 (XPS Fig. 3.8). Usually, the metallic Nb and Ta exhibit passivating nature in the nitric acid medium [88]. For 450MG ribbon, the E_{corr} values is shifted to nobler potential, attributed to the surface of thermally oxidized film enriched with Nb_2O_5 (65%) and Ta_2O_5 (26%).

Table 5.4 Potentiodynamic polarization parameters for as-spun, thermally oxidized at 450 °C (450 TO-MG), and thermally oxidized at 550 °C (550 TO-MG) of the $\text{Ni}_{60}\text{Nb}_{30}\text{Ta}_{10}$ ribbon samples in 1, 6, and 11.5 M HNO_3 environments at room temperature in aerated condition.

Alloy condition	Potentiodynamic polarization parameters											
	E_{corr} vs (Ag/AgCl)			I_{corr}			E_{pass} vs (Ag/AgCl)			I_{pass}		
	mV			nA/cm ²			mV			nA/cm ²		
	1M	6M	11.5M	1M	6M	11.5M	1M	6M	11.5M	1M	6M	11.5M
As-spun MG	359	457	764	0.51	4	20	481	652	895	1.1	36	58
450 TO-MG	405	520	855	0.15	0.6	3.1	528	698	945	0.3	3.2	12
550 TO-MG	258	415	663	0.9	25	138	423	621	760	3	85	204

The differences in E_{corr} are attributed to the fact that the passive film form on as-spun MG ribbon is different from the thermally oxidized film. In contrast, the E_{corr} value of therm

-ally oxidized film on the 550MG sample was shifted to the active potential with respect to the as-spun ribbon due to the role of surface composed of NiO (67 %) and Ni₂O₃ (28.5 %). The shift of the E_{corr} to the higher potential with the increase of nitric acid concentration also indicated the higher oxidizing power of the acid [82]. For all the samples studied, the I_{corr} and I_{pass} increased with the increasing concentration revealing the severity of the effects of nitric acid concentrations (Table 5.4). The order of I_{corr} and I_{pass} in nitric acid solution followed in the order as 550MG > as-spun MG > 450MG. The low I_{corr} and I_{pass} of the 450MG ribbon sample indicating that the higher corrosion resistance of the thermally oxidized insulator film. The high corrosion resistance of 450MG in nitric acid implied that the better stability of thermally oxidized with Nb₂O₅ and Ta₂O₅ enriched oxide film. The stable film on 450MG sample forms a barrier for diffusion of electrolytes and dissolution of cation through the film, thereby improving the corrosion resistance. In contrast, the high I_{corr} and I_{pass} values on 550MG sample with respect to as-spun MG indicated low corrosion resistance of oxide film composed of NiO and Ni₂O₃ on the surface in the nitric acid medium. The highly defective Ni-oxide film on the surface of 550MG sample allows the easy penetration of the anions from the solution. In such a case, the diffusion of the oxidizing nitric acid is more feasible, due to the protective Nb- and Ta-oxide which are completely absent on the surface. Generally, high defect densities in the oxide/passive films are more prone to the corrosion attacks [82]. However, the marginally higher corrosion resistance of the as-spun MG ribbon compared to the 550 TO-MG samples is attributed to lower defect density of the n-type semiconducting film formed when compared to highly defective p-type semiconducting film (Fig. 5.8a and 5.8c). However, low I_{corr} and I_{pass} values are imparted to the better corrosion resistance ability of thermally oxidized film on 450MG samples in comparison to the as-spun and 550 TO-MG and the results comparable with impedance analyses.

In comparison to 450 °C oxidation the Ni₆₀Nb₄₀ amorphous ribbon sample (450AR sample), the thermally oxidized Ni₆₀Nb₃₀Ta₁₀ metallic glass at 450 °C (450MG) exhibits slightly lower I_{corr} and I_{pass} . The low values of I_{corr} and I_{pass} of 450 °C Ni₆₀Nb₃₀Ta₁₀ oxidized sample are due to the compact amorphous Nb₂O₅-Ta₂O₅ oxide film. Relatively, higher values of the I_{corr} and I_{pass} on 450 °C Ni₆₀Nb₄₀ oxidized sample are due to Nb₂O₅ film. Similarly, for as-spun Ni₆₀Nb₃₀Ta₁₀ metallic glass, relatively low corrosion and passivation current density are observed when compared to that of Ni₆₀Nb₄₀ amorphous ribbon. This is due to the passive film formed on as-spun Ni₆₀Nb₃₀Ta₁₀ MG in nitric acid both with Nb- and Ta-oxide (Fig. 3.8), while passive film contributed only Nb-oxide on Ni₆₀Nb₄₀ amorphous ribbon [88].

5.2.2.3 Mott-Schottky analyses of the of as-spun and thermally oxidized Ni₆₀Nb₃₀Ta₁₀ glassy alloy.

The flat band potential (potential in which the slope intersect at $1/C^2 = 0$) for the as-spun ribbon was shifted to the higher potential with an increase in the concentrations from 1, 6, to 11.5 M nitric acid indicating that the higher oxidizing nature of nitric acid (Fig.5.8 (a)). It can be noted that the passive films formed on the as-spun ribbon exhibited higher slopes as the concentration of nitric acid decreases. However, the donor density (N_d) of n-type film on as-spun ribbon sample increased marginally with increases in nitric acid concentration from 1 to 11.5 M nitric acid (Table 5.5). Thus, it is assumed that the donor density of the passive film on the as-spun metallic glass electrode is a function of solution concentration [85]. The increment of the defect density with nitric acid concentration could be attributed to the increases of the thickness of passive film by generating more oxygen ion vacancies and cation interstitials. As discussed earlier, oxygen vacancies and cation interstitials are point defects in the n-type semiconducting film which are responsible for the current carrier in the semiconductor film [114]. The thickness of the passive film and the donor density increased with the solution concentration when the electrode is exposed to the nitric acid solution [85].

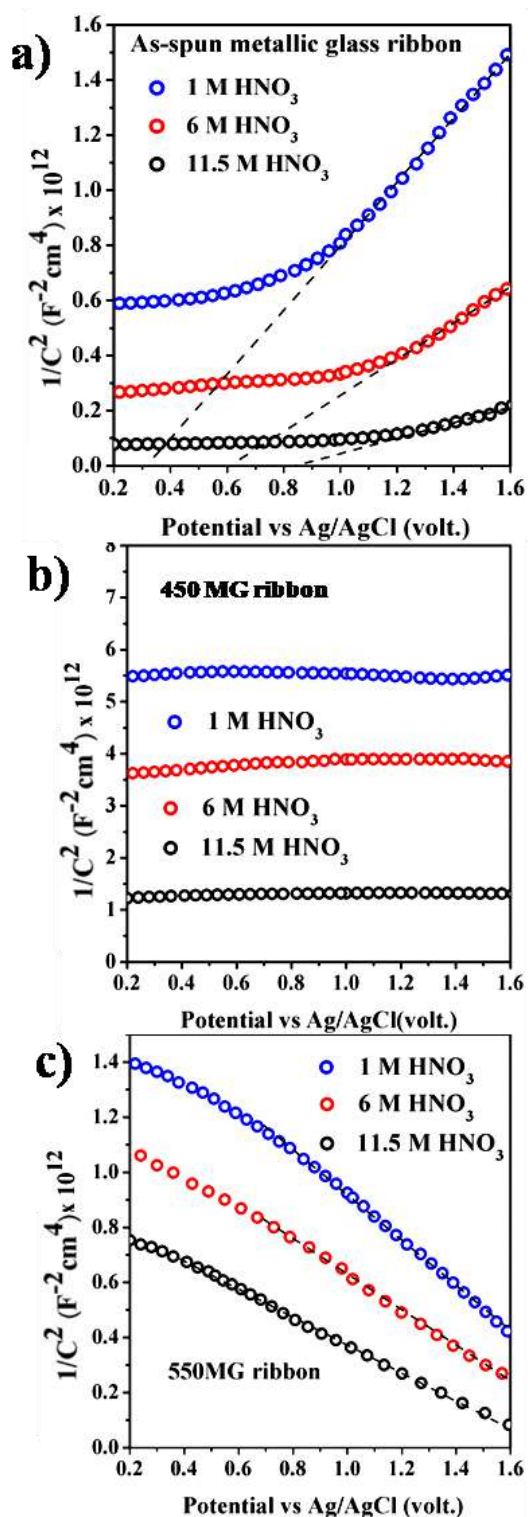


Figure 5.8 Mott-Schottky plots obtained in 1, 6, and 11.5 M nitric acid environment; (a) as-spun $\text{Ni}_{60}\text{Nb}_{30}\text{Ta}_{10}$ metallic glass ribbon, (b) thermally oxidized $\text{Ni}_{60}\text{Nb}_{30}\text{Ta}_{10}$ ribbon sample at 450 °C (450 TO-MG), (c) thermally oxidized $\text{Ni}_{60}\text{Nb}_{30}\text{Ta}_{10}$ ribbon sample at 550 °C (550 TO-MG).

Chapter 5

The stability of the passive film is dependent on the concentration of the nitric acid. Higher concentrations of the nitric acid lower the stability of the passive film. The donor density increases with the concentration of the nitric acid, indicating the more defective and less stable nature of the passive film formed.

Table 5.5 Defect densities obtained from the Mott-Schottky analyses for as-spun and thermally oxidized at 550 °C (550-MG), of the Ni₆₀Nb₃₀Ta₁₀ ribbon samples in 1, 6 and 11.5 M HNO₃ environment at room temperature in aerated condition [85].

Alloy condition	Defect density					
	N _d (cm ⁻³)			N _a (cm ⁻³)		
	1M	6M	11.5 M	1M	6M	11.5M
As-spun MG	2x 10 ¹⁷	2x 10 ¹⁸	8x 10 ¹⁸	-	-	-
550 TO-MG	-	-	-	6x 10 ¹⁸	8x 10 ¹⁹	5x 10 ²⁰

In Fig.5.8 (b), the slope of space charge capacitance did not change with respect to the applied potential for 450MG sample in 1, 6 and 11.5 M nitric acid which revealed that the thermally oxidized film is insulator in nature. The observation of insulator properties of the thermally oxidized film on 450MG sample is due to the surface of the film enriched with high dielectric oxide Nb₂O₅ and Ta₂O₅ as evidenced from XPS results (Fig.4.13d-f). The photoelectrochemical measurements for amorphous Nb₂O₅ and Ta₂O₅ film are reported to possessed high dielectric properties (or insulator) and the large band gap of 3.5-4.1 eV [115]. Franco et al. [115] reported that the Nb₂O₅ usually behaves as an n-type semiconductor, but doping of the right proportion of Ta₂O₅ changes it into the insulator. In the present work, the surface proportions of 450MG ribbon obtained from XPS study (Fig. 4.13d-f) for Nb₂O₅ (67%) and Ta₂O₅ (24%) are in good agreements with the reported value [115]. For the thermally oxidized amorphous Ta₂O₅ film, Fleming et al. reported that defect concentration located at the metal/insulator interface and remarkably reduced when moving towards the

Ta₂O₅ film which could arise due to the annihilation of the defect concentration by Ta⁵⁺ ions [116].

In contrast, the negative slope as shown in Fig.5.8 (c) indicates a p-type semiconducting oxide film for the 550MG ribbon in nitric acid. The defect density (N_a) on Ni-oxide enriched film increased with the solution concentration (Table 5.1 and Table 5.5) [85]. In comparison with the n-type semiconducting film on the as-spun ribbon, relatively higher defect density was observed on p-type semiconducting film on 550 TO-MG samples in nitric acid solution. (Table 5.4). Grubac et al. [117] reported that the p-type semiconducting film on Ni-oxide enriched surface. The Ni²⁺ or ³⁺ ions are incapable of annihilating of the cation vacancies on Ni-oxide film; thereby resulted in more acceptor density generated on 550 MG films when the nitric acid concentration increased [117]. Mott-Schottky studied revealed that the Ni-oxide film on 550MG sample is highly defected compared to the insulator oxide film enriched with Nb₂O₅-Ta₂O₅ on the 450MG sample (Table 5.5).

The passive film on as-spun Ni₆₀Nb₃₀Ta₁₀ metallic glass and Ni₆₀Nb₄₀ amorphous alloys, exhibited n-type semiconducting with lower defect densities when compared to the 550 °C oxidized Ni₆₀Nb₃₀Ta₁₀ and Ni₆₀Nb₃₀ samples (Table 5.5 and 5.1) [85]. However, the donor density on as-spun Ni₆₀Nb₃₀Ta₁₀ metallic glass is relatively higher than the as-spun Ni₆₀Nb₄₀ amorphous alloy in 11.5 M nitric acid. The addition of Ta in Ni-Nb system decreases donor densities in the passive film in concentrated nitric acid. This is due to the stable Nb- and Ta-oxide passive film on as-spun Ni₆₀Nb₃₀Ta₁₀ MG in nitric acid (Fig. 3.8). However, the thermally oxidized Ni₆₀Nb₃₀Ta₁₀ metallic glass at 450 °C (450MG) exhibited insulating behavior while for 450AR Ni₆₀Nb₄₀ sample; n-type semiconducting behavior was observed. In contrast, both thermally oxidized samples at 550 °C exhibits p-type

semiconducting behavior with higher defect density, which is due to the surface enriched with defective NiO and Ni₂O₃.

5.2.2.4 Effect of nitric acid concentration

The shift of the E_{corr} to nobler potential with increasing nitric acid concentration is due to the electro-active species, which were effectively reduced on the amorphous oxide film [41, 82]. Because the amorphous oxide film provided more surface area compared to the crystalline alloy.

However, the corrosion reactions in high concentrated nitric acid involve the generation of electro-active species such as nitrous acid (HNO₂) contributing to the autocatalytic reaction [41, 82]. The generation of the HNO₂ resulted from the oxidant such as NO₂ by autocatalytic reduction of HNO₃ on electrode surface [41, 82]. Evans [118] originally proposed and validated the mechanism that deals with autocatalytic corrosion of metal in a nitric acid environment. The autocatalytic reduction of HNO₃ to HNO₂ and then to NO₂ occur in a higher concentration of the nitric acid (> 8 M HNO₃) [82, 118].



The generations of nitrate ions by the auto-protonation of the nitric acid are also reported [118].



The active oxidizing species in the concentrated 11.5 M nitric acid medium [41,82] could promote dissolution on the 550MG film. In all concentrated of nitric acid, the amorphous oxide film on 450MG sample provides protective barrier for the corrosion against the corrosive species. The higher corrosion resistance of 450MG sample is attributed due to amorphous film enriches with Nb₂O₅ and Ta₂O₅. The corrosion current and passivation

current density marginally increases for thermally oxidized and as-spun metallic glass sample with increment of the nitric acid concentration (Table 5.3). Similarly, the polarization resistance decreases marginally of all the sample with increment of the nitric acid concentration from 1, 6, to 11.5 M. The variation of E_{corr} , I_{corr} , I_{pass} and R_p with nitric acid are attributed to higher oxidizing power of the concentrated [41, 82]. Aggressive nature of the concentrated nitric acid could be due to the generation of HNO_2 which affects the stability of the oxide film [41, 82] and the aggressive order of nitric acid solution followed: 11.5 M > 6 M > 1 M.

5.2.3 Electrochemical corrosion behavior of as-spun and thermal oxidized $\text{Ni}_{50}\text{Nb}_{25}\text{Zr}_{25}$ in 11.5 M nitric acid.

The trans-passive corrosion under the highly oxidizing nitric acid condition is a major issue for the structural components such as stainless steel (SS) of type 304L, and nitric acid grade alloys used in spent nuclear fuel reprocessing plants [41, 82]. Any process delaying the trans-passivity or enhancing the resistance to the trans-passive breakdown of the alloys is important for the application in the concentrated nitric acid environment. Previous studied showed that the adequate corrosion resistance of the thermally oxidized film formed on $\text{Ni}_{60}\text{Nb}_{40}$ and $\text{Ni}_{60}\text{Nb}_{30}\text{Ta}_{10}$ metallic glass in 11.5 M nitric acid. However, the thermal oxidation of $\text{Ni}_{60}\text{Nb}_{40}$ and $\text{Ni}_{60}\text{Nb}_{30}\text{Ta}_{10}$ ribbon at 450 °C exhibited improved corrosion resistance in 11.5 M nitric acid but it also exhibited trans-passivity breakdown near 2 V. This also could be due to the thin oxidized film formed at 450 °C and 550 °C. In contrast, thermally oxidized $\text{Ni}_{50}\text{Nb}_{25}\text{Zr}_{25}$ metallic glass at 400 °C forms relatively thicker amorphous oxide film in the air-environments. The distinct corrosion behavior of thermally oxidized $\text{Ni}_{50}\text{Nb}_{25}\text{Zr}_{25}$ metallic glass was observed compared to thermally oxidized $\text{Ni}_{60}\text{Nb}_{40}$ and $\text{Ni}_{60}\text{Nb}_{30}\text{Ta}_{10}$ metallic glass in 11.5 M nitric acid.

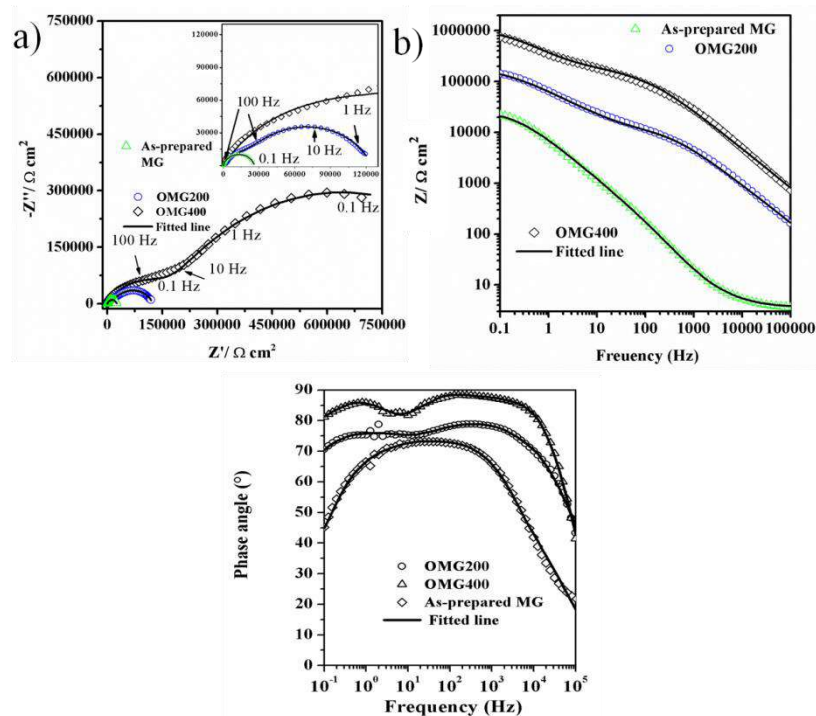
5.2.3.1 EIS behaviours of as-spun and thermal oxidized Ni₅₀Nb₂₅Zr₂₅.

Figure 5.9 Impedance results of the as-prepared and thermally oxidized metallic glass (OMG) ribbon in 11.5 M nitric acid at room temperature; (a) Nyquist plots, (b) Bode modulus, and (c) Bode phase.

Fig.5.9 showed the results of the EIS measurement of as-prepared and thermally oxidized metallic glass ribbon in 11.5 M nitric acid environment at respective open circuit potential (OCP). Good agreement between experimental and corresponding K-K transformed data confirming that the present system satisfied the linearity of the system. Fig.5.9 (a), and Fig.5.9 (b), show the Nyquist, Bode modulus and Bode phase respectively. The Nyquist plot (Fig.5.9 (a)) exhibits only one capacitive loop for the as-prepared (or as-spun) metallic glass, and the alloy/electrolyte interface was replica by a simple Randles circuit ($R_s (R_p \parallel CPE_{MG})$) (Fig.5.10 (a)). However, the Nyquist plot of thermally oxidized metallic glass at 200 (herein after 200MG) and at 400 (herein after 400MG) ribbons showed a high frequency and low-frequency capacitive loop. The high-frequency capacitive loop is directly proportional to the

surface film resistance, while a low-frequency capacitive loop corresponded to the charge transfer resistance [119]. Air-oxidized Ni₅₀Nb₂₅Zr₂₅ metallic glass sample at 200 °C and 400 °C exhibited two times constant while as-prepared metallic glass exhibited one time constant. Bode phase results is consistency with the Nyquist and Bode modulus.

By comparing 400MG sample with the 200MG specimen, an increased diameter of first capacitive loops for the 400MG sample is attributed to higher film resistance. The good fitting of the experimental impedance data of thermally oxidized metallic glass sample using the equivalent circuit ($R_s(CPE_{OMG1} \parallel R_f(CPE_{OMG2} \parallel R_{ct}))$) is shown along with the substrate/film/electrolyte interface in a schematic diagram (Fig.5.10 (b)).

The low χ^2 values indicated the best fit for the fitting quality of the proposed equivalent circuit and the fitted parameters are summarized in Table 5.6. In Fig.5.9 (b), the Bode modulus plots of oxidized metallic glass exhibited three discrete regions (I) at high frequency, demonstrating the solution resistance, (II) intermediate frequency of range roughly 1000 Hz to 100 Hz revealed a capacitive behaviour of barrier film (III) at low frequency from 10 Hz to 0.1 Hz is an indicative of second capacitive behaviour. The absence of a frequency independent Z region at a low frequency can be an indicative of a diffusion-controlled corrosion process. The Z value in low-frequency region is appeared to very high for oxidized metallic glass when compared to the as-prepared MG sample. Considering the Nyquist plot with two capacitive loops, i.e., the two-time corrosion resistance of oxidized MG sample depends on the sum of the oxide film resistance (R_f) and the charge transfer resistance (R_{ct}), which is given as R_t , the total resistance. The total resistance, R_t , ($R_t = R_f + R_{ct}$) is approximately equal to the polarization resistance (R_p).

In Table 5.6, 400MG (745 ± 1) k Ω cm² sample exhibits a higher value of total R_p compare to the 200MG (125 k Ω cm²) and as-prepared MG (26 k Ω cm²)

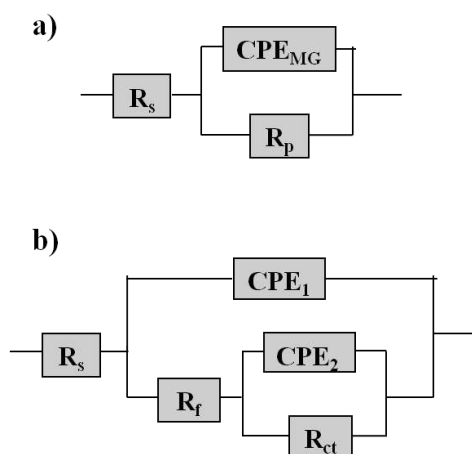


Figure 5.10 The equivalent circuits with schematic of substrate/film/electrolyte interface of the passive film: (a) $[R_s(CPE||R_p)]$ circuits used for fitting of the experimental impedance data obtained from as-prepare ribbon, and (b) $(R_s(CPE_{OMG1} || R_f(CPE_{OMG2} || R_{ct})))$ circuits used for fitting of the experimental impedance data obtained from OMG ribbon.

Table 5.6 Electrochemical Impedance spectroscopy parameters obtained for as-prepared and oxidized metallic glass (OMG) sample in 11.5 M nitric acid.

Sample	Electrochemical parameters							
	R_s	R_p	C_{MG}	R_f	R_{ct}	$R_p=(R_f + R_{ct})$	C_1	C_2
	Ωcm^2	$\text{k}\Omega\text{cm}^2$	$\mu\text{F}/\text{cm}^2$	$\text{k}\Omega\text{cm}^2$	$\text{k}\Omega\text{cm}^2$	$\text{k}\Omega\text{cm}^2$	nF/cm^2	nF/cm^2
As-spun MG	3 ± 1	26 ± 0.1	19.3 ± 0.2	--	--	--	--	--
OMG200	203 ± 1	--	--	30 ± 0.4	97 ± 0.4	127 ± 0.8	37 ± 1	155 ± 2
OMG400	856 ± 2	--	--	174 ± 0.5	574 ± 0.5	748 ± 1	125 ± 2	998 ± 4

The difference in the R_s indicates the distinct behavior of thermally oxidized sample and as-prepared metallic glass in 11.5 M nitric acid solution. It can be seen that polarization resistance (R_p) of the alloy significantly increased after oxidation in air at 200 °C and 400 °C. The higher R_p of both oxidized metallic glass revealed higher corrosion resistance compared to the as-prepared glassy ribbon. The improved corrosion resistances are attributed to excellent protective nature of the thermal oxide film in concentration of nitric acid medium. A dense protective amorphous ZrO_2 and Nb_2O_5 film on surface oxide layer of 400MG sample

significantly enhance R_p values in 11.5 M nitric acid medium. A low value of R_p of the as-prepared glassy sample shows that the high charge transfer across the oxide film/electrolyte interface may be attributed to the formation of the thin defective passive film.

However, the only single time constant is observed for thermally oxidized $Ni_{60}Nb_{40}$ and $Ni_{60}Nb_{30}Ta_{10}$ metallic glass in 11.5 M nitric acid, while two time constants are observed for thermal oxidized $Ni_{50}Nb_{25}Zr_{25}$ metallic glass. The appearance of the single time constants in impedance spectra on thermally oxidized $Ni_{60}Nb_{40}$ and $Ni_{60}Nb_{30}Ta_{10}$ metallic glass are due to the formation of thin film (Chapter 4) which remain intact to the substrate. However, the two time constants on thermally oxidized $Ni_{50}Nb_{25}Zr_{25}$ metallic glass is attributed to the formation of the relatively thicker oxide film (Fig.4.).

5.2.3.2 Potentiodynamic polarization behavior of as-spun and thermal oxidized $Ni_{50}Nb_{25}Zr_{25}$ in 11.5 M nitric acid.

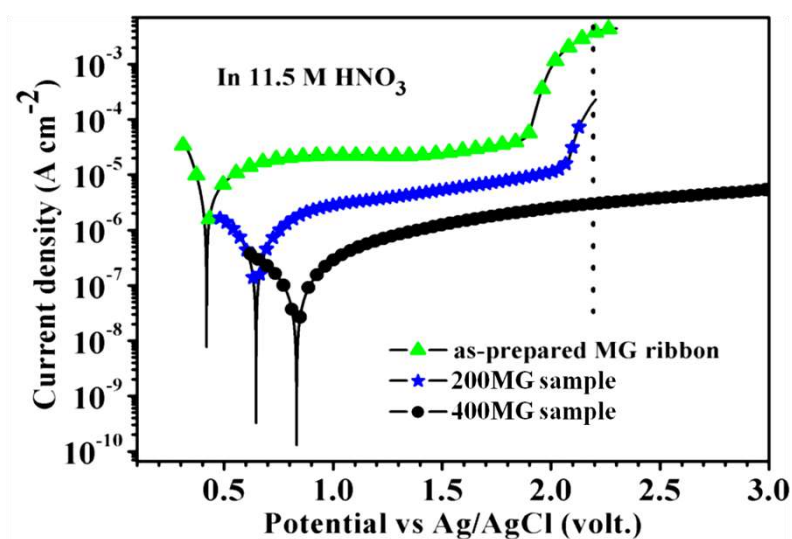


Figure 5.11 Potentiodynamic polarization curves for the as-prepared and thermally oxidized $Ni_{50}Zr_{25}Nb_{25}$ metallic glass (200-OMG and 400-OMG) in 11.5 M nitric acid medium at room temperature.

Chapter 5

The potentiodynamic polarization results of the as-prepared and thermally oxidized MG ribbons in the concentrated nitric acid environment are shown in Fig.5.11. The corrosion current density (I_{corr}), passive current density I_{pass} , corrosion potential E_{corr} , and trans-passive potential E_{trans} are presented in Table 5.7. The as-prepared $\text{Ni}_{50}\text{Zr}_{25}\text{Nb}_{25}$ metallic glassy ribbon exhibits a passive region from 618 mV to 1887 mV (Ag/AgCl). In addition, the corrosion potential (E_{corr}) is shifted to the nobler side for oxidized sample compared to the as-prepared glassy alloy. Just above E_{corr} , polarization curve shows no active-passive transition, indicating both as-prepared and oxidized sample alloy exhibit spontaneous passivation. The E_{corr} of the as-prepared and oxidized metallic glass sample vary indicating the nature of the films are different due to the different chemistry of the oxide structure. The shift of E_{corr} to more noble potentials for oxidized metallic glass also indicated that an oxide layer coated metallic glass are less prone to corrosion attack in nitric acid solution.

Table 5.7 Potentiodynamic polarization parameters obtained of as-prepared and oxidized metallic glass ribbon sample in 11.5 M nitric acid.

Alloy condition /3 M HNO_3	Electrochemical parameters				
	E_{corr} Vs (Ag/AgC)	i_{corr}	E_{pass}	j_{pass}	E_{trans}
	mV	$\mu\text{A}/\text{cm}^2$	mV	$\mu\text{A}/\text{cm}^2$	mV
As-prepared MG	420	10.5	618	15.5	1887
OMG200	648	0.7	826	2.04	2058
OMG400	834	0.15	973	0.273	--

However, the I_{corr} and I_{pass} decreased in the following order: as-prepared MG > 200MG > 400MG ribbon samples. In 11.5 M nitric acid, the oxidized metallic glass alloys show significantly lower I_{corr} and I_{pass} compared to that of the as-prepared metallic glass ribbon. The decreases in I_{corr} and I_{pass} are indicative of higher corrosion resistance of oxidized metallic glassy sample compared to the as-prepared alloy which is due to the pre-form amorphous oxide film on the glassy alloy. In general, an oxide film with amorphous structure exhibited higher corrosion resistance to their structural and compositional homogeneity. Since the

amorphous metal oxides are densely packed (Fig. 4.18b), the diffusion of corrosive electrolytes or ions in the amorphous layer is more difficult.

In comparison to the as-prepared ribbon, the 200MG sample exhibited relatively wider passive region (from 826 mV to 2058 mV). For 400MG ribbon sample, an exceptionally distinct behavior was observed. The 400MG alloy exhibited significantly wider passive region, and trans-passive breakdown was not observed even up to 3 V (Ag/AgCl) in 11.5 M nitric acid. By comparing 400MG samples with 200MG sample, a remarkably large passive region of 400MG sample is attributed to the thick oxide film (721 nm) formed. A thicker oxide film with amorphous structure has significant effect to counter early trans-passive breakdown in concentrated nitric acid medium. Similarly, the surface composition of the oxide layer also plays an important role in the film resistance and passivation ability in oxidizing nitric acidic solution [85]. Similarly, the corrosion resistance of ZrO_2 and Nb_2O_5 are much higher than Ni-oxide (NiO and Ni_2O_3), an increment of ZrO_2 and Nb_2O_5 on the surface enhance the corrosion resistance. Based on the XPS depth profile results (Fig.5.24), the Ni-depleted within 0-125 nm depth, whereas oxide layer are enriched with ZrO_2 and Nb_2O_5 for 400MG sample. Since amorphous structure of ZrO_2 and Nb_2O_5 oxide are packed with very few defect densities, the diffusion of active oxidizing species (NO_3^- , NO_2^- , and NO_2) could slow down to a great extent and isolated inner metallic substrate from those aggressive species. It is well known that amorphous Nb_2O_5 and ZrO_2 oxide film exhibits strong corrosion resistance in many different acidic or aqueous solutions [120]. Lower corrosion resistance of OMG200 sample than that of 400MG sample is attributed to the lower thickness of the protective oxide film (106 nm).

5.2.3.3 Film stability behaviour of as-prepared and thermally oxidized Ni₅₀Zr₂₅Nb₂₅ metallic glass after polarization at 2.2 V (Ag/AgCl) in 11.5 M nitric acid.

To compare the stability and breakdown of the passive/oxide film interface, the as-prepared and oxidized metallic glassy alloy was potentiostatically polarized at 2.2 V (Ag/AgCl) in 11.5 M nitric acid for 1 h. The polarized samples were characterized by high-resolution scanning electron microscopy (SEM).

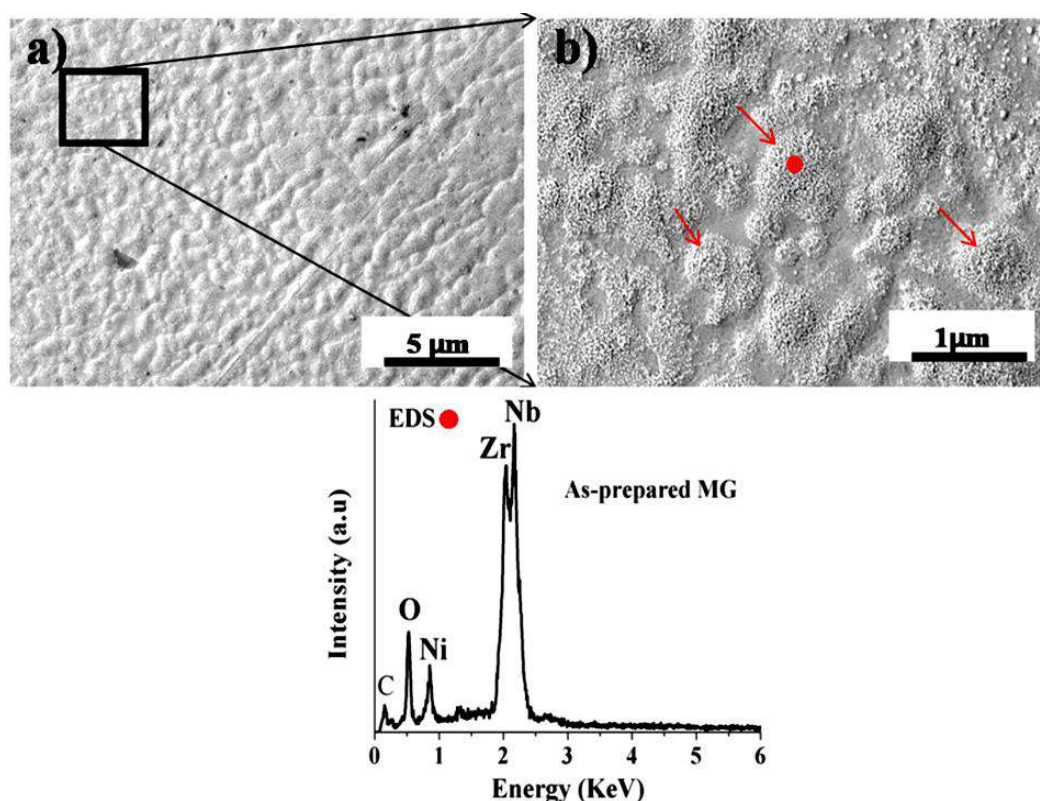


Figure 5.12 The SEM images in different magnifications of the as-prepared MG sample surface ((a) 5 μm and (b) 1 μm)) after potentiostatic polarization test at 2.2 V (Ag/AgCl) in 11.5 M nitric acid environments.

As-prepared sample shows a severe non-uniform attack on the surface attributed to the easy breakdown of the thin passive film following trans-passive dissolution (Fig.5.12(a-b)), respectively. In the higher magnified image (Fig. 12b) shows several island type features on

the surface. Energy dispersive X-ray spectrometry (EDS) on those island exhibits a higher percentage of nobler elements e.g Nb and Zr with a small fraction of Ni and O.

Comparing to the as-prepared glassy alloy, the surface of the 200MG sample undergoes insignificant attack as shown in Fig.5.13(a-b). EDS point analyses shows that the attacked surface are composed of Ni, Nb, Zr and O. The EDS results exhibits low intensity of Ni content after polarization of metallic glass and 200MG in nitric acid, which confirmed that trans-passive dissolution the Ni and its oxide.

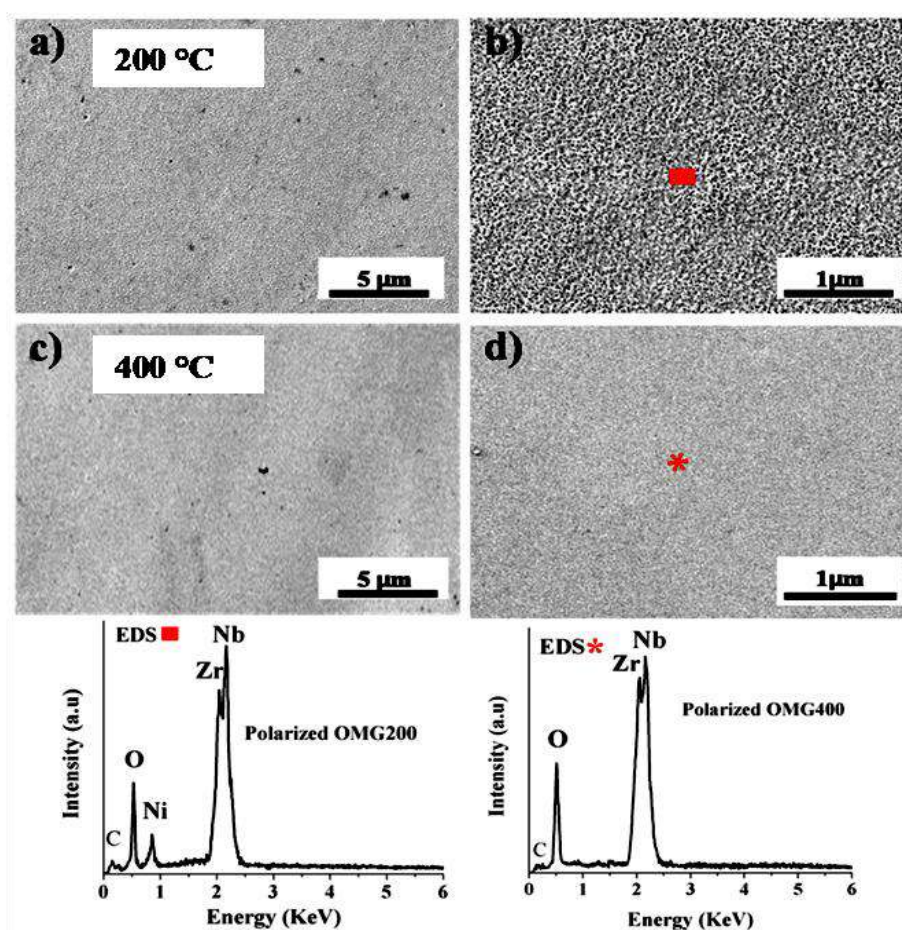


Figure 5.13 SEM and EDS images of the sample surface after potentiostatic polarization test at 2.2 V (Ag/AgCl) in 11.5 M nitric acid environments; (a-b) for 200MG, and (c-d) for 400MG sample.

However, SEM micrographs at low and higher magnification (Fig.5.13(c-d)) showed that the surface of a thicker oxide layer on 400MG sample was uniform with no any attack.

Chapter 5

The EDS of polarized 400MG metallic glass sample show only Nb, Zr and O peak and no Ni peak was observed. Before and after polarization, the film on 400MG sample is stable and similar in the composition. Similarly, SEM results of the 400MG sample (Fig. 4. 13 (c-d)) shows smooth and un-attacked surface which is an indicative of higher stability of the thick oxide film. Such a thick amorphous oxide film is highly desirable for retarding trans-passive breakdown or shifting trans-passive to the much higher potential (beyond 3 V (Ag/AgCl)).

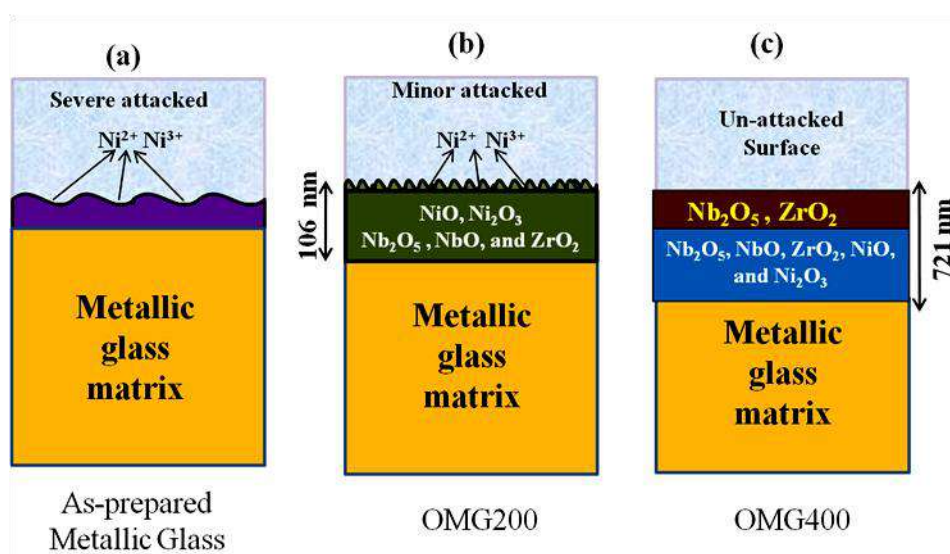


Figure 5.14 Schematic diagram representing the corrosion process in 11.5 M HNO₃ environment (a) passive film on the as-prepared metallic glass undergoes a severe attack following the Ni ions dissolution. (b) The thermally oxidized film at 200 °C sample show minor attack and along with Ni ions dissolution (c) The thick Nb₂O₅ and ZrO₂ film at 400 °C with no sign of corrosion attack in 11.5 M nitric acid.

Moreover, similar composition observed before and after polarization in EDS analyses further confirmed the high stability of oxide film formed on 400MG sample. The potentiostatic polarization and electrochemical impedance spectroscopy results confirmed the protective oxide film on oxidized MG at 400 °C which significantly improved corrosion resistance in concentrated nitric acid solution.

Schematic diagram proposed to understand the corrosion behavior of the as-prepared and thermally oxidized metallic glass sample is shown in Fig.5.14. The breakdown of as-prepared MG and 200MG sample could be initiated by the preferential dissolution of active Ni-cation (Ni^{2+} , and Ni^{3+}) in the film. The film on 400MG sample did not undergo breakdown up to 3V (Ag/AgCl) which is due to the surface film enriched with only ZrO_2 and Nb_2O_5 as evident from XPS results. It has also been recently reported [113] that the Ni-oxide is highly defective (acceptor or defect density of $2.1 \times 10^{-22} \text{ cm}^{-3}$) p-type semiconducting oxide, while ZrO_2 (donor density of $3.8 \times 10^{-19} \text{ cm}^{-3}$) and Nb_2O_5 (donor density of $7.5 \times 10^{-18} \text{ cm}^{-3}$) exhibits stable n-type semiconducting oxide with low defect density. Further, the preferential dissolution of Ni-cation, and growth of the pits on the surface of the $\text{Ni}_{62}\text{Nb}_{38}$ metallic glass in hydrochloric acid solution was reported [30].

Similarly, the trans-passive dissolution of the Ni and its oxide on metallic glass lead to the severe attack (Fig.5.12). Since the Zr and Nb had lower mobility compare to Ni, the dissolution of Zr and Nb oxide are much slower compared Ni-oxide. Finally, Zr^{4+} and Nb^{5+} are accumulated and appeared in the form of an island on the surface of the as-prepared metallic glass (Fig.5.12(b)). In a highly oxidizing nitric acid, dissolution of the Ni-oxide in nitric acid can be represented as follows.



5.3 Summary

- a) Potentiodynamic polarization results showed that the both thermally oxide film on 450 °C oxidized $\text{Ni}_{60}\text{Nb}_{40}$ and $\text{Ni}_{60}\text{Nb}_{30}\text{Ta}_{10}$ MG sample exhibited highly protective barrier to the nitric acid environment when compared as-spun and 550 °C oxidized MG sample.
- b) The oxidized $\text{Ni}_{60}\text{Nb}_{30}\text{Ta}_{10}$ at 450 °C (450MG) exhibited marginally higher corrosion resistance compared to the 450 °C oxidized $\text{Ni}_{60}\text{Nb}_{40}$ amorphous alloy in 11.5 M nitric

acid. For 450 °C oxidation, higher corrosion resistance of $\text{Ni}_{60}\text{Nb}_{30}\text{Ta}_{10}$ is attributed due to the surface comprising of Nb_2O_5 - Ta_2O_5 .

- c) The EIS studies show a single time constant (one loop) for as-spun and oxidized metallic glass $\text{Ni}_{60}\text{Nb}_{40}$ and $\text{Ni}_{60}\text{Nb}_{30}\text{Ta}_{10}$ MG sample. The polarization resistance of as-spun and oxidized $\text{Ni}_{60}\text{Nb}_{30}\text{Ta}_{10}$ metallic glass is higher than the $\text{Ni}_{60}\text{Nb}_{40}$ amorphous system. With increasing the nitric acid concentration, the impedance of both as-spun and oxidized $\text{Ni}_{60}\text{Nb}_{30}\text{Ta}_{10}$ decreases attributed to the higher oxidizing nature of the nitric acid.
- d) The Mott-Schottky analysis confirmed the n-type semiconducting film nature both for as-spun $\text{Ni}_{60}\text{Nb}_{40}$ and $\text{Ni}_{60}\text{Nb}_{30}\text{Ta}_{10}$ MG sample ribbon, while the p-type semiconducting film on the both thermally oxidized sample at 550 °C. However, 450 °C oxide film on $\text{Ni}_{60}\text{Nb}_{40}$ alloy sample exhibits protective n-type semiconductivity, while 450 °C oxidized $\text{Ni}_{60}\text{Nb}_{30}\text{Ta}_{10}$ MG sample behaved as an insulator in the nitric acid environment.
- e) Distinct polarization behaviour was observed for oxidized $\text{Ni}_{60}\text{Nb}_{25}\text{Zr}_{25}$ at 400 °C in 11.5 M nitric acid when compared to the oxidized $\text{Ni}_{60}\text{Nb}_{40}$ and $\text{Ni}_{60}\text{Nb}_{30}\text{Ta}_{10}$ MG ribbons sample. The oxidized $\text{Ni}_{60}\text{Nb}_{25}\text{Zr}_{25}$ MG metallic glass at 400 °C does not exhibit trans-passive breakdown even up to 3 V (Ag/AgCl), while as-prepared and oxidized metallic glass at 200 °C exhibits trans-passive breakdown at 1.887 V and 2.058 V (Ag/AgCl), respectively.

6 Corrosion behavior of Ni-based metallic glassy coating

This chapter deals with the investigation on the corrosion behavior of the $\text{Ni}_{60}\text{Nb}_{30}\text{Ta}_{10}$ metallic glass coated on structural materials of type 304 L SS by Magnetron Sputtering technique and its comparison with the bare 304 L SS in the nitric acid medium using different electrochemical techniques and characterization methods such as XRD, SEM and XPS, etc. The potentiodynamic polarization and EIS results of the $\text{Ni}_{60}\text{Nb}_{30}\text{Ta}_{10}$ coating at 200 °C exhibits higher corrosion resistance compared to that of RT coating and bare 304 L SS. Corrosion rate evaluation in boiling 11.5 M nitric acid that indicated a lower corrosion rate (0.1 mm/y) for the 200 °C coating compared to bare 304 L SS are discussed.

6.1 Introduction

Depositing protective metallic glass coatings on the convention structural and engineering material is a known technique to prevent corrosion. The inter-granular corrosion under the highly oxidizing nitric acid condition is a major issue for the structural components such as stainless steel (SS) of type 304L, and nitric acid grade alloys used in spent nuclear fuel reprocessing plants [82]. The conventional structural alloy such as type 304 L stainless steel (SS) cannot be used in concentrated nitric acid (>9 M HNO_3), as they undergo severe end grain and inter-granular corrosion attack [41]. Comparative studies in Chapter 3 provided inputs in that the $\text{Ni}_{60}\text{Nb}_{30}\text{Ta}_{10}$ metallic glass glassy alloys exhibited higher corrosion resistant when compared to their crystalline parts in concentrated nitric acid medium. Thus, an attempt to deposit $\text{Ni}_{60}\text{Nb}_{30}\text{Ta}_{10}$ metallic glassy alloys as protective coatings on conventional alloys of type 304L SS to enhance the performance and minimize the inter-granular corrosion was carried out.

DC magnetron sputtering technique is a suitable method to produce glassy coating, because the process can achieve a rapid deposition of the atomic layer in random passion and

also provides the high cooling rates that are necessary to quench the sputtered atoms to a glass former alloy into the glassy state. The major advantage of magnetron sputtering in devolving metallic glass for engineering purpose, in contrast to other production techniques like melt spinning, the glassy nature can be obtained in a larger surface area and easy fabrication in short time.

Therefore, this chapter deals with the deposition of the Ni-based metallic glass of composition $\text{Ni}_{60}\text{Nb}_{30}\text{Ta}_{10}$ by DC magnetron sputtering technique onto the traditional structural materials of type 304 L stainless steel. The corrosion properties of the Ni-based glassy coatings will be evaluated in 1, 6, and 11.5 M nitric acid solution solutions at room temperature. In addition, the corrosion resistance of the coated 304 L SS is compared with bare 304 L SS.

6.2 Results and discussion

6.2.1 Synthesis of $\text{Ni}_{60}\text{Nb}_{30}\text{Ta}_{10}$ Thin Film Metallic glass (TFMG) coatings.

The starting material as 3 inch diameter $\text{Ni}_{60}\text{Nb}_{30}\text{Ta}_{10}$ sputtering disk target was obtained from Apphia Advanced Materials Pte Ltd. India and the purity of the elements of Ni (99.9%), Nb (99.9%) and Ta (99.9%) was used to prepare commercial $\text{Ni}_{60}\text{Nb}_{30}\text{Ta}_{10}$ sputtering disk target disk. The $\text{Ni}_{60}\text{Nb}_{30}\text{Ta}_{10}$ disk was directly used as a target in magnetron sputtering for the deposition of the metallic glassy coating on type 304 L SS.

The processing conditions of the sputtered deposit into a glass coating on 304 L SS was carried out at room temperature (RT) and 200 °C. Prior to deposition, the sputtering chamber was evacuated to a base pressure of 3×10^{-6} mbar, and high purity argon gas (grade-1) was used as the sputtering gas. The working pressure was 3×10^{-3} mbar. The sputtering power was

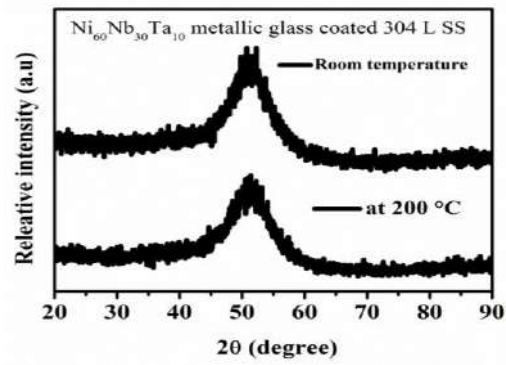


Figure 6.1 XRD of $\text{Ni}_{60}\text{Nb}_{30}\text{Ta}_{10}$ amorphous alloy in the form of coating prepared Magnetron sputtering.

6.2.2 Surface and cross-sectional analyses of TFMG coating.

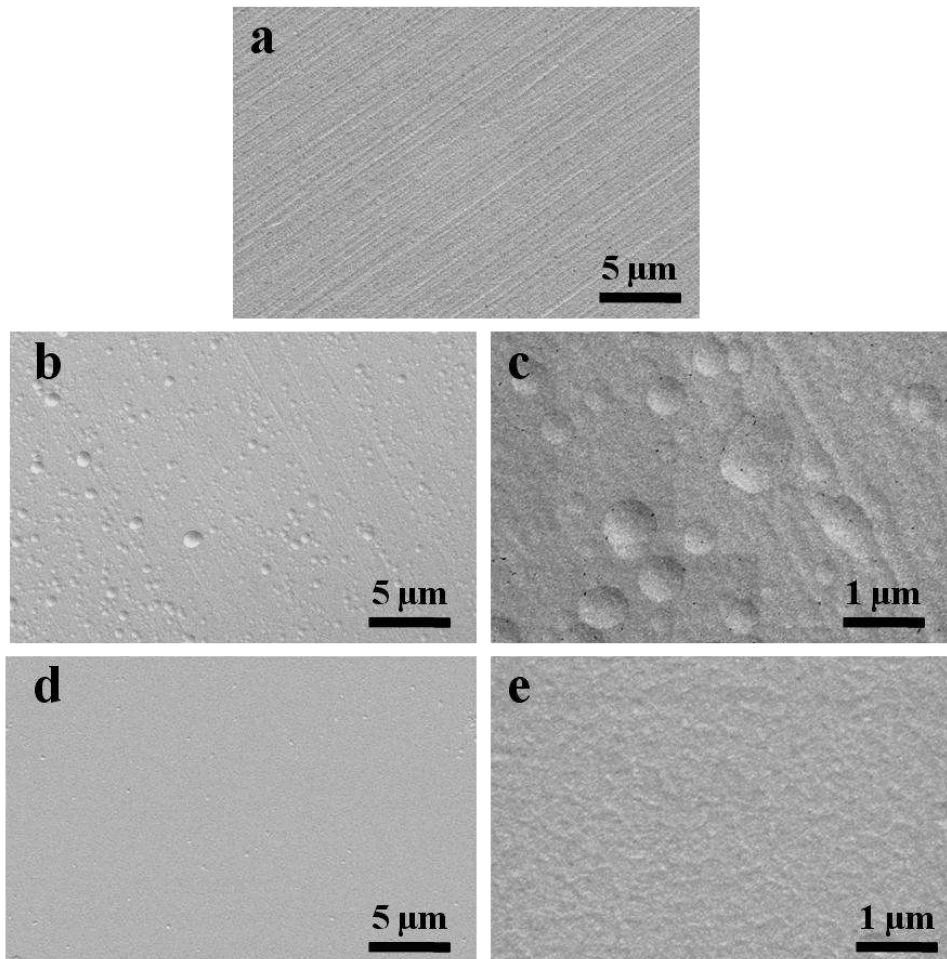


Figure 6.2 Microstructure of the (a) bare 304 L SS, (b-c) $\text{Ni}_{60}\text{Nb}_{30}\text{Ta}_{10}$ Metallic glass coating deposited at RT, and (c-d) $\text{Ni}_{60}\text{Nb}_{30}\text{Ta}_{10}$ Metallic glass coating deposited at 200 °C.

35W and duration of deposition was 1 h. The GIXRD pattern of the TFMG coating at RT and 200 °C (shown in Fig.6.1) exhibited halo peak at a diffraction angle of 50 ° (2 theta), suggesting an amorphous structure formation.

Before deposition, the polishing tracks are visible on the polished type 304 L SS. However, no visible track after deposition TFMG coating deposited at both conditions. No other defects such as micro-segregations or oxides could be detected in this coating. The metallic glass coating at RT exhibits various dimple shape like feature on the surface. On the other hands, the coating deposited at 200 °C are free from the dimple shape like feature and smooth morphology was observed. The smoother surface at 200 °C could be due to the thermal energy provided at 200 °C results in the proper arrangements of the sputter atoms during deposition which finally improves adhesion with 304 L SS substrate.

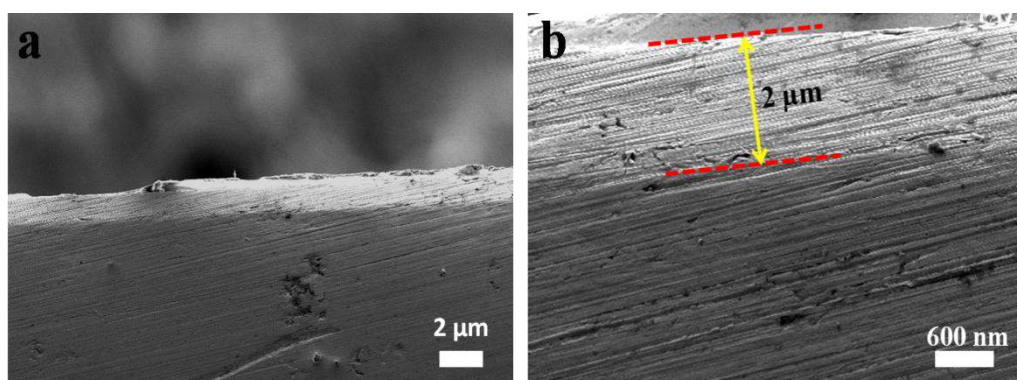


Figure 6.3 200 °C -TFMG/304 L SS substrate cross-sectional images.

In Fig.6.3, the SEM investigations were performed on the TFMG coat /substrate cross-section to determine the thickness of the film deposited on type 304 L SS substrate. The cross-section views indicated the clear contrast of thicknesses of the TFMG coating deposited at 200 °C. The SEM investigations revealed that the metallic glass coating exhibits dense structure and free from the pores and cracks. But scratches are visible which are generated

during the polishing the interface for cross-sectional analyses. The absence of the pores at the interface indicated that the interfaces are less defective and improved adhesion of the coating with the substrate.

6.2.3 XPS studies of the surface as well as depth passive film on the immersed metallic glass coated 304 L SS sample.

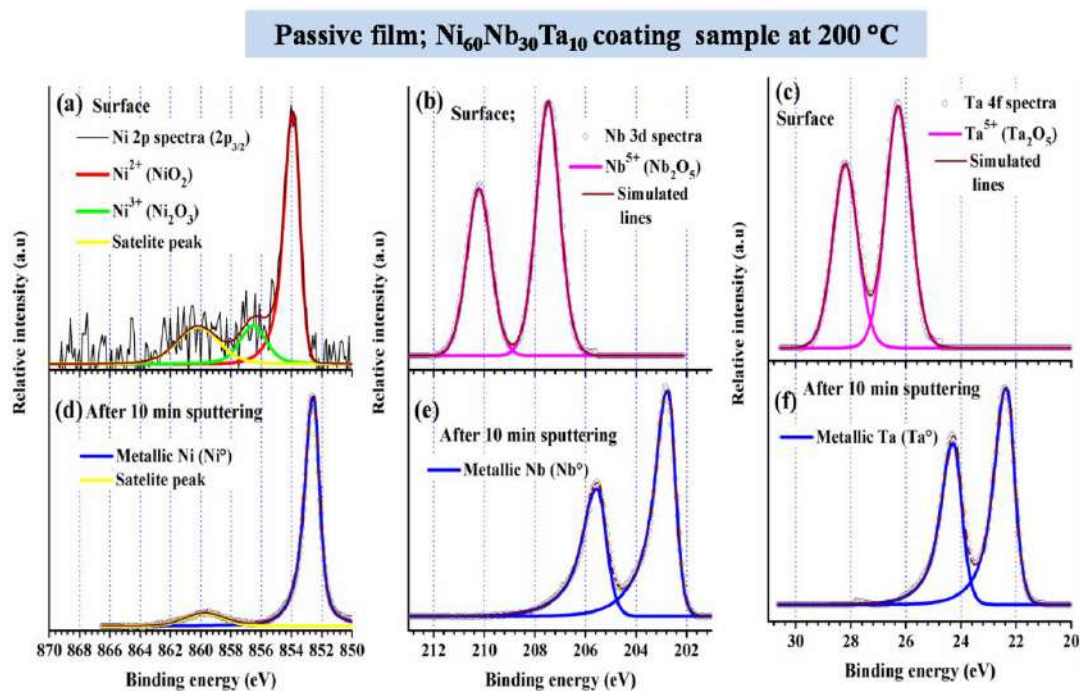


Figure 6.4 (a-c) High-resolution XPS spectra obtained on the surface of the passive film (a-c) of the 200 °C-coating after immersion test in boiling 11.5 M nitric acid for 24 h.; for surface peak (a) NiO, Ni₂O₃ (Ni 2p), (b) Nb₂O₅ (Nb 3d), and (c) Nb₂O₅ (Ta 4f). Complete metallic peak after 10 min sputtering (a) Metallic Ni (Ni 2p), (b) Metallic Nb (Nb 3d), and (c) Metallic Ta (Ta 4f).

The XPS results of the 200 °C and RT Ni₆₀Nb₃₀Ta₁₀ metallic glassy coating after immersion test in boiling 11.5 M nitric acid medium for 24 h. are presented in Fig.6.4(a-c) and 6.5(a-c), respectively. The surface of the passive film on the RT glassy alloy coating composed of composed of Nb₂O₅, and Ta₂O₅, NiO, and Ni₂O₃ with their metallic state while

200 °C coating comprises only oxide film on the surface. The intensity of the Nb₂O₅, and Ta₂O₅ peak on the 200 °C glassy coating are significantly higher than RT coating, indicating the concentration of the Nb₂O₅, and Ta₂O₅ higher than the RT coating. In contrast, the Ni-concentration is higher on RT glassy coating than the 200 °C glassy coating. This suggested that the passivation ability of the smooth surface of 200 °C glassy coating is relatively higher than the rough RT glassy coating.

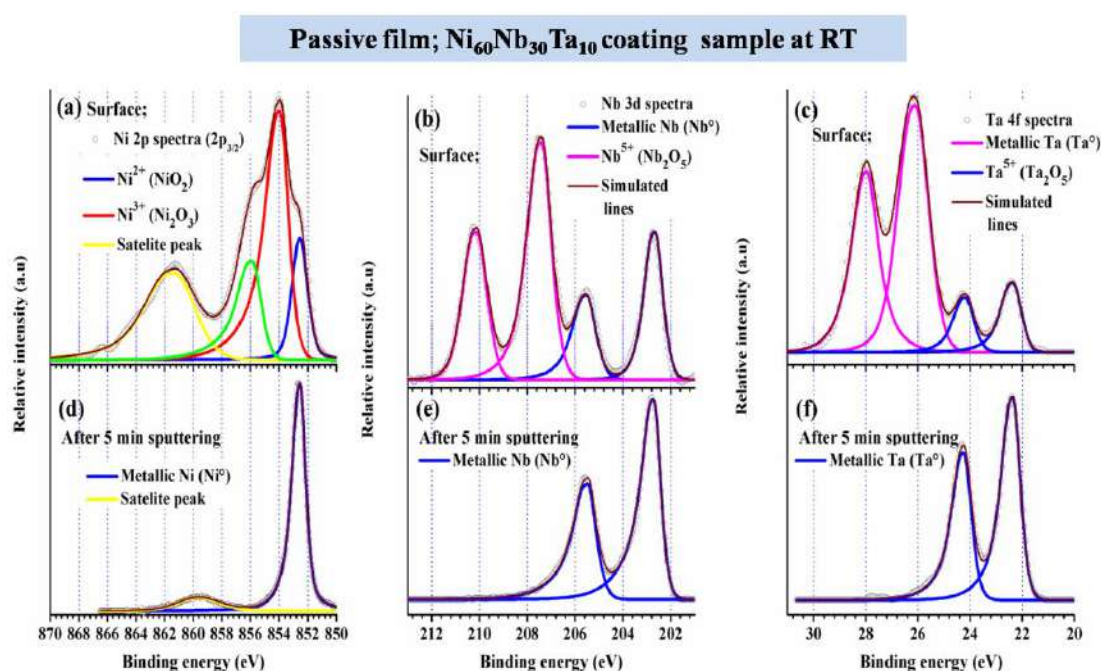


Figure 6.5 High-resolution XPS spectra obtained on the surface of the passive film for RT-coating after immersion test in boiling 11.5 M nitric acid for 24 h.; for surface peak (a) Ni 2p (b) Nb 3d, and (c) Ta 4f. After 5 min sputtering (a) Metallic Ni (Ni⁰), (b) Metallic Nb (Nb⁰), and (c) Metallic Ta (Ta⁰).

The film/substrate interface is considered when the oxide peak disappeared and metallic peak re-appeared. The metallic peak appeared after 10 min sputtering for 200-Coating passive film and 5 min sputtering for RT-Coating passive film. As per the sputtering rate, the ratio was found at 10 nm depth for metallic glass and 5 nm depth for crystallized sample. Based on this assumption, the thickness of the passive film (≈ 10 nm) on 200 °C Ni₆₀Nb₃₀Ta₁₀ metallic

glassy coating is relatively higher than the crystallized film (≈ 5 nm) on the RT glassy alloy coating. The formation of the thicker film reveals the growth of the amorphous passive film on the smooth glassy structure, which is more compared to the rough dimple shape morphology.

6.2.4 Comparison of the potentiodynamic polarization behaviour of TFMG coated and bare 304 L SS substrate in 1, 6 and 11.5 M nitric acid.

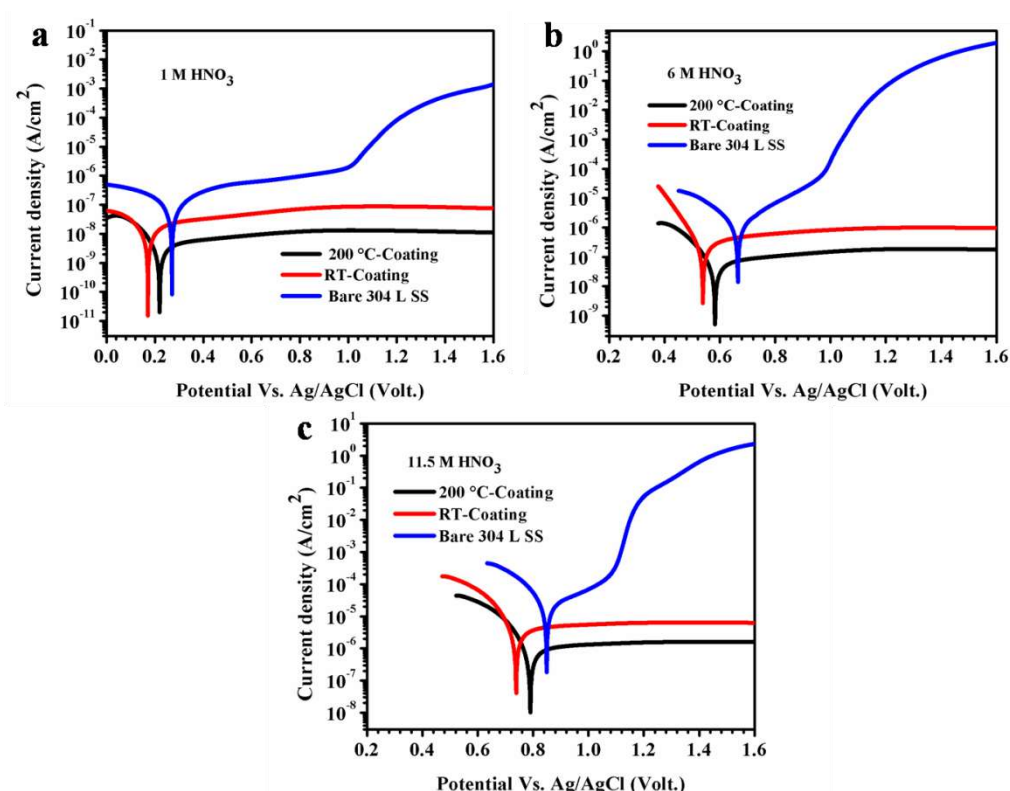


Figure 6.6 (a-c) Potentiodynamic polarization obtained from as-spun Ni₆₀Nb₃₀Ta₁₀ metallic glass coated and bare 304 L SS (a) in 1M, (b) 6 M, and (c) 11.5 M nitric acid.

The potentiodynamic polarization tests on the uncoated and Ni₆₀Nb₃₀Ta₁₀ TFMG coated 304 L SS at RT and 200 °C were performed out in 1M (Fig.6.6 (a)), 6 M (Fig.6.6 (b)), and 11.5M (Fig. 6.6 (c)) nitric acid medium. The scan rate (0.166 mV/s) is used for potentiodynamic polarization of the metallic glass coated 304 L SS and bare 304 L SS. For both the glassy coating, the trans-passive region did not appear up to 1.6 V (Ag/AgCl). The E_{corr} value of

Chapter 6

both TFMG coating in all three nitric acid concentrations is marginally lower than bare 304 L SS sample, indicating that the high oxidizing nature of the nitric acid effects on the uncoated 304 L SS when compared to the metallic glassy coating [82] (Table 6.1).

Table 6.1 Potentiodynamic polarization parameters of metallic glass coated and bare 304 L SS in 1, 6 and 11.5 M nitric acid.

Alloy condition	Potentiodynamic polarization parameters					
	E _{corr} vs (Ag/AgCl)			I _{corr}		
	mV			nA/cm ²		
	1M	6M	11.5M	1M	6M	11.5M
Bare 304 L SS	270	665	851	87	1025	16826
RT Coating	171	544	742	11	178	2038
200 Coating	225	585	793	2.2	36.4	517

However, with increasing the nitric acid concentration, the E_{corr} values are shifted to the nobler potential which is due to enhance autocatalytic reduction with the concentration [41]. The nobler E_{corr} value could be due to the auto-catalytic reduction of the nitrate anions [41]. Moreover, much larger E_{corr} shift also indicates that the oxidant species such as NO₃⁻, NO₂⁻, and NO etc. formed in higher numbers under concentrated nitric acids which exert a higher redox potential [82]. In addition, the slight differences in E_{corr} values for the RT and 200 °C metallic glass coating sample indicating the difference in the chemical composition of the passive films and surface roughness. Higher surface roughness could allow more autocatalytic reduction. Just after E_{corr}, no active-passive transition is observed revealing the spontaneous passivation ability of both the sample.

For all the samples studied, the I_{corr} and I_{pass} increased with the increasing concentration revealing the severity of the effects of nitric acid concentrations. The order of I_{corr} and I_{pass} in nitric acid solution followed the order as 304 L SS > RT glassy coating > 200 °C glassy coating. The I_{corr} and I_{pass} values are found to be a significantly higher than the for bare 304

Chapter 6

L SS, when compared to the glassy coating in all the nitric acid solution. The lower corrosion resistance of the 304 L SS is attributed to the presence of the grain boundary which is the preferential site for the corrosion initiation [41]. In addition, the passive film formed on the 304 L SS is different in composition when passive film formed on glassy alloys coating and that could also be one of the reasons for low corrosion resistance of the 304 L SS. However, the higher corrosion resistance of the metallic glassy coating over 304 L SS is attributed to the absence of preferential attacking site such as grain boundary and stacking fault, crystalline defect etc [39]. Hence, chemically homogenous glassy structure favored the formation of a stable amorphous passive layer when comparing to the conventional crystalline materials i.e., 304 L SS. However, the low I_{corr} and I_{pass} of the 200 °C glassy coating indicating that the relatively higher corrosion resistance when compared to the RT glassy coating. The higher corrosion resistance of smooth 200 °C in nitric acid implied that the better stability of relatively thicker passive film due to enrichment with Nb_2O_5 and Ta_2O_5 oxide.

Thicker passive film on 200 °C glassy coating results in a stable barrier for diffusion of electrolytes and dissolution of metal cation through the film, thus improving the corrosion resistance. In contrast, the relatively higher I_{corr} and I_{pass} values on RT glassy coating sample with respect 200 °C glassy coating, indicated low corrosion resistance. The low corrosion resistance of the RT glassy coating is attributed to the formation of the thin passive film on the rough surface. The stability of the film is also dependent on the chemical composition of the passive film. The XPS studies on immersed 200 °C glassy coating sample confirmed that the passive film is relatively thicker and enriched with stable Nb_2O_5 and Ta_2O_5 oxide when compared to the RT glassy coating. In such cases, the diffusion of the oxidizing nitric acid is more feasible, due to the low concentration of the protective Nb- and Ta-oxide which are incorporated to the surface. Generally, thin defective passive films are highly prone to the corrosion attacks [49]. By comparing glassy alloys coating with 304 L SS sample, larger

passive width of metallic glassy coating is attributed due to the very different chemical composition of the passive film formed on the glassy alloys and 304 L SS. The passive film formed on the glassy alloy is enriched with the stable Nb_2O_5 and Ta_2O_5 oxide while the passive film on 304 L SS is mainly comprised of Cr_2O_3 . It is known that the Cr_2O_3 is comparatively less stable than Nb_2O_5 and Ta_2O_5 oxide. This studies confirmed that the metallic glassy coated type 304 L SS at 200 °C process show a low I_{corr} and I_{pass} values which is imparted better corrosion resistance ability when compared to the RT glassy coating and bare 304 L SS in the nitric acid solution.

6.2.5 Electrochemical impedance analyses of TFMG coated and bare 304 L SS substrate in 1, 6 and 11.5 M nitric acid.

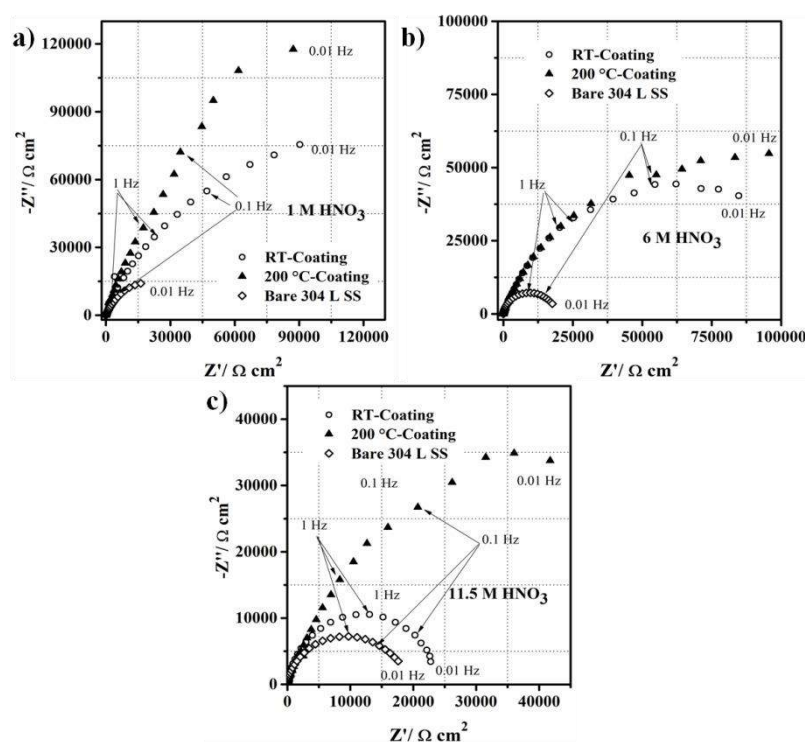


Figure 6.7 (a-c) Electrochemical impedance spectra (Nyquist plots) obtained on the room temperature (RT), 200 °C metallic glass coated and bare 304 L SS sample (a) in 1M, (b) 6 M, and (c) 11.5 M nitric acid.

Chapter 6

Table 6.2 EIS parameters of metallic glass coated and bare type 304 L SS in 1, 6, and 11.5 M nitric acid.

Sample	Electrochemical parameters								
	R_s (Ωcm^2)			R_p ($\text{k}\Omega\text{cm}^2$)			C ($\mu\text{F}/\text{cm}$)		
	1 M	6 M	11.5 M	1 M	6 M	11.5 M	1 M	6 M	11.5 M
Bare 304 L SS	3.5	2.6	1.8	17.3	16.3	15.6	9.2	10.6	12.1
RT Coating	3.4	2.5	1.7	85	76	23.8	7.6	8.3	10.1
200 Coating	3.4	2.6	1.8	121.6	95.6	41.7	5.7	6.9	8.2

Electrochemical impedance spectroscopy (EIS) experiments were carried out for the RT, 200 °C-coating and bare 304 L SS samples at their respective OCP in 1 M (Fig.6.7 (a)), 6 M (6.7 (b)) and 11.5 M (6.7 (c)) nitric acid. The frequency used for the EIS experiment on metallic glassy coating is in the range of 10 kHz to 0.01 Hz. The appearance of the single semi-circle for all sample studies indicates the capacitance behavior of the coatings. [122]. However, for all sample studied, a decreased in R_p with increasing the concentration of the nitric acid were observed. The R_p for SS and metallic glass coating in 1, 6 and 11.5 M nitric acid followed in the order: 200°C-Coating > RT-Coating > 304 L SS. The polarization resistance for the coating at 200 °C is higher than RT coating, indicating better quality of the coating compared to RT coating. High R_p indicates that the low charge transfer across the 200°C-Coating oxide/electrolytes interface which is attributed to compact passive film enriched with Nb_2O_5 and Ta_2O_5 . Thus, revealing that the oxide film formed on the RT-Coating surface is inferior in quality.

6.2.6 Mott-Schottky behavior of TFMG coated and bare 304 L SS nitric acid.

The Mott-Schottky experiments were carried out at fixed frequency of 1000 Hz to understand defective nature of the passive film on glassy coating and bare 304 L SS sample within the passive range of 0.1 to 1.6 V (Ag/AgCl) as shown in Fig.6.8 (a-c) [85]. The Mott-Schottky plot (Fig.6.8 (a-b)) with positive linear slope indicated the formation of an n-type semiconducting passive film on both RT and 200 °C glassy coating in 1, 6, 11.5 M nitric acid

[85]. The flat band potential (potential in which the slope intersect at $1/C^2 = 0$) for both RT and 200 °C glassy coating was shifted to the higher potential with an increase in the concentrations, indicating that the higher oxidizing nature of nitric acid.

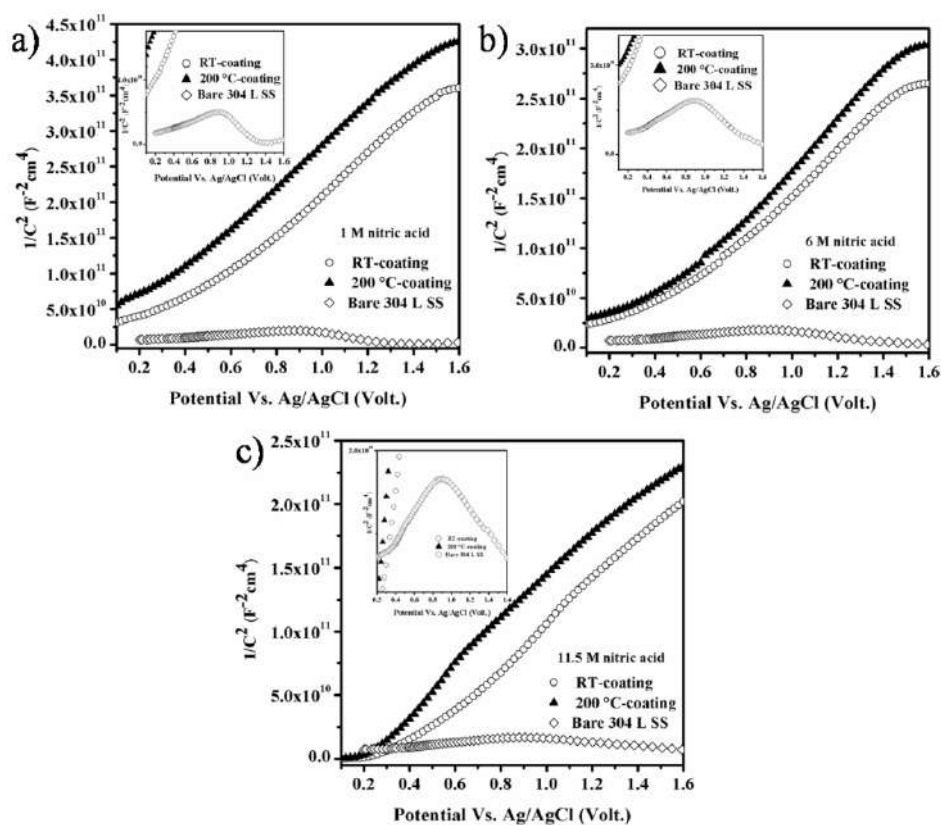


Figure 6.8 Mott-Schottky plots of RT, 200 °C-Coating, and bare 304 L SS sample; (a) in 1 M, (b) in 6 M, and (c) in 11.5 M nitric acid.

It need to be noted that the passive films formed on both RT and 200 °C glassy coating exhibited higher slopes as the concentration of nitric acid decreases. These results suggested that the donor density (N_d) of n-type film on both coating ribbon sample increased marginally with increases in nitric acid concentration from 1 to 11.5 M nitric acid (Table 6.3). However slightly different in the semiconducting behavior is observed for the 304 L SS in nitric acid medium when compared to the glassy coating. Bare 304 L SS shows first n-type semiconductor within the potential range roughly 0.1 to 1.1 V (Ag/AgCl) and then it change to the p-type semiconductor (within trans-passive region), as shown by enlarging region in

Chapter 6

Fig, 6.8 (a-c). The reason for the n-type semiconductor could be due to the formation of Cr_2O_3 enriched film and p-type semiconducting due to the inner Fe-oxide [114]. Similarly, the increases in the defect density of the passive film on 304 L SS with increasing nitric acid concentration were observed. Thus, it is assumed that the defect density of the passive film on the both RT and 200 °C glassy coated and 304 L SS is a function of solution concentration. The increment of the defect density with nitric acid concentration could be attributed to the increases of the thickness of passive film by generating more oxygen ion vacancies and cation interstitials [118-121].

Table 6.3 Defect density of the passive film on metallic glassy coating and bare 304 L SS in 1, 6, 11.5 M nitric acid.

Sample	Mott-schottky Parameters		
	Donor density ($N_d \times 10^{19} / \text{cm}^{-3}$)		
	1 M	6 M	11.5 M
Bare 304 L SS	9	13	19
RT Coating	1.7	3.5	6.7
200 Coating	0.8	1.6	3.8

Moreover, due to the higher growth rate of the passive film, there is limited time for the atoms/ions to diffuse to the 'right' position, and more defects could generate in the passive film, and the donor density gradually increases correspondingly. After the passive film formation has initiated on the metallic glassy coating surface, the subsequent growth process will be determined by the flux of oxygen vacancies and cation interstitials in the film [122]. The oxygen vacancies and cation interstitials must be transported from the metal/film interface to the film/solution interface.

However, for all three nitric acid solutions, the defect densities of semiconducting film on both glassy coating are significantly lower than that of bare 304 L SS sample which further indicates the stability of the amorphous passive film. Further the passive film on 200 °C glassy coating with low defect density effectively prevents the diffusion of electrolyte to

the film and dissolution of cations into the solution, thereby improving the corrosion resistance. In contrast, significantly higher defect N_d and N_a observed for 304 L SS alloy compared to the glassy alloy revealed that the less protective nature of the passive film on crystalline 304 L SS compared to the crystalline free glassy alloys. TFMG coated 304 L SS exhibited higher corrosion resistance compared to the bare 304 L SS and thus, the metallic glass coating shows improved corrosion resistance which will be beneficial for the nitric acid application.

6.2.7 Weight loss measurements in 11.5 M nitric acid environment under the boiling condition and surface analyses.

The corrosion resistance of both RT and 200 °C $Ni_{60}Nb_{30}Ta_{10}$ metallic glass coating was evaluated by weight loss measurements in boiling 11.5 M HNO_3 at 120 °C for 240 h as per ASTM 262 practice C test. [41, 88, 107]. The metallic glass coating side was exposed in 11.5 M nitric acid and other side of the substrate was covers with elastomeric silica gel. The elastomeric silica gel is chemically inert in nature and stable in concentrated nitric acid even up to boiling condition, even temperature up to 400 °C. During the immersion test, the 120 °C temperature was monitoring by using the thermometer. The initial weight of each sample was measured accurately and the samples were exposed to the test solutions in a setup consisting of a cold finger condenser that refluxes the acid vapor into the test solution, as described elsewhere [107]. The corrosion resistance was evaluated by weight loss measurements after exposing them to 11.5 M HNO_3 for 240 h under boiling condition in 11.5 M HNO_3 . The corrosion rate of RT and 200 °C $Ni_{60}Nb_{30}Ta_{10}$ coating in 11.5 M HNO_3 was about 0.5 mm/y and 0.1 mm/y, respectively. To compare the corrosion rate of metallic glass coating with bare 304 LSS in boiling 11.5 M nitric acid, the 304 L SS also exposed for 240 h. The corrosion rate of the bare 304 L SS (1.3 mm/y) was higher than the corrosion rate of 200 °C $Ni_{60}Nb_{30}Ta_{10}$ coated 304 L SS samples. On the other hand, the

Chapter 6

difference in the corrosion rate between RT coating, and bare 304 L SS is not significant and that could be due to the lesser passive film stability on rough surface (Fig. 6.2b-c) on RT coating during the immersion test.

Table 6.4 Weight loss verses immersion time for RT, and 200 °C coating along with 304 L SS in 11.5 M nitric acid.

Immersion time (in hours)	Weight loss (in mg)		
	RT coating	200 °C Coating	Bare 304 L SS
48	0.02	0.01	0.2
96	0.03	0.01	0.23
144	0.04	0.02	0.2
240	0.05	0.023	0.2

To understand the dissolution kinetics, the weight loss vs time are presented in table (6.4). The change in weight is measured in an interval of every 48 hrs immersion in 11.5 M nitric acid. The mass changes in metallic glassy coating are lower with the immersion time when compared to the 304 L SS. However the relatively lower weight loss observed for 200 °C coating compared to the RT coating. Therefore, the corrosion rate on metallic glassy coating is lower than that of bare 304 L SS.

After immersion test in boiling 11.5 M nitric acid for 24 h, the surface of both glassy coating was characterized by SEM techniques, as shown in Fig.6.9. The smooth morphology (Fig.6.9 (a)) indicated that the formation of uniform passive film on the 200 °C metallic glass coating. In contrast, the RT coating is undergone minor dissolution which may be due to the dissolution of those dimple shape particle. On the other hand, 304 L SS shows severe inter-granular corrosion attack (Fig.6.9 (b)).

To understand the long term corrosion test, the surface of 200 °C-Coating and RT-Coating was further characterized by the SEM technique after immersion test in boiling 11.5 M nitric acid for 240 h, as shown in Fig.6.9, and 6.10, respectively. The surface undergoes

Chapter 6

minor attack and several black spots appeared. In contrast, the surface of the RT-coating after 240 h immersion test undergoes local attack (Fig. 6.10) and several pitting were observed on the coating.

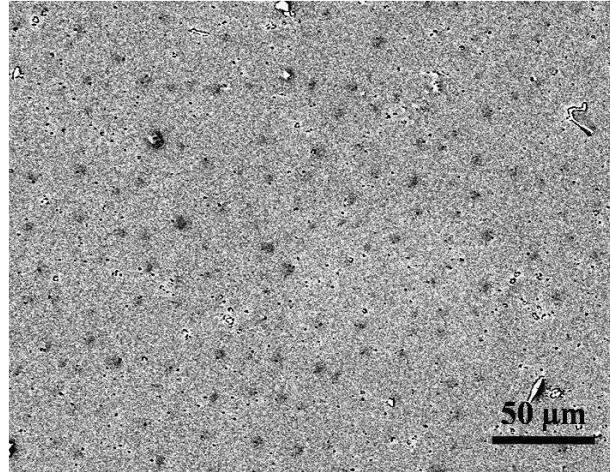


Figure 6.9 Surface morphology of 200 °C-metallic glass coating sample after immersion test for 240 h in 11.5 M nitric acid solution under boiling condition.

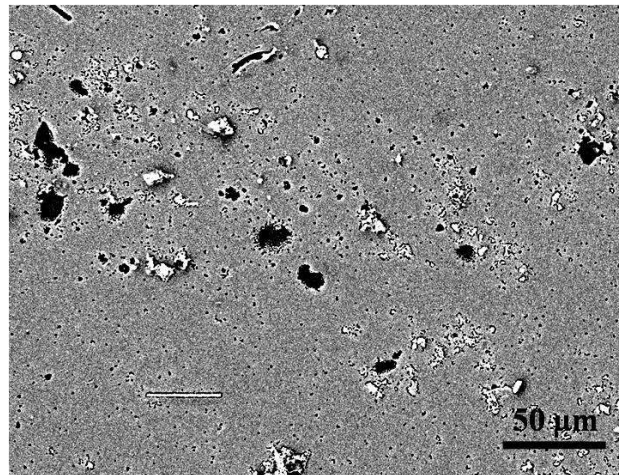


Figure 6.10 Surface morphology of severely attacked RT-metallic glass coating sample after immersion test for 240 h in 11.5 M nitric acid solution under boiling condition.

Chapter 6

On the other hand, after immersion test in boiling 11.5 M nitric acid for 240 h bare 304 L SS undergoes severe intergranular corrosion attack around the grain boundary and grain dropping features are observed, as shown in Fig.6.11.

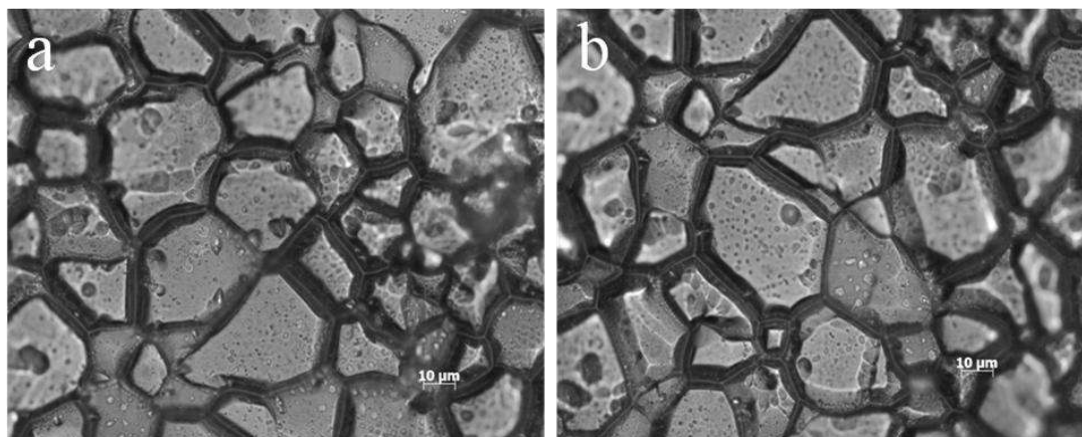


Figure 6.11 Surface morphology (Optical images) of severely Inter-granular attacked of bare 304 L SS sample after immersion test for 240 h in 11.5 M nitric acid solution under boiling condition.

A thick passive film with amorphous structure has a key effect to counter early stage trans-passive breakdown. The formation of the thin film on RT glassy coating could be due to the higher coating roughness of the surface (fig. 6.2c) and affects the growth of the passive. Therefore, the thin passive film of about 4.5 nm film formed on the RT coating when compared to the 9 nm on the 200 °C coating sample. Reason for the thin film on rough coating may be the less stability and/or dissolution of the passive film. The coating deposited at RT could be intact substrate with lower adhesion which ultimately affects the formation of the stable passive film at coating/electrolyte interface.

Present studies confirmed that the thin film metallic glass coated (TFMG) 304 L SS at 200 °C is beneficial compared to the bare 304 L SS for concentrated nitric acid application. Further, the passive film on 200 °C glassy coating with low defect density exhibited high

corrosion resistance and successfully minimized inter granular corrosion (IGC) for long term boiling exposure in 11.5 M nitric acid.

6.3 Summary

- a. The XRD confirms the amorphous structure of the $\text{Ni}_{60}\text{Nb}_{30}\text{Ta}_{10}$ metallic glass coating deposited at room temperature (RT) and 200 °C. The SEM studies shows the surface of RT coating is relatively rougher and droplet like feature is observed while deposited at 200 °C, surface is relatively smoother.
- b. The sputter deposited TFMG $\text{Ni}_{60}\text{Nb}_{30}\text{Ta}_{10}$ coating on 304 L SS at RT and 200 °C exhibited remarkably wider passive region and higher corrosion resistance compared to the bare 304 L SS. The high corrosion resistance of the metallic glass coating is attributed due to the formation of homogeneous or amorphous Nb_2O_5 and Ta_2O_5 passive film. Further, the metallic glass coating deposited at 200 °C process a relatively better corrosion resistance compared to RT coating. The high corrosion resistance of the 200 °C metallic glass coating is due to the better adhesion of the film/substrate interface compared to RT coating.
- c. The higher corrosion resistance of 200°C-Coating is attributed to the formation of the protective thick passive film (≈ 9 nm) enriched with the Nb_2O_5 and Ta_2O_5 on the surface. The low corrosion resistance of the RT-coating is the inferior quality of which readily undergoes dissolution in 11.5 M nitric acid. However, the severe inter-granular attack was observed on the bare 304 L SS in 11.5 M nitric acid under the boiling condition for 240 h.

7 Conclusion and future work

7.1 Conclusion

- a. The $\text{Ni}_{60}\text{Nb}_{30}\text{Ta}_{10}$ Metallic Glass exhibits higher corrosion resistance than its partially crystalline counterparts in 11.5 M nitric acid medium. Formation of α -Ni decreases corrosion resistance of the partially crystalline sample. The passive film formed on metallic glass is relatively thicker and stable while the defective film is formed on the crystallized sample and α -Ni dissolve preferentially in 11.5 M nitric acid.
- b. The oxidation kinetics of both ribbon ($\text{Ni}_{60}\text{Nb}_{40}$ & $\text{Ni}_{60}\text{Nb}_{30}\text{Ta}_{10}$) followed two stage parabolic rate laws at 450 and 550 °C in air. Oxidation of $\text{Ni}_{50}\text{Nb}_{25}\text{Zr}_{25}$ MG at 200 °C and 400 °C follows initial, linear rate law and then changed into the parabolic rate law.
- c. The XPS analyses showed that the oxidation of $\text{Ni}_{60}\text{Nb}_{40}$ amorphous alloy at 450 °C comprises predominantly of Nb_2O_5 oxide on the surface, while $\text{Ni}_{60}\text{Nb}_{30}\text{Ta}_{10}$ metallic glass is enriched with Nb_2O_5 and Ta_2O_5 . In contrast, oxidation at 550 °C, comprises only of NiO and Ni_2O_3 . However, oxidation of $\text{Ni}_{50}\text{Nb}_{25}\text{Zr}_{25}$ at 400 °C comprised only of Nb_2O_5 , and ZrO_2 on the surface.
- d. The Mott-Schottky analysis confirmed the n-type semiconducting film formation on the both as-spun $\text{Ni}_{60}\text{Nb}_{40}$ and $\text{Ni}_{60}\text{Nb}_{30}\text{Ta}_{10}$ MG sample ribbon, while the p-type semiconducting film on the both thermally oxidized sample at 550 °C. However, 450 °C oxide film on $\text{Ni}_{60}\text{Nb}_{40}$ alloy exhibits protective n-type semiconductivity while 450 °C oxidized $\text{Ni}_{60}\text{Nb}_{30}\text{Ta}_{10}$ MG sample as an insulator in the nitric acid environment.
- e. Potentiodynamic polarization showed the $\text{Ni}_{60}\text{Nb}_{30}\text{Ta}_{10}$ metallic glass exhibits higher corrosion resistance in as-spun and oxidized state among three metallic glasses. However, thermally oxidized $\text{Ni}_{50}\text{Nb}_{25}\text{Zr}_{25}$ at 400 °C sample exhibits wider passive region among all the metallic glass attributed to the higher film oxide film thickness.

- f. The sputter deposited TFMG $\text{Ni}_{60}\text{Nb}_{30}\text{Ta}_{10}$ coating on 304 L SS at RT and 200 °C exhibited remarkably wider passive range and high corrosion resistance compared to the bare 304 L SS. The high corrosion resistance of the metallic glass coating is attributed to the formation of homogeneous or amorphous Nb_2O_5 and Ta_2O_5 passive film.

7.2 Future work

The degradation of alloy materials in a highly aggressive and corrosive nitric acid environment in spent nuclear fuel reprocessing plants is an important issue, and understanding its corrosion processes and the mechanism is essential in providing understanding to its reliability for used in a plutonium-uranium redox extraction (PUREX) reprocessing plant. Moreover, stainless steels (304L SS, nitric acid grade SS, etc), titanium, and zirconium and its alloys have been used for nitric acid applications. Similarly, Bulk Metallic Glasses (BMG) alloys are being explored as a potential candidate material for spent nuclear fuel reprocessing applications. Therefore, it focuses on nitric acid corrosion of BMG and its coating on type 304L SS in highly oxidizing and simulated reprocessing environments need more elaborate investigations.

Furthermore, corrosion processes in nitric acid is affected by a number of factors, some of which include NO_x gases, dissolved species, radiation, boiling temperature, heat transfer, and powerful oxidizers (Ce^{4+} , Ru^{4+} , Ru^{8+} , Fe^{4+} , Cr^{6+} , Pu^{6+} , etc.) from the fission products, etc, The various corrosion mechanisms involved under such conditions in nitric acid require more detail investigation for the applicability of BMG alloys in reprocessing plant applications.

Other area of Future work includes the followings:

- a. Providing more understanding on the nitric corrosion mechanisms of BMG alloys and its coating in different reprocessing environmental conditions.

Chapter 7

- b. Mechanical properties of the Ni-based metallic glass coating such as adhesion, wear and hardness and its correlation with corrosion resistance.
- c. Synthesis of thicker metallic glassy coating on Ti and corrosion evolution in concentrated nitric acid medium.
- d. Providing more understanding on the corrosion behaviours of Ni-based metallic glasses in different medium such as, NaCl and HCl.

References

Reference

- [1] Asami K., Habazaki H., Kawashima K., Hashimoto K., On the unusual morphology of pitting corrosion of amorphous Ni-Zr alloys, *Corros. Sci.* 34 (1993) 445. doi:10.1063/1.2187516.
- [2] R. Brüning, K. Samwer, Glass transition on long time scales, *Phys. Rev. B.* (1992). doi:10.1103/PhysRevB.46.11318.
- [3] J. Jayaraj, studies on the corrosion behaviour of metallic glass, PhD thesis, (n.d.).
- [4] W.L. Johnson, Thermodynamic and kinetic aspects of the crystal to glass transformation in metallic materials, *Prog. Mater. Sci.* (1986). doi:10.1016/0079-6425(86)90005-8.
- [5] Uhlmann D.R., A kinetic treatment of glass formation, *J. Non. Cryst. Solids.* 7 (1972) 337. doi:10.1016/j.scriptamat.2007.04.033.
- [6] N. Mattern, H. Hermann, S. Roth, J. Sakowski, M.-P. Macht, P. Jovari, J. Jiang, Structural behavior of Pd₄₀Cu₃₀Ni₁₀P₂₀ bulk metallic glass below and above the glass transition, *Appl. Phys. Lett.* (2003). doi:10.1063/1.1567457.
- [7] U. Geyer, S. Schneider, W.L. Johnson, Y. Qiu, T.A. Tombrello, M.P. Macht, Atomic diffusion in the supercooled liquid and glassy states of the Zr_{41.2}Ti_{13.8}Cu_{12.5}Ni₁₀Be_{22.5} alloy, *Phys. Rev. Lett.* (1995). doi:10.1103/PhysRevLett.75.2364.
- [8] M.D. Demetriou, W.L. Johnson, Shear flow characteristics and crystallization kinetics during steady non-isothermal flow of Vitreloy-1, *Acta Mater.* (2004). doi:10.1016/j.actamat.2004.03.034.
- [9] Z.P. Lu, Y. Li, C.T. Liu, Glass-forming tendency of bulk La-Al-Ni-Cu-(Co) metallic glass-forming liquids, *J. Appl. Phys.* (2003). doi:10.1063/1.1528297.
- [10] X. Ji, Y. Pan, Gibbs free energy difference in metallic glass forming liquids, *J. Non. Cryst. Solids.* (2007). doi:10.1016/j.jnoncrysol.2007.04.015.
- [11] S.C. Glade, R. Busch, D.S. Lee, W.L. Johnson, R.K. Wunderlich, H.J. Fecht, Thermodynamics of Cu₄₇Ti₃₄Zr₁₁Ni₈, Zr_{52.5}Cu_{17.9}Ni_{14.6}Al₁₀Ti₅ and Zr₅₇Cu_{15.4}Ni_{12.6}Al₁₀Nb₅ bulk metallic glass forming alloys, *J. Appl. Phys.* (2000). doi:10.1063/1.372975.
- [12] T. Egami, (1997), Universal criterion for metallic glass formation, *Material Science and Engineering A*, 261 (1997) 226-228.
- [13] T. Egami, Y. Waseda, Atomic size effect on the formability of metallic glasses, *J. Non. Cryst. Solids.* (1984). doi:10.1016/0022-3093(84)90210-2.
- [14] D.B. Miracle, D. V Louzguine-Luzgin, L. V Louzguina-Luzgina, A. Inoue, An assessment of binary metallic glasses: correlations between structure, glass forming ability and stability, *Int. Mater. Rev.* (2010). doi:10.1179/095066010x12646898728200.
- [15] D.B. Miracle, The density and packing fraction of binary metallic glasses, *Acta Mater.*

References

- (2013). doi:10.1016/j.actamat.2013.02.005.
- [16] P. Duwez, Metallic glasses-historical background, in: 2012. doi:10.1007/3540104402_2.
- [17] A. Inoue, X.M. Wang, W. Zhang, Developments and applications of bulk metallic glasses, in: *Rev. Adv. Mater. Sci.*, 2008.
- [18] S.N. Mathaudhu, J.T. Im, R.E. Barber, I.E. Anderson, I. Karaman, K. Ted, Progress in Consolidation of Amorphous Zr-based Powder into Bulk Metallic Glass, *MRS Proc.* (2002). doi:10.1557/proc-754-cc3.5.
- [19] H.S. Chen, Thermodynamic considerations on the formation and stability of metallic glasses, *Acta Metall.* (1974). doi:10.1016/0001-6160(74)90112-6.
- [20] A.J. Drehman, A.L. Greer, D. Turnbull, Bulk formation of a metallic glass: Pd₄₀Ni₄₀P₂₀, *Appl. Phys. Lett.* (1982). doi:10.1063/1.93645.
- [21] Q.K. Jiang, G.Q. Zhang, L. Yang, X.D. Wang, K. Saksl, H. Franz, R. Wunderlich, H. Fecht, J.Z. Jiang, La-based bulk metallic glasses with critical diameter up to 30 mm, *Acta Mater.* 55 (2007) 4409–4418. doi:10.1016/j.actamat.2007.04.021.
- [22] W. Chen, Y. Wang, J. Qiang, C. Dong, Bulk metallic glasses in the Zr-Al-Ni-Cu system, *Acta Mater.* (2003). doi:10.1016/S1359-6454(02)00596-7.
- [23] A. Peker, W.L. Johnson, A highly processable metallic glass: Zr_{41.2}Ti_{13.8}Cu_{12.5}Ni_{10.0}Be_{22.5}, *Appl. Phys. Lett.* (1993). doi:10.1063/1.110520.
- [24] F.E. Jayaraj J., Kim Y.C., Kim K.B., Seok H.K., Corrosion behaviors of Fe_{45-x}Cr₁₈Mo₁₄C₁₅B₆Y₂M_x (M=Al, Co, Ni, N and x=0, 2) bulk metallic glasses under conditions simulating fuel cell environment, *J. Alloys Compd.* (n.d.). doi:10.1016/j.actamat.2004.04.023.
- [25] V. Ponnambalam, S.J. Poon, G.J. Shiflet, Fe–Mn–Cr–Mo–(Y, Ln)–C–B (Ln = Lanthanides) bulk metallic glasses as formable amorphous steel alloys, *J. Mater. Res.* (2004). doi:10.1557/jmr.2004.0374.
- [26] K.D.H. Park J.M., Chang H.J., Han K.H., Kim W.T., Enhancement of plasticity in Ti-rich Ti–Zr–Be–Cu–Ni bulk metallic glasses, *Scr. Mater.* 9 (2005) 1. doi:10.1021/acsami.7b12504.
- [27] D.C. Qiao, G.Y. Wang, P.K. Liaw, V. Ponnambalam, S.J. Poon, G.J. Shiflet, Fatigue behavior of an Fe₄₈Cr₁₅Mo₁₄Er₂C₁₅B₆ amorphous steel, *J. Mater. Res.* (2007). doi:10.1557/jmr.2007.0047.
- [28] J. Schroers, Processing of bulk metallic glass, *Adv. Mater.* (2010). doi:10.1002/adma.200902776.
- [29] M. Chen, A brief overview of bulk metallic glasses, *NPG Asia Mater.* (2011). doi:10.1038/asiamat.2011.30.
- [30] T. D., (1981), 12B, 217, *Metall. Trans.* 12B (1981) 217. doi:10.1021/nl201766h.

References

- [31] Y. Li, S.J. Poon, G.J. Shiflet, J. Xu, D.H. Kim, J.F. Löffler, Formation of Bulk Metallic Glasses and Their Composites, *MRS Bull.* (2007). doi:10.1557/mrs2007.123.
- [32] H.S. Shin, Y.J. Jung, K.H. Kim, J.H. Ahn, H. Kato, A. Inoue, Deformation behavior of a Zr₅₅Al₁₀Ni₅Cu₃₀ bulk metallic glass at high temperatures, in: *Metastable, Mech. Alloy. Nanocrystalline Mater.*, 2005.
- [33] A. Bolcavage, U.R. Kattner, A reassessment of the calculated Ni-Nb phase diagram, *J. Phase Equilibria.* (1996). doi:10.1007/BF02665782.
- [34] M. Lee, B. Donghyun, W. Kim, D.H. Kim, Ni-Based Refractory Bulk Amorphous Alloys with High Thermal Stability, *Mater. Trans.* 10 (2003) 2084–2087. doi:10.2320/matertrans.44.2084.
- [35] Z.M. Wang, J. Zhang, X.C. Chang, W.L. Hou, J.Q. Wang, Structure inhibited pit initiation in a Ni-Nb metallic glass, *Corros. Sci.* 52 (2010) 1342–1350. doi:10.1016/j.corsci.2009.12.014.
- [36] K. Zhang, X. Gao, Y. Dong, Q. Xing, Y. Wang, Effect of annealing on the microstructure, microhardness, and corrosion resistance of Ni₆₂Nb₃₃Zr₅ metallic glass and its composites, *J. Non. Cryst. Solids.* 425 (2015) 46–51. doi:10.1016/j.jnoncrysol.2015.05.027.
- [37] P. Fauvet, Corrosion issues in nuclear reprocessing plants, in: *CEA, Fr.*, 2012. doi:10.1016/S1359-6454(02)00166-0.
- [38] S. Ningshen, U. Kamachi Mudali, 2 - Uniform Corrosion of Austenitic Stainless Steels, *Corrosion of Austenitic Stainless Steels*, (Book Chapter) 2002, 37-73.
- [39] B. Raj, U.K. Mudali, Materials development and corrosion problems in nuclear fuel reprocessing plants, *Prog. Nucl. Energy.* 48 (2006) 283–313. doi:10.1016/j.pnucene.2005.07.001.
- [40] U.K. Mudali, R.K. Dayal, J.B. Gnanamoorthy, Corrosion studies on materials of construction for spent nuclear fuel reprocessing plant equipment, *J. Nucl. Mater.* 203 (1993) 73–82. doi:10.1016/0022-3115(93)90432-X.
- [41] S. Ningshen, U. Kamachi Mudali, S. Ramya, B. Raj, Corrosion behaviour of AISI type 304L stainless steel in nitric acid media containing oxidizing species, *Corros. Sci.* (2011). doi:10.1016/j.corsci.2010.09.023.
- [42] Y.Q. Cheng, E. Ma, Atomic-level structure and structure-property relationship in metallic glasses, *Prog. Mater. Sci.* (2011). doi:10.1016/j.pmatsci.2010.12.002.
- [43] S.J. Pang, T. Zhang, K. Asami, A. Inoue, Synthesis of Fe-Cr-Mo-C-B-P bulk metallic glasses with high corrosion resistance, *Acta Mater.* (2002). doi:10.1016/S1359-6454(01)00366-4.
- [44] M. Naka, K. Hashimoto, T. Masumoto, Corrosion resistance of amorphous alloys with chromium, *J. Jpn. Inst. Met.* 38 (1974) 835.
- [45] P.F. Gostin, A. Gebert, L. Schultz, Comparison of the corrosion of bulk amorphous steel with conventional steel, *Corros. Sci.* 52 (2010) 273–281.

References

- doi:10.1016/j.corsci.2009.09.016.
- [46] J. Li, L. Yang, H. Ma, K. Jiang, C. Chang, J.Q. Wang, Z. Song, X. Wang, R.W. Li, Improved corrosion resistance of novel Fe-based amorphous alloys, *Mater. Des.* (2016). doi:10.1016/j.matdes.2016.01.100.
- [47] S.J. Pang, T. Zhang, K. Asami, A. Inoue, Bulk glassy Fe-Cr-Mo-C-B alloys with high corrosion resistance, *Corros. Sci.* (2002). doi:10.1016/S0010-938X(02)00002-1.
- [48] K. Asami, S.-J. Pang, T. Zhang, A. Inoue, Preparation and Corrosion Resistance of Fe-Cr-Mo-C-B-P Bulk Glassy Alloys, *J. Electrochem. Soc.* (2002). doi:10.1149/1.1490537.
- [49] X.P. Nie, X.H. Yang, L.Y. Chen, K.B. Yeap, K.Y. Zeng, D. Li, J.S. Pan, X.D. Wang, Q.P. Cao, S.Q. Ding, J.Z. Jiang, The effect of oxidation on the corrosion resistance and mechanical properties of a Zr-based metallic glass, *Corros. Sci.* 53 (2011) 3557–3565. doi:10.1016/j.corsci.2011.06.032.
- [50] H.F. Li, Y.F. Zheng, Recent advances in bulk metallic glasses for biomedical applications, *Acta Biomater.* (2016). doi:10.1016/j.actbio.2016.03.047.
- [51] W.H. Jiang, F. Jiang, B.A. Green, F.X. Liu, P.K. Liaw, H. Choo, K.Q. Qiu, Electrochemical corrosion behavior of a Zr-based bulk-metallic glass, *Appl. Phys. Lett.* (2007). doi:10.1063/1.2762282.
- [52] D. Zander, B. Heisterkamp, I. Gallino, Corrosion resistance of Cu-Zr-Al-Y and Zr-Cu-Ni-Al-Nb bulk metallic glasses, *J. Alloys Compd.* (2007). doi:10.1016/j.jallcom.2006.08.112.
- [53] A. Gebert, K. Buchholz, A.M. El-Aziz, J. Eckert, Hot water corrosion behaviour of Zr-Cu-Al-Ni bulk metallic glass, *Mater. Sci. Eng. A.* (2001). doi:10.1016/S0921-5093(01)01248-5.
- [54] C.H. Huang, J.C. Huang, J.B. Li, J.S.C. Jang, Simulated body fluid electrochemical response of Zr-based metallic glasses with different degrees of crystallization, *Mater. Sci. Eng. C.* (2013). doi:10.1016/j.msec.2013.06.007.
- [55] C.L. Qiu, Q. Chen, L. Liu, K.C. Chan, J.X. Zhou, P.P. Chen, S.M. Zhang, A novel Ni-free Zr-based bulk metallic glass with enhanced plasticity and good biocompatibility, *Scr. Mater.* (2006). doi:10.1016/j.scriptamat.2006.06.018.
- [56] V.R. Raju, U. Kühn, U. Wolff, F. Schneider, J. Eckert, R. Reiche, A. Gebert, Corrosion behaviour of Zr-based bulk glass-forming alloys containing Nb or Ti, *Mater. Lett.* (2002). doi:10.1016/S0167-577X(02)00725-5.
- [57] H.C. Kou, Y. Li, T.B. Zhang, J. Li, J.S. Li, Electrochemical corrosion properties of Zr- and Ti-based bulk metallic glasses, *Trans. Nonferrous Met. Soc. China (English Ed.)* (2011). doi:10.1016/S1003-6326(11)60750-4.
- [58] A. Gebert, A.A. Kündig, L. Schultz, K. Hono, Selective electrochemical dissolution in two-phase La-Zr-Al-Cu-Ni metallic glass, *Scr. Mater.* (2004). doi:10.1016/j.scriptamat.2004.07.021.
- [59] D.P. Wang, S.L. Wang, J.Q. Wang, Relationship between amorphous structure and
-

References

- corrosion behaviour in a Zr-Ni metallic glass, *Corros. Sci.* 59 (2012) 88–95.
doi:10.1016/j.corsci.2012.02.017.
- [60] H. Habazaki, T. Sato, A. Kawashima, K. Asami, K. Hashimoto, Preparation of corrosion-resistant amorphous Ni-Cr-P-B bulk alloys containing molybdenum and tantalum, *Mater. Sci. Eng. A.* (2001). doi:10.1016/S0921-5093(00)01571-9.
- [61] H. Katagiri, S. Meguro, M. Yamasaki, H. Habazaki, T. Sato, A. Kawashima, K. Asami, K. Hashimoto, An attempt at preparation of corrosion-resistant bulk amorphous Ni-Cr-Ta-Mo-P-B alloys, *Corros. Sci.* (2001). doi:10.1016/S0010-938X(00)00068-8.
- [62] C. Qin, K. Asami, H. Kimura, W. Zhang, A. Inoue, *Electrochemistry Communications* Surface characteristics of high corrosion resistant Ni – Nb – Zr – Ti – Ta glassy alloys for nuclear fuel reprocessing applications, 10 (2008) 1408–1410.
doi:10.1016/j.elecom.2008.07.024.
- [63] C. Qin, K. Asami, H. Kimura, W. Zhang, A. Inoue, Electrochemical and XPS studies of Ni-based metallic glasses in boiling nitric acid solutions, *Electrochim. Acta.* 54 (2009) 1612–1617.
- [64] M. Hasegawa, Ellingham Diagram, in: *Treatise Process Metall.*, 2013.
doi:10.1016/B978-0-08-096986-2.00032-1.
- [65] G.C. Wood, High-temperature oxidation of alloys, *Oxid. Met.* (1970).
doi:10.1007/BF00603581.
- [66] D.R.H. Flores K.M., Crack-tip plasticity in bulk metallic glasses *Material* 319–321, 511., *Sci. Eng. A.*, 511 (2001) 319–321.
- [67] A. Atkinson, Transport processes during the growth of oxide films at elevated temperature, *Rev. Mod. Phys.* 57 (1985) 437–470. doi:10.1103/RevModPhys.57.437.
- [68] D.A. Schroers J., Nguyena T., Keeffe S.O., Thermoplastic forming of bulk metallic glass—Applications for MEMS and microstructure fabrication, in press., *Mater. Sci. Eng. A*, 2006 n Press. (n.d.). doi:10.1016/j.corsci.2015.11.036.
- [69] G.C. Wood, F.H. Stot, J.G. Fountain, The mechanism of high – temperature oxidation of directionally solidified Ni₃Al-Ni₃Nb eutectic, *Corros. Sci.* 19 (1979) 441–455.
- [70] J.P. Lin, L.L. Zhao, G.Y. Li, L.Q. Zhang, X.P. Song, F. Ye, G.L. Chen, Effect of Nb on oxidation behavior of high Nb containing TiAl alloys, *Intermetallics.* (2011).
doi:10.1016/j.intermet.2010.08.029.
- [71] K.R. Lim, T.H. Cho, S.H. Park, M.Y. Na, K.C. Kim, Y.S. Na, W.T. Kim, D.H. Kim, A novel approach to exploring glassy alloys with high oxidation resistance in the supercooled liquid region, *Corros. Sci.* 111 (2016) 846–849.
doi:10.1016/j.corsci.2016.05.001.
- [72] S.H. Park, K.R. Lim, M.Y. Na, K.C. Kim, W.T. Kim, D.H. Kim, Oxidation behavior of Ti-Cu binary metallic glass, *Corros. Sci.* 99 (2015) 304–312.
doi:10.1016/j.corsci.2015.07.027.
- [73] K.R. Lim, J.M. Park, S.S. Jee, S.Y. Kim, S.J. Kim, E.S. Lee, W.T. Kim, A. Gebert, J.

References

- Eckert, D.H. Kim, Effect of thermal stability of the amorphous substrate on the amorphous oxide growth on Zr-Al-(Cu,Ni) metallic glass surfaces, *Corros. Sci.* 73 (2013) 1–6. doi:10.1016/j.corsci.2013.04.009.
- [74] C. Poddar, J. Jayaraj, C. Mallika, U. Kamachi Mudali, Oxidation behaviour of Ni₆₀Nb₃₀Ta₁₀ metallic glass below its glass transition temperature, *J. Alloys Compd.* 728 (2017) 1146–1152. doi:10.1016/j.jallcom.2017.09.040.
- [75] S.W.J. V.C. Anitha, A.N. Banerjee, Recent Developments in TiO₂; as n- and p- type Transparent Semiconductors: Synthesis, Modification, Properties, and Energy-related Applications, *J. Mater. Sci.* 50 (2015) 7495–7536. doi:10.1016/j.corsci.2010.01.027.
- [76] A. Caron, C.L. Qin, L. Gu, S. González, A. Shluger, H.J. Fecht, D. V. Louzguine-Luzgin, A. Inoue, Structure and nano-mechanical characteristics of surface oxide layers on a metallic glass, *Nanotechnology.* 22 (2011). doi:10.1088/0957-4484/22/9/095704.
- [77] B. Walz, P. Oelhafen, H.J. Güntherodt, A. Baiker, Surface oxidation of amorphous NiZr alloys, *Appl. Surf. Sci.* 37 (1989) 337–352. doi:10.1016/0169-4332(89)90495-9.
- [78] W. Kai, Y.T. Chen, F.P. Zheng, W.S. Chen, R.T. Huang, L.W. Tsai, H.H. Huang, W. Zhang, Air Oxidation of a Ni₅₃Nb₂₀Ti₁₀Zr₈Co₆Cu₃ Glassy Alloy at 400–550 °C, *Oxid. Met.* 86 (2016) 205–219. doi:10.1007/s11085-016-9632-1.
- [79] S. Lu, S. Sun, G. Tu, X. Huang, K. Li, The effect of yttrium addition on the air oxidation behavior of Zr-Cu-Ni-Al bulk metallic glasses at 400–500 °C, *Corros. Sci.* 137 (2018) 53–61. doi:10.1016/j.corsci.2018.03.024.
- [80] Dieter G., *Mechanical Metallurgy*, Third edition, New York McGraw-Hill B. Company. (1986).
- [81] ASTM Standars, *Conducting Potentiodynamic Polarization Resistance Measurements*, 2003. doi:10.1520/G0059-97R09.2.
- [82] S. Ningshen, U. Mudali, G. Amarendra, B. Raj, Corrosion assessment of nitric acid grade austenitic stainless steels, *Corros. Sci.* 51 (2009) 322–329.
- [83] Hsu, C. H., & Mansfeld, F. (2001). Technical Note: Concerning the Conversion of the Constant Phase Element Parameter Y₀ into a Capacitance. *CORROSION*, 57(9), 747–748.
- [84] A. Aballe, M. Bethencourt, F.J. Botana, M. Marcos, M.A. Rodríguez-Chacón, Corrosion monitoring of the AA2024 alloy in NaCl solutions by electrochemical noise measurements, *Rev. Metal.* (1998).
- [85] C. Poddar, J. Jayaraj, S. Ningshen, Passive film characteristics and corrosion behavior of thermally oxidized Ni₆₀Nb₃₀Ta₁₀ metallic glass in nitric acid medium, *J. Alloys Compd.* 783 (2019) 680–686. doi:10.1016/j.jallcom.2018.12.335.
- [86] M. P. Seah, W. A. Dench, "Quantitative electron spectroscopy of surfaces: A standard data base for electron inelastic mean free paths in solids, *Surface and Interface Analysis*, 1 (1979) 2–11, doi:10.1002/sia.740010103
- [87] C. Parigger, Atomic force microscopy, in: *Handb. Phys. Med. Biol.*, 2010.
-

References

- doi:10.1201/9781420075250.
- [88] J. Jayaraj, D. Nanda Gopala Krishna, C. Mallika, U. Kamachi Mudali, Passive film properties and corrosion behavior of Ni-Nb and Ni-Nb-Ta amorphous ribbons in nitric acid and fluorinated nitric acid environments, *Mater. Chem. Phys.* 151 (2015) 318–329. doi:10.1016/j.matchemphys.2014.11.073.
- [89] Z.M. Wang, J. Zhang, J.Q. Wang, Pit growth in a Ni-Nb metallic glass compared with its crystalline counterpart, *Intermetallics*. 18 (2010) 2077–2082. doi:10.1016/j.intermet.2010.06.010.
- [90] F. Ciesielczyk, P. Bartczak, K. Wieszczycka, K. Siwinska-Stefanska, M. Nowacka, T. Jesionowski, Adsorption of Ni(II) from model solutions using co-precipitated inorganic oxides, *Adsorption* 2 (2019) 1-12.
- [91] J. Jayaraj, A. Gebert, L. Schultz, Passivation behaviour of structurally relaxed Zr₄₈Cu₃₆Ag₈Al₈metallic glass, *J. Alloys Compd.* 479 (2009) 257–261. doi:10.1016/j.jallcom.2009.01.056.
- [92] R.D. Shannon, Revised effective ionic radii and systematic studies of interatomic distances in halides and chalcogenides, *Acta Crystallogr. Sect. A*. 32 (1976) 751–767. doi:10.1107/S0567739476001551.
- [93] Z. Song, X. Bao, U. Wild, M. Muhler, G. Ertl, Oxidation of amorphous Ni-Zr alloys studied by XPS, UPS, ISS and XRD, *Appl. Surf. Sci.* 134 (1998) 31–38. doi:10.1016/S0169-4332(98)00249-9.
- [94] J. Moulder, W. Stickle, P. Sobol, K. Bomben, *Handbook of X-ray Photoelectron Spectroscopy*, 1995. doi:10.1002/sia.740030412.
- [95] O. Knacke, O. Kubaschewski, K. Hesselmann, *Thermo-chemical Properties of Inorganic Substances*, Second Edition, Springer, Verlag 1991, (n.d.).
- [96] Z. Song, D. Tan, F. He, X. Bao, Surface segregation behaviors of amorphous Ni 65 Nb 35 alloy under oxidation in O₂ at various temperatures, *Appl. Surf. Sci.* (1999) 142–149. <http://www.sciencedirect.com/science/article/pii/S0169433298004668>.
- [97] J.R. Scully, A. Gebert, J.H. Payer, Corrosion and related mechanical properties of bulk metallic glasses, *J. Mater. Res.* 22 (2007) 302–313. doi:10.1557/jmr.2007.0051.
- [98] V. Schroeder, C.J. Gilbert, R.O. Ritchie, Comparison of the corrosion behavior of a bulk amorphous metal, Zr_{41.2}Ti_{13.8}Cu_{12.5}Ni₁₀Be_{22.5}, with its crystallized form, *Scr. Mater.* 38 (1998) 1481–1485. doi:10.1016/S1359-6462(98)00089-X.
- [99] J.R. Scully, A. Gebert, J.H. Payer, Corrosion and related mechanical properties of bulk metallic glasses, *J. Mater. Res.* 22 (2007) 302–313. doi:10.1557/jmr.2007.0051.
- [100] K.R. Lim, J.M. Park, S.J. Kim, E.S. Lee, W.T. Kim, A. Gebert, J. Eckert, D.H. Kim, Enhancement of oxidation resistance of the supercooled liquid in Cu-Zr-based metallic glass by forming an amorphous oxide layer with high thermal stability, *Corros. Sci.* 66 (2013) 1–4. doi:10.1016/j.corsci.2012.09.018.
- [101] E. Sikora, D.D. Macdonald, Nature of the passive film on nickel, *Electrochim. Acta*.

References

- 48 (2002) 69–77.
- [102] A.S. Bondarenko, G.A. Ragoisha, Variable Mott-Schottky plots acquisition by potentiodynamic electrochemical impedance spectroscopy, *J. Solid State Electrochem.* (2005). doi:10.1007/s10008-005-0025-7.
- [103] S. Clima, G. Pourtois, S. Van Elshocht, S. De Gendt, M.M. Heyns, D.J. Wouters, J.A. Kittl, Dielectric Response of Ta₂O₅, NbTaO₅ and Nb₂O₅ from First-Principles Investigations, in: 2009. doi:10.1149/1.3122128.
- [104] K.R. Zavadil, J.A. Ohlhausen, P.G. Kotula, Nanoscale Void Nucleation and Growth in the Passive Oxide on Aluminum as a Prepitting Process, *J. Electrochem. Soc.* 153 (2006) B296. doi:10.1149/1.2207739.
- [105] R. Busch, J. Schroers, W.H. Wang, Thermodynamics and Kinetics of Bulk Metallic Glass, *MRS Bull.* (2007). doi:10.1557/mrs2007.122.
- [106] D. V. Louzguine-Luzgin, C.L. Chen, L.Y. Lin, Z.C. Wang, S. V. Ketov, M.J. Miyama, A.S. Trifonov, A. V. Lubenchenko, Y. Ikuhara, Bulk metallic glassy surface native oxide: Its atomic structure, growth rate and electrical properties, *Acta Mater.* 97 (2015) 282–290. doi:10.1016/j.actamat.2015.06.039.
- [107] J. Jayaraj, C. Thinaharan, S. Ningshen, C. Mallika, U. Kamachi Mudali, Corrosion behavior and surface film characterization of TaNbHfZrTi high entropy alloy in aggressive nitric acid medium, *Intermetallics.* (2017). doi:10.1016/j.intermet.2017.06.002.
- [108] V.P. Zhdanov, B. Kasemo, Cabrera-Mott kinetics of oxidation of nm-sized metal particles, *Chem. Phys. Lett.* (2008). doi:10.1016/j.cplett.2008.01.006.
- [109] A.T.F. Jr., Space Charge in Growing Oxide Films. IV. Rate Effects Deduced by an Averaging Technique, *J. Chem. Phys.* 44 (1964) 3335. doi:doi: 10.1063/1.1725004.
- [110] P. Kofstad, *High Temperature Corrosion*, Elsevier Applied Science Publisher Ltd, England, 1988.
- [111] U. Otgonbaatar, W. Ma, M. Youssef, B. Yildiz, Effect of niobium on the defect chemistry and oxidation kinetics of tetragonal ZrO₂, *J. Phys. Chem. C.* (2014). doi:10.1021/jp504874v.
- [112] S. Ghosh, S. Roychowdhury, V. Kain, B.P. Sharma, P.V.A. Padmanabhan, K.K. Ray, Feasibility of ceramic coating to guard stainless steels against intergranular corrosion, *Surf. Eng.* (2008). doi:10.1179/174329408x281858.
- [113] E. McCafferty, Validation of corrosion rates measured by the Tafel extrapolation method, *Corros. Sci.* (2005). doi:10.1016/j.corsci.2005.05.046.
- [114] D.D. MacDonald, The history of the Point Defect Model for the passive state: A brief review of film growth aspects, in: *Electrochim. Acta*, 2011: pp. 1761–1772. doi:10.1016/j.electacta.2010.11.005.
- [115] F. Di Franco, G. Zampardi, M. Santamaria, F. Di Quarto, H. Habazaki, Characterization of the Solid State Properties of Anodic Oxides on Magnetron Sputtered Ta, Nb and Ta-Nb Alloys, *J. Electrochem. Soc.* (2011).

References

- doi:10.1149/2.031201jes.
- [116] R.M. Fleming, D. V. Lang, C.D.W. Jones, M.L. Steigerwald, D.W. Murphy, G.B. Alers, Y.H. Wong, R.B. Van Dover, J.R. Kwo, A.M. Sergent, Defect dominated charge transport in amorphous Ta₂O₅ thin films, *J. Appl. Phys.* (2000). doi:10.1063/1.373747.
- [117] Z. Grubac, Z. Petrovic, J. Katic, M. Metikos-Hukovic, R. Babic, The electrochemical behaviour of nanocrystalline nickel: A comparison with polycrystalline nickel under the same experimental condition, *J. Electroanal. Chem.* 645 (2010) 87–93. doi:10.1016/j.jelechem.2010.04.018.
- [118] U.R. Evans, *The corrosion and Oxidation of Metals*, Edward Arnold, London, 1960. p. 324.
- [119] D.A. Harrington, P. Van Den Driessche, Mechanism and equivalent circuits in electrochemical impedance spectroscopy, in: *Electrochim. Acta*, 2011. doi:10.1016/j.electacta.2011.01.067.
- [120] H. Ardelean, I. Frateur, P. Marcus, Corrosion protection of magnesium alloys by cerium, zirconium and niobium-based conversion coatings, *Corros. Sci.* (2008). doi:10.1016/j.corsci.2008.03.015.
- [121] O.P. Thakur, C. Prakash, R.K. Sharma, Study of dielectric and piezoelectric properties of Pb(Ni,Nb)O₃-Pb(Zr,Ti)O₃ ceramics using mechanically activated powder, *J. Mater. Sci.* (2007). doi:10.1007/s10853-006-1120-6.
- [122] C. Poddar, J. Jayaraj, S. Ningshen, U.K. Mudali, Effect of thermal oxidation on the oxide characteristic and corrosion behavior of Ni₆₀Nb₄₀ amorphous ribbon in nitric acid, *Appl. Surf. Sci.* (2019). doi:10.1016/j.apsusc.2019.02.089.